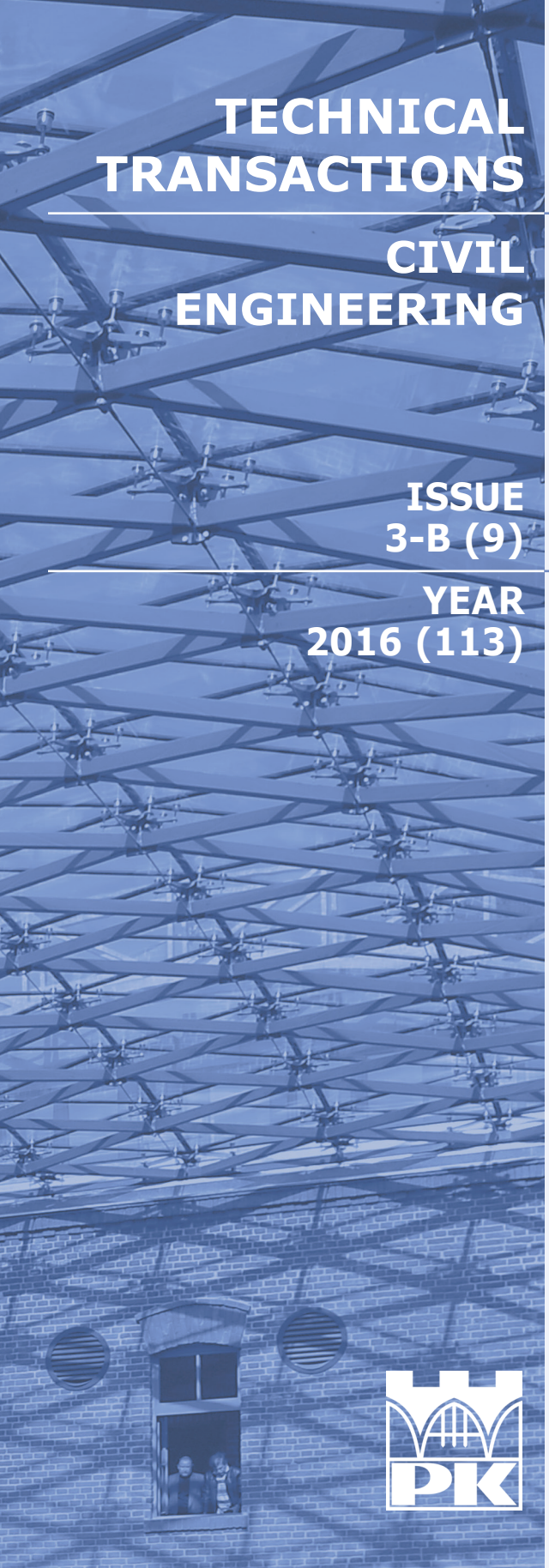

TECHNICAL TRANSACTIONS
CZASOPISMO TECHNICZNE

CIVIL ENGINEERING
BUDOWNICTWO

ISSUE 3-B (9)
ZESZYT 3-B (9)

YEAR 2016 (113)
ROK 2016 (113)

WYDAWNICTWO POLITECHNIKI KRAKOWSKIEJ

TECHNICAL TRANSACTIONS | CZASOPISMO TECHNICZNE

CIVIL ENGINEERING | BUDOWNICTWO

ISSUE 3-B (9) | ZESZYT 3-B (9)
YEAR 2016 (113) | ROK 2016 (113)

Basic version of each Technical Transactions magazine is its online version
Pierwotną wersją każdego zeszytu Czasopisma Technicznego jest jego wersja online
www.ejournals.eu/Czasopismo-Techniczne www.technicaltransactions.com www.czasopismotechniczne.pl

Civil Engineering Series
3-B/2016

TECHNICAL TRANSACTIONS | CZASOPISMO TECHNICZNE
CIVIL ENGINEERING | BUDOWNICTWO
3-B/2016

DOI: 10.4467/2353737XCT.16.207.5956

PIOTR BOŃKOWSKI*, MACIEJ YAN MINCH**

SELECTED PROBLEMS RELATING TO STRUCTURAL CALCULATIONS OF BUILDINGS LOCATED IN MINING AREAS IN TERMS OF PREVENTIVE PROTECTION

WYBRANE PROBLEMY PROJEKTOWANIA KONSTRUKCJI BUDYNKÓW NA TERENACH GÓRNICZYCH W ASPEKCIE ZABEZPIECZEŃ PROFILAKTYCZNYCH

A b s t r a c t

This paper discusses the effect of the cross-sectional dimensions of the main structural members of a frame building on the internal forces generated in it by mining-induced tremors and choice of a code combination of actions on the dimensioning of a building structure. A numerical analysis of a reinforced concrete building was carried out for different cross-sectional dimensions of its loadbearing system subjected to mining-induced seismicity occurring in the Legnica-Glogow Copper District (LGOM) area. Additionally, a simplified cost analysis for a selected column was performed.

Keywords: mining damage, numerical analysis, dynamic loads

S t r e s z c z e n i e

W artykule przedstawiono wpływ wielkości przekrojów układu nośnego budynku szkieletowego na siły wewnętrzne wywołane wstrząsem górniczym oraz wpływ doboru kombinacji normowej obciążeń na wymiarowanie konstrukcji. Przedstawiono analizę numeryczną żelbetowego budynku o zróżnicowanych wymiarach przekroju układu nośnego, który został poddany oddziaływaniom parasejsmicznym występującym na obszarze LGOM. Dodatkowo przeprowadzono uproszczoną analizę kosztową analizowanych wariantów obliczeń dla wybranego słupa.

Słowa kluczowe: szkody górnicze, analiza numeryczna, obciążenia dynamiczne

* M.Sc. Eng. Piotr Bońkowski, Department of Mechanics and Structural Engineering, Opole University of Technology.

** Ph.D. Eng. Maciej Yan Minch, Faculty of Civil Engineering, Wroclaw University of Technology.

1. Introduction

Protection of a building against mining damages is a very important and challenging problem for many areas in Poland [3]. Since one of the mining damage aspects are mining-induced tremors, it is crucial to know how different factors influence the costs of building protection.

The additional internal forces generated in a building structure by a mining-induced tremor are the result of several factors, such as: the loadbearing system's geometry and stiffness, the distribution of masses in the structure and the peculiarities of the mining-induced tremor [1, 2, 14]. Since the dynamic characteristics of the tremor are beyond the building designer's control, one primary task is to design the loadbearing system so as to minimise the costs involved in the additional protection of the building against seismically-induced loads. Besides the loadbearing system stiffening geometry, also the ratios of the stiffnesses of the particular structural members need to be determined. The analysis of a reinforced concrete building structure carried out in this paper shows that increasing structural stiffness by increasing the cross sections of the building's frame loadbearing system members does not always lead to a reduction in the overall costs of the construction project.

Also, the effect of a selected code combination of ultimate limit state loads on building structure dimensioning – a still unresolved problem in the technical literature – is analysed in this paper.

2. Computational model

A schematic of the computational model is shown in Figs. 1–2. The grid lines mark off 9 fields designated with the letters from *a* to *i*, respectively. In order to eliminate any effects due to computational system stiffness and mass distribution irregularity, the structure has the form of a simple regular solid. The building's loadbearing system consists of eight reinforced concrete columns braced together with reinforced concrete beams (described further as respectively "Columns 1" and "Beams"), located on the perimeter of inner field *e* and twelve outer reinforced concrete ("Columns 2") in the exterior corners of the other fields. The floors of the particular storeys are monolithic reinforced concrete slabs. The structure is settled on medium dense sand deposits, which "C" ground type according to code [12]. The columns on the perimeter of field *e* are fixed to 6×6 m foundation slab in the model they are elastically fixed in the subsoil, whose elasticity modulus is k_z = 500 MN/m. Others columns are fixed 2.5×2.5 m foundations and the elastic modulus in model k_z = 225 MN/m was assumed. The skeleton bracing the building against the action of horizontal forces is situated within axes 2–4/B–D.

Two structural models, in which the stiffness of the system was changed by modifying the stiffness of its individual members, were analysed. The geometric dimensions of the members in Model 1 and in reference Model 2, where the stiffness of selected linear elements was increased, are presented in Table 1. In Model 2, the dimensions of the geometric cross sections of the members belonging to the groups: Columns 1 and Beams were increased mainly to make the structure more rigid and to minimise second order effects.

For the numerical analysis, the bar structure (columns and beams) and the surface structure (floors) were divided into finite elements. The computational models were subjected to analysis in the SAP2000 v. 17.2 program.

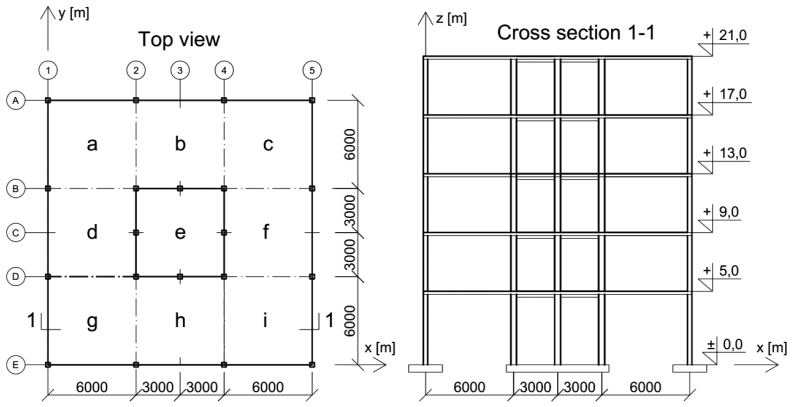

Fig. 1. Modular axes and cross section of basic model

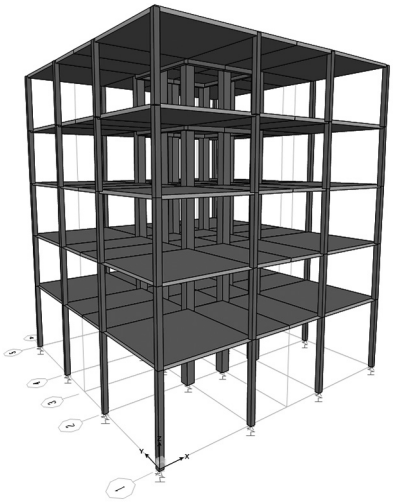

Fig. 2. 3D view of analysed basic model

Table 1

Dimensions of structural members in Model 1 and Model 2

	Column 1	**Column 2**	**Beam**	**Slab**
Model 1	40×40 cm	30×30 cm	20×40 cm	20 cm
Model 2	60×60 cm	30×30 cm	30×60 cm	20 cm

Exemplary computations of the internal forces changing along the height of the structure, the dimensioning of the members and a cost analysis were carried out for the corner columns of field *e*.

Loads' take down and dimensioning were performed in accordance with the procedures described in the current Eurocode [7–12]. The following assumptions concerning the loads were made:

- The snow load as for zone 1, with a characteristic value of 0.56 kN/m^2.
- The wind load on the walls as for wind zone 1, with a total characteristic value of 0.73 kN/m^2.
- The characteristic operational loading of the floors amounting to 4.2 kN/m^2.
- The characteristic operational loading of the roof slab amounting to 0.4 kN/m^2.
- The additional dead weight of the floors, including that of the finishing layers, amounting to 1.75 kN/m^2.
- The additional dead weight of the roof slab, including that of the finishing layers, amounting to 1.78 kN/m^2.

The following additional assumptions necessary for the computations were made:

- The response spectrum method defined for the LGOM (Legnica-Glogow Copper District) area by Zembaty [13] (terrain C with acceleration $a = 0.6$ m/s^2) was to be used.
- Grade C30/37 concrete used for all the structural members.
- The steel with yield point $f_{yk} = 500$ MPa.
- The XC3 exposure class of the columns.
- In dimensioning, the second order effects were to be taken into account using the nominal curvature method.
- For the dynamic calculations, the stiffness of the members was assumed to be equal to half of the nominal stiffness, in accordance with pt. 4.3.1(6) of the EC8 code [12].

An important element of any structural analysis is the selection of a proper code combination of loads to ensure that the minimal and maximal internal forces will be obtained. The technical literature does not explicitly specify which combination of loads should be used when a seismically-induced tremor needs to be taken into account.

Formulas (1–6) define the above problem and the different load combination variants:

$$F_d = \sum_1^m \gamma_{fi} G_{ki} + 0.8 \sum_1^n \gamma_{fi} Q_{ki} + F_a \tag{1}$$

$$E_d = E\left\{G_{k,j}; \psi_{2,i} Q_{k,i}; A_{Ed}\right\} \; j \geq 1, i \geq 1 \tag{2}$$

$$E_d = E\left\{G_{k,j}; (\psi_{1.1} \text{or } \psi_{2.1}) Q_{k,1}; \psi_{2,i} Q_{k,i}; A_d\right\} \; j \geq 1, i \geq 1 \tag{3}$$

$$E_d = E\left\{\gamma_{G,j} G_{k,j}; \gamma_g \psi_{0.1} Q_{G,k}; \gamma_{Q,i} \psi_{0,i} Q_{k,i}; A_w\right\} \; j \geq 1, i \geq 1 \tag{4}$$

$$E_d = E\left\{\gamma_{G,j} G_{k,j}; \gamma_{Q,i} \psi_{0,i} Q_{k,i}; \left(A_w \text{ or } A_g\right)\right\} \; j \geq 1, i \geq 1 \tag{5}$$

$$E_d = E\left\{\gamma_{G,j} G_{k,j}; \gamma_g Q_{G,k}; \gamma_{Q,i} \psi_{0,i} Q_{k,i}\right\} \; j \geq 1, i \geq 1 \tag{6}$$

where:

F_d, E_d – design action effect,
γ_{fi} – safety factor according to [6],

G_k – characteristic permanent action according to [6] (eq. (1)) or [7] (eq. (2–6)),
Q_k – characteristic variable action according to [6] (eq. (1)) or [7] (eq. (2–6)),
F_a – accidental action according to [6],
ψ_2 – factor for quasi-permanent value of a variable action according to [7],
A_{Ed} – design value of seismic action according to [7],
ψ_1 – factor for frequent value of a variable action according to [7],
A_d – design value of an accidental action,
γ_G – partial factor for permanent actions according to [7],
γ_g – partial factor for continuous deformations according to [4, 13],
ψ_0 – factor for combination value of variable action according to [4, 13],
γ_Q – partial factor for variable actions according to [7],
A_w – design value of an accidental action from mining tremors according to [4, 13],
A_g – design value of an accidental action from non-continuous mining deformations according to [4, 13].

Problems relating to the adoption of a combination of loads are discussed in, e.g., [4, 5, 13]. According to the former Polish standard [6], formula (1) should be used (as for accidental actions). Code EC0 [7] distinguishes a seismic combination according to formula (2) and an extraordinary combination according to formula (3). Variable loads in the new code are treated as characteristic loads (without the safety factor). In [4, 13] a synthesis of the two codes, in the form modified consistently with formulas (4) and (5) was proposed. Factors $\psi_{0.1}$ and $\psi_{0,i}$ are equal to 0.8. Different guidelines for defining load combinations can be found in [14], where it is recommended to use relations consistent with formula (3), as for the sustained loads. A completely different, controversial proposal would be to treat the seismic load not as an accidental load, which (acc. to standard [7]) "is unlikely to occur on a given structure during the design working life", but as a variable load, consistently with formula (6).

One should also note that as the safety factors change, so do the shares of the masses having a bearing on the vibration parameters, which results in a change in the natural vibration period and in a change in the values of the inertial forces arising from the accelerations of the system masses.

The internal forces according to combination (3) (Model 1a) and the ones according to combination (5) (Model 1b) are compared in this paper.

3. Comparative analysis

The natural vibration periods for the analysed models are presented in Table 2. Five presented modes are needed by [12] to achieve 90% of the total mass of the structure by the sum of the effective modal masses. Mode shapes of vibrations for "Model 1a" are presented on (Fig. 3) for other models they are similar. Since calculations showed that the first mode of vibration for the two models was torsional, the second mode of vibration was adopted as the basic one and marked on the response spectrum diagram (Fig. 4).

Table 2

Natural vibration period of computational models [s]

Mode of vibration	Model 1a	Model 1b	Model 2
1	2.801	3.548	1.964
2	2.563	3.247	1.520
3	2.547	3.227	1.502
4	0.883	1.116	0.627
5	0.806	1.019	0.463

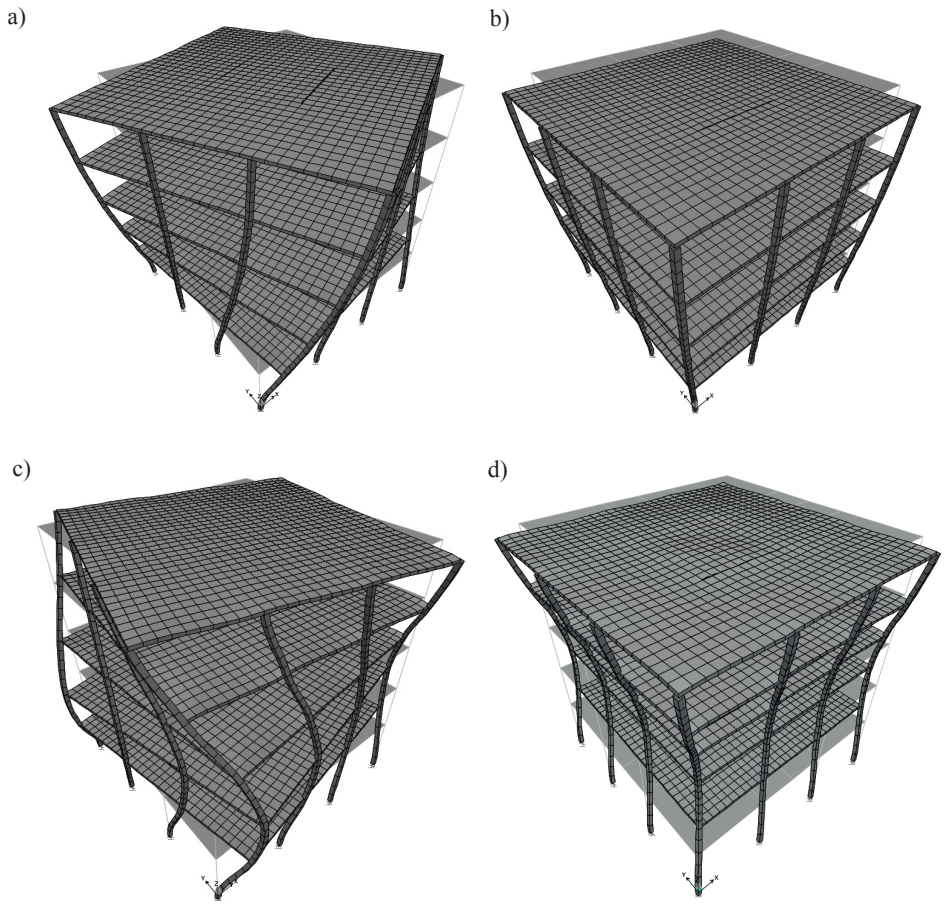

Fig. 3. Mode shapes of vibrations for "Model 1a": a) 1st mode, b) 2nd mode, 3rd mode similar, c) 4th mode, d) 5th mode

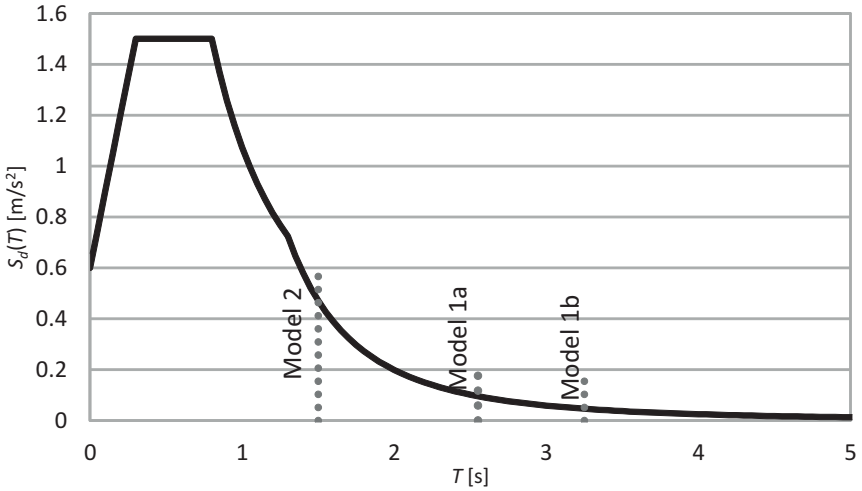

Fig. 4. Acceleration response spectrum acc. to Zembaty [9] for the LGOM area. Second form of natural period was marked with red lines

The successive forms of vibration can be taken into account in structural calculations in several ways [2]. The main two ways are: the SRSS combination (7) and the CQC combination (8). The SRSS combination can be used when the vibration periods of the particular forms do not differ by more than 10%. In the CQC combination, the interdependence between the vibrations forms is defined by a correlation coefficient, which depends on the structure's damping and on the ratio between the particular vibration frequencies. Considering that the differences between the vibration periods of the analysed models are small and that the CQC combination can be easily implemented in modern computer programs for calculating building structures in seismic areas, this combination was used in the analysis presented below.

$$r_o = \sqrt{\sum_{i=1}^{N} r_{io}^2} \tag{7}$$

$$r_o = \sqrt{\sum_{i=1}^{N}\sum_{n=1}^{N} \rho_{in} r_{io} r_{no}} \tag{8}$$

where:

r_o – the total effect of the impacts,
ρ_{in} – the coefficient of the correlation between the vibration forms,
r_{io} – the effect of the action of the i-th form of vibration,
r_{no} – the effect of the action of the n-th form of vibration.

The envelopes of the combinations of internal forces in the column situated in node 4D are shown (along the column height) in the diagrams in Figs. 5–7. In order to better interpret the results, the wind load along the 0Y direction was neglected. The combinations, which do not take into account mining-induced tremors, are referred to as "static 1a" and "static 2" for

model 1 and model 2 respectively, while the combinations, which take into account dynamic impacts, are designated as respectively “dynamic 1a”, “dynamic 1b” and “dynamic 2”.

The required bar area along the column height in node 4D is shown in Fig. 8. Symmetric reinforcement in both directions x and y of the column cross-sectional area was assumed. The computational criterion was to minimise the amount of reinforcement by, e.g., bundling (as far as possible) rebars in the column’s corners and using the commercially available rebar cross sections. The computed amount of reinforcement is only approximate since auxiliary

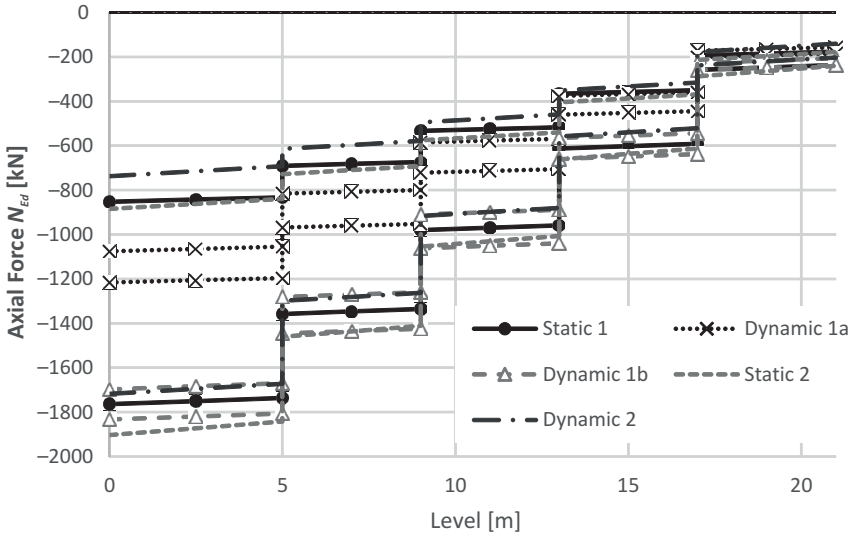

Fig. 5. Envelope of axial forces N_{Ed} in column in node 4D

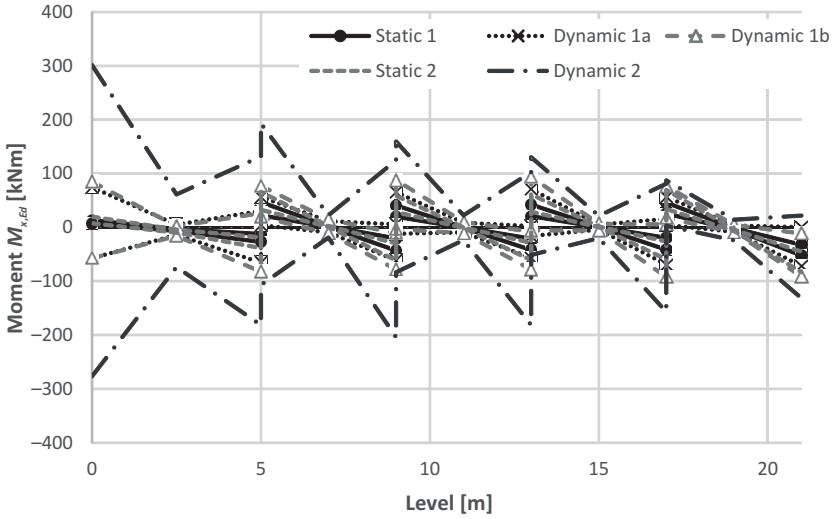

Fig. 6. Envelope of moments $M_{x,Ed}$ in column in node 4D

and excess reinforcement (laps, anchorages, etc.) needed to properly construct a structural member were not included.

Reinforcement costs were compared for the reinforcement amount necessary from the point of view of the structure's loadbearing capacity. The additional amount of reinforcement required for laps and reinforcement anchorages was not taken into account.

The following average prices of the materials were assumed: reinforcement steel – 2.00 PLN/kg and grade C30/37 concrete – 280 PLN/m^3.

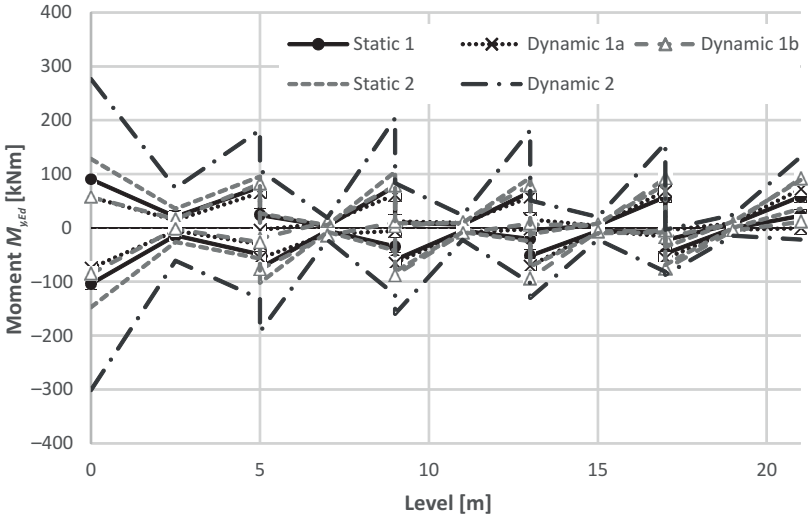

Fig. 7. Envelope of moments $M_{y,Ed}$ in column in node 4D

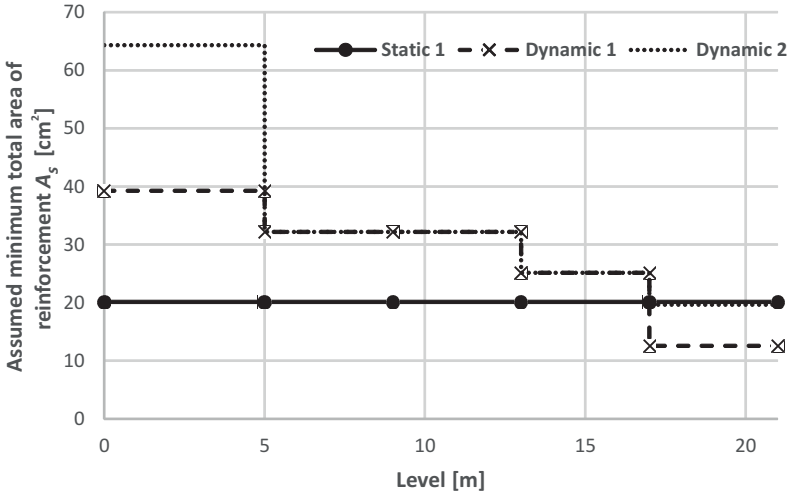

Fig. 8. Total required reinforcement area. In level interval of 5–17 dynamic 1 graph coincides with reinforcement value of dynamic 2

Table 3

Approximate costs of materials necessary to build column in node 4D

	Static 1	Dynamic 1a	Dynamic 1b	Dynamic 2
Reinforcement weight	332 kg	431 kg	470 kg	595 kg
Reinforcement cost	664 PLN	862 PLN	940 PLN	1190 PLN
Concrete volume	3.36 m^3	3.36 m^3	3.36 m^3	7.56 m^3
Concrete cost	941 PLN	941 PLN	941 PLN	2117 PLN
Total cost	1605 PLN	1803 PLN	1881 PLN	3307 PLN

4. Conclusion

The analysis has indicated several important factors having a bearing on the optimum design of building structures in mining areas.

The obvious conclusion is that when the dimensions of the cross sections are increased, the stiffness of the structure also increases and consequently the natural vibration period decreases (Tab. 2). However, the structural engineer must be aware that this change may have a highly adverse effect on the internal forces produced in the structure by seismically-induced loads. A comparison of Model 1 and Model 2 shows that when the cross sections of the columns in Model 2 were increased, the natural vibration period decreased by about 40%, but the S_d value increased several times in comparison with that in Model 1 (Fig. 2). An analysis of the graphs of the internal forces produced by the static load (Figs. 5–7) shows that the change in the stiffness of the interior columns did not result in a substantial redistribution of the internal forces. Therefore, one can assume that if the cross sections were increased, the steel consumption would significantly decrease. However, when designing a building structure in an area where mining damage occurs, one should take into account the increased dynamic loads. If the designer incorrectly assumed that by increasing the concrete cross section the amount of reinforcement would be reduced, this would result in 25% higher expenditures on reinforcing rods (Fig. 8, Tab. 3), not to mention the higher cost due to the increased consumption of concrete.

A mining-induced tremor has a more adverse effect on reinforced concrete columns than a static load (e.g. a wind load). In the analysed model, the moments generated by the dynamic combinations were at best close to the static ones, and at worst they were over twice higher. Moreover, during a tremor the column is bent in two directions. One should also note that in dynamic combinations the beneficial effect of the compressive axial force is much smaller.

The choice of a proper code combination of loads is not obvious. As shown in the example, when the more conservative approach [4–6, 13] than the one strictly complying with [14] is adopted, larger masses of the structure are taken into account, whereby the natural vibration periods are considerably lowered (Tab. 2). In the LGOM area, this may entail a reduction in the resultant acceleration acting on the loadbearing structure masses (Fig. 2). Due to all the above factors, the internal forces in the building's geometric system (Figs. 5–7) do not

differ significantly, regardless of the adopted combination, and consequently the cost of the preventive protection of the structure against seismically-induced impacts does not change significantly (Fig. 8, Tab. 3).

It should be added that because of the ongoing research into the forms of response spectra in mining areas in Poland and the implementation of code EC8 [12] in dynamic design, problems have arisen, which affect analytical results due to interpretation difficulties involved in mainly the unambiguous definition of calculation assumptions modelling the dynamics of a building structure. One can mention here problems connected with the choice of a proper response spectrum and the definition of a proper code combination.

References

[1] Bońkowski P., Minch M.Y., *Effect of building shape irregularity on internal forces generated by mining-induced tremors* (in Polish), "Materiały Budowlane" 6/2015, 56–57.

[2] Chopra A.K., *Dynamics of Structures: Theory and Applications to Earthquake Engineering*, Fourth Edition, Prentice Hall 2012.

[3] Florkowska L., *Building protection against the backdrop of current situation and growth perspectives for polish mining industry*, "Archives of Mining Sciences" Vol. 57, Issue 3, 645–655.

[4] Kawulok M., *Mining damage in construction* (in Polish), ITB, Warsaw 2015.

[5] Kwiatek J., *Civil structures in mining damage areas*, GIG, Katowice 2007.

[6] Polish Standard PN-82/B-02000: Building Loads. Principles of determining load values (in Polish).

[7] PN-EN 1990:2004 Eurocode 0: Foundations of structural design (in Polish).

[8] PN-EN 1991-1-1:2004 Eurocode 1: Impacts on structures. Part 1–1: General impacts. Weight by volume, deadweight, operational load in buildings (in Polish).

[9] PN-EN 1991-1-3 Eurocode 1: Impacts on structures. Part 1–3: General impacts – Snow load (in Polish).

[10] PN-EN 1991-1-4 Eurocode 1: Impacts on structures. Part 1–4: General impacts – Wind load (in Polish).

[11] PN-EN 1992-1-1:2008 Eurocode 2: Design of concrete structures. Part 1–1: General rules and rules for buildings (in Polish).

[12] PN-EN 1998-1:2005. Design of structures subject to seismic impacts. Part 1: General rules, seismic impacts and rules for buildings (in Polish).

[13] Szulc J., Lipski Z., Kawulok M., Cholewicki A., *Principles for determining loads and checking ultimate limit states of buildings located in mining areas with reference to EUROCODES* (in Polish), ITB, Warsaw 2012.

[14] Zembaty Z. et al., *Industry guidelines for designing enclosed buildings in LGOM, taking into account mining-induced tremor dynamic impacts. Volume I – Design guidelines* (in Polish), Opole University of Technology Publishing House, Opole 2012.

TECHNICAL TRANSACTIONS | CZASOPISMO TECHNICZNE
CIVIL ENGINEERING | BUDOWNICTWO
3-B/2016

DOI: 10.4467/2353737XCT.16.208.5957

PAWEŁ BOROŃ, JOANNA DULIŃSKA*

SEISMIC PERFORMANCE OF A REINFORCED CONCRETE BRIDGE UNDER A SEQUENCE OF SEISMIC SHOCKS USING THE CONCRETE DAMAGE PLASTICITY MODEL

ODPOWIEDŹ DYNAMICZNA MOSTU ŻELBETOWEGO NA SEKWENCJĘ WSTRZĄSÓW SEJSMICZNYCH Z ZASTOSOWANIEM MODELU BETONU PLASTYCZNEGO ZE ZNISZCZENIEM

Abstract

This paper investigates the dynamic performance of a concrete bridge under a sequence of earthquakes. The PGA of the mainshock and the aftershock were comparable. The concrete damage plasticity model of material was assumed to represent the plastic behaviour of the bridge. Firstly, the mainshock was applied to the bridge, then the aftershock was imposed on the structure which had already been weakened by the first shock. The analysis of plastic and damage measures revealed that the aftershock had a considerable effect upon the structure in terms of enlarging zones affected by irreversible strains or additional damage evolution.

Keywords: seismic sequence, reinforced concrete bridge, concrete damage plasticity model

Streszczenie

W artykule przedstawiono analizę odpowiedzi dynamicznej mostu żelbetowego na sekwencję wstrząsów sejsmicznych. Wartości PGA dla wstrząsu głównego oraz wtórnego były porównywalne. W celu przedstawienia plastycznej pracy konstrukcji zastosowano model betonu plastyczny ze zniszczeniem. Analiza stref plastycznych oraz uszkodzeń elementów wykazała znaczący wpływ obu wstrząsów na konstrukcję. Wstrząs wtórny, działający na konstrukcję wcześniej uszkodzoną przez wstrząs główny, wywołuje zwiększenie strefy odkształceń plastycznych, rozwój zarysowań oraz degradację sztywności.

Słowa kluczowe: wstrząs wtórny, most żelbetowy, model betonu plastyczny ze zniszczeniem

* M.Sc. Eng. Paweł Boroń, Prof. D.Sc. Ph.D. Eng. Joanna Dulińska, Institute of Structural Mechanics, Cracow University of Technology.

1. Introduction

Within a short period of time, large seismic events are usually followed by several aftershocks. Since aftershocks affect structures that have already been weakened during a mainshock, they can play a crucial role in the dynamic behaviour of a structure in terms of irreversible plastic strains and accumulated damage. Structures may go plastic or even collapse during aftershocks since they have already become degraded and cracked during main shocks.

Over the last decade, the dynamic response of structures under replicated seismic shocks has been extensively studied. Concrete structures in particular may suffer severe damage when exposed to a sequence of earthquakes [5, 6, 11]. Representative examples of damage to structures observed under multiple earthquakes can be found in contemporary studies [1, 2].

In the paper, the dynamic performance of a reinforced concrete bridge subjected to a mainshock-aftershock seismic sequence is investigated. In order to compare damages under repeated shocks and assess the impact of both events on the bridge, the concrete damage plasticity model, which describes multi-hardening plasticity and damage (cracking), was implemented. Only advanced constitutive models of concrete, that include damage and failure phenomena, may demonstrate inelastic behaviour and progressive damage of the concrete bridge under repetitive shocks.

2. Basic parameters of the structure

In this study, an existing reinforced concrete bridge was analysed as a structure subjected to a sequence of seismic shocks. The total length of the three-span road bridge was 84 m. The length of the middle span was 29 m and the length of the outer spans was 27.5 m (Fig. 1).

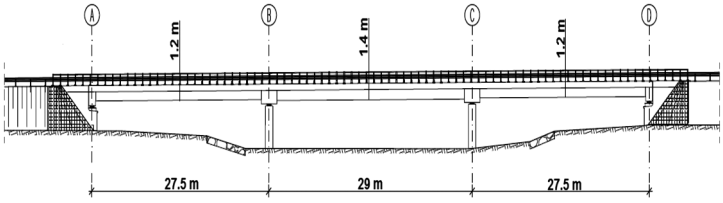

Fig. 1. The three-span reinforced concrete bridge – side view

The bridge was built as a pre-stressed concrete beam-slab structure. Every span consisted of eleven prefabricated reinforced T-shape beams (Fig. 2). T24 and T27 beams were used in the outer and the middle spans, respectively. These types of beam differed from each other with respect to their dimensions. The dimensions of the T27 beam were as follows: height – 110 cm, width of lower part – 27 cm, width of top part – 84 cm. The dimensions of the T24 beam were slightly different: height – 100 cm, width of bottom part – 24 cm, width of top – part 84 cm. The beams were made of B50 (C40/45) concrete. Each beam was equipped with twenty-four pre-stressing tendons with a diameter of 15.5 mm to produce the compressive stress that balanced the tensile stress that the girders would otherwise experience.

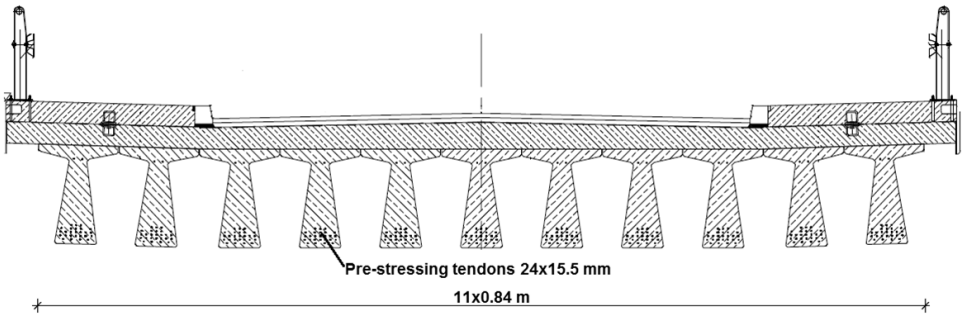

Fig. 2. The cross-section of the bridge superstructure

The bridge deck was built as a slab monolithically connected with the beams. The slab thickness varied from 20 cm at the thinnest point to 30 cm at the thickest point. The bridge superstructure was supported on pillars and abutments by stiff bearings. There were four bearings located on every support.

3. The numerical model of the bridge

In order to carry out the dynamic analysis of the bridge, a numerical model of the structure was created using the ABAQUS software [12]. In the model, all structural elements (i.e. beams, slabs, bearings, pillars and abutments) were taken into account. The geometry and dimensions of the elements were taken from the technical description of the object.

In the model, a link between the top surface of the beam and the slab was provided by a 'TIE' constraint that makes the translational and rotational degrees of freedom equal for a pair of surfaces [12]. The pre-stressing tendons of the beams and the reinforcement of the bridge slab were also taken into consideration in the model since the ABAQUS software allows for the insertion of rebar layers into concrete structures as 'fuzzy layers' [5].

It was assumed that the bridge is located on stiff subsoil; therefore, the soil-structure interaction was not considered. The fixed boundary conditions were imposed on pillars and abutments that reflected the high rigidity of the bridge subsoil.

Two kinds of finite elements, provided by the ABAQUS software, were used in the numerical model – solid elements C3D8R and continuum shell elements CS8R (8 nodes with 3 degree of freedom in both cases). Solid elements were used to model the beams, the pillars and the abutments, whereas the thin slab was discretised with continuum shell elements. Such a manner of discretisation allowed a reduction of the number of degree of freedom in the entire model and the accelerations of calculations. To improve the efficiency of calculations, the FE mesh was densified only in areas where stress concentration was predicted (i.e. in the middle of each span and at the ends of each beam). In total, the mesh consisted of around 150.000 solid and 23.000 shell elements. Further densification of the mesh did not introduce noticeable changes to the results.

The numerical model of the bridge is shown in Fig. 3. The meshing of the beams is shown in Fig. 4. The beam located in the central span of the bridge with the FE mesh densified in the middle of span and at the end is presented in Fig. 4a; the details of the FE mesh of the beam end are displayed in Fig. 4b.

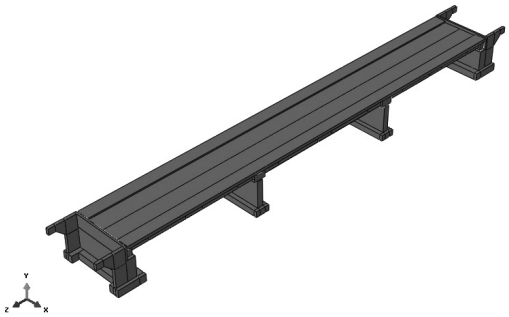

Fig. 3. The numerical model of the bridge

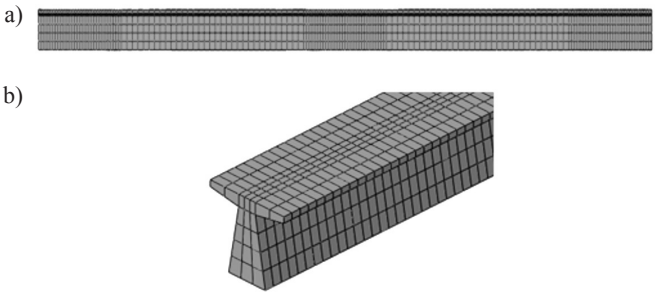

Fig. 4. (a) FE mesh densified in the middle of the span and at the end of the beam located in the central span; (b) details of the FE mesh used for the analysis of the pre-stressed concrete beam

4. Parameters of the concrete damage plasticity material model

To represent the elastic-plastic behaviour of the concrete bridge under a sequence of seismic shocks, the concrete damage plasticity model (CDP) was assumed as a constitutive model of the concrete material [8, 10]. The CDP model, implemented in the ABAQUS software, allows the description of all phenomena typical of the concrete material that occur during cyclic loading [3, 4, 9]. The CDP model uses concepts of the combination of non-associated multi-hardening plasticity and scalar damaged elasticity to represent the inelastic behaviour of concrete and to describe the irreversible damage that occurs during the fracturing process.

Different material parameters for tension and compression were defined in the model that allowed precise imitation of the realistic behaviour of the concrete material in a complex state of stress. Stress-strain dependence in tension and in compression for B50 concrete is shown in Fig. 5a and 5b, respectively [7].

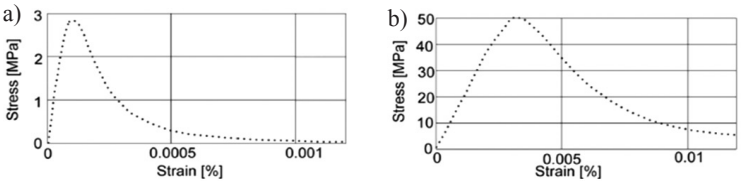

Fig. 5. Dependence σ–ε for B50 concrete in: (a) tensile test, (b) compression test [7]

Except typical engineering measure, like strain, logarithmic strain or equivalent plastic strain could be analysed in this model of concrete material. In large deformation analysis, logarithmic strain (LE) allows the description of strain more precisely than engineering measures. Expressing strain in a logarithmic form allows the comparison of the current element length directly with the initial element length. This strain could be described by equation (1):

$$\varepsilon = \ln \frac{l_0 + \Delta l}{l_0} = \ln \frac{l_1}{l_0} \tag{1}$$

where:

l_0 – initial length,
l_1 – current length,
Δl – increase in length.

In the CDP model, the effect of material damage is taken into consideration. The yield surface is controlled by two hardening variables representing equivalent plastic strains: $\tilde{\varepsilon}_t^{pl}$ and $\tilde{\varepsilon}_c^{pl}$, linked to failure mechanisms under tension and compression loading, respectively. To describe the damage process of the concrete material stiffness degradation, scalar value d, tensile damage variable d_t, compressive damage variable d_c are implemented (SDEG, DAMAGET and DAMAGEC, respectively).

Tensile and compressive stiffness degradation parameters depend on the level of equivalent plastic strain $\tilde{\varepsilon}^p$:

$$d_c = d_c\left(\tilde{\varepsilon}_c^{pl}\right) \tag{2.1}$$

$$d_t = d_t\left(\tilde{\varepsilon}_t^{pl}\right) \tag{2.2}$$

where:

$\tilde{\varepsilon}_c^{pl}$ – compressive equivalent plastic strain,
$\tilde{\varepsilon}_t^{pl}$ – tension equivalent plastic strain.

Equivalent plastic strain $\tilde{\varepsilon}^{pl}$ (marked in the ABAQUS as PEEQ – for compression, PEEQT – for tension) describes the total plastic strain level in elements. This parameter allows the determination of increases of plastic strain for every step of analysis and to follow the process of strain accumulation. In the CDP model, these parameters was described as follows:

$$\tilde{\varepsilon}_t^{pl} = \tilde{\varepsilon}_t^{ck} - \frac{d_t}{\left(1 - d_t\right)} \cdot \frac{\sigma_t}{E_0} \tag{3.1}$$

$$\tilde{\varepsilon}_t^{ck} = \varepsilon_t - \varepsilon_{0t}^{el} \tag{3.2}$$

$$\varepsilon_{0t}^{el} = \frac{\sigma_t}{E_0} \tag{3.3}$$

$$\tilde{\varepsilon}_c^{pl} = \tilde{\varepsilon}_c^{in} - \frac{d_c}{(1-d_c)} \cdot \frac{\sigma_c}{E_0} \tag{3.4}$$

$$\tilde{\varepsilon}_c^{in} = \varepsilon_c - \varepsilon_{0c}^{el} \tag{3.5}$$

$$\varepsilon_{0c}^{el} = \frac{\sigma_c}{E_0} \tag{3.6}$$

where:

$\tilde{\varepsilon}_t^{ck}$, $\tilde{\varepsilon}_c^{in}$ – cracking strain, crushing (inelastic) strain,
$\varepsilon_{t,c}$ – total strain (tensile, compressive),
$\varepsilon_{0t,c}^{el}$ – elastic strain (tension, compression) in undamaged material,
E_0 – initial stiffness.

The CDP model uses concepts of non-associated, multi-hardening plasticity. The illustration of the cracking strain used for the definition of tension stiffening data is shown in Fig. 6a. The illustration of the crushing strain used for the definition of compression hardening data is presented in Fig. 6b.

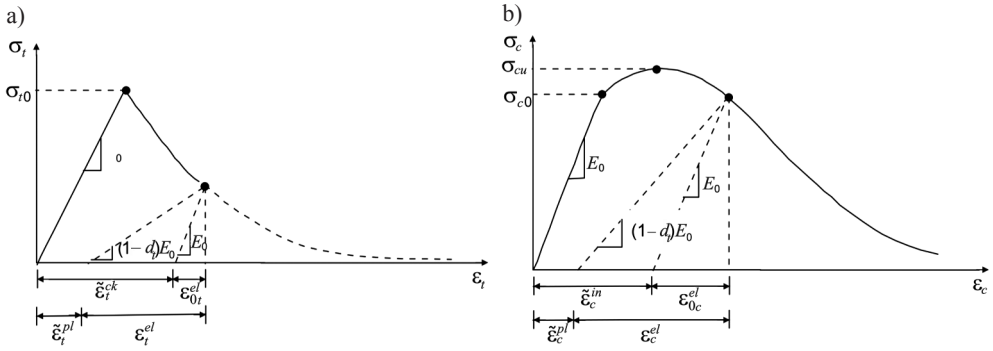

Fig. 6. Illustration of: (a) the cracking strain used for the definition of tension stiffening data, (b) the crushing strain used for the definition of compression hardening data [12]

Knowing the way in which damage parameters were determined, the parameter of the total stiffness degradation can be presented. The degree of stiffness degradation for elements depends on the relative occurrence of damage to tension and compression. This relation can be expressed by equation (4):

$$(1-d) = (1-d_c)(1-d_t) \tag{4}$$

Tensile damage variable d_t and compressive damage variable d_c can take values from zero (undamaged material) to one (total loss of strength).

The degradation process can be described by equation (5):

$$\sigma = (1-d) \cdot D_{0el} : (\varepsilon - \varepsilon_{pl}) \tag{5}$$

where:

σ – stress matrix,
d – stiffness degradation parameter,
D_{0el} – elastic stiffness matrix,

ε – strain matrix,
ε^{pl} – plastic strain.

The values of d_t and d_c parameters can be obtained experimentally. In this article, the value of parameter d was adopted from paper [7].

The values of the material parameters for B50 concrete are presented in Table 1. Other parameters of the concrete material were adopted as follows: tensile strength – 2.7 MPa, compressive strength – 49 MPa, dilation angle 38°.

Table 1

Parameters of the concrete damage plasticity model for B50 concrete [7]

Parameter		Value	
Young modulus		37 GPa	
Poisson ratio		0.2	
Density		2500 kg/m^3	
Damage parameters			
Strain (tension)	d_t [–]	Strain (compression)	d_c [–]
0	0	0	0
0.00016	0.406	0.000761	0
0.00028	0.696	0.00255	0.195
0.00068	0.920	0.00567	0.596
0.00108	0.980	0.0117	0.895

5. Data of the mainshock and the aftershock

In the dynamic analysis, a registered sequence of Aquilliano seismic shocks was used for the kinematic excitation of the bridge [13]. The sequence consisted of the mainshock and the aftershock. The shocks occurred on 30th March 2009 in Italy with an interval of two hours. The original range of acceleration was scaled by 1.4 in the case of the mainshock and by 15 in the case of the aftershock to obtain similar values of PGA for both shocks. The time history of accelerations in three directions (horizontal north-east, horizontal south-west, vertical) are shown in Fig. 7–8.

It can be observed that the maximal value of acceleration in the NE direction for the mainshock was 1.97 m/s^2, whereas for the SW direction – 1.24 m/s^2. For the aftershock, these values equalled: 2.01 m/s^2 for the NE direction and the 1.77 m/s^2 for the SW direction. Values of horizontal PGA for both shocks were very close – 2.33 m/s^2 and 2.67 m/s^2 for the mainshock and aftershock, respectively. This case of seismic sequence differs from the typical sequence of shocks. In the vast majority of registered sequences, the mainshock is stronger than the aftershock. However, examples of sequences when the main shock is lower than (or equal to) the aftershock can be found from seismic databases (e.g. Itaca.net, PEER) [13, 14].

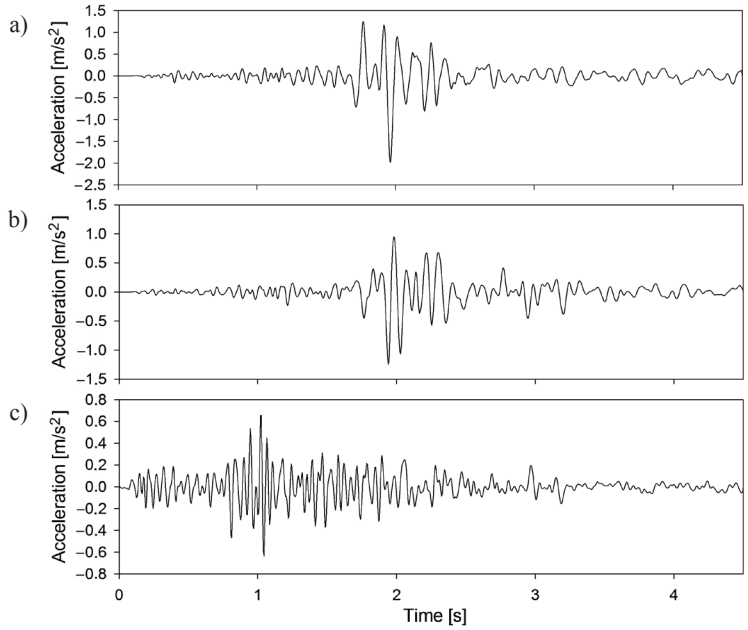

Fig. 7. Time history of accelerations of the mainshock in direction: (a) horizontal NE, (b) horizontal SW, (c) vertical Z

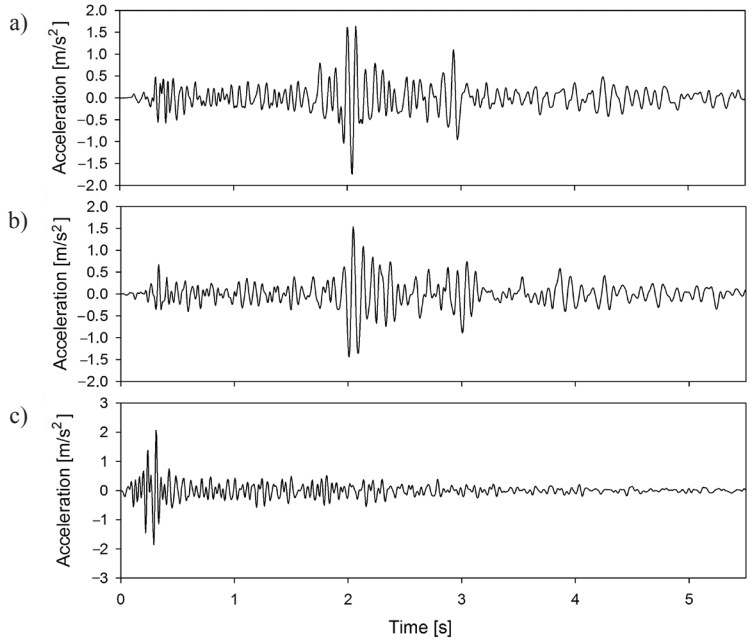

Fig. 8. Time history of accelerations of the aftershock in direction: (a) horizontal NE, (b) horizontal SW, (c) vertical Z

6. Dynamic analysis of the bridge under the sequence of seismic shocks

The dynamic responses of the bridge to both shocks were calculated using full-time history analysis. This was carried out with the Hilber-Hughes-Taylor time integration algorithm provided by the ABAQUS software. As the damage and failure model of concrete implements strong material nonlinearity, a step of numerical integration was not fixed. The step varied from 10^{-6} to 10^{-2} s, according to convergence requirements. The geometric nonlinearity was also taken into account.

The selected shocks were attached to the supports of the bridge as ground motions in three directions. In the longitudinal direction, the NE component was implemented; in the transverse direction, the SW component was applied.

For the dynamic analysis, the Rayleigh model of mass and stiffness proportional damping was applied. The damping coefficients $\alpha = 0.56$ (referring to mass proportional damping) and $\beta = 0.0013$ (referring to stiffness proportional damping) were determined for damping ratios of 5% for the first (5.36 Hz) and second (6.70 Hz) natural frequency.

The seismic performance of the bridge under the sequence of the mainshock and the aftershock was investigated in two steps. In the first step, the mainshock was applied to the structure; this resulted in the occurrence of some plastic and damage to areas of the bridge. The aftershock was then imposed on the bridge structure which had already been weakened by the first shock. The observed evolution of plastic and damage measures, incorporated into the concrete damage plasticity model of the material, allowed the assessment of the impact of both shocks on the bridge.

The basic variable that describes the concrete material performance during the shocks is the tensile damage parameter that shows the concrete material degradation in tension.

The bottom view of the beams of the outer bridge span after the entire sequence of shocks is shown in Fig. 9. It can be observed that the damage of structure occurred mainly in the middle of the bottom side of the outer span.

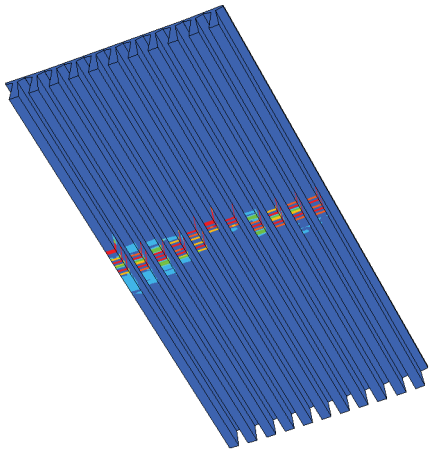

Fig. 9. The damaged area (coloured) in the middle of the outer span – bottom view

Detailed maps of tensile damage distribution in the middle of the span after the first and the second shock are displayed in Fig. 10.

On the basis of these maps, the noticeable increase in the level of damage to the structure due to the secondary shock can be observed. The largest changes in the level of damage were located in the area indicated in Fig. 10. During the mainshock, the tensile damage variable takes non-zero values in the middle of all beams. During the aftershock, the progress of deterioration that began during first shock takes place. The appearance of new damaged zones of the structure can be easily identified.

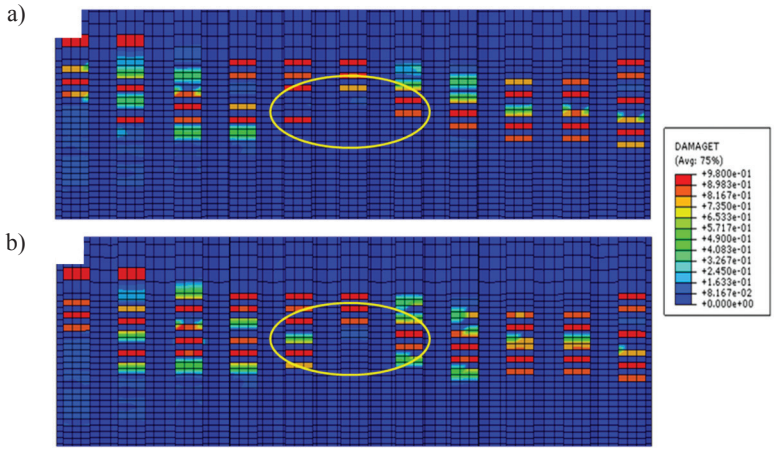

Fig. 10. Maps of tensile damage distribution in the middle of the span: (a) after the mainshock, (b) after the aftershock

To present the seismic performance of the bridge in terms of inelastic and damage behaviour of the concrete material under the sequence of the mainshock and the aftershock, a detailed time history analysis was carried out at numerous points of the superstructure. The results are shown at points P1, P2 and P3 located in the middle of the span (Fig. 11).

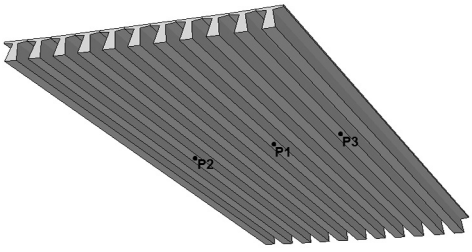

Fig. 11. Location of points selected to dynamic analysis

The following time histories of the plastic and damage measures at selected points were examined and are presented in Figs 12–14: logarithmic maximal and minimal principal

strain (LEP_{max} and LEP_{min}), equivalent plastic strain in tension (PEEQT), tensile damage parameter (DAMAGET). Logarithmic strain shows the dependence of total strain on time. For geometrically nonlinear analysis, logarithmic strain is the measure that takes into account the continuous variation of length. In the case of the concrete damage plasticity model, equivalent plastic strains in tension (PEEQT) and in compression (PEEQT) are separate measures of plastic behaviour under tension and compression. Hence, the equivalent plastic strain in tension is a parameter that controls the evolution of the cracking surface – this is linked to failure mechanism under tension loading. The tensile damage variable (DAMAGET) indicates damage occurring in the structure due to cracking. Finally, the stiffness degradation parameter (SDEG) indicates the loss of strength – it takes values from zero (representing undamaged material) to one (representing total loss of strength).

The time histories of plastic and damage measures at point P1, located in the central zone of the span, are shown in Fig. 12. When the amplitude of the ground oscillations enlarged substantially during the mainshock (2 sec) the concrete material went plastic (Fig. 12a) and failure of the concrete material (DAMAGET) occurred due to severe tension (Fig. 12b). The tensile damage at point P1 also contributed to the degradation of stiffness (SDEG). Until the onset of the first damage, the element stiffness had an initial value. The element damage triggered a sharp decrease of stiffness which was proportional to the tensile damage at the same moment (Fig. 12b).

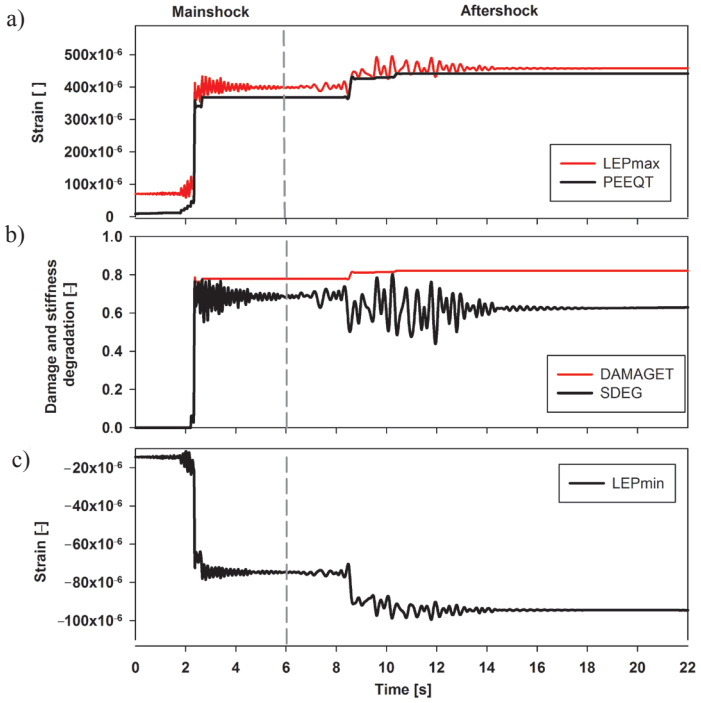

Fig. 12. Time histories at point P1 during the sequence of shocks: (a) logarithmic maximal principal strain (LEP_{max}) and equivalent plastic strain in tension (PEEQT); (b) tensile damage (DAMAGET) and stiffness degradation (SDEG) parameters; (c) logarithmic minimal principal strain (LEP_{min})

During the aftershock, only a small increase in principal stresses (both maximal and minimal) as well as in damage and stiffness degradation parameters were noticed. It is worth noting that the increase in the absolute value of minimal strain and the oscillations of this measure during the aftershock (2.4 sec) caused a slight recovery of the average element stiffness as well as the oscillation of this degradation measure (Fig. 12b). This phenomenon occurred due to the increase of compressive strain that partially closed cracks. After the mainshock, the average stiffness reduction reached 70% at point P1 whereas at the end of the aftershock, it was at a level of 60%.

On the basis of Fig. 12, it can be easily observed that the element damage occurred mostly during the first shock. The aftershock (with PGA comparable to the mainshock PGA) resulted only in a slight increase in the damage level. At the end of the mainshock, damage at point P1 was at a level of 80%, whereas after the secondary shock, it increased only by about 2–3%.

A different scenario, as far as the impact of both shocks is concerned, occurred at point P2 (Fig. 13). Contrary to the results obtained at point P1, only slight damage (1–2%) was recognised at point P2 during the mainshock. In actuality, this element was damaged during the secondary shock. Within 2.4 seconds of the aftershock, a significant leap of tensile damage (DAMAGET) appeared at point P2 (Fig. 13b). At the end of the aftershock, tensile damage of the element reached 80%.

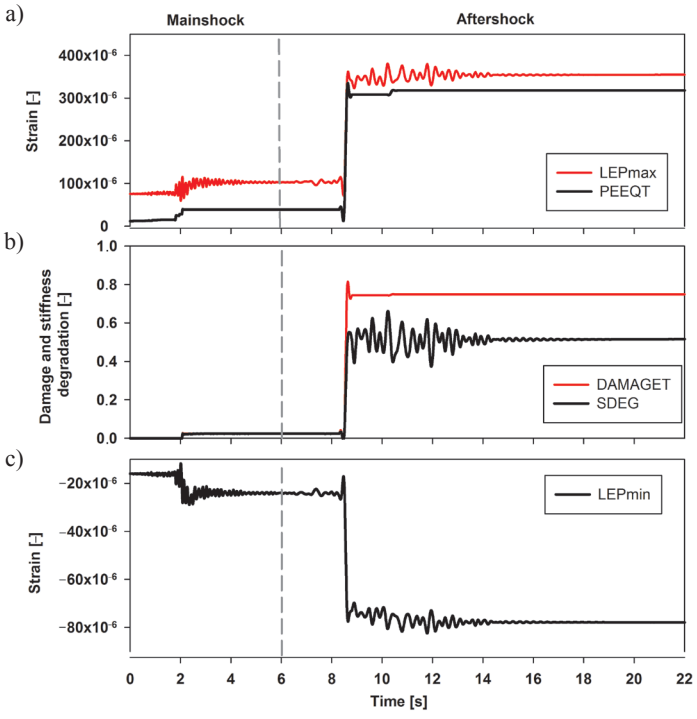

Fig. 13. Time histories at point P2 during the sequence of shocks: (a) logarithmic maximal principal strain (LEP_{max}) and equivalent plastic strain in tension (PEEQT); (b) tensile damage (DAMAGET) and stiffness degradation (SDEG) parameters; (c) logarithmic minimal principal strain (LEP_{min})

The rapid increase of plastic strain and tensile damage parameter were accompanied by the violent stiffness degradation at point P2. After 2.4 seconds of the aftershock, the oscillations of compressive strain produced the oscillations of stiffness. Finally, at the end of the aftershock, the stiffness degradation at point P2 reached 50%.

Finally, the dynamic performance of the concrete beam at point P3 was analysed. Diagrams presenting the time histories of plastic and failure parameters at point P3 during the sequence of shocks are shown in Fig. 14.

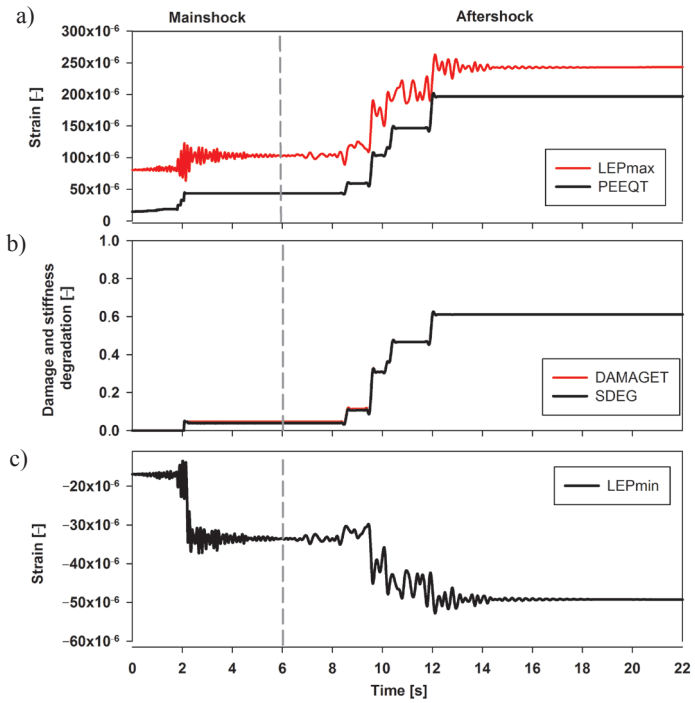

Fig. 14. Time histories at point P3 during the sequence of shocks: (a) logarithmic maximal principal strain (LEP_{max}) and equivalent plastic strain in tension (PEEQT); (b) tensile damage (DAMAGET) and stiffness degradation (SDEG) parameters; (c) logarithmic minimal principal strain (LEP_{min})

It can be noticed on the basis of Fig. 14 that damage to the element P3 appeared during both shocks. All diagrams clearly show consecutive stages of the increase in plastic and damage measures at point P3. They revealed that the first noticeable increase in principal strains, both compressive and tensile, occurred during the mainshock (Fig. 14b); however, the stiffness parameter indicated only a slight stiffness reduction (5%).

The progressive significant destruction at point P3 can be observed during the aftershock. Contrary to the previously examined points, P1 and P2, the stiffness degradation at point P3 did not appear rapidly but proceeded in time. Finally, the level of damage and stiffness reduction reached 65%.

The phenomenon of progressive damage is clearly visible in Fig. 14b. A strong correlation between the values of strain and the degree of the element damage could be observed. Because the element strain increased gradually, the tensile damage measure (DAMAGET) and the stiffness degradation parameter (SDEG) also enlarged gradually in relatively small leaps. An oscillation of the stiffness value was not observed. Despite the increase of minimal strain level, stiffness did not recover; this suggests that the element P3 was located in the tensioned zone where 'closing up' cracks did not appear.

7. Conclusion

The analysis of the dynamic performance of the reinforced concrete bridge subjected to the sequence of seismic shocks using the CDP material model allowed the formulation of the following conclusions:

1. Both the mainshock and the aftershock strongly affected the analysed bridge. The plastic behaviour and damage of the concrete material appeared in the bottom part of the outer span of the bridge. The increase in the element damage was accompanied by stiffness degradation which decreased proportionally to the degree of damage. The level of stiffness reduction reached 80% in the analysed zone.
2. Several scenarios of structure degradation can be distinguished under the sequence of the mainshock and aftershock with similar values of PGA. The damage and failure of some elements may occur during the mainshock only with the aftershock not increasing the degradation of the structure. However, the situation may be the opposite of this – the mainshock may not impose any damage to the structure, its degradation may be due to the aftershock only. Finally, the damage and failure process may propagate throughout the entire sequence of shocks.
3. The analysis revealed that the reduced element stiffness may be partially regenerated. This phenomenon occurs in elements where significant increase of compressive strain is observed and 'closing up' cracks appear.

References

[1] Abdelnaby A., *Response of reinforced concrete structures under multiple earthquakes*, [PhD thesis], Urbana (IL), University of Illinois at Urbana-Champaign, 2012.

[2] Abdelnaby A., Elnashai, A., *Response of degrading RC frames under replicate motions*, Proc. of the 15th World Conference on Earthquake Engineering (15WCEE), Lisbon 2012.

[3] Dulinska J.M., Jasinska D., *Performance of steel pipeline with concrete coating (modeled with concrete damage plasticity) under seismic wave passage*, Applied Mechanics and Materials 459, 2014, 608–613.

[4] Dulinska J.M., Szczerba R., *Assessment of concrete bridge performance under moderate seismic shock using concrete damage plasticity model*, Procedia Engineering 57, 2013, 1319–1328.

[5] Fakharifar M., Chen G., Sneed L., Dalvand A., *Seismic performance of post-mainshock FRP/steel repaired RC bridge columns subjected to aftershocks*, Composites Part B: Engineering 72, 2015, 183–198.
[6] Huang W., Qian J., Fu Q., *Damage assessment of RC frame structures under mainshock-aftershock seismic sequences*, Proc. of the 15th World Conference on Earthquake Engineering (15WCEE), Portugal, Lisbon 2012.
[7] Jankowiak T., Łodygowski T., *Identification of parameters of concrete damage plasticity constitutive model*, Foundations of Civil and Environmental Engineering 6, 2005.
[8] Kmiecik P., Kamiński M., *Modeling of reinforced concrete structures and composite structures with concrete strength degradation taken into consideration*, Archives of Civil and Mechanical Engineering XI (3), 2011, 623–636.
[9] Lee J., Fenves, G.L., *Plastic-damage model for cyclic loading of concrete structures*, Journal of Engineering Mechanics 124(8), 1998, 892–900.
[10] Lubliner J., Oliver S., Onate E., *A plastic-damage model for concrete*, International Journal of Solid and Structures 25 (3), 1989, 229–326.
[11] Zhai, Ch-H., Zheng, Z., Li, S., Xie L-L., *Seismic analyses of a RCC building under mainshock–aftershock seismic sequences*, Soil Dynamics and Earthquake Engineering 74(7), 2015, 46–55.
[12] Abaqus 6.14 Analysis User's Manual.
[13] itaca.mi.ingv.it (access:10.11.2015).
[14] peer.berkley.edu (access:10.11.2015).

TECHNICAL TRANSACTIONS | **CZASOPISMO TECHNICZNE**
CIVIL ENGINEERING | BUDOWNICTWO
3-B/2016

DOI: 10.4467/2353737XCT.16.209.5958

JOANNA DULIŃSKA, IZABELA MURZYN*

THE DYNAMIC RESPONSE OF AN ARCH FOOTBRIDGE TO SELECTED TYPES OF DYNAMIC LOADING

ODPOWIEDŹ DYNAMICZNA ŁUKOWEJ KŁADKI DLA PIESZYCH NA WYBRANE OBCIĄŻENIA DYNAMICZNE

Abstract

The dynamic analysis of a fifty-meter-long arch footbridge built in Poland is presented in the paper. The investigation focused on the comparison of dynamic responses to different types of dynamic loading, specifically pedestrian movement, traffic loads, mining tremors and seismic shocks. The FE model was created in the ABAQUS software. It transpired that the vibration level exceeded the thresholds 'slightly felt' in case of both, pedestrian and traffic loadings. The results also suggest that the safety of the structure is not threatened by this level of mining and seismic vibrations.

Key words: footbridges, kinematic loading, footbridge vibration

Streszczenie

W pracy zaprezentowane zostało porównanie odpowiedzi dynamicznej wybranej kładki dla pieszych na różnego rodzaju obciążenia: użytkowe, komunikacyjne, pochodzenia górniczego oraz sejsmiczne. Do przeprowadzonej analizy został wybrany obiekt łukowy o rozpiętości teoretycznej 50 m. Obliczenia wykonano w pakiecie ABAQUS. Analiza wykazała, że drgania spowodowane ruchem komunikacyjnym oraz przejściem pieszego są na poziomie „lekko odczuwalny". Dla drgań sejsmicznych oraz górniczych nie został przekroczony poziom zakłócający bezpieczeństwo konstrukcji.

Słowa kluczowe: kładki dla pieszych, obciążenie kinematyczne, dynamika kładek dla pieszych

* Prof. D.Sc. Ph.D. Eng. Joanna Dulińska, M.Sc. Eng. Izabela Murzyn, Institute of Structural Mechanics, Faculty of Civil Engineering, Cracow University of Technology.

1. Introduction

Footbridges are structures which are designed to carry people over obstacles. It needs to be highlighted that nowadays, these objects are strategic facilities of public infrastructure They make it possible to conduct the flow of pedestrians over obstacles, among which, the following are the most common: rivers, railways, tram lines and highways.

It should also be pointed out that great progress in construction techniques, building materials and calculation methods have supported architects and engineers in their tendency to design modern footbridges that are longer and lighter than older examples [6, 14]. What is important is that this trend demonstrates itself in the dynamic properties of the footbridges. As a consequence, they have relatively lower a first natural frequency than, for example, in bridges and buildings.

In the current engineering literature, there are many cases of pedestrian bridges which have natural frequencies that are close to the critical frequencies of dynamic excitations produced by pedestrians. Potentially, this may cause the resonance phenomenon induced by pedestrians using the structure [6–7, 14].

The next problem, which can appear during the exploitation of the footbridge, is vibratory comfort disruption. One of the most significant examples from recent civil engineering history is the case of the Millennium Bridge (London, England). Its dynamic behaviour that emerged on the opening day (10th June 2000) attracted the attention of scientists and engineers and underlined more than 1000 works and over 150 broadcasts by media around the world [5, 14].

It should be noted that it is not only pedestrian traffic that is a source of the dynamic loads of footbridges [8–9]. These structures can also be exposed to kinematic excitation originating from seismic or paraseismic phenomena such as mining tremors and traffic loads.

In the presented work, the authors focused on the dynamic behaviour of an arch footbridge [8, 10] under selected dynamic loading, i.e. pedestrian movement, traffic load, a mining tremor and a seismic shock. In the first step of the analysis, the dynamic characteristics of the bridge were estimated. Calculations of the dynamic responses of the footbridge to the selected loads were then carried out. Finally, the results obtained for particular types of loading were compared with thresholds for intensity perception of vertical vibration for people.

2. Footbridges – basic issues

Due to their intended, footbridges differ from conventional bridges. Firstly, these structures are lighter and more slender than bridges. Secondly, they are used in a different way – users are located directly on the deck of the structure, staying there longer than people who are travelling across a bridge by car. Pedestrians directly feel the dynamic behaviour of footbridges. At the design stage, footbridges require more attention to ensure proper functional features and comfortable use [3, 6, 14].

People are not only the major recipients of the vibration behaviour of footbridges, they are also a source of dynamic loading. In the vast majority of cases, excessive oscillations

of pedestrian bridges lead to serviceability problems, i.e. the vibration comfort of users is reduced.

It is obvious that human susceptibility to vibrations is very high. People react to oscillations according to their individual perception. It is also well known that the magnitude of the oscillations to which human beings are exposed may be defined in terms of physical measures, e.g. displacement, velocity or acceleration [6]. Therefore, the main purpose of dynamic investigation of footbridges is their vibration comfort criteria assessment [6, 14].

The determination of the vibration acceptance thresholds for these structures refers to the physiological effects on the human body (optical, mechanical, acoustic). Moreover, it transpired that human vibration perception for people is frequency dependent. Human exposure to vibrations of different frequency ranges can cause different reactions: from 0.1 to 0.8 Hz – seasickness; from 0.8 to 10.0 Hz – harmful effects to eyes and decreases in work quality; from 0.9 to 3.0 Hz, 5.0 to 8.0 Hz, and 9.0 to 10.0 Hz – fundamental resonance of a human body; from 1.0 to 1.5 Hz – disrupted breathing; from 1.5 to 4.0 Hz – lack of coordination of limbs; from 5.0 to 10.0 Hz – adverse effects on the cardiovascular system [6].

To evaluate the impact of oscillation on people, an appropriate parameter should be selected. In the frequency range of 1–10 Hz, perception of oscillation is proportional to acceleration, while in the range of 10–100 Hz, it is proportional to velocity. The human perception thresholds are presented in Table 1 (CEB 1991). Accelerations units adopted as the vibration comfort criteria for footbridges are given in [6]. There are some standards dedicated to assessing the impact of vibrations on footbridge pedestrians (BS 5400 1978, ISO 10137 2007). The guidelines for design practice are also presented in Eurocodes (EN 1990:2002/Al:2005) [6].

Table 1

The limits of human perception of vertical vibration (CEB 1991) [6]

Description	Range of frequency 1–10 Hz Max. vibration acceleration [m/s^2]	Range of frequency 10–100 Hz Max. vibration velocity [mm/s]
Slightly perceivable	0.034	0.500
Clearly perceivable	0.100	1.300
Unpleasant	0.550	6.800
Intolerable	1.800	13.800

3. Dynamic loading generated by a single pedestrian

Human-induced dynamic loading may cause strong vibrations of a structure. In extreme cases, this type of loading may cause the collapse of a structure [14]. In the literature, there are some aspects connected with human-induced dynamic loading which are considered as being crucial for footbridge safety: ranges of pacing frequencies for

different type of human motion, time function of vertical and horizontal dynamic forces, and the 'lock-in' effect [2, 6, 14].

As previously mentioned, forces generated by pedestrians can be very dangerous for pedestrian bridges, especially when this type of load can induce any resonant phenomena. The ranges of frequency typical for different human movements are summarised in Table 2 [1–2]. Other important types of dynamic human-induced forces which may have an effect on footbridges appear due to some kind of loads generated through inappropriate usage (jumping, bouncing or horizontal body swaying). However, these types of people motion are not typical of normal footbridge use [6].

Table 2

Typical pacing frequencies for walking, running and jumping on the spot [1–2]

Type of movement	The range of frequencies [Hz]			
	Total range	Slow	Normal	Fast
Walking	1.40–2.40	1.40–1.70	1.70–2.20	2.20–2.40
Running	1.90–3.30	1.90–2.20	2.20–2.70	2.70–3.30
Jumping	1.30–3.40	1.30–1.90	1.90–3.00	3.00–3.40

It must be pointed out that the motion of the human body is a complex biomechanical process. The entire mathematical formulation of this process is quite difficult. The human body generates forces during movement which affect the footbridge deck. In civil engineering, the approximate estimation of these dynamic forces is sufficient. These forces are time-dependent functions. They have three components in the space: horizontal-lateral, horizontal-longitudinal and vertical. However, the vertical component has the largest magnitude; therefore, only this component is taken into consideration in dynamic calculations. The main parameters which affect the value of the human-induced force function are: body weight, frequency of stepping, type of walkway surface [6].

Running and walking are the most predictable kind of pedestrian motions, both of them are periodic, changing in time and space. The loading generated by one moving (walking or running) pedestrian is modelled as a sum of dynamic and static components by formula [12]:

$$F(t) = G\left[1 + \sum_{i=1}^{n} A_i \sin\left(2i\pi\, f_s t - \varphi_i\right)\right] \quad i = 1, 2, ..., n \tag{1}$$

where:

f_s – the fundamental loading frequency,

G the body weight,

A_i, φ_i – the amplitude and the phase angel of the i-th harmonic, respectively.

The function loading generated by one moving pedestrian (walking or running) is shown in Fig. 1.

However, equation (1) is sufficient for walking, where each step overlaps with the previous and, in effect, makes the force continuous. In the case of running, this assumption is not

appropriate. The loading generated by a running pedestrian has a discontinuous nature. In this case, a half-sine model, suggested in [6], seems to be much more appropriate. In Table 3, coefficients for equation (1) referring to different kinds of motion are summarised [12].

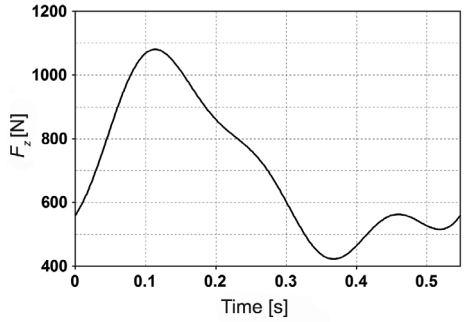

Fig. 1. Function loading generated by one moving pedestrian (walking or running)

Table 3

Coefficients of the Fourier decomposition [12]

Type of movement	A_1	φ_1	A_2	φ_2	A_3	φ_3
Walking	0.4	0	0.1	1.57	0.1	1.57
Running	1.6	0	0.7	0.00	0.2	0.00
Jumping	1.7	0	1.1	1.73	0.5	1.73

4. Kinematic loadings

Pedestrians are not the only source of dynamic loading of footbridges; these structures are also exposed to kinematic excitation originating from seismic or paraseismic phenomena such as mining tremors or traffic loads – these types of vibration arise outside of the structure. Vibrations are transmitted to the structure through the ground and they are imposed on foundations.

In this study, the calculation of the dynamic responses of the footbridge to different kinds of kinematic excitations were performed. Three types of excitation were analysed – traffic load, mining tremor and seismic shock. In all cases, three components of ground motion were taken into account, horizontal motion in a north-south direction (NS), horizontal motion in a west-east direction (WE), and vertical motion (Z). Additionally, the seismic and mining shocks had similar maximal accelerations.

To assess the impact of traffic vibrations on the footbridge, ground accelerations resulting from the passage of a truck recorded in three directions were used (Fig. 2).

To evaluate the impact of vibrations of mining origin on the structure, a mining shock registered in three directions in the Legnica-Glogow Copperfield (LGC) was analysed (Fig. 3) [15]. The shock was classified as one of the strongest events since this area was equipped with monitoring systems.

To estimate the impact of seismic vibrations on the structure, a natural shock registered in Central Italy (S. Polo Matese) was applied (Fig. 4) [16]. The phase of strong ground motion of the shock lasted approximately 8 seconds.

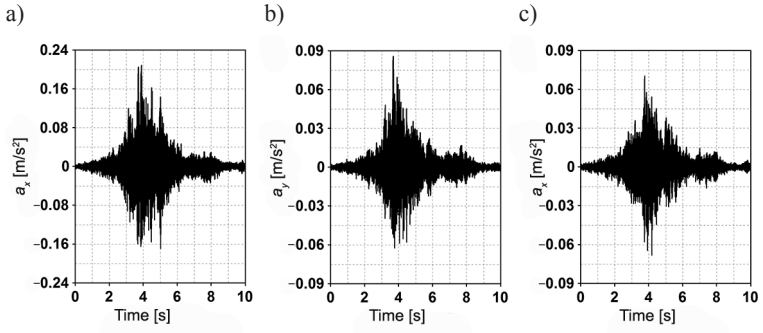

Fig. 2. Time histories of ground accelerations for truck passage: a) horizontal direction (x), b) horizontal direction (y), c) vertical direction (z)

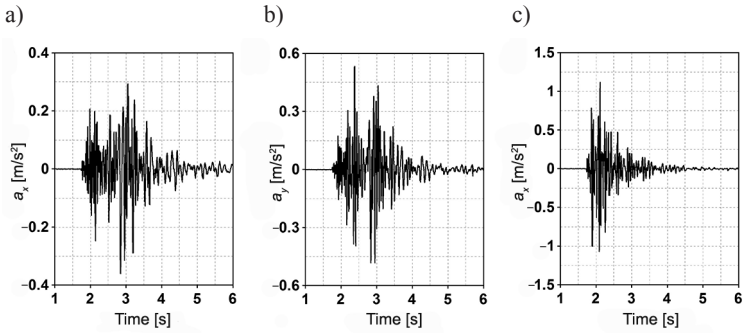

Fig. 3. Time histories of the mining tremor accelerations: a) horizontal direction (x), b) horizontal direction (y), c) vertical direction (z) [15]

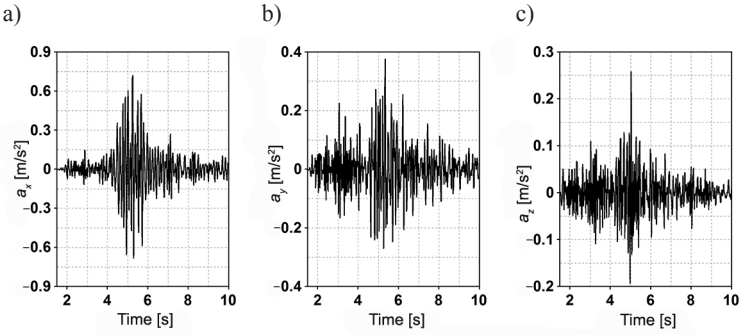

Fig. 4. Time histories of the seismic shock accelerations: a) horizontal direction (x), b) horizontal direction (y), c) vertical direction (z) [16]

5. Geometry and basic dimension of the footbridge

The analysed single-span footbridge is located in Poland. The footbridge is dedicated to carry pedestrians over the highway. The deck of the bridge is connected to the two steel arches by hangers (M56). A cross-section of the footbridge is shown in Fig. 5.

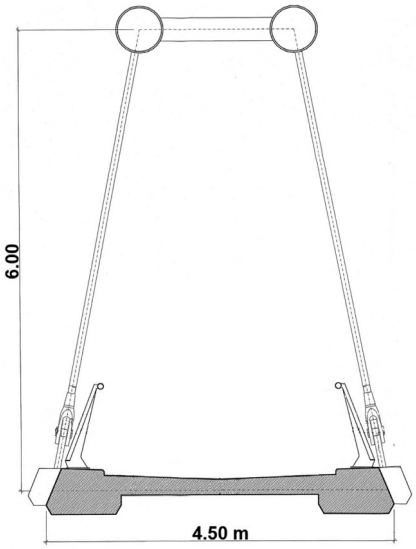

Fig. 5. Cross-section of the arch footbridge [8]

The basic technical parameters of the footbridge are as follows [8, 11]: length of the footbridge 51.60 m; arch span 46.72 m; usable width of footbridge 3.00 m; entire width of footbridge 4.50 m; height 0.60 m. The structure is equipped with elastomeric bearings. The elasticity modulus of the structural steel was 210 GPa. Poisson's ratio was assumed as 0.29. The material data of concrete were assumed to be as follows: elasticity modulus – 39 GPa, Poisson's ratio – 0.17, mass density – 2500 kg/m^3. The dimensions of the footbridge were adopted according to literature [4, 8, 11]. The structure was fixed to the ground that reflected a rigidity of a stiff subsoil under the object.

6. Results of the dynamic analysis of the footbridge

The numerical model of the structure was prepared with the ABAQUS software package [13]. In the model, different types of elements were used. Beam elements were applied for an arch, girders and crossbars. Truss elements were used for hangers. The deck was discretised with shell elements. Finally, solid elements were used for the pillars. The model with points selected for dynamic analysis (red dots) is presented in Fig. 6. In the paper, only the results obtained at point A are presented.

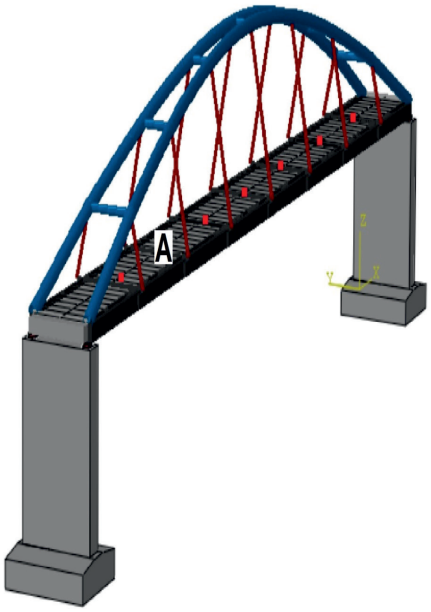

Fig. 6. The FE model of the footbridge with points selected for dynamic analysis (red dots)

Elastic truss elements with no compressive stiffness (the 'no compression' option) [13] were used for the hangers to guarantee that compressive stresses would not be generated during dynamic analysis. However, when such elements are used, instability of the model usually occurs. This difficulty was overcome by overlaying each truss element which had no compression stiffness with another element which had a small degree of compression stiffness. This technique enables the creation of non-zero stiffness that stabilises the model.

In the investigation all hangers were modelled as trusses (T3D2) with the 'no compression' option. For the model stabilisation, beam elements (B31) were introduced. The level of 5% of the hangers' stiffness was implemented for the stabilizing elements. The *Tie* constraints [13] were applied to guarantee identical kinematic behaviour of the truss and the beam elements.

In the first stage of numerical investigation, the natural frequencies of the footbridge were evaluated. The modes of natural vibration are presented in Fig. 7.

The first natural frequency of the footbridge was 1.6 Hz – this means that the lowest frequency is located within the range 1.4 to 2.4 Hz which represents a typical walking pace frequency (Tab. 1). Therefore, the dynamic response of the footbridge to human movement should be calculated for a single pedestrian walking.

The second stage of numerical investigation was the estimation of the dynamic response of the footbridge to selected dynamic loads. Modal analysis was carried out in which the twenty lowest modes of vibration were considered with a damping ratio of 2% for each mode.

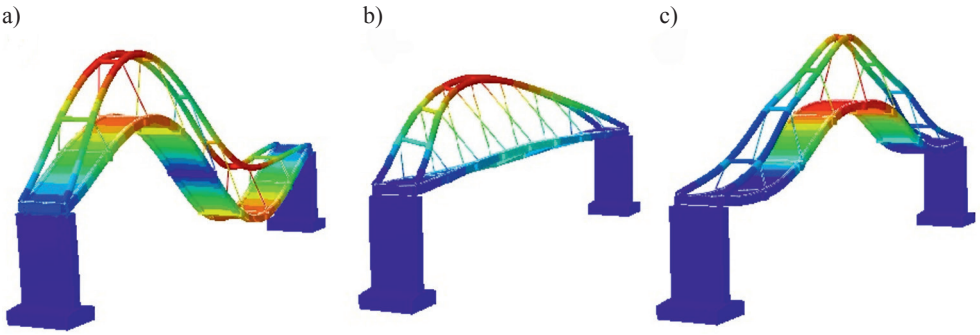

Fig. 7. Natural vibrations of the footbridge: a) first mode (frequency 1.6 Hz), b) second mode (frequency 2.5 Hz), c) third mode (frequency 3.1 Hz)

Firstly, the dynamic response of the footbridge to a single pedestrian walking was evaluated. The model of forces generated by a single pedestrian walking, represented by equation (1), was used. The following values were used for the analysis: pedestrian weight – G = 700 N; first natural frequency of footbridge – f_s = 1.6 Hz. Coefficients of the Fourier decomposition A_i and φ_i were assumed from Table 2 for type of movement – walking. The dynamic performance of the footbridge subjected to the registered vibrations from truck passage (see Fig. 2) was then assessed. Finally, the dynamic behaviour of the structure under seismic and mining shocks was considered.

The results of the dynamic analysis of the footbridge are presented in Figs. 8–9. The time histories of accelerations, shown in Figs. 8 and 9, refer to the four above-mentioned cases of dynamic loading. The time histories of accelerations were calculated for all points (Fig. 6). However, the results are presented only for point A. At this point, the maximum value of acceleration was obtained during pedestrian passage.

The time histories of accelerations, obtained as the dynamic response to a single pedestrian walking as well as to the truck passage (see Fig. 8), were compared with human perception of vertical vibration (CEB 1991) [6]. The maximum values of accelerations obtained at point A in response to a single pedestrian walking and to the passage of the truck are summarised in Table 4.

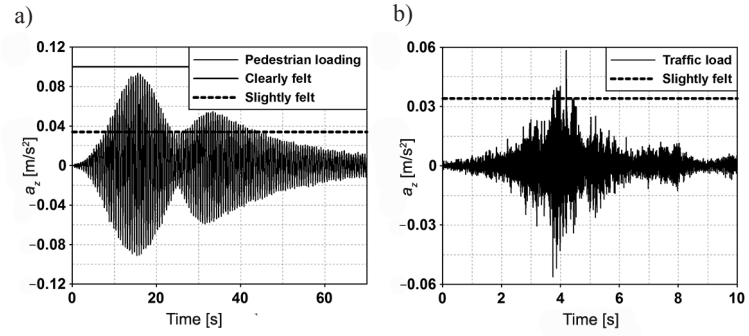

Fig. 8. Time history of vertical accelerations (a_z) obtained at representative point A (Fig. 6) for: a) a single pedestrian walking, b) the truck passage

Table 4

Maximum values of accelerations obtained at point A for pedestrian and traffic loadings

Type of loading	Acceleration [m/s^2]	Human perception of vertical vibration (CEB 1991) [6]
Pedestrian loading	0.09	Slightly perceivable
Traffic load	0.06	Slightly perceivable

The time histories of accelerations obtained as the dynamic response to the mining shock and the natural seismic event are shown in Fig. 9. The maximum values of accelerations obtained at point A in response to the mining and seismic shocks are summarised in Table 5.

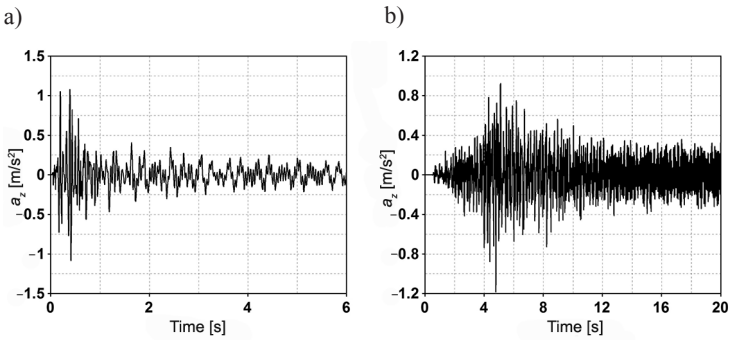

Fig. 9. Time history of vertical accelerations (a_z) obtained at representative point A (Fig. 6) for: a) the mining tremor, b) the seismic shock

Table 5

Maximum values of accelerations obtained at point A for mining and seismic shocks

Type of loading	Acceleration [m/s^2]
Mining tremor	1.08
Seismic shock	1.23

7. Conclusions

The dynamic characteristics of the existing arch pedestrian footbridge, i.e. the natural frequencies and the modes of vibration, were evaluated with the ABAQUS software package. The response of the footbridge to the different types of dynamic loading were also assessed. The final remarks can be formulated on the basis of the performed analysis:

- the solution of the eigenproblem revealed that the natural frequencies of the footbridge are relatively low – they correspond with the frequency of pedestrian steps (walking) which may cause in the resonance phenomenon,
- the maximum vertical accelerations evaluated for the pedestrian and the traffic loading reached 0.09 m/s^2, and 0.06 m/s^2, respectively. This level of vibrations exceed the 'slightly perceivable' thresholds (by CEB 1991),
- the maximum accelerations obtained for the mining and seismic shocks were 1.08 and 1.23 m/s^2, respectively. Safety of the structure is not threatened by this level of vibration (although vibrations exceed the 'unpleasant' thresholds).

References

[1] Bachmann H., Ammann W., *Vibrations in Structures Induced by Man and Machines* IABSE – AIPC – IVBH, Zürich 1987.

[2] Baumann K., Bachmann H., *Durch Menschen verursachte dynamische Lasten und deren Auswirkungen auf Balkentragwerke*, Bericht 7501-3, Institut für Baustatik und Konstruktion (IBK), ETH Zürich, Birkhäuser Verlag, Basel–Boston–Berlin 1988.

[3] Bilszczuk J.,W. Barcik et al., *Design of steel footbridges*, Lower Silesia Educational Publisher House (DWE), Wroclaw 2004.

[4] Buckle I., Nagarajaiah S., Ferrell K., *Stability of Elastomeric Isolation Bearings: Experimental Study*, Journal of Structural Engineering 128(1), 2002, 3–11.

[5] Dallard P., Fitzpatrick T., Flint A., Low A., Smith R., Willford M., Roche M., *London Millennium Bridge: Pedestrian-induced lateral vibration*, Journal of Bridge Engineering 6(6), 2001, 412–417.

[6] Flaga A., *Mosty dla pieszych*, WKL, Warsaw 2011.

[7] Murzyn I.J., *Dynamic characteristics of a cable-stayed pedestrian and cyclists footbridge 120 m long*, International Journal of Earth Sciences and Engineering 7(1), 2014, 313–319.

[8] Murzyn I.J, *Dynamic response of pedestrian and cyclist footbridge to communication load*, Logistyka 4, 2014, 4701–4708.

[9] Murzyn I.J, *Dynamic response of a pedestrian bridge to traffic load*, Technical Transactions, Civil Engineering 5–B, 2014, 189–194

[10] Murzyn I.J, *Vibration comfort criteria assessment for pedestrians and cyclist footbridge with a span of 50 m*, Logistyka 4, 2014, 4715–4716.

[11] Kałuża J., Skulski B., Wazowski M.: *The report of the test load for the footbridge (the footbridge KP-214A, over the highway A1)*, Construction Engineering Research Laboratory ASPEKT Sp. z o.o., Jaworzno 2012.

[12] Occhiuzzi A., Spizzuoco M., Ricciardelli F., *Loading models and response control of footbridges excited by running pedestrians*, Structural control and health monitoring 15(3), 2008, 349–368.

[13] Simulia Corp., *ABAQUS Users' Manual v. 6.13*, Dassault Systemes Simulia Corp., Providence, RI.

[14] Zivanovic S., Pavic A., Reynolds P., *Vibration serviceability of footbridges under human-induced excitation: a literature review*, Journal of Sound and Vibration 279, 2005, 1–74.
[15] The European Strong-Motion Database: Polkowice (Polska), 30.09.2002 (20:40:33 UTC).
[16] ITACA (Italian Accelerometric Archive) version 2.0: S. Polo Matese 1, 2014.01.20 (07:12:40 UTC).

TECHNICAL TRANSACTIONS | **CZASOPISMO TECHNICZNE**
CIVIL ENGINEERING | BUDOWNICTWO
3-B/2016

DOI: 10.4467/2353737XCT.16.210.5959

TOMASZ FALBORSKI, ROBERT JANKOWSKI*

EFFECTIVENESS OF A MATHEMATICAL MODEL IN SIMULATING NONLINEAR MECHANICAL BEHAVIOUR OF A SEISMIC ISOLATION SYSTEM MADE OF POLYMERIC BEARINGS

OCENA EFEKTYWNOŚCI MODELU MATEMATYCZNEGO DO OPISU NIELINIOWEGO ZACHOWANIA WIBROIZOLACJI SEJSMICZNEJ W POSTACI ŁOŻYSK POLIMEROWYCH

Abstract

The present study was focused on determining the effectives of a nonlinear mathematical model in simulating complex mechanical behaviour of a seismic isolation system made of Polymeric Bearings. The proposed mathematical model defines the lateral force as a nonlinear function of the shear displacement and the deformation velocity. The effectiveness of the proposed mathematical model was verified by comparing the seismic response of a 2.30 m high two-storey structure model with the results obtained from the detailed numerical analysis. The results obtained from the numerical investigation using lumped-mass models confirmed that the proposed nonlinear mathematical model can be successfully adopted to simulate the complex mechanical behaviour of the Polymeric Bearings in numerical studies..

Keywords: Polymeric Bearings, base isolation, mathematical model, shaking table testing, earthquakes, dynamic excitations

Streszczenie

W pracy dokonano oceny efektywności modelu matematycznego, opisującego nieliniowe zachowanie prototypu wibroizolacji sejsmicznej w postaci Łożysk Polimerowych. W zaproponowanym modelu matematycznym siła pozioma jest nieliniową funkcją przemieszczenia oraz prędkości. Oceny efektywności modelu matematycznego do opisu nieliniowego zachowania łożysk polimerowych dokonano poprzez porównanie wyników badań eksperymentalnych przeprowadzonych na stole sejsmicznym, w których dwupiętrowy model konstrukcji o całkowitej wysokości 2,30 m poddano różnym obciążeniom dynamicznym, z wynikami analiz numerycznych. Duża zgodność wyników analiz numerycznych z wynikami otrzymanymi z badań eksperymentalnych potwierdziła poprawność zaproponowanego modelu matematycznego do symulacji zachowania Łożysk Polimerowych.

Słowa kluczowe: Łożyska Polimerowe, wibroizolacja sejsmiczna, model matematyczny, stół sejsmiczny, trzęsienia ziemi, wymuszenia dynamiczne

* Ph.D. Tomasz Falborski, Assistant Professor, Prof. Ph.D. Robert Jankowski, Department of Metal Structures and Construction Management, Faculty of Civil and Environmental Engineering, Gdańsk University of Technology.

1. Introduction

Earthquakes are identified among the most severe and unpredictable threats to structures all around the world. Strong ground motions may cause of lot damage in a wide variety of ways, sometimes leaving thousands of casualties in their wake. During the last few years alone, the world has witnessed many major earthquakes, five of which have caused far-reaching consequences of a national scale for Haiti (January 2010), Chile (February 2010), New Zealand (February 2011), Japan (March 2011), and Turkey (October 2011). Damaging earthquakes also take place from time to time in Poland (although their effects are not so dangerous as in other countries.

In spite of a number of available technical solutions of protecting structures against seismic forces, earthquake peril remains the most sinister and unpredictable natural disaster, for which many countries are still not fully prepared. Due to the randomness of occurrence, destructive potential, and insufficient early-warning systems, there is an incessant need of developing and improving earthquake protective systems against seismic loads and their devastating effects in order to minimise the loss of life and property damage.

Base isolation is considered to be one of the most popular and effective structural control methods of protecting structures against seismic forces. Generally, base isolation systems work by separating the building from the horizontal components of the earthquake ground motion by introducing a layer with low horizontal stiffness between the structure and its foundation [3–9]. The main concept of this strategy is to modify structural dynamic properties, such as the fundamental period of vibration and the damping ratio, so that structures can respond more favourably to dynamic excitations. Base isolators, such as Lead-Rubber Bearings, High-Damping Rubber Bearings, and Friction Pendulum Bearings, are commonly used in practice in many earthquake-prone countries in order to enhance structural safety and reliability. However, the past few decades have witnessed a tremendous progress in material engineering. Because of the impressive range of useful and exceptional properties, new materials play an essential and ubiquitous role in many fields of science, also including earthquake engineering. The recent development of polymeric materials has resulted in an increased number of new isolators and modifications of the existing ones.

The present paper aims to verify the effectiveness of a nonlinear mathematical model in simulating complex mechanical behaviour of a prototype seismic isolation system made of Polymeric Bearings (PBs). In order to construct the seismic bearings considered in research, a specially prepared elastomer with improved damping characteristics was employed. The proposed mathematical model was adopted in numerical analysis, where the previously examined two-storey experimental model subjected to various seismic excitations, was idealised as a multi-degree-of-freedom system.

2. Polymeric Bearings

In order to construct the seismic isolation bearings considered in this research, a specially prepared flexible polyurethane-based elastomer was employed. It was produced by one of the top international chemical companies specifically for this investigation program. The

chemical composition of this polymer includes certain additives in order to improve its damping properties, which are extremely desirable for energy-dissipation devices, particularly for seismic isolation bearings. The basic mechanical properties of this polymer have already been determined and the results obtained presented in previous publications (see, for example, [10–14]). Generally, the analysed polymer is markedly nonlinear and its mechanical behaviour strongly depends on the strain rate, which is typical for viscoelastic materials [12]. More importantly, a relatively high value of the loss factor obtained from the Dynamic Mechanical Analysis (DMA) confirms its high damping and energy-dissipation properties [13].

PB is made up of a polymer cylinder (28 mm in diameter and 28 mm high) with a centrally located hole (14 mm in diameter) into which a pin-ended steel core (6 mm in diameter) is inserted. Two additional steel anchor plates (30 mm in diameter and 15 mm high) are mounted at both ends of the polymer cylinder. The total height of the PB is 58 mm. The basic components of the PB are shown in Fig. 1.

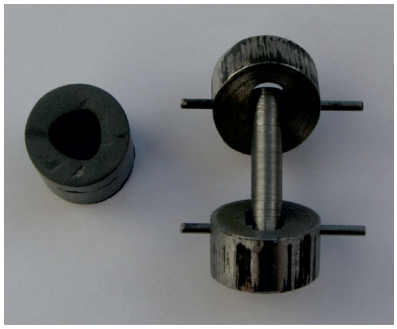

Fig. 1. Components of the PB: a polymer cylinder with a centrally located hole (left) and pin-ended steel core with the anchor plates (right)

The proposed prototype solution ensures that the steel core sustains vertical forces, while the polymer cylinder is subjected to shearing. This way, the steel core prevents the polymer cylinder from carrying vertical loads, which could possibly lead to undesirable bulging of the bearing. It should be underlined, however, that due to uniaxial (horizontal) shaking table used in the investigation, the PBs were intentionally constructed as one-dimensional devices. A multi-dimensional version of the PB has also been proposed and already submitted to the Polish Patent Department [15].

3. Shaking table tests

In order to conduct the experimental investigation, a two-storey structure model was firstly prepared. The welded steel frames were constructed using rectangular hollow section elements (RHS 15×15×1.5 mm). The columns were arranged in a rectangular pattern with spacing of 0.465 m along the longitudinal direction and 0.556 m along the transverse one. Additionally, diagonal bracing was used in the sidewall planes to counteract transverse and torsional vibrations. Moreover, three concrete plates (50×50×7 cm) were employed in order

to simulate the weight of floors and a foundation slab. The welded steel frames were clamped together using M10 bolts. Eventually, the two-storey structure model is 2.30 m high and weighs 148 kg. The experimental model, with and without the PBs, is shown in Fig. 2.

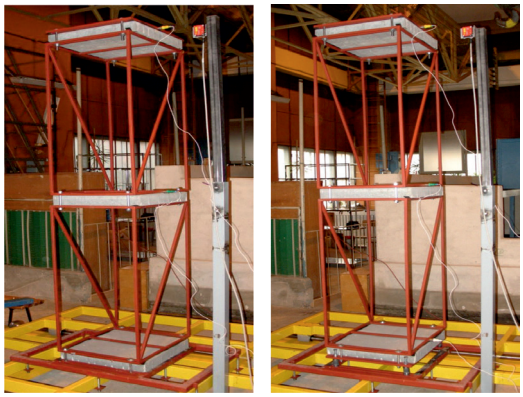

Fig. 2. Fixed-base (left) and base-isolated (right) two-storey structure model

The dynamic properties of the analysed two-storey structure model, fixed-base and base-isolated, were evaluated by conducting the free vibration and sine sweep tests. The results obtained were used to determine the natural frequencies as well as the damping ratios of the experimental model with and without the PBs. In the next stage, the seismic response of the analysed two-storey structure model, fixed-base and base-isolated, during various earthquake ground motions, was extensively studied. The investigation was carried out using the middle-sized shaking table located at the Gdańsk University of Technology (GUT), Poland. The effectiveness of the PBs in reducing structural vibrations was verified by comparing the peak accelerations experienced by the tested model with and without the base isolation system. The results obtained from the comprehensive shaking table study, which explicitly confirm the effectiveness of the PBs as a prototype base isolation system, have already been presented in previous publications [16–18].

4. Mathematical model

In nonlinear structural dynamics, there are many different approaches, which can be applied to simulate the mechanical behaviour of base isolation devices. Most of the frequently adopted models, however, are limited to those exhibiting general hysteretic behaviour and cannot be used for an accurate simulation of the force-displacement characteristics of the seismic bearings considered in this study. On the other hand, more complex mathematical models for base isolation devices [19–23] were evaluated for different base isolators and are not appropriate for numerical analysis of the PBs. Therefore, in the present study, a new nonlinear mathematical model to simulate the complex behaviour of the PBs under dynamic excitations is proposed, as defined by Equations 1–3. The proposed model defines the lateral force as a nonlinear function of the shear displacement $u_b(t)$, and the deformation

velocity $\dot{u}_b(t)$. In this approach, function parameters $a_1 \div a_5$ were estimated by curve fitting the Equation 1 to the experimentally obtained hysteresis loops using the least squares optimisation method. In order to obtain hysteresis loops, four PBs, supporting a concrete slab (50×50×7 cm), were mounted on the shaking table platform and subjected to dynamic oscillatory tests. The experimental testing was carried out with the excitation frequency of 2 Hz for different shear strain levels. The evaluated set of the function parameters $a_1 \div a_5$ is summarised in Table 1 and the results of the curve fitting algorithm are presented in Fig. 3. The normalised mean square error calculated for the presented fit was calculated to be 4.44%. The results clearly demonstrate that the proposed mathematical model with the evaluated set of function parameters fits the experimental results quite accurately, and therefore can be used for further numerical simulations.

$$F_b(u_b(t),\dot{u}_b(t)) = K_b(u_b(t),\dot{u}_b(t)) \cdot u_b(t) + C_b \cdot \dot{u}_b(t) \tag{1}$$

$$K_b(u_b(t),\dot{u}_b(t)) = a_1 + \frac{a_2}{\cos h[a_3 \dot{u}_b(t)] \cdot \cos h[a_4 u_b(t)]} \tag{2}$$

$$C_b = a_5 \tag{3}$$

Table 1

Evaluated set of the function parameters

Parameter	Estimated value
a_1	38.657 [N/m]
a_2	36.300 [N/m]
a_3	23.253 [s/m]
a_4	331.626 [1/m]
a_5	2.193 [kg/s]

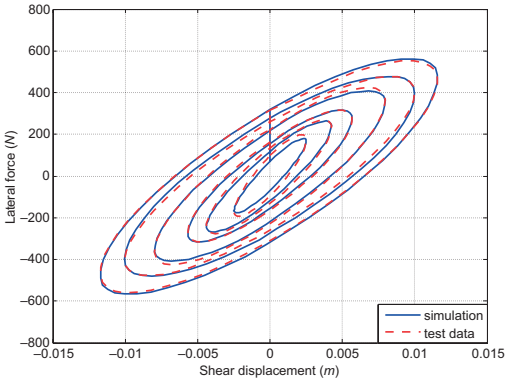

Fig. 3. Results of the curve fitting of the proposed nonlinear mathematical model into the experimentally obtained hysteresis loops

5. Numerical analysis

In order to perform the numerical evaluation of seismic response of the previously examined experimental model, lumped-mass systems were adopted [24, 25]. The fixed-base two-storey structure model was idealised as a two-degree-of-freedom (2-DOF) system, whereas for the base-isolated one, a three-degree-of-freedom (3-DOF) system was employed. The numerical simulation of seismic response of the structure model with and without the PBs was performed with the use of the proposed mathematical model (Equations 1–3). The analysed model was subjected to the El Centro earthquake of 1940, and Northridge earthquake of 1994. In order to conduct the numerical evaluation of dynamic response, the unconditionally stable Newmark's average acceleration method was applied [26]. The results obtained from the investigation are presented in Fig. 4–11. Additionally, the Fast Fourier Transform (FFT) functions are also shown in Fig. 12–15. The peak accelerations computed at the top of the analysed two-storey structure model with and without the PBs during different seismic excitations are briefly reported in Table 2.

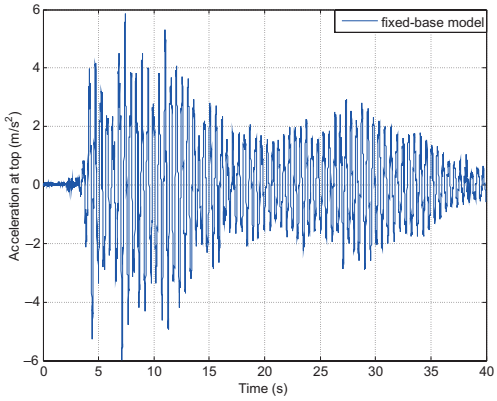

Fig. 7. Time-acceleration history plot for the base-isolated model during the 1940 El Centro earthquake (numerical analysis)

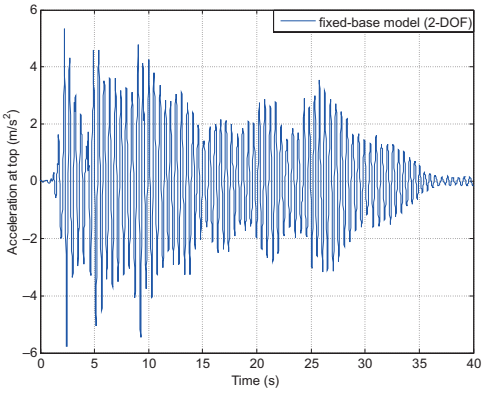

Fig. 8. Time-acceleration history plot for the fixed-base model during the 1994 Northridge earthquake (shaking table test)

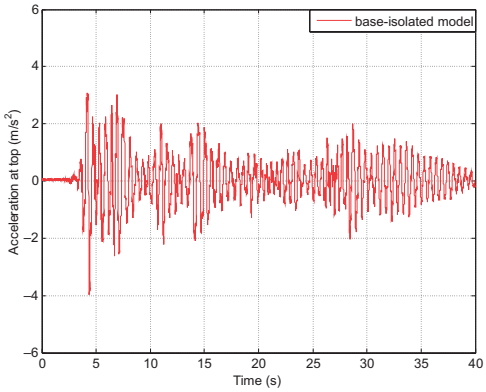

Fig. 4. Time-acceleration history plot for the fixed-base model during the 1940 El Centro earthquake (shaking table test)

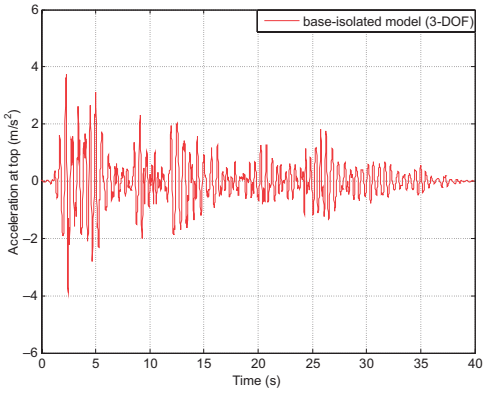

Fig. 5. Time-acceleration history plot for the fixed-base model during the 1940 El Centro earthquake (numerical analysis)

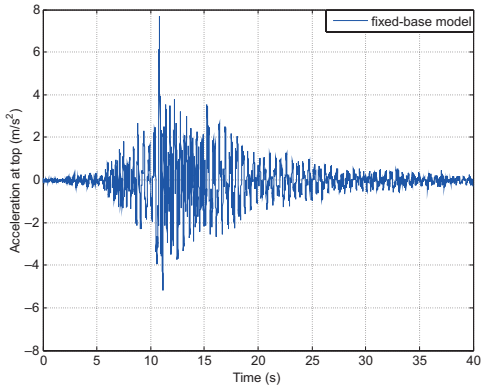

Fig. 6. Time-acceleration history plot for the base-isolated model during the 1940 El Centro earthquake (shaking table test)

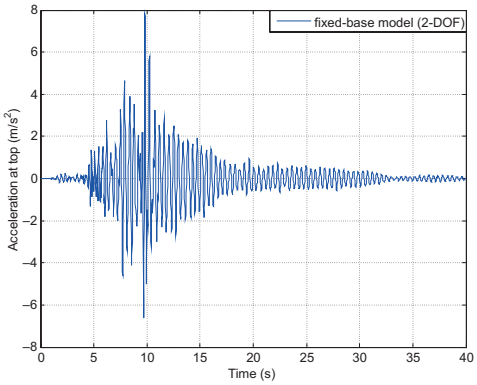

Fig. 9. Time-acceleration history plot for the fixed-base model during the 1994 Northridge earthquake (numerical analysis)

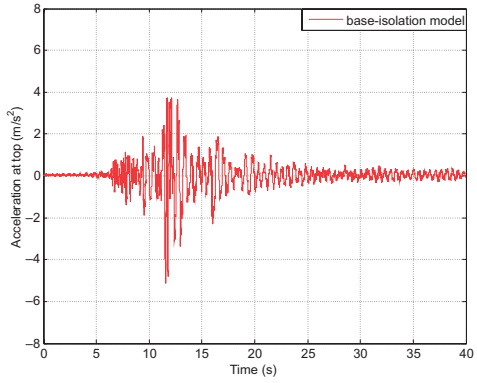

Fig. 10. Time-acceleration history plot for the base-isolated model during the 1994 Northridge earthquake (shaking table test)

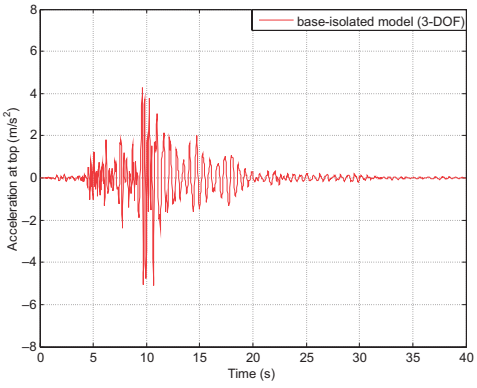

Fig. 11. Time-acceleration history plot for the base-isolated model during the 1994 Northridge earthquake (numerical analysis)

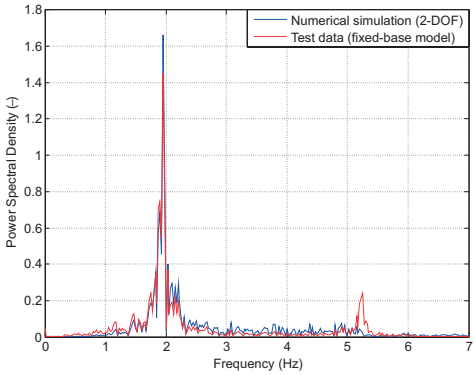

Fig. 12. Comparison between the FFT functions for the fixe-base model under the 1940 El Centro earthquake

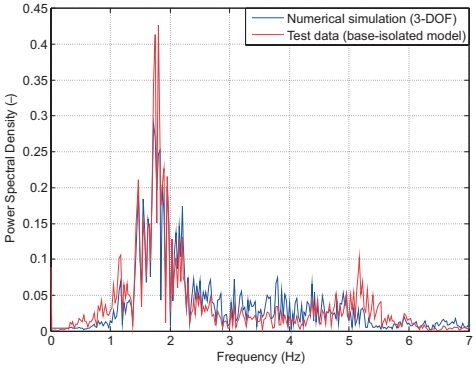

Fig. 13. Comparison between the FFT functions for the base-isolated model under the 1940 El Centro earthquake

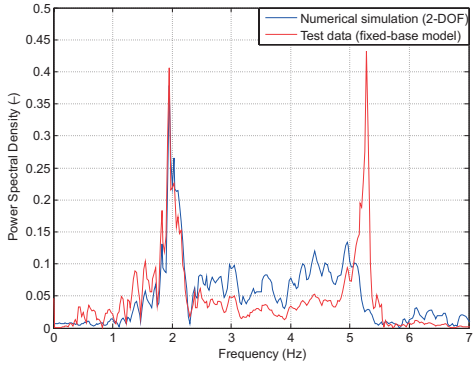

Fig. 14. Comparison between the FFT functions for the fixed-base model under the 1994 Northridge earthquake

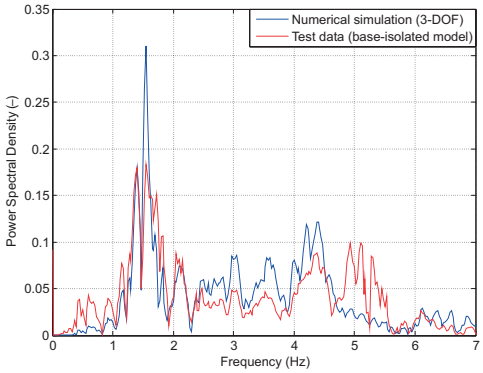

Fig. 15. Comparison between the FFT functions for the base-isolated model under the 1994 Northridge earthquake

Table 2

Results of the numerical investigation with the use of lumped-parameter models

Dynamic excitation	Peak acceleration computed at the top of the numerical model (m/s^2)		Reduction (numerical analysis)	Reduction (shaking table study)
	Fixed-base model (2-DOF)	Model isolated with the PBs (3-DOF)		
El Centro earthquake, 18.05.1940 (NS component, PGA = 1.535 m/s^2)	5.77	3.89	33%	33%
Northridge earthquake, 17.01.1994 (Santa Monica station, EW component, PGA = 4.332 m/s^2)	7.85	5.10	35%	33%

where PGA denotes the *Peak Ground Acceleration*.

6. Results and conclusions

The results obtained from the numerical analysis confirm that the proposed nonlinear mathematical model (Equations 1–3) can be successfully adopted for numerical simulations of the PBs. Inspection of Table 2 indicates that the reduction in the computed peak accelerations at the top of the analysed numerical model due to installation of the PBs is very similar to that observed during shaking table investigation. Also, the experimentally obtained results confirm the high effectiveness of the PBs in reducing structural vibrations due to earthquake ground motions. Additionally, the time-acceleration history plots and FFT functions obtained for the fixed-base structure modelled as a 2-DOF system are consistent

with the results of the experimental investigation, which confirms the accuracy in assuming lumped parameters to characterize the analyzed two-storey structure model.

The results of the present study have confirmed both the high effectiveness of the PBs as a prototype base isolation system and the proposed mathematical model (both in time and frequency domain). Nevertheless, further development of the PBs is planned. Subsequent studies will include numerical simulations with the use of Finite Element Analysis as well as the experimental tests of a full-scale multi-dimensional PBs.

Acknowledgements

The authors are thankful to prof. Arkadiusz Kwiecień and Ph.D. Bogusław Zając (Faculty of Civil Engineering, Cracow University of Technology, Poland) for providing the polymeric specimens, which were used to construct the PBs considered in this research.

References

[1] Zembaty Z., Cholewicki A., Jankowski R., Szulc J., *Trzęsienia ziemi 21 września 2004 r. w Polsce północno-wschodniej oraz ich wpływ na obiekty budowlane*, Inżynieria i Budownictwo, vol. LXI, No. 1, 2005, 3–9.

[2] Zembaty Z., Jankowski R., Cholewicki A., Szulc J. *Trzęsienie ziemi 30 listopada 2004 r. na Podhalu oraz jego wpływ na obiekty budowlane*, Inżynieria i Budownictwo, vol. LXI, No. 9, 2005, 507–511.

[3] Buckle I.G., *Passive control of structures for seismic loads*, Proceedings of the 12th World Conference on Earthquake Engineering, Paper No. 2825, Auckland, Jan 30 – Feb 4, 2000, 1–8.

[4] Kelly J.M., *Earthquake-Resistant Design with Rubber*, Springer-Verlag, New York 1993.

[5] Mayes R.L., Naeim F., *Design of structures with seismic isolation*, [in:] Naeim F. (Ed.): *The Seismic Design Handbook*, Kluwer Academic, Boston 2001.

[6] Naeim F., Kelly J.M., *Design of Seismic Isolated Structures: From Theory to Practice*, John Wiley & Sons, New York 1999.

[7] Robinson W.H., *Lead-rubber hysteretic bearings suitable for protecting structures during earthquakes*, Earthquake Engineering and Structural Dynamics, Vol. 10, 1982, 593–604.

[8] Skinner R.I., *An Introduction to Seismic Isolation*, John Wiley & Sons, New York 1993.

[9] Yang Y.B., Chang K.C., Yau J.D., *Base isolation*, [in:] Chen W.F., Scawthorn C. (Eds.), *Earthquake Engineering Handbook*, CRC Press, London 2003.

[10] Falborski T., *Experimental determination of basic mechanical properties of elastomeric polymer*, Advances in Chemical and Mechanical Engineering, Vol. 1, 2012, 147–150.

[11] Falborski T., Jankowski R., *Experimental study on static and dynamic properties of polymer mass*, Current Scientific Challenges in Concrete and Steel Structures and Concrete Technology, Vol. 1, 2011, 41–48.

[12] Falborski T., Jankowski R., Kwiecień A., *Experimental study on polymer mass used to repair damaged structures*, Key Engineering Materials, Vol. 488–489, 2012, 347–350.
[13] Falborski T., Kwiecień A., Strankowski M., Piszczyk Ł., Jankowski R., *The influence of temperature on properties of the polymer flexible joint used for strengthening historical masonries*, Structural Analysis of Historical Constructions, Vol. 1, 2012, 816–822.
[14] Falborski T., Strankowski M., Piszczyk Ł., Jankowski R., Kwiecień A., *Experimental examination of an elastomeric polymer*, Technology and Art, Vol. 3, 2012, 98–101.
[15] Falborski T., Jankowski R., *Łożysko polimerowe do redukcji i tłumienia drgań, zwłaszcza konstrukcji budowlanych*, Patent Application No. P-401953.
[16] Falborski T., Jankowski R., *Shaking table experimental study on the base isolation system made of polymer bearings*, Proceedings of the 15th World Conference on Earthquake Engineering, Paper No. 2119, Lisbon, Sep 24–28, 2012, 1–8.
[17] Falborski T., Jankowski R., *Polymeric Bearings – a new base isolation system to reduce structural damage during earthquakes*, Key Engineering Materials, Vol. 569–570, 2013, 143–150.
[18] Falborski T., Jankowski R., *Reduction of vibrations of steel structure models with polymeric bearings – experimental study*, Current Scientific Challenges in Concrete and Steel Structures, Material Technology and Structural Fire Protection, Vol. 1, 2014, 1–8.
[19] Hwang J.S., Wu J.D., Pan T.C., Yang G., *A mathematical hysteretic model for elastomeric isolation bearings*, Earthquake Engineering and Structural Dynamics, Vol. 31, 2002, 771–789.
[20] Jankowski R., *Nonlinear rate dependent model of HDRB*, Bulletin of Earthquake Engineering, Vol. 1, 2003, 397–403.
[21] Kikuchi M., Aiken I.D., *An analytical hysteresis model for elastomeric seismic isolation bearings*, Earthquake Engineering and Structural Dynamics, Vol. 26, No. 2, 1997, 1–17.
[22] Pan T.S., Yang G., *Nonlinear analysis of base-isolated MDOF structures*, Proceedings of the 11th World Conference on Earthquake Engineering, Paper No. 1534, 1996, 1–8.
[23] Tsai C.S., Chiang T.C., Chen B.J., Lin S.B., *An advanced analytical model for high damping rubber bearings*, Earthquake Engineering and Structural Dynamics, Vol. 32, 2003, 1373–1387.
[24] Chopra A.K., *Dynamics of Structures: Theory and Applications to Earthquake Engineering*, Prentice Hall, New Jersey 1995.
[25] Clough R., Penzien J., *Dynamics of Structures*, McGraw-Hill, New York 1975.
[26] Newmark N.M., *A method of computing for structural dynamics*, Journal of the Engineering Mechanics Division, Proceedings of the American Society of Civil Engineers, Vol. 85, No. EM3, Paper No. 2094, 1959, 67–94.

TECHNICAL TRANSACTIONS | **CZASOPISMO TECHNICZNE**
CIVIL ENGINEERING | BUDOWNICTWO
3-B/2016

DOI: 10.4467/2353737XCT.16.211.5960

IWONA GALMAN, JAN KUBICA*

AN ATTEMPT TO DESCRIBE THE STIFFNESS DEGRADATION OF BRICK MASONRY SUBJECTED TO UNIAXIALLY CYCLIC COMPRESSIVE LOADS

PROPOZYCJA OPISU PROCESU DEGRADACJI MURU PODDANEGO CYKLICZNEMU, OSIOWEMU ŚCISKANIU

A b s t r a c t

The paper presents the results of laboratory experiments carried out on eight clay brick masonry wallettes of two types under cyclic compressive loading. Based on the results, the failure envelopes were determined, presented and discussed, as were common points stress-strain relationships for both series of specimens. The analytical description of the kinetic of stiffness degradation (with proposed appropriate formulae and experimentally determined parameters) was elaborated and proposed.

Keywords: clay brick masonry; compression; cyclic load; stiffness degradation; envelope curve; common-point curve

S t r e s z c z e n i e

W pracy zaprezentowano wyniki badań 8 murów (dwóch serii) z cegły ceramicznej pełnej poddanej cyklicznej sile ściskającej. Zależność naprężenie – odkształcenie zostało omówione dzięki znajomości krzywej punktów wspólnych i obwiedni z badań cyklicznych. Podjęto próbę analitycznego opisu procesu degradacji sztywności muru.

Słowa kluczowe: ściany murowe; ściskanie; obciążenie cykliczne; degradacja sztywności; krzywa punktów wspólnych, obwiednia

* Ph.D. Iwona Galman, Prof. Jan Kubica, Department of Structural Engineering, Silesian University of Technology.

Notation

$[D_{cr}]$ – stiffness matrix of material after cracking;
$[D_c]$ – stiffness matrix of material for linear-elastic behaviour;
ω – damage parameter, (scalar value from the range <0;1>);
ω_{cc} – damage parameter for masonry under uniaxially cyclic compression;
ε_{cr} – strain corresponding to first crack appearance;
ε_{pl} – strain corresponding to the beginning of the quasi-plastic behaviour of the cyclically loaded masonry (rapidly growth of deformations);
E_i – values of secant modulus of elasticity determined for *i*-th cycle;
$E_{0,1}$ – values of secant modulus of elasticity determined for first cycle;
a_i, b_i, c_i, d_i – empirically determined coefficients (table values).

1. Introduction

When analysing any material in any stress state, it is necessary to know the limit values of certain parameters related to its cracking and/or failure. The characteristics of stresses (compressive, tensile or shear) as a function of strains which limit the elastic and plastic behaviour of the material, with plastic-brittle or perfectly-plastic failure mode, allows the defining of boundary or failure curves (in plane state) or surfaces (in spatial state). These functions must not only represent the parameters of the masonry components but they must also be representative of failure modes. For many years, attempts have been made to develop more and more complex failure criteria and material models dedicated mainly to the analysis of the behaviour of masonry. There is vast available literature in this topic. It is worth mentioning that a well-known and commonly used model developed by Lourenço [1] and Lourenço & Rots [2]. Generally, the model is based on the assumption of the two well-known failure criteria: Rankine criterion in tensile stresses range and Hill's criterion in compressive stresses range. Another interesting model was developed by Lubliner, Olivier, Oller & Oñate [3] which, although being developed and used for the analysis of concrete structures, has recently been more often used for the numerical analysis of masonry – also in Silesian University of Technology [4]. It is an elastic-plastic-damage model (e-p-d), commonly referred to as the Barcelona model.

In more precise numerical analyses of masonry walls subjected to cyclic loading, including cyclic compression, it is necessary to apply a material model taking into account the phenomenon of material degradation due to increasing stresses and strains. The process of material degradation is usually accounted for by the introduction of specific parameters (coefficients of mostly constant values) modifying certain entries of the stiffness matrix. As the material degradation progresses, the stiffness of masonry changes after cracking (represented by matrix $[D_{cr}]$). According to continuum fracture mechanics (equivalence of strain in cracked masonry and equivalent uncracked masonry with elastic characteristics) the changes in material can be represented in the form of a modified elasticity matrix describing the behaviour of the material in an elastic phase ($[D_c]$). A general form for the calculation of a modified stiffness matrix after the appearance of cracks in the material is as follows:

$$[D_{cr}] = (1-\omega)[D_c] \tag{1}$$

The scalar parameter (coefficient) ω takes values between 0 and 1. In cases where there is no fracture in the material, the value of ω is 0. When a fracture develops, the value of the coefficient asymptotically reaches a maximum of ω = 1 when the fracture reaches the point of failure.

The process of fracture development as a function of strains ω(ε) relationship for a given material is usually not easy to define. It depends not only on the stress and strain states and corresponding limit values but also on the parameters characterising material properties (which have a random nature) and on the loading history.

In the case of masonry walls subjected mainly to compressive loads, the modulus of elasticity is the basic property characterising the material. When compressive loads act in a cyclic manner, based on the values of the modulus of elasticity (secant modulus from the stresses range from 0 to 1/3 σ_{max}) determined for subsequent loading cycles, it is possible to determine the parameter ω_{cc} (for masonry under uniaxial cyclic compression) from the following formulae:

$$E_i = E_{0.1}(1-\omega_{cc}) \tag{2}$$

$$\omega_{cc} = \frac{E_{0.1} - E_i}{E_{0.1}} \tag{3}$$

Thus, laboratory tests of cyclic compressive loading of masonry are performed. They allow to define the behaviour of walls beyond the elastic behaviour, the characteristics of hardening (softening) laws at compression and material degradation (changes of the modulus of elasticity during loading cycles).

Cyclic loads are not only loads of seismic or paraseismic (mining) origin but also loads induced by heavy vehicular and railway traffic as well as being due to tunnel works and different types of machines and equipment located in industrial buildings. Knowledge about the behaviour of masonry under cyclic loading will allow for better protection against such effects for both newly-designed and existing buildings. The problem of the influence of repetitive loads on the behaviour of masonry has frequently been discussed in Poland by Ciesielski et al. [5]. However, as there are still no definite specifications for the selection of the mechanical parameters of masonry under complex dynamic loading, further investigation and tests in this area should be performed.

The issue of the behaviour of masonry walls subjected to cyclic compressive loading has been investigated for 20 years by Sinha et al. [6–9], AlShebani [10] and Tiwari [11]. Researchers defined the boundary curves and common-point curves with exponential or polynomial functions with variable empirical coefficients. Information from these analyses is interesting from a qualitative point of view. However, as the tests were conducted on a different type of masonry to those which are used in Central Europe, the results have no practical use, not only in Poland. Moreover, the results of these investigations were often contradictory to each other; therefore, it was considered necessary to analyse the issue based on the own tests of masonry walls made of the most popular components: ceramic bricks with cement-lime mortar.

2. Experimental tests

The experimental investigations we performed on two types of test specimens made of clay brick of class '15' (f_b = 18.7 N/mm^2) and cement-lime mortar (1 : 1 : 6) class M5 (f_m = 6.8 N/mm^2). Elements of CV type were used to determine the compressive strength of masonry according to the method given in EN 1052-1:2001 [12]. Masonry specimens of an MW type were used for the testing of masonry with higher overall dimensions (according to requirements specified in standard [12]) and with most popular thicknesses used in the construction of load-bearing walls in Poland (1 brick, i.e. 250 mm). English bond (also very popular in Poland) was applied so the longitudinal joint was formed in every second layer.

Measuring frames with inductive sensors to measure deformations to an accuracy of 0.0002 mm were located on the both sides of the masonry wallette. The measurement base recording vertical and horizontal deformations was equal to 300 mm in the case of CV models and 600 mm in the case of MW series wallettes.

The tests of the CV type masonry wall specimens (smaller specimens) were performed using a hydraulic press machine with a 2000 kN range capacity while the tests of the MW masonry wallettes were carried out with using a hydraulic press machine with a maximal range of 6000 kN. Before placing the specimen in the press machine, both the top and the bottom surfaces of each specimen were levelled with a cement mortar. To eliminate friction between the surfaces of the steel heads of the machine and specimen's surfaces special pads were used; these pads were made of Teflon (thickness of pad – 10 mm) for the CV series specimen and a double layer of polyurethane foil with graphite grease between them for the MW series specimens. The shape, dimensions of the testing specimens and the view of both types of test specimens prepared for testing is shown below in Fig. 1.

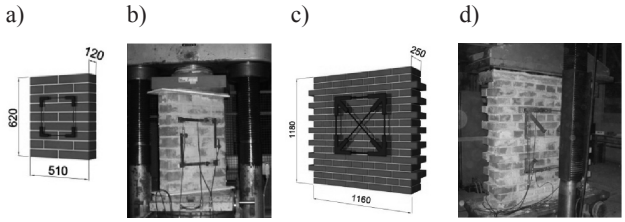

Fig. 1. The shape, dimensions and view of both types of specimens prepared for testing: a) CV type; b) MW type

The tested elements were cyclically loaded with the load increasing in each cycle. The loading velocity was equal to 2 kN/s. The first level of load for the CV series masonry specimens was equal to 50 kN and then increased by 50 kN in each cycle. The first level of load for the MW series wallettes was equal to 300 kN, followed by 600, 900 and 1200 kN, and the next cycles – until failure of the element – were increased by steps of 150 kN. During each cycle, the load was sustained for approx. 3 minutes to stabilise the state of deformations. The loading history for cyclically compressed masonry is graphically presented in Fig. 2. In total, eight specimens were tested (3 – CV type and 5 – MW type).

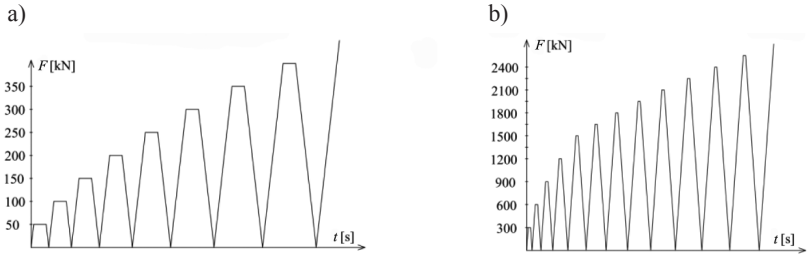

Fig. 2. Loading history for testing of specimens: a) CV series; b) MV series

3. Results and discussion

Cyclic tests allow the definition of a failure envelope of the stress–strain relationship (σ–ε) and determining the common points, i.e. the locations of the intersection of the loading curve in a given cycle with an unloading curve from the previous cycle. Each common point provides information about transformation of the material from the initial to secondary deformation states connected with the process of failure development (progressive degradation). Typically, the σ–ε relationship for masonry subjected to cyclic loading with depicted characteristic curves is presented in Fig. 3a. To eliminate small changes of the material and strength differences, further comparison of results was conducted on normalised relationships σ_i/σ_{max},$-\varepsilon_i/\varepsilon(\sigma_{max})$. Averaged, normalised failure envelopes and common-points curves for the CV and MW masonry wallettes are shown in Fig. 3b.

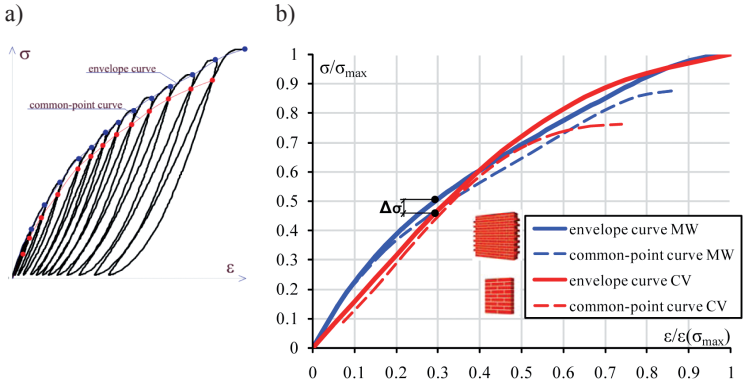

Fig. 3 σ–ε relationship for masonry subjected to cyclic loading: a) typically with characteristic curves: envelope curve and common-points curve; b) normalised for MW and CV series models

In analysing the above-mentioned relationships, it can be noticed that in the initial range of compressive stresses, i.e. up to approx. $0.6\sigma_{max}$, in case of masonry with a thickness of ½ brick (CV series), the resultant relationships are linear which signifies close-to-elastic behaviour of the masonry. On the other hand, from analysis of the relationships determined

in the tests of specimens with a thickness of 1 brick (MW series), it appears that the diagrams from the very beginning up to the level of approx. 30% of σ_{max} (first visible crack appearance) have a curvilinear character (linear elastic behaviour of the material). Then, in the range from 30% to approx. 75% of σ_{max} (when this are rapidly increasing plastic-brittle damage deformations) fracture development stabilises at a similar level and the diagram has a more or less linear character. This observation can be explained by the fact that in masonry walls with greater thickness, there is an unbound longitudinal joint located in the axis of the wall which has an effect on the behaviour of that wall – this is because of the applied bonding of the elements in subsequent layers of the walls. When stresses exceed the value of 75% of σ_{max}, the process of fracture and disintegration of the material is very quick (rapid) leading to the state of.

In the presented cases, failure envelopes and common-points curves run parallel up to the level of cracking stresses (σ_{cr}). The occurrence of further plastic deformations, fractures and cracks causes visible splitting along their trajectories – the common-points curve descends rapidly.

Describing the curves with fourth-order polynomials, the following formula was used:

$$\frac{\sigma}{\sigma_{max}} = a \cdot \left(\frac{\varepsilon}{\varepsilon(\sigma_{max})} \right)^4 + b \cdot \left(\frac{\varepsilon}{\varepsilon(\sigma_{max})} \right)^3 + c \cdot \left(\frac{\varepsilon}{\varepsilon(\sigma_{max})} \right)^2 + d \cdot \frac{\varepsilon}{\varepsilon(\sigma_{max})} \tag{4}$$

Table 1

Constant coefficients of polynomial function $\sigma/\sigma_{max,i} - \varepsilon/\varepsilon(\sigma_{max,i})$ for eq. (4)

series	curve	values of constant coefficients			
		a	***b***	***c***	***d***
MW	envelope curve	–2.17	5.00	–4.47	2.64
	common-points curve	–4.19	8.14	5.57	2.72
CV	envelope curve	1.16	–2.52	0.87	1.49
	common-points curve	4.75	–8.96	4.19	0.92

As the $\Delta\sigma$ parameter characterises the kinetics of the degradation process developing the difference in compressive stresses between failure envelope and common-point curve, it was used and determined according to the scheme presented in Fig. This allows the graphical representation of the process of degradation, which is shown in Fig. 5.

Except the initial phase of loading in the case of both MW and CV masonry wallettes, the $\Delta\sigma - \varepsilon/\varepsilon(\sigma_{max})$ relationship can be described with an exponential function:

$$\Delta\sigma = a_1 \cdot e^{b_1 \cdot \frac{\varepsilon}{\varepsilon(\sigma_{max})}} \tag{5}$$

The relationship ($\Delta\sigma - \varepsilon_i/\varepsilon(\sigma_{max})$) presented in Fig. 4 indicates that in the case of small masonry specimens with thickness of ½ brick (CV series models), the chain process of material degradation begins for strains of a magnitude over approx. 35% of ultimate strains

($\varepsilon(\sigma_{max})$). This corresponds to the situation of the appearance of the first cracks. It is slightly different in the case of masonry walls with a thickness of 1 brick (masonry wallettes of MW series) with a longitudinal joint in every second layer. The first zone of visible fracture development and stiffness degradation was observed in the range of strains from almost the beginning until approx. 35% of ultimate strains ($\varepsilon(\sigma_{max})$). The degradation process then stabilises up to a level of strains of approx. 0.75 ($\varepsilon(\sigma_{max})$) when a sudden increase of strains is observed. Probably at this moment, the plastic zone with some fractures and material internal damage is reached. Intensive strain development begins, this is caused by both the development of unrecoverable plastic strains and the progressive development of cracking (fracture). This situation took place up to the state of failure of the masonry.

Table 2

Constant coefficients of exponential function $\Delta\sigma - \varepsilon/\varepsilon(\sigma_{max})$ for eq. (5)

series	constant coefficient values	
	a_1	b_1
MW	0.0041	4.91
CV	0.0037	3.53

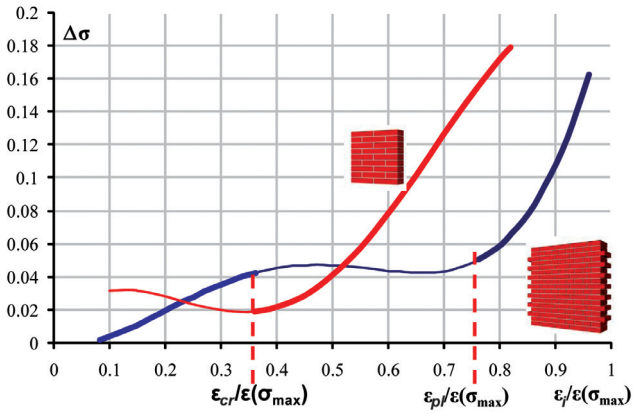

Fig. 4. Resultant $\Delta\sigma - \varepsilon_f/\varepsilon(\sigma_{max})$ relationships for **MW** and **CV** masonry specimens

In the case of smaller specimens (CV series) based on the equations (3) and (5), the process of stiffness degradation as a function depending on stress (σ) and strains (ε) state, can be expressed as:

$$\omega_{cc} = F(\sigma,\varepsilon) = c_1 \cdot \frac{\varepsilon}{\varepsilon(\sigma_{max})} \tag{6}$$

where value of coefficient c_1 is presented in Table 3.

The function of the failure progress during cyclic loading $\omega_{cc} - \varepsilon/\varepsilon(\sigma_{max})$ of CV masonry wallettes is shown in Fig. 5a; for the MW series masonry wallettes, refer to Fig. 5b.

The situation becomes more complicated in the case of masonry wallettes with a longitudinal joint in every second layer (MW series specimens). As is shown in Fig. 5b, the $\omega_{cc} - \varepsilon/\varepsilon(\sigma_{max})$ relationship has a similar to linear character only in the initial phase of loading. After exceeding the specific value of strain (ε_{cr}) which corresponds to the cracking strain (in the presented tests, this corresponded to a level of strain of approx. 0.35 $\varepsilon/\varepsilon(\sigma_{max})$), the curvature of the function changes. From that point up to about 0.75 $\varepsilon/\varepsilon(\sigma_{max})$, stabilisation of the fracture development was observed. A sudden increase in a fracture parameter was observed after exceeding the value of strains – this can be taken as corresponding with plastic strains (here, this level was equal to approx. $0.75\varepsilon/\varepsilon(\sigma_{max})$). To better visualise the $\omega_{cc} - \varepsilon/\varepsilon(\sigma_{max})$ relationship, characteristic points up to the appearance of cracking are marked as filled points while they are marked as empty points after cracking.

a) b)

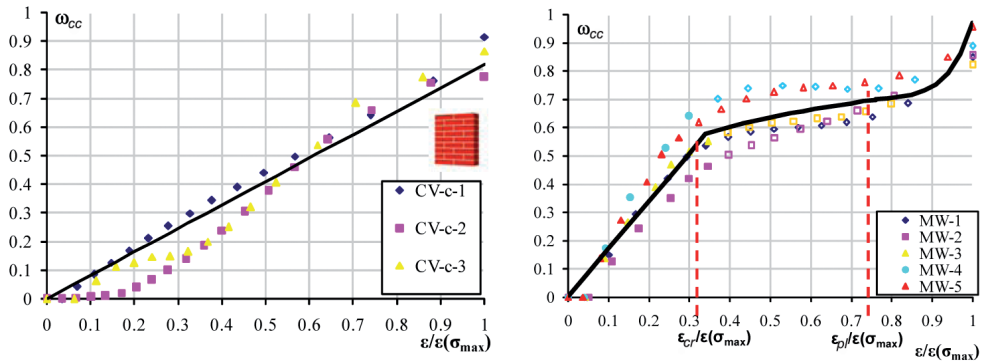

Fig. 5 $\omega_{cc} - \varepsilon/\varepsilon(\sigma_{max})$ relationship: a) for **CV** masonry specimens; b) for **MW** masonry specimens

The proposed function describing the material degradation process in the case of the masonry wallettes with a longitudinal joint (models of MW series) was defined depending on the value of strains as a continuous interval relationship – a combination of linear, logarithmic and power functions:

$$\omega_{cc} = F(\sigma,\varepsilon) = \begin{cases} b_2 \cdot \dfrac{\varepsilon}{\varepsilon(\sigma_{max})} & \varepsilon \le \varepsilon_{cr} \\ \sigma(\varepsilon_{cr}) + b_3 \cdot \ln \dfrac{\varepsilon}{\varepsilon(\sigma_{max})} + d_2 & \varepsilon_{cr} < \varepsilon \le \varepsilon_{pl} \\ \sigma(\varepsilon_{pl}) + b_4 \cdot \left(\dfrac{\varepsilon}{\varepsilon(\sigma_{max})}\right)^{d_3} & \varepsilon < \varepsilon_{pl} \end{cases} \tag{7}$$

Table 3

Constant coefficients used in eq. (6) and (7)

constant coefficient values					
c_1	b_2	b_3	b_4	d_2	d_3
0.82	1.70	0.15	0.27	0.16	17.00

The proposed functions [6 & 7] were graphically presented with continuous lines in Fig. 5. The differences in the character of the $\omega_{cc} - \varepsilon/\varepsilon(\sigma_{max})$ relationship between the CV and MW masonry wallettes correlate to the differences observed in $\Delta\sigma - \varepsilon_i/\varepsilon(\sigma_{max})$ relationships.

4. Summary and conclusions

The progressive degradation process of masonry walls occurs as a result of low frequency cyclic compression. Investigations into the relationship between the failure envelope and common-points curve is necessary and useful for the description of the yield surface changes during the loading process. Stresses below the common-points curve cause only reduced plastic strains in masonry while stresses over that curve lead to the formation of unrecoverable plastic strains. Common-points curve up to the level of σ_{cr} (stresses corresponding to the first crack appearance) run parallel below the envelope curve for cyclic tests. After exceeding cracking stresses, a sudden change in the curvature of the common-point curve is observed due to the degradation of masonry caused by cracking and fracture. Based on the result of the presented tests and analytical analysis, the following conclusions may be formulated:

- the differences in compressive stresses between the failure envelope and the common-points curve characterises the process of fracture development of masonry elements subjected to uniaxial cyclic compressive loads in a vertical direction;
- knowledge of the values of the modulus of elasticity in subsequent cycles allows determining the fracture (damage) coefficient (ω) described as a function dependent on the stresses and strains in a masonry wall as opposed to typically taking this parameter as a scalar value from the range <0;1>. This approach may be useful in the case of the numerical modelling of masonry walls with a internal longitudinal joint (e.g. when the thickness of the wall is equal to or higher than the length of the masonry unit);
- fracture (damage) coefficient in case of the masonry with longitudinal joints (e.g. the most popular English bond or Flemish bond) subjected to cyclic compressive loads in direction perpendicular to bed joints may be expressed using the continuous interval function proposed in eq. (7). In the first range from 0 to achieving the cracking strain value ε_{cr} (in presented tests corresponding with $0.35\ \varepsilon/\varepsilon(\sigma_{max})$), the fracture coefficient was described with a linear function. Then, in the range from ε_{cr} to ε_{pl} ($0.35\ \varepsilon/\varepsilon(\sigma_{max})$ to $0.75\ \varepsilon/\varepsilon(\sigma_{max})$ it is described with a logarithmic function. In the third range, from ε_{pl} ($0.75\ \varepsilon/\varepsilon(\sigma_{max})$), up to failure, the degradation process was described by the power function;
- the proposed mathematical description of the fracture (damage) coefficient function $\omega_{cc} = F(\sigma,\varepsilon)$ has not too universal character; this is due to the limited number of tested specimens and using only one type of masonry units and mortar. Further investigations, both experimental and analytical, are necessary.

References

[1] Lourenço P.B., *Computational strategies for masonry structures*. PhD Dissertation, Delft University of Technology, Delft University Press, The Netherlands 1996.

[2] Lourenço P.B., Rots J.G., *A multi-surface interface model for the analysis of masonry structures*, J. Engng. Mech., ASCE, 7, 1997, 660–668.

[3] Lubliner J., Olivier J., Oller S., Oñate E., *A Plastic-Damage Model for Concrete*, Int. J. of Soils and Struct., 25, 1989, 299–329.

[4] Wawrzynek A., Cińcio A., Fedorowicz J., *Numerical Verification of the Barcelona Model Adapted for Brick Walls*, Proc. of the 7th Int. Masonry Conf., London 2006, 84.

[5] Ciesielski R., Maciąg E., Tatara T., *Evaluation of dynamic properties of masonry buildings on the basis of traffic induced vibrations*, Proc. Conf. "Traffic Effects on Structures and Environment", Strbskie Pleso, 1987, 445–451.

[6] Naraine K., Sinha S., *Behaviour of Brick Masonry Under Cyclic Compressive Loading*, Journal of Construction Engineering and Management, 1989, 1432–1445.

[7] Chaubey U., Sinha S., *Cyclic compressive loading response of brick masonry*, Journal of Masonry International, Vol. 4, No. 3, 1991, 94–98.

[8] AlShebani M., Sinha S., *Stress-Strain Characteristics of Brick Masonry Under Uniaxial Cyclic Loading*, Journal of Structural Engineering, Vol. 125, No 6, 1999, 600–604.

[9] Senthivel R., Sinha S., *Behaviour of Calcium Silicate Brick Masonry Under Cyclic Uniaxial Compression*, Masonry. Proc. 6th Int. Masonry Conference, Vol. 9, 2002, 412–422.

[10] AlShebani M., *Permissible Stress Level of Brick Masonry under Compressive Cyclic Loading*, Journal of Civil Engineering and Architecture, Vol. 7, 2013, 153–157.

[11] Tiwari V., Chaubey U., *Experimental Study Of Fly-Ash Brick Masonry Under subjected To Cyclic Loading*, International Journal of Science Technology & Engineering, Vol. 1, Issue 1, 2014.

[12] EN 1052-1 Methods of test for Masonry – Part 1: Determination of compressive strength.

TECHNICAL TRANSACTIONS | CZASOPISMO TECHNICZNE
CIVIL ENGINEERING | BUDOWNICTWO
3-B/2016

DOI: 10.4467/2353737XCT.16.212.5961

HALINA GARBALIŃSKA, JAROSŁAW STRZAŁKOWSKI*

WAVE AMPLITUDES OF TEMPERATURE AND HEAT FLUX IN THE SURROUNDINGS OF EXTERNAL WALLS

AMPLITUDY FALI TEMPERATURY I STRUMIENIA CIEPŁA W OTOCZENIU ŚCIAN ZEWNĘTRZNYCH

Abstract

In this paper, the thermal dynamic characteristics of exterior walls with variant concrete solutions of load-bearing layer were analysed. The main aim of this study was to compare the amplitudes of wave fluctuations of internal temperature and internal heat flux depending on the construction material used. Calculations were made for partitions with a structural layer made from lightweight concrete composites, autoclaved aerated concrete and reinforced concrete. Very good damping properties were obtained for the partitions made of concrete composites. The obtained data suggests that such solutions provide much smaller fluctuations of temperature and heat flux in comparison to materials with low specific heat.

Keywords: dynamic thermal characteristics, transfer matrix, lightweight concrete composites, heat flux

Streszczenie

W niniejszej pracy poddano analizie zbiór danych dotyczących dynamicznych charakterystyk cieplnych ścian zewnętrznych o różnie dobranej pod względem materiałowym warstwie konstrukcyjnej. Głównym celem pracy było porównanie amplitud wahań fali temperatury wewnętrznej i wewnętrznego strumienia ciepła w zależności od użytego materiału warstwy nośnej. Rozpatrzono przegrody z warstwą konstrukcyjną wykonaną z rozmaitych lekkich kompozytów betonowych, betonów komórkowych oraz betonu zbrojonego. Bardzo dobre właściwości tłumiące przegrody uzyskano dla kompozytów betonowych. Otrzymane dane wykazują, że tego typu rozwiązania zapewniają zdecydowanie mniejsze wahania fali temperatury i strumienia ciepła w porównaniu do materiałów o niskim cieple właściwym.

Słowa kluczowe: dynamiczne charakterystyki cieplne, macierz przejścia, lekkie kompozyty betonowe, strumień ciepła

* Prof. Halina Garbalińska, M.Sc. Eng. Jarosław Strzałkowski, Department of Building Physics and Building Materials, Faculty of Civil Engineering and Architecture, West Pomeranian University of Technology Szczecin.

1. Introduction

New, stricter requirements for energy savings make it necessary to look for customised solutions designed to improve the energy efficiency of buildings, which is the subject of numerous research projects both in Poland [1] and abroad [2].

The reduction in the value of thermal transmittance turns out to be insufficient to achieve the goal of almost zero-energy building design. Nowadays, new solutions are sought which can positively affect the reduction of energy consumption through the use of various types of heavy building materials. Tests performed in [3] show explicit differences in the energy consumption of buildings with differently set load-bearing and insulating layers as well as the influence of the thickness of heavy layers.

Due to the complex problem of non-stationary heat flow through the partitions, in conjunction with the effects of both sunlight radiation and ventilation in buildings, efforts are taken to determine parameters that could replace the thermal transmittance U which describes only stationary heat flux. For this purpose, a dynamic coefficient of thermal resistance is described [4]. This coefficient takes into account the effect of thermal mass in calculations of the real heat flux through the building partition. Another approach presented in [5] involves the use of a dimensionless global heat transfer coefficient which is based on harmonically varying conditions of temperature on both sides of the wall. This factor additionally takes into account the influence of solar radiation.

Apart from use of alternative energy sources and innovative installation solutions, the influence of materials used in construction is also worth considering. This problem was undertaken by Taylor [6] who compiled and compared all sorts of traditional building materials for interior finish used as an additional thermal mass. There were also some efforts taken to determine the heat capacity of various building materials depending on its density or thermal conductivity [7]. Studies were also performed to assess the relationship between the moisture of the material and the increase of its thermal conductivity λ and volumetric specific heat c_v [8].

In this paper, we tested the dynamic thermal characteristics [9] of typical two-layer walls with different load-bearing materials. We analysed which type of concrete composite was most effective with regard to energy savings.

2. Design conditions

2.1. Analysed wall

The calculation of amplitude fluctuation of temperature and heat flux on both sides of the partition was made on the basis of norm [10] which enables solving the Fourier equation in harmonically variable boundary conditions. The scheme of the tested partition is shown in Figure 1.

The calculations were made for seven wall solutions which differed in the kind of load-bearing material. Each of the analysed variants must also meet the minimum requirements of thermal insulation in accordance with [11]. The thickness of all layers was constant. This

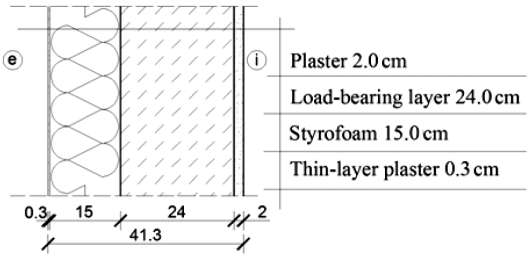

Fig. 1. Scheme of the analysed wall

allowed to comparison the influence of the tested concretes on the amplitudes regardless of the thickness of the materials. The surface resistance of the boundary layer was also taken into account. The parameters of the partition are shown in Table 1.

Table 1

Parameters of the particular layers of the external wall

No.	Layer	d m	λ W/(m·K)	ρ kg/dm^3	c_v MJ/(m^3·K)
1	plaster	0.020	0.40	1.00	1.00
2	load-bearing layer	0.240	tab. 2	tab. 2	tab. 2
3	styrofoam	0.150	0.04	0.03	0.042
4	thin-layer plaster	0.003	1.00	1.80	1.80

The analysis was made for the seven different concretes presented in Table 2. The data of the dynamic thermal characteristics, with a particular emphasis on the periodic thermal transmittance and internal area heat capacities, were discussed in [12].

The first four materials shown in Table 2 indicated by symbols LEC and LYT are concretes based on expanded clay aggregate and fly ash aggregate respectively. Composites based on lightweight aggregates are an interesting alternative to normal concrete, and they still have untapped potential in Poland. The usefulness of clay raw materials for the production of lightweight aggregates from the south-eastern area of Poland were investigated by Panna et al. [13].

The specific heat of the load-bearing materials is presented in relation to the volume instead of weight because it accurately reflects the relationship between the wall thickness and heat capacity in comparison to the mass of the wall.

The analysed composites were made in two variants: non-aerated (N) and aerated (A). These concretes were made for the purpose of currently ongoing research project. The properties of air-entrained concretes were the subject of multi-faceted research conducted by Kulová et al. [14]. The authors conducted tests of air-entrained composites with the addition of brick powder.

The study also included the simulation of partitions with a load-bearing layer made of autoclaved aerated concretes. The influence of bulk density and moisture on the thermal parameters of autoclaved aerated concrete has been discussed by Unčík et al. [15]. Physical properties of the autoclaved aerated concretes and reinforced concrete were determined based on [16].

Table 2

Parameters of the particular load-bearing layers and *U* coefficients of whole partitions

No.	Material	λ W/(m·K)	ρ kg/dm³	c_v MJ/(m³·K)	*U* – whole partition W/(m²·K)
1	LEC/N	0.73	1.35	1.76	0.232
2	LYT/A	0.32	1.03	1.55	0.212
3	LEC/N	1.07	1.86	1.78	0.238
4	LYT/A	0.66	1.50	1.70	0.231
5	Reinforced concrete	1.70	2.20	1.85	0.243
6	Autoclaved aerated concrete 600	0.21	0.60	0.50	0.195
7	Autoclaved aerated concrete 400	0.14	0.40	0.34	0.176

2.2. Calculation method

According to the algorithm shown in [5], the transfer matrixes *Z* were calculated for all seven variants and different fluctuation periods. On this basis, it was possible to bind the complex amplitudes of temperature and heat flux on one side with the conditions on the opposite side of the partition – this is illustrated by the following equation:

$$\begin{bmatrix} \hat{\Theta}_e \\ \hat{q}_e \end{bmatrix} = \begin{bmatrix} Z_{11} & Z_{12} \\ Z_{21} & Z_{22} \end{bmatrix} \cdot \begin{bmatrix} \hat{\Theta}_i \\ \hat{q}_i \end{bmatrix} \tag{1}$$

The above equation enables defining the magnitude of the complex amplitude of temperature and heat flux, if the values on the other side are known. The complex amplitudes allow defining the magnitude of the amplitude of the harmonically changing function (the module of the complex number) and the faze shift (the argument of the complex number). The complex amplitudes are presented in the exponential form of a complex number in the following form:

$$\hat{\Theta}_{\pm} = \left|\hat{\Theta}\right| \cdot e^{\pm i\psi} \tag{2}$$

$$\hat{q}_{\pm} = \left|\hat{q}\right| \cdot e^{\pm i\varphi} \tag{3}$$

It is assumed that the temperature on both sides of the partition oscillates around the average value and that the heat flux fluctuates around the value equal to:

$$\overline{q} = U \cdot \left(\Theta_i - \Theta_e\right). \tag{4}$$

On this basis and in this study, we put different starting conditions on one side of the partition and then analysed the acquired data from the other side, depending on the variant of load-bearing material.

3. Analysis results

3.1. Variant I

In the first variant, the external temperature was set at –10°C while the temperature inside was constant at 20°C. On this basis, the amplitudes of internal heat flux were compared. The results of the test are shown in Figure 2. The thermal diffusivity of the analysed concretes is presented in Figure 3.

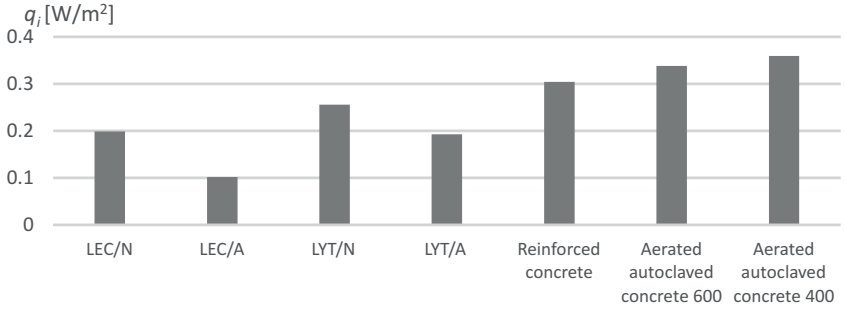

Fig. 2. The amplitudes of the internal heat flux for the 24-hour fluctuation period

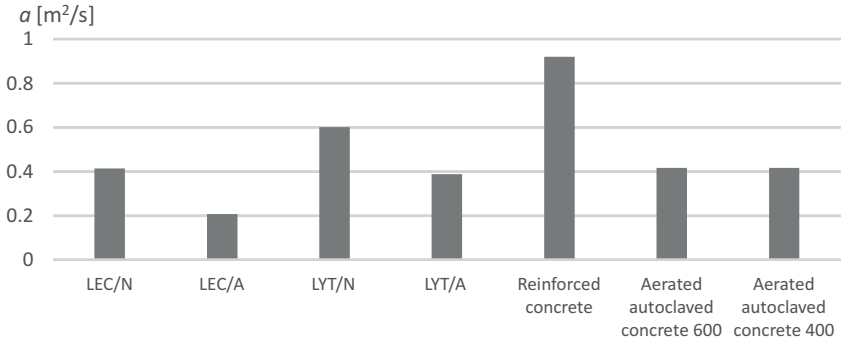

Fig. 3. Thermal diffusivity of the tested load-bearing materials

The results indicate that materials with a high specific heat and reduced thermal diffusivity enable achieving a constant temperature at considerably lower heat flux jumps on the internal surface of the partition due to temperature fluctuation on the external side of

the wall. Lightweight concretes of which the thermal conductivity λ had significantly lower values than reinforced concrete, have enabled a reduction of the heat flux amplitudes on the inner side of the partition. Despite their low thermal diffusivity, the autoclaved aerated concretes do not reduce the q_i peaks as efficiently as lightweight concretes and their values are comparable to normal reinforced concrete.

3.2. Variant II

In the second variant, the external temperature was set at 25°C and its fluctuation at 5°C. The average internal temperature was again set at 20°C; however, this time we set a constant value of internal heat flux. This enabled comparison of the samples with regard to fluctuation of the temperature inside, as shown in Figure 4.

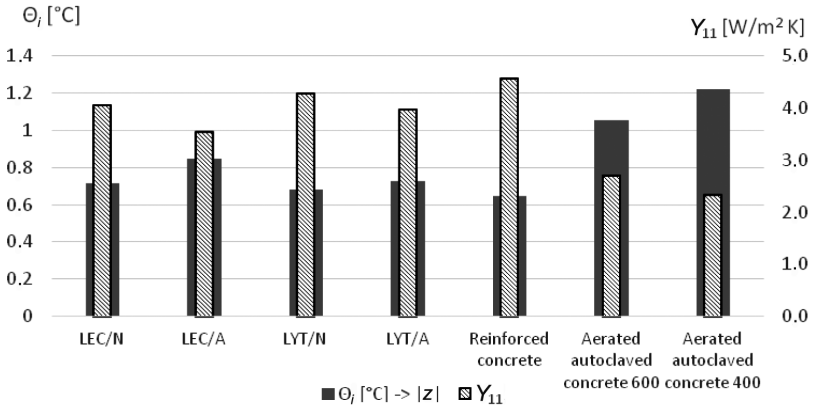

Fig. 4. The amplitudes of the internal temperature and internal admittances for the 24-hour fluctuation period

Again, the materials with higher specific heat obtained more favourable values of amplitudes. The largest fluctuations were observed for autoclaved aerated concretes of which the amplitude reached as much as 1.2°C with only 5°C external temperature variations. The specific heat c_v has a greater impact on the variation of temperature fluctuation than the thermal conductivity coefficient λ. This is the reason why the lowest fluctuation was observed for the partition with normal reinforced concrete. The relationship between internal admittance and temperature amplitude is clearly seen – the higher the value of the internal heat admittance, the lower the values of temperature fluctuation.

The exemplary distributions of the internal temperature fluctuations for a longer variation period of 168 hours are shown in Figure 5. The presented results for autoclaved aerated concrete of class 600, non-aerated concrete based on expanded clay and reinforced concrete indicate that concretes based on lightweight aggregates can represent a good alternative to normal concrete. The differences between the amplitudes of both variants are nonsignificant and are definitely preferable to the values for the ACC variant.

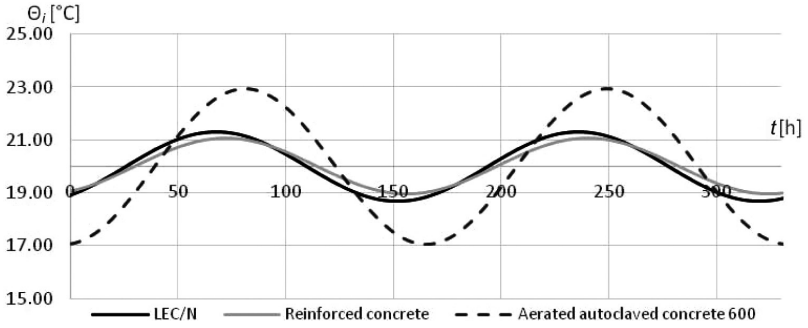

Fig. 5. Plot of internal temperature for the 168-hour fluctuation period

3.3. Required heating power

The heating power required to maintain a constant internal temperature was calculated for the examined partitions. The power value was estimated as the sum of the average heat flux (static heat flow) and the product of thermal transmittance for the period of 24 hours and the amplitude of external temperature (quasi-dynamic heat flow), described by the formula:

$$\Phi = U \cdot \Delta\Theta + Y_{12} \cdot \hat{\Theta}_e \tag{5}$$

The formula binds the average value of heat flux density with the fluctuation of heat flux caused by the variation of the temperature (harmonic fluctuation). We assumed that the outdoor temperature was –10°C, its amplitude was equal to 10°C and that the internal temperature was 20°C. The results are shown in Figure 6.

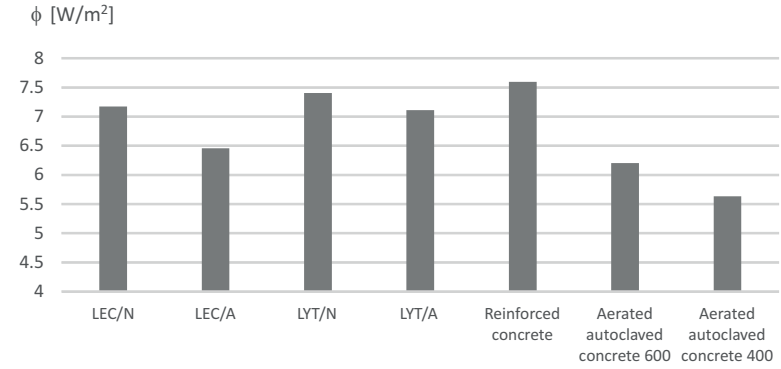

Fig. 6. Required heat power needed for maintaining constant temperature for fluctuations of 24 hours

It is worth mentioning that the required heating power in the case of the use of partitions with aerated autoclaved concretes was similar to partitions with lightweight composite concretes, although the thermal transmittance values for composites are between 0.212 and 0.238 W/(m²·K) and for AAC, it is 0.195 W/(m²·K).

4. Conclusions

The results of investigation into the dynamic properties of partitions and amplitudes of temperature and heat flux presented in this paper clearly indicate the need for a much more in-depth analysis than an assessment based solely on the comparison of the thermal transmittance of each variant. Although the comparison concerned only a few kinds of concrete composites, the obtained differences between each of the variants are clear. Materials of high specific heat such as lightweight concrete composites based on fly ash aggregate enable the significant reduction of the internal fluctuation of temperature, which, especially in low energy buildings [17], may be important for the overall energy efficiency of the building. Therefore, dynamic thermal analysis in the real climate conditions in which the building will function may be very useful.

The research of lightweight cement composites was realised as a part of research project no 2014/13/N/ST8/00091 financed by the National Science Centre, Poland.

References

[1] Kisielewicz T., *Pojemność cieplna a komfort termiczny w budynkach energooszczędnych*, Materiały Budowlane, vol. 9, 2014, 51–55.

[2] Zhang Y., Zhou G., Lin K., Zhang Q., Di H., *Application of latent heat thermal energy storage in buildings: State-of-the-art and outlook*, Building and Environment, vol. 42, 2007, 2197–2209.

[3] Kossecka E., Kośny J., *Influence of insulation configuration on heating and cooling loads in a continuously used building*, Energy and Buildings, vol. 34, 2002, 321–331.

[4] Al-Sanea A., Zedan M., Al-Hussain S., *Effect of thermal mass on performance of insulated building walls and the concept of energy savings potential*, Applied Energy, vol. 89, 2012, 430–442.

[5] Oliveti G., Arcuri N., Mazzeo D., De Simone M, *A new parameter for the dynamic analysis of building walls using the harmonic method*, International Journal of Thermal Sciences, vol. 88, 2015, 96–109.

[6] Taylor R., Miner M., *A metric for characterizing the effectiveness of thermal mass in building materials*, Applied Energy, vol. 128, 2014, 156–163.

[7] Garbalińska H., Bochenek M., *Izolacyjność termiczna a akumulacyjność cieplna wybranych materiałów ściennych*, Czasopismo Techniczne. Architektura, vol. 108, 2011, 89–96.

[8] Garbalińska H., Siwińska A, *Pojemność cieplna wybranych materiałów ściennych*, Materiały Budowlane, vol. 2, 2012, 43–45.

[9] Cerne B., Medved S., *The dynamic thermal characteristics of lightweight building elements with a forced ventilated cavity and radiation barriers*, Energy and Buildings, vol. 37, 2005, 972–981

[10] PN-EN ISO 13786:2008. Thermal performance of building components – Dynamic thermal characteristics – Calculation methods.
[11] Rozporządzenie Ministra Transportu, Budownictwa i Gospodarki Morskiej z dnia 5 lipca 2013 r. zmieniające rozporządzenie w sprawie warunków technicznych, jakim powinny odpowiadać budynki i ich usytuowanie.
[12] Garbalińska H., Strzałkowski J., *Transmitancje cieplne dwuwarstwowych ścian zewnętrznych zróżnicowanych materiałem nośnym. V Konferencja Solina'2014 Innowacyjne Technologie Energooszczędne, czerwiec 2014.*
[13] Panna W., Wyszomirski P., Gasek K., Dudek R., Łabuz A., *Hot stage microscopy in determining the suitability of selected clay rocks from south-eastern Poland to manufacture lightweight aggregates*, Cement Wapno Beton, vol. 2, 2015, 79–87.
[14] Kulovaná T., Vejmelková E., Keppert M., Rovnaníková P., Ondráček M., Keršner Z., Černý R., *Air-entrained concrete technology as an effective tool for increasing the limits of brick powder percentage in blended Portland cement binders*, Cement Wapno Beton, vol. 1, 2015, 11–24.
[15] Unčík S., Struhárová A., Hlavinková M, Sabová A., Balkovic S., *Effect of bulk density and moisture content on the properties of aerated autoclaved concrete*, Cement Wapno Beton, vol. 4, 2013, 189–196.
[16] PN-EN ISO 6946:1999 – Komponenty budowlane i elementy budynku – Opór cieplny i współczynnik przenikania ciepła – Metoda obliczania.
[17] Kisielewicz T., *Wpływ izolacyjnych, dynamicznych i spektralnych właściwości przegród na bilans cieplny budynków energooszczędnych*, Monografia 36, Kraków 2008.

TECHNICAL TRANSACTIONS | CZASOPISMO TECHNICZNE
CIVIL ENGINEERING | BUDOWNICTWO
3-B/2016

DOI: 10.4467/2353737XCT.16.213.5962

ANNA JAKUBCZYK-GAŁCZYŃSKA, ADAM KRISTOWSKI,
ROBERT JANKOWSKI*

THE APPLICATION OF NEURAL NETWORKS IN FORECASTING THE INFLUENCE OF TRAFFIC-INDUCED VIBRATIONS ON RESIDENTIAL BUILDINGS

ZASTOSOWANIE SZTUCZNYCH SIECI NEURONOWYCH W PROGNOZOWANIU WPŁYWU DRGAŃ KOMUNIKACYJNYCH NA BUDYNKI MIESZKALNE

Abstract

Traffic-induced vibrations may cause the cracking of plaster, damage to structural elements and, in extreme cases, may even lead to the structural collapse of residential buildings. The aim of this article is to analyse the effectiveness of a method of forecasting the impact of vibrations on residential buildings using the concept of artificial intelligence. The article presents several alternative forecasting systems for which it is not necessary to carry out laborious and costly measurement tests. The results show that artificial neural networks can be an effective tool for estimating the impact of traffic-induced vibrations on buildings; however, more cases need to be analysed in order to validate the system.

Keywords: traffic-induced vibrations, artificial neural networks, residential buildings

Streszczenie

Drgania komunikacyjne związane z ruchem drogowym mogą powodować w budynkach mieszkalnych zarysowania i spękania tynków, uszkodzenia elementów konstrukcji, a w sytuacjach skrajnych mogą prowadzić nawet do katastrofy budowlanej. Celem artykułu jest analiza efektywności metody prognozowania wpływu drgań na budynki mieszkalne przy wykorzystaniu idei sztucznej inteligencji. W artykule przedstawiono kilka alternatywnych systemów prognozujących wpływ drgań komunikacyjnych, w których nie jest konieczne przeprowadzanie pracochłonnych i kosztownych badań pomiarowych. Wyniki badań pokazują, że sztuczne sieci neuronowe mogą być dobrym narzędziem do prognozowania wpływu drgań komunikacyjnych na budynki, jednakże niezbędna jest większa liczba zbadanych przypadków dla uwiarygodnienia systemu.

Słowa kluczowe: drgania komunikacyjne, sztuczne sieci neuronowe, budynki mieszkalne

* M.Sc. Anna Jakubczyk-Gałczyńska (Ph.D. student), Assist. Prof. Ph.D. Adam Kristowski, Prof. Ph.D. D.Sc. Robert Jankowski, Department of Metal Structures and Construction Management, Faculty of Civil and Environmental Engineering, Gdansk University of Technology.

1. Introduction

There are many causes of building vibrations, some of these are constant dynamic encumbrances, others are temporary [6]. The most common causes include: earthquakes [21, 22], mining tremors (paraseismic vibrations) [10, 11], large mechanical vibrating entities, air pressure, movement of large masses of people or vibrations resulting from vehicles/trains using nearby roads/tracks [3, 14]. The last of these, often referred as traffic-induced vibrations, may cause the cracking of plaster, peeling of paint and loosening of plaster [3, 6]. Severe damage to structural elements or even construction disasters may also take place. The approximate distances of impact of vibrations on residential buildings are given in [5] as: 25 m from the centre of tram tracks and also the outer lane road; 40 m from the metro tunnel wall; 50 m from the centre of railway tracks. In addition to the impact of traffic-induced vibrations on buildings, the impact on people residing in buildings is also important [15]. This problem is particularly noticeable when people are exposed to prolonged vibrations and noise [5].

Many factors relating to the road upon which vehicles are driving and also the characteristics of the building may have an influence on the value of vibration. In order to determine the effect of traffic-induced vibrations on structures, relatively time-consuming and expensive measurements should be performed using specialised equipment. Conducting such measurements for all buildings located on a road may prove to be unprofitable from an economic point of view. Modern technology that is still evolving presents a number of possible solutions to these problems. One approach to diagnosing the impact of vibrations on a residential building is an expert system using artificial neural networks (ANNs) which is able to assess, with relatively high probability, the risk of the impact of vibrations without the necessity to perform measurements on a given building.

ANNs are widely used in civil engineering. Kuźniar & Chudyba used a neural network in forecasting the impact of vibrations of mining tremors on buildings [2, 9–11]. Another example of using this type of algorithm is the system described in [4] which uses the network to create ranking of bridges. The aim was to create a system which, based on several factors, would determine whether the bridge was in need urgent renovation. The authors were able to obtain satisfactory results and the system has been implemented in the General Directorate for National Roads and Motorways. Kogut in [8] applied ANNs in road problems based on [12], the aim of the study was to identify the critical time needed to cross a main road in Ohio. The author took various environmental, meteorological, ecological and social factors into account. The network correctly classified up to 87.5% correct responses with an acceptable error of 5%. The author of the study described in [8] also took into consideration the use of a network to determine the expected level of carbon monoxide air pollution within the vicinity of intersections in central Seattle. The network correctly described 70% of the values relative to the tested data. An ANN algorithm was also applied to assess the degree of technical wear of historical monuments (more in [20]).

As far as the authors are aware, ANNs have not yet been applied to estimate the impact of traffic-induced vibrations on buildings in relation to the standard [14] – this article presents the first such attempt. During the performance of tests, different measuring situations were classified according to specific criteria which were later applied to build a system based on ANN.

2. Studies of the influence of traffic-induced vibrations on buildings

A method of determining the impact of traffic-induced vibrations on buildings depends on the situation to be analysed. According to [5], four cases are possible:

- building designed but not yet built, the source of vibrations is predicted;
- building designed but not yet built, the source of vibrations is known;
- building already constructed, the source of vibrations is predicted;
- building already constructed, the source of vibrations is known.

In the first case, a computational model of the building is designed and the numerical analysis is performed, for example, by using the finite element method. In the second situation, ground vibration measurements are performed at the intended location. In the third case, vibrograms from a similar situation are applied. In the last case, the measurements of vibrations are performed, vibrograms are created, results are filtered and compared to the standard values [14].

Vibration studies are performed (see [5, 7, 14]) for short term loadings (occurring less than 3 minutes per day), long-term (occurring at least 3 minutes, maximum of 30 minutes per day) and regular (occurring above 30 minutes a day) to determine their influence upon the building. The analysis is then performed according to the standard [14]. Depending on the size of the vibrations, the resulting chart is located in one of the five zones of danger.

In this study, the vibration field measurements taken on four residential buildings are presented (Fig. 1). The source of vibrations was related to the movements of vehicles with varying tonnages and number of axles, travelling at different speeds. For each building, a series of several tests was conducted. As the outcome of the tests, after the analysis in 1/3 octave bands, authors received about 400 results for each building. The peak values were selected and plotted on Dynamic Influence Scale I graph (DIS I). Fig. 2 and Fig. 3 show examples of graphs of peak accelerations with respect to the centre frequencies. After performing an analysis consistent

Fig. 1. Buildings tested for traffic-induced vibrations (arrows indicate the locations of vibration sensors)

with [14], it was determined that three single-family houses fall into zone I (no impact of traffic-induced vibrations), and one of the buildings (no. 4) is in zone II (no impact on the design although there is a significant increase in the possibility of accelerated wear of plaster).

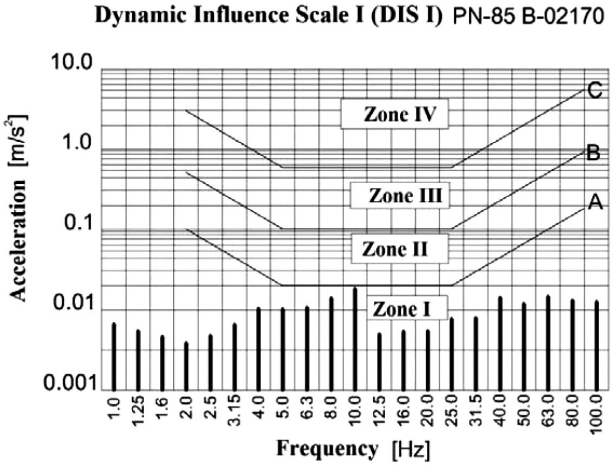

Fig. 2. Chart of peak accelerations with respect to the centre frequencies made for building no. 3 on the DIS I chart [14]

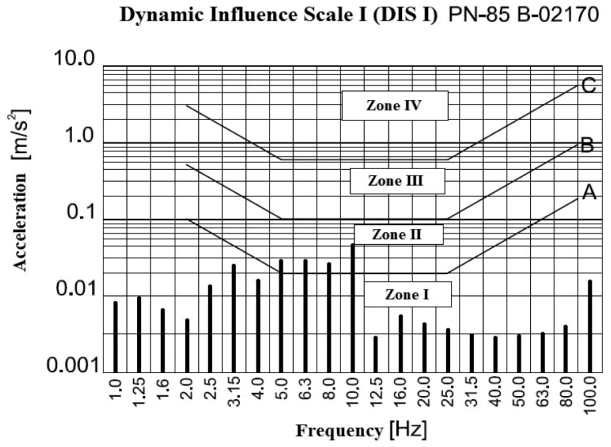

Fig. 3. Chart of peak accelerations with respect to the centre frequencies made for building no. 4 on the DIS I chart [14]

3. The application of artificial neural networks

The construction of the network was based on the principles described in [16, 18–19]. The first step was to create the database necessary to begin construction of an algorithm. The next step was to create the network itself. Factors that may affect traffic-induced vibrations

[3, 17] are: road type; road surface type; road surface condition; soil type; vehicle speed; weight of vehicles; vibration durability; shape and dimensions of building; distance from road; type of construction; basement; as well as possible natural, deliberate or accidental vibration-damping factors.

Eight networks were created in the *Matlab Neural Network Toolbox* program [13] using the back-propagation algorithm with the Levenberg-Marquardt learning algorithm. The group of training samples was selected which was submitted for the neural network. The field results obtained for this group were compared with the results obtained by the network (verification phase). In addition, prior to the completion of the network, testing samples were determined. These samples were not submitted to the network during the 'learning' stage. When the mean square error (MSE – see [1]) was satisfactory, the process of designing the network was completed [2, 16].

For each network considered in the study, the patterns were divided in the following way: 70% – learning samples, 15% – verifying samples and 15% – testing samples. Moreover, fourteen different factors were randomly taken into account in the networks. Eight different neural networks with one hidden layer were created – these were different from one another in the way in which they included different factors and in the number of neurons in the hidden layer (for each network – 1, 3, and 10 neurons were assumed).

The random combination of the following factors were taken into account: D_d – type of road; D_n – type of pavement; D_{sn} – state of road surface; D_p – speed of vehicle [km/h]; D_c – weight of vehicle [t]; D_d – sustainability of vibration; B_k – shape of the building; B_o – distance from road; B_r – year of construction; B_k – type of construction; B_p – basement; a_{xy} – peak acceleration in x and y orientations. On the output, the expected value was responsible for the information, whether the traffic-induced vibrations doesn't affect to the tested building (zone I according to DIS I [14]) or whether the impact is possible (zone II and higher). Therefore, the expected output value was equal to 0 or 1. Input vectors for the subsequent networks were assumed as follows:

- $X_{(6x1)} = \{D_d, D_n, D_{sn}, D_p, D_c, a_{xy}\}$
- $X_{(6x1)} = \{B_K, B_o, B_r, B_k, B_p, a_{xy}\}$
- $X_{(11x1)} = \{D_d, D_n, D_{sn}, D_p, D_c, B_K, B_o, B_r, B_k, B_p, a_{xy}\}$
- $X_{(8x1)} = \{D_d, D_n, B_K, B_o, B_r, B_k, B_p, a_{xy}\}$
- $X_{(6x1)} = \{D_d, D_n, B_K, B_o, B_r, a_{xy}\}$
- $X_{(5x1)} = \{D_d, D_n, D_{sn}, B_o, a_{xy}\}$
- $X_{(6x1)} = \{B_K, B_o, B_r, B_k, B_p, a_{xy}\}$
- $X_{(3x1)} = \{D_{sn}, B_o, a_{xy}\}$

After the learning network process in the *Matlab* program, the results shown in Table 1 were obtained. As a comparison of a network, MSE was calculated which shows the difference between the outputs achieved with the measurements and the results obtained by the action of the network. The results in Table 1 indicate that errors in the operation of an artificial neural network with different architecture and the established parameters are relatively small and do not exceed 3.92102×10^{-1} for the learning samples, 7.21951×10^{-1} for the validating samples and 3.00633×10^{0} for the testing samples. The smallest error of learning samples (1.15277×10^{-10}) was obtained for network no. 4 with the structure of 8–10–1. On the other hand, network no. 3, in which all parameters of the

building and the road were taken into account, proved to be the least effective, since the error obtained was the largest and amounted to 1.21547×10^0 for verifying samples for the structure of 11–1–1.

4. Closing remarks

The purpose of this article was to present the results of the operation of an expert system based on artificial neural network activity which was applied to assess the impact of traffic-induced vibrations on buildings. Based on the analysis performed so far, we achieved a relatively low error value for artificial neural networks with different architecture and different established parameters. The obtained results are therefore promising and demonstrate the effectiveness of the system. It should be noted, however, that the actual database of results includes a relatively small number of different cases. Therefore, the next stage of research will be to perform measurements on a larger sample of residential buildings (at least 30 buildings are planned to be tested). The upgrading of the created networks, as well as checking other artificial intelligence algorithms, e.g. support vector machines, which can be also helpful in forecasting the impact of traffic-induced vibrations on buildings, will then be conducted. It is also planned to use different types of network [13] to compare the performance results.

Table 1

Characteristics of neural networks and errors of individual samples

No. of network and its architecture	MSE – training samples [–]	MSE –verification samples [–]	MSE – testing samples [–]
Network no. 1: 6-1-1	9.35191×10^{-9}	4.62128×10^{-1}	2.99485×10^{-2}
Network no. 1: 6-3-1	3.73315×10^{-1}	2.59167×10^{-3}	1.39104×10^{-2}
Network no. 1: 6-10-1	1.65689×10^{-4}	1.32041×10^{-6}	4.03857×10^{-1}
Network no. 2: 6-1-1	1.87873×10^{-1}	2.89750×10^{-1}	1.92824×10^{-1}
Network no. 2: 6-3-1	2.00448×10^{-4}	3.81108×10^{-1}	3.93508×10^{-2}
Network no. 2: 6-10-1	2.66272×10^{-5}	4.80413×10^{-2}	2.22438×10^{1}
Network no. 3: 11-1-1	1.83628×10^{-9}	1.21547×10^{0}	3.79064×10^{-1}
Network no. 3: 11-3-1	1.33541×10^{-1}	7.21951×10^{-1}	7.49835×10^{-1}
Network no. 3: 11-10-1	2.01744×10^{-1}	2.65415×10^{-2}	4.88491×10^{-2}
Network no. 4: 8-1-1	5.51261×10^{-2}	3.44147×10^{-1}	9.78215×10^{-3}
Network no. 4: 8-3-1	5.18379×10^{-5}	5.99858×10^{-1}	6.19752×10^{-1}
Network no. 4: 8-10-1	1.15277×10^{-10}	2.94855×10^{-1}	3.50704×10^{-3}
Network no. 5: 6-1-1	2.26650×10^{-1}	1.63530×10^{-1}	8.85599×10^{-2}

Network no. 5: 6-3-1	1.45447×10^{-1}	1.60828×10^{-2}	2.88384×10^{-2}
Network no. 5: 6-10-1	5.69944×10^{-2}	3.23589×10^{-3}	8.09436×10^{-3}
Network no. 6: 5-1-1	3.92102×10^{-1}	6.33194×10^{-2}	3.39044×10^{-2}
Network no. 6: 5-3-1	1.06009×10^{-1}	4.26290×10^{-2}	3.34781×10^{-2}
Network no. 6: 5-10-1	2.78595×10^{-3}	5.06962×10^{-4}	1.07499×10^{-2}
Network no. 7: 6-1-1	1.92296×10^{-2}	2.35511×10^{-1}	5.21189×10^{-2}
Network no. 7: 6-3-1	1.18251×10^{-2}	9.96684×10^{-1}	1.21119×10^{-1}
Network no. 7: 6-10-1	1.50109×10^{-1}	1.45799×10^{0}	3.00633×10^{-1}
Network no. 8: 3-1-1	7.40723×10^{-2}	2.76347×10^{-1}	1.01870×10^{-2}
Network no. 8: 3-3-1	6.62319×10^{-4}	1.44327×10^{-5}	1.75400×10^{-3}
Network no. 8: 3-10-1	4.88014×10^{-8}	4.79749×10^{-1}	4.47896×10^{-3}

References

[1] Bendat J.S., Piersol A.G. *Random data: analysis and measurement procedures*, Wiley-Interscience, USA 1971.

[2] Chudyba Ł., *Wpływ typu sieci neuronowej na dokładność prognozowania przekazywania drgań pochodzenia górniczego z gruntu na budynek*, Czasopismo Techniczne, 108, z. 3, 2011, s. 3–12.

[3] Hunaidi O., *Traffic vibrations in buildings*, Construction Technology Update, no. 39, 2000, 1–6.

[4] Janas L., Miller B., *Zastosowanie sieci neuronowych do wspomagania zarządzania obiektami mostowymi*, Zeszyty Naukowe Politechniki Rzeszowskiej, z. 58, nr 3/III, 2011, 181–190.

[5] Kawecki J., Stypuła K., *Zapewnienie komfortu wibracyjnego ludziom w budynkach narażonych na oddziaływania komunikacyjne*, Wydawnictwo Politechniki Krakowskiej, Kraków 2013.

[6] Kawecki J., *Dynamic actions on building objects*, Folia Scientiarum Universitatis Technicae Resoviensis, vol. 276, 2011, 115–134.

[7] Kawecki J., Stypuła K., *Błędy w diagnozach dotyczących oceny wpływów dynamicznych na budynki*, Czasopismo Techniczne z. 1-M, 2008, 127–136.

[8] Kogut J., *Analiza spektrum odpowiedzi drgań drogowych*, Rozprawa doktorska, Politechnika Krakowska, Wydział Inżynierii lądowej, Instytut Mechaniki Budowli, Kraków 1999.

[9] Kuźniar K., *Estimation of dynamic response of buildings with load bearing walls using response spectra and neural networks*, Journal of Theoretical and Applied Mechanics, vol. 40, 2002, 483–495.

[10] Kuźniar K., *Neural networks for the analysis of mine-induced building vibrations*, Computer Assisted Mechanics and Engineering Sciences, vol. 18, 2011, pp. 147–159.
[11] Kuźniar K., Waszczyszyn Z., *Neural networks for the simulation and identification of building subjected to paraseismic excitations*, Intelligent Computational Paradigms in Earthquake Engineering, 2007, 393–432.
[12] Moseholm L., Silva J., Larson T., *Forecasting carbon monoxide concentrations near a sheltered intersection using video traffic surveillance and neural networks*, Transportation Research Part D: Transport and Environment vol. 1, No. 1, 1996, 15–28.
[13] Neural Network Toolbox for Use with Matlab. User's Guide. Version 3.0. The MathWorks, Inc. 2006.
[14] PN-85 B-02170. Ocena szkodliwości drgań przekazywanych przez podłoże na budynki. Polski Komitet Normalizacji Miar i Jakości, Warszawa 1985.
[15] PN-88/B-02171. Ocena wpływu drgań na ludzi w budynkach. Polski Komitet Normalizacji Miar i Jakości, Warszawa 1988.
[16] Ossowski S., *Sieci neuronowe w ujęciu algorytmicznym*, Warszawa 1996.
[17] Rozporządzenie Ministra Transportu i Gospodarki Morskiej z dnia 2 marca 1999 roku w sprawie warunków technicznych. jakim powinny odpowiadać drogi publiczne i ich usytuowanie (Dz. U. z 1999 r. nr 43, poz. 430).
[18] Stęgowski Z., *Sztuczne sieci neuronowe*, Wydawnictwa Naukowo-Techniczne, Kraków 2004.
[19] Tadeusiewicz R., *Sieci neuronowe*, Akademicka Oficyna Wydawnicza, Warszawa 1993.
[20] Urbański P., *Zastosowanie sztucznych sieci neuronowych do oceny stopnia zużycia technicznego wybranej grupy budynków mieszkalnych*, Statystyka i data mining w badaniach naukowych, StatSoft Polska, 2004, 105–119.
[21] Zembaty Z., Cholewicki A., Jankowski R., Szulc J., *Trzęsienia ziemi 21 września 2004 r. w Polsce północno-wschodniej oraz ich wpływ na obiekty budowlane*, Inżynieria i Budownictwo, vol. LXI, no. 1, 2005, 3–9.
[22] Zembaty Z., Jankowski R., Cholewicki A., Szulc J., *Trzęsienie ziemi 30 listopada 2004 r. na Podhalu oraz jego wpływ na obiekty budowlane*, Inżynieria i Budownictwo, vol. LXI, no. 9, 2005, 507–511.

TECHNICAL TRANSACTIONS | CZASOPISMO TECHNICZNE
CIVIL ENGINEERING | BUDOWNICTWO
3-B/2016
DOI: 10.4467/2353737XCT.16.215.5964

KRZYSZTOF KOZIOŁ*

IMPACT OF THE SELECTION OF DIFFERENT COMPUTATIONAL MODELS OF PARTITION WALLS FOR STRUCTURE RESPONSE DUE TO VIBRATIONS CAUSED BY CAR TRAFFIC

WPŁYW WYBORU MODELU OBLICZENIOWEGO ŚCIAN DZIAŁOWYCH NA ODPOWIEDŹ BUDYNKU NA DRGANIA SPOWODOWANE RUCHEM SAMOCHODÓW

Abstract

Creating a computational model of the existing building, in which there are non-structural components, taking into account a variety of operating factors, possible reassignment of objects and the accompanying load changes cause doubt about which scheme of work of the partition wall should be applied. This paper presents an analysis of the effect of vibration caused by the use of cars for people staying in the building, depending on the different computational models of heavy type partition walls. The selection of work schemes of elements in the structure is not always clear from its purpose and should be adapted to the purpose it serves. The study shows four alternative models of work and analysis of the partition walls in the building, which use the kinematic loading resulting from car traffic as an ordering criterion adopted for the analysis of computational models, the influence of vibration on people in the buildings in accordance with the PN-88/B-02171 standard. As proved by the calculations performed for the chosen residential building, the differences between the responses applied to the excitation reach several percent. In order to estimate the safely comfort of the inhabitants, the computational model should take into account any possibility of changing the work schemes of elements, which would appear to have no effect on the estimated parameter.

Keywords: *traffic induced vibrations, non-structural components, impact of vibrations on people*

* Ph.D. Krzysztof Kozioł, Institute of Structural Mechanics, Faculty of Civil Engineering, Cracow University of Technology.

Streszczenie

Budując model obliczeniowy budynku istniejącego, w którym elementy niekonstrukcyjne ze względu na różnorodne czynniki eksploatacyjne, ewentualne zmiany przeznaczenia obiektów i towarzyszące temu zmiany obciążeń, nasuwają się wątpliwości co do przyjmowania schematów ich pracy. W opracowaniu przedstawione są analizy wpływów drgań spowodowanych ruchem samochodów na ludzi przebywających w budynku w zależności od alternatywnych modeli obliczeniowych ścian działowych typu ciężkiego. Dobór schematu pracy elementu w konstrukcji nie zawsze wynika z jego przeznaczenia i powinien być dopasowany do celu, któremu służy. W opracowaniu dobrano cztery alternatywne modele (pracy i analizy) ścian działowych w budynku, który poddano obciążeniu kinematycznemu pochodzącemu od ruchu samochodów. Jako kryterium szeregując przyjęte do analizy modele obliczeniowe zastosowano wpływy drgań na ludzi w budynkach zgodnie z normą PN-88/B-02171. Jak wynika z obliczeń dla przyjętego budynku mieszkalnego różnice pomiędzy odpowiedziami konstrukcji na zadane wymuszenie wynoszą kilkanaście procent. Dążąc do bezpiecznego oszacowania komfortu przebywania ludzi w budynku należy w modelach obliczeniowych uwzględnić ewentualne możliwości zmian schematów pracy elementów, które wydawałoby się, że nie mają wpływu na szacowany parametr.

Słowa kluczowe: drgania komunikacyjne, drgania drogowe, elementy niekonstrukcyjne, wpływy drgań na ludzi

1. Introduction

When analysing the response of a structure subjected to vibrations caused by communication influences, one is often faced with the dilemma of how to take into account the response of the secondary structure elements when analysing the object. These so-called "non-structural" elements affect the dynamic characteristics of the structure. By increasing the mass of the structure, they change frequencies, mode shapes and damping of the object. In many cases (especially in case of inappropriate construction), they may change the stiffness of the whole structure.

According to the standard provision [1] regarding the mass of the object beyond its constant part Q'_k, one must add a part of the long-term variable load Q''_k according to the relationship:

$$m_k = \frac{Q'_k + \lambda \cdot Q''_k}{g} \tag{1}$$

wherein the value of participation factor λ depends on the purpose of the building and is equal to:
$\lambda = 0.4$ for residential buildings and public utility buildings,
$\lambda = 0.6$ for other types of buildings.

Additionally, when designing a building, it is recommended to consider its work in three stages of construction:

- building subjected to constant load, excluding loadings due to finishing works (taking into account only the weight of structural elements),

- completed building (including the loads resulting from finishing works), but without the variable loadings,
- completed building, loaded with a constant load with reduced, according to the formula (1) long-term part of the variable load.

The study shows the influence of traffic induced vibrations on people residing in buildings, depending on the approach to taking into account the partition walls in the facility, which are treated as a constant load. The value of the operating load was assumed as 2.0 kN/m^2.

As defined in [2, 7], a partition wall is a vertical partition that separates an inner space inside the object. Its removal should not affect the behaviour of the structure as a whole. Due to the additional features, which the partition wall can perform, it reaches different weights, and therefore appears in a heavy variant (made of bricks or breezeblocks) and light variant (made of gypsum boards fixed to wood or steel frame, etc.).

During the designing process, a partition wall can be treated as a linear load located in a specific place or as a surface load, which is equivalent to the weight of the partition wall. In order to assume the partition wall as a linear load, it should not be fixed to the adjacent walls and its transverse rigidity should be zero. There is no material that satisfies such requirements; therefore, partition walls have an effect on the structure response to load of dynamic character.

The paper presents an example, which includes four ways of taking into account partition walls in the building.

- Fig. 1. Model 1 – partition wall treated as a linear load located at the line dividing space of the room. It is a typical example of a partition wall that satisfies the definition
- Fig. 2 Model 2 is an equivalent of the partition wall in the form of a surface load often used in “open-space” areas.

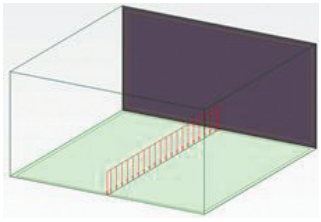

Fig. 1. Model 1 partition wall regarded as a linear load

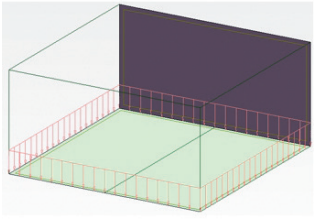

Fig. 2. Model 2 partition wall regarded as a substitute surface load

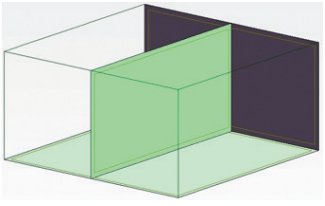

Fig. 3. Model 3 partition wall fixed peripherally to the structure

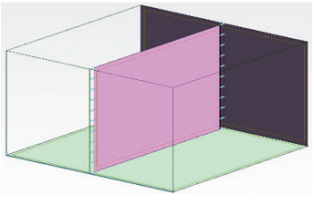

Fig. 4. Model 4 partition wall connected with the structure on vertical sides

- Fig. 3. Model 3 – damaged partition wall where the ceilings are placed on it, and in addition, the partition wall is connected to the side walls.
- Fig. 4. Model 4 – damaged partition wall where the ceilings are placed on it and the partition wall is not connected to the side walls

In the analysed example, it is assumed that the partition wall is a heavy type – the volumetric density exceeds the value of 10 kN/m^3. In the case of static-strength analysis, it is often assumed as a surface replacement of the partition walls, which depends on the dimensions of the obtained surfaces. Its value changes from 0.25 kN/m^2 to 1.25 kN/m^2. In the analysed example, partition walls have a thickness of 14 cm and are made of a material with a volumetric density of 15 kN/m^3, which, taking into account walls in the analysed object, can be replaced with an equivalent surface load of the 1 kN/m^2.

It was assumed that during construction of the partition wall, between the top edge and the roof, a gap of 1 cm was left, which is filled with a material with a Young modulus E = 10 MPa. The response analysis of the structure due to the load caused by the movement of the car around the equilibrium position resulting from the static analysis of the structure, established after applying loads resulting from constant and variable loads, was considered. If the deflection value of the floor at the location of the partition wall is aligned with the dimension of the space between the upper edge of the partition wall and the bottom of the ceiling, then the calling rests on the partition wall, causing it to cooperate in the transfer of loads.

However, it should be noted that for the 3rd and 4th variant, partition walls are involved in the load transfer, but in elastically – the amount of loads gathered from the floor slabs depends on the stiffness of the supports and the bearing walls.

When analysing the response of the structure due to the dynamic load, it is good to know its dynamic characteristics, particularly natural frequencies. As is apparent from the literature [3–4], including non-structural elements has little effect on the change in basic frequency vibration. However, the response of the building (especially in the case of effect on people inside) to the dynamic forces particularly affects "local" vibrations. These are vibration components for which the share of modal mass in the form of natural vibrations is similar to the share of the mass of the structural element extracted from the structure. Table 1 shows the analysis of the natural problem in case of the local structure segment for the solutions adopted in partition walls modelling.

Table 1

Natural frequencies of the calling slabs for different models of partition walls

Nb	Model 1	Model 2	Model 3	Model 4
[–]	[Hz]	[Hz]	[Hz]	[Hz]
1	4.78	4.19	24.41	12.22
2	27.63	19.65	32.95	38.49
3	37.98	27.42	47.47	43.39

As shown in Table 1 the initial local frequencies of the structure in which the walls are treated as linear load (model variant 1) achieve the lowest value and are close (in the

case of the first natural frequency) to the frequency vibration in case of model 2. For model variant 3 and 4, the initial frequencies are significantly higher, which is understandable, as the partition wall acts as a support, the stiffness increases with the amount of fastening the wall itself, but also with the amount of deflection of the floor slab. Therefore, during the analysis of the structure response, the ratio variable loads influence λ is quite an important parameter.

2. Analysed problem description

Computational analysis was carried out on four-storey building with a basement, constructed with traditional technology. All walls were made with full bricks. Thickness of the walls amounted, respectively: the outer walls 51 cm, internal longitudinal walls 38 cm. The ceilings were made with reinforced concrete with a thickness of 12 cm, the roof was made as a wooden rafter framing. The building was built on the brick continuous footing with a width of 60 cm at a depth of 2.9 m below ground level. The numerical model was created using the following materials:

- Concrete (floors and staircases) – Young modulus E = 20.0–26.00 GPa; Poisson's ratio $\nu = 0.2$, mass density $\rho = 2450$ kg/m^3,
- Brick (bearing walls and foundations) – Young modulus E = 2.0 GPa, Poisson's ratio $\nu = 0.25$, mass density $\rho = 1600$ kg/m^3,
- Filling material above partition walls – Young modulus E = 10 [MPa], Poisson's ratio $\nu = 0.4$,
- Wood – Young modulus E = 9.0 GPa, mass density $\rho = 650$ kg/m^3.

In the analysis, the following values of live load were applied:

- in residential areas 2.0 kN/m^2,
- on staircases an corridors 2.50 kN/m^2,

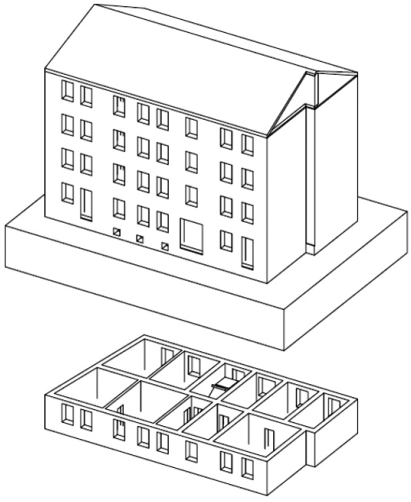

Rys. 5. FEM model of the analysed building

In the building, there were only surface elements – ceilings and walls; therefore, they were modelled as shell elements. Due to the minor importance of the roof structure, it was modelled as a surface element with characteristics corresponding to the isotropic wooden shell with static rigidity corresponding to the real roof structure.

The calculations were performed using direct integration of equations of motion assuming the integration step as $\Delta t = 0.001$ s. The dynamic load of the object constituted kinematic excitations described in the time domain by accelerations, which have been measured on the analysed object. Those accelerations were taken from the vibration database created at the Institute of Structural Mechanics, Cracow University of Technology. Those excitations were applied in model supports – interface of the building with the ground. Exemplary excitations in the form of acceleration waveforms are presented on Fig. 6–8. As a result of structure loading using the analysed vibrograms, the highest values of WODL during the measurements performed on the real object were obtained.

Due to the fact that in all of the analysed floor model reactions on the ground caused by static loads are similar and differences in the global (in the object as a whole structure) dynamic characteristics of the object are similar; therefore, any load difference originating from passing cars can be neglected. Results of the influence on people (prepare according [5–6]) staying inside on floor 4 for each of the floor models are visualised in Figures 9–12.

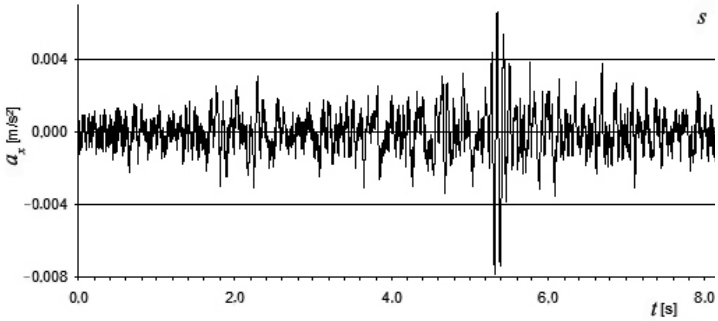

Rys. 6. Acceleration of the building foundation in the direction of its longer axis due to moving truck

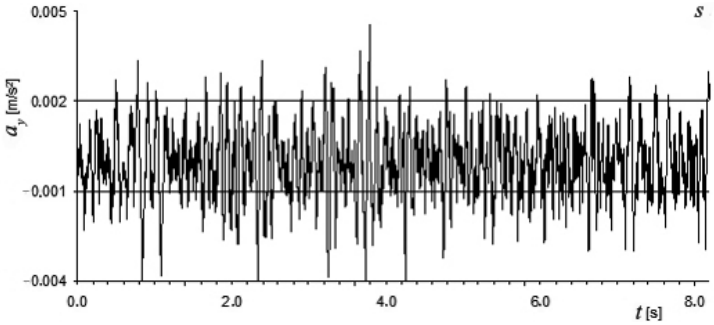

Rys. 7. Acceleration of the building foundation in the direction of its shorter axis due to moving truck

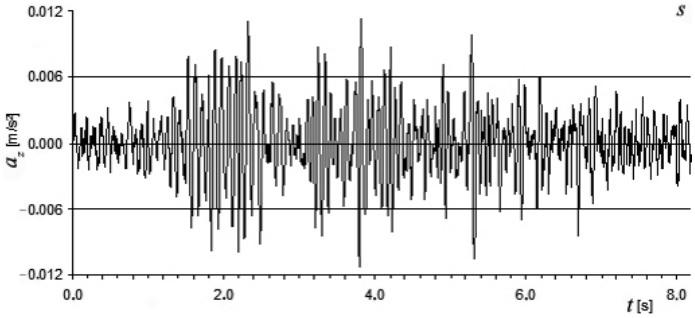

Rys. 8. Acceleration of the building foundation in the vertical direction due to moving truck

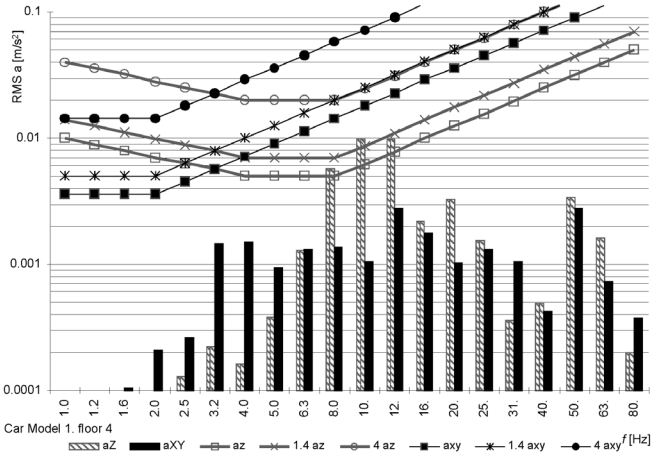

Fig. 9. Impact of vibrations on people staying on floor 4 for model variant No. 1

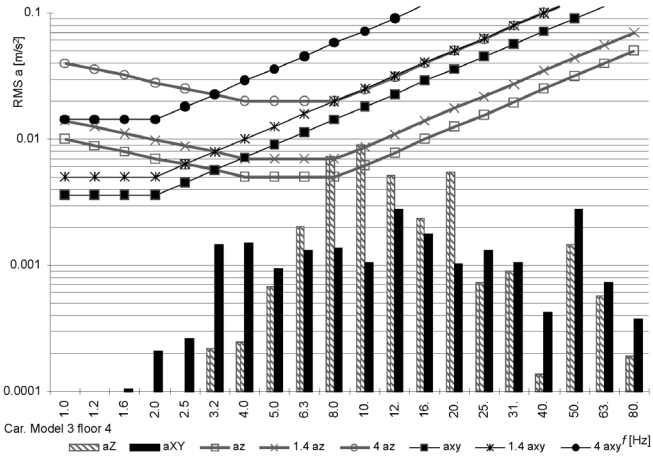

Fig. 10. Impact of vibrations on people staying on floor 4 for model variant No. 2

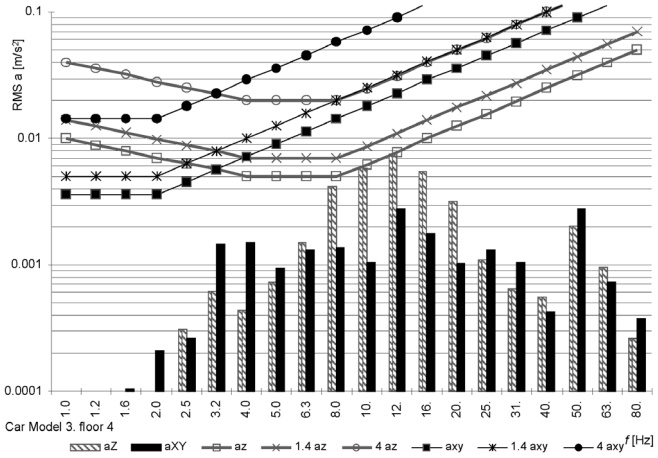

Fig. 11. Impact of vibrations on people staying on floor 4 for model variant No. 3

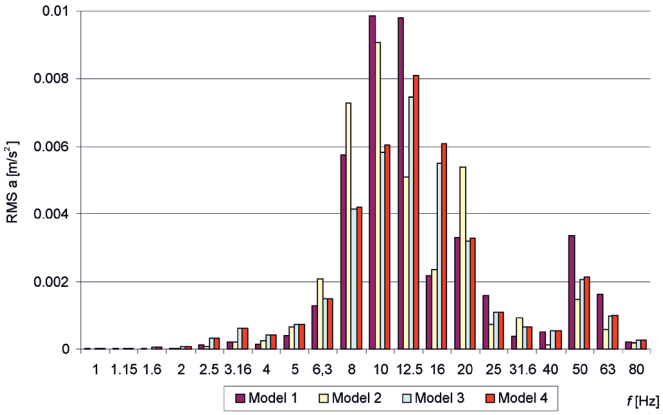

Fig. 12. Impact of vibrations on people staying on floor 4 for model variant No. 4

As it is evident from the analyses in case of omissions impact rigidity of partition walls (Fig. 9–10), we obtain the most unfavourable RMS value in the vertical direction. The limit perceptibility of vibrations by people is reached, whereas for the floor model variant No. 1, exceeding of the border of perceiving vibrations is higher. Taking into account the stiffness of the partition walls (Fig. 11–12), it lowers the threshold of perceptibility of vertical vibration.

3. Conclusions

Comparative analysis of the vibration perceptibility originating from car traffic (Figure 13) shows that the method of constructing partition walls (which followed proper computational model assumption) has an impact on the results obtained for the comfort of

inhabitants. For the analysed building (Table 3), these differences reach 50% in the range of dominant frequencies of vibrations. Distribution of extreme values of influence of vibrations on people suggests that if the vibrations are caused by the use of cars, the magnitude of the effects of vibrations on humans increases with the level of the building.

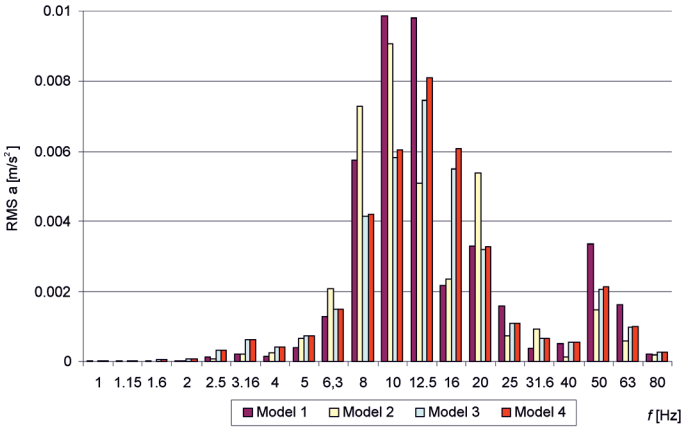

Fig. 13. Influence of vertical vibration on people in building for floor model variant No. 1–4

In the analysed structure, assumption of linear nature of this growth is a good fitting of trend line as evidenced by the determination coefficient (R2 > 0.9). The extreme values of the vibrations' influence on humans listed in Table 3 suggest that the responses of the structure are similar for FEM model 1 and 2 as well as for model 3 and 4. However, analysis of the response in the full frequency range (Fig. 13) shows that it is not. Along with the change of the model, the dominant frequency of the structure response is also changing. During construction of partition walls, the type of its support must be therefore chosen to "move away" from the dominant frequency excitations.

Table 2

Extreme values of vibrations' influence on people (WODL) – the ratio of the RMS value to the threshold of perceptibility of vibrations

FLOOR		1	2	3	4	Trend line	R^2
Model 1	WODL	0.42	0.77	1.16	1.59	0.3912x + 0.0085	0.9980
	f	10.0	10.0	10.0	10.0		
Model 2	WODL	0.39	0.71	1.07	1.46	0.3598x + 0.0078	0.9980
	f	10.0	10.0	10.9	10.0		
Model 3	WODL	0.25	0.45	0.68	0.96	0.2586x + 0.0274	0.9890
	f	10.0	10.0	10.0	10.0		
Model 4	WODL	0.26	0.47	0.71	1.04	0.2364x + 0.0053	0.9960
	f	10.0	10.0	10.0	12.5		

As is apparent from the obtained results, a replacement of the partition walls with equivalent load – Model 1 and Model 2 (which appears to be less labour-intensive during FEM modelling), is safer in terms of its impact on people (vibrations generated by traffic load) than the introduction of additional FEM elements in the form of partition walls (Model 3–4), which significantly increase the size of the computational task.

References

[1] PN-85/B-02170 (polish standard), "Evaluation of the harmfulness of building vibrations due to ground motion".

[2] P.B.Lourenco. "Computations of historical masonry constructions", Pro Struct Eng, vol. 4, no. 3, 2002, 301–319.

[3] Kawecki J., Kozioł K., Stypuła K., *Application of measurement database in dynamic diagnostics and design*, Proc. of the International Conference on Experimental Vibration Analysis for Civil Engineering Structures EVACES'09, ed. by Jan Bień, Wrocław University of Technology, Wrocław 14–16 October 2009, 181–182.

[4] Kawecki J., Stypuła K., *Ensuring vibrational comfort for people in buildings exposed for transport impact*, Publishing House of Cracow University of Technology, Cracow 2013.

[5] PN-88/B-02171 (polish standard), Evaluation of vibration influence on people in buildings.

[6] ISO 2631-2, Guide to the evaluation of human exposure to whole body vibration. Part 2 – Vibration in buildings, 2003, International Organization for Standardization.

[7] Ristie D., Yamada Y., Lemura H., *Stress-strain based modeling of hysteretic structures under earthquake induced bending and varying axial loads*, Research report No. 86-ST-01, Journal of Civil Engineering, Kyoto University, Kyoto–Japan 1986.

TECHNICAL TRANSACTIONS | CZASOPISMO TECHNICZNE
CIVIL ENGINEERING | BUDOWNICTWO
3-B/2016

DOI: 10.4467/2353737XCT.16.216.5965

BARBARA KOŻUCH, TADEUSZ TATARA*

SELECTED RESULTS OF VIBRATIONS PROPAGATION IN GROUND SUBSURFACE LAYERS CAUSED BY TRAIN RUNS

WYBRANE WYNIKI PROPAGACJI DRGAŃ W WARSTWACH PRZYPOWIERZCHNIOWYCH GRUNTU OD PRZEJAZDÓW POCIĄGÓW

A b s t r a c t

The study presents a selection of free-field vibration measurement results (the horizontal component *x* vibration is perpendicular to the axis of the track) in the ground surface layer, in one of the three measuring polygons. Pendolino, InterCity and InterRegio trains, excited free-field vibrations. Results for speeds of 120 and 160 km/h were analysed to have comparison that is more tangible.

Keywords: trains, free-field vibration, propagation

S t r e s z c z e n i e

W pracy przedstawia się wybrane wyniki pomiarów drgań gruntu (składowa pozioma x drgań prostopadła do osi toru) w przypowierzchniowej warstwie, w jednym z trzech poligonów pomiarowych. Drgania gruntu wzbudzane były przejazdami pociągu Pendolino i składów InterCity oraz InterRegio. W celach porównawczych analizuje się przejazdy z prędkościami 120 i 160 km/h.

Słowa kluczowe: pociągi, drgania gruntu, propagacja

* M.Sc. Eng. Barbara Kożuch, Prof. Ph.D. D.Sc. Tadeusz Tatara, Faculty of Civil Engineering, Cracow University of Technology.

1. Introduction

In November of 2013, homologation and velocity tests took place. One of the twenty newly purchased Pendolino trains (Electric Multiple Unit – EMUs 250) was crossing the Psary–Góra Włodowska section (approximately 36 km) located within the Central Rail Line (CRL) No. 4. Electric Multiple Unit was running with dedicated speeds. Parameters such as acceleration and displacement of rails, mechanical vibrations of individual elements of railway tracks and noise were measured. Geotechnical conditions in the surroundings of the railway line were also analysed. Measurements were carried out during three weekends in November. The train was following the first track with two tracks closed for other vehicles. During weekdays, similar studies were done for vehicles running the (CRL) section. Similar studies were mentioned in paper [1].

The paper presents selected results of measurements of free-field vibration (horizontal component of vibration (x) – perpendicular to the axis of the track) in the surface layer, in one of the three measuring polygons. Passages of the Pendolino (EMU 250), the InterCity and the InterRegio trains induced free-field vibrations. The data from the trains' runs at a speed of 120 and 160 km/h is a basis for comparison.

The staff of an accredited Laboratory of Structural Mechanics at the Cracow University of Technology (Accreditation No. AB 826) conducted vibration measurements.

The analysis was performed based on the knowledge and experience of the research team, and it is also available in the references [2–4].

2. Measuring polygon

During research, ground conditions were also monitored to check if they have any significant influence on the propagation of vibrations.

In the cross-examination, measurements of the soil properties were carried out at two places (at the foot of the railway embankment and at a distance of 20 m) located near the points at which the attachment sensors (accelerometers) measured free-field vibrations. Fig. 1 shows a cross-section of a geological lithographic profile.

Based on the properties of the ground, it turned out that the substrate is layered. In the profile under a thin layer of humus soil consists of natural coarse and incohesive (sand, sandy silt with depth in the passing sands with gravels, drilled a single interbeddings powder) layers. In the audited profile, there was no groundwater. On this basis, it was concluded that the ground is in the vadose zone. The tested soil was humid [5, 6].

Free-field vibration measurements were made with piezoelectric accelerometers' PCB Piezotronics and the SCADAS Mobile's LMS International analyser. The relative standard uncertainty of the maximum signal acceleration must not exceed ± 11.61%, which is the sum of the deviations of nominal sensors and amplifier distortion by the digital recorder and the accuracy as well as the linearity of the amplifier. In the test, profile arrangement of sensors is shown in Figure 2. Seven sensors recording the horizontal vibrations perpendicular to the axis were arranged sequentially – first under the railway embankment, further every ten meters in a direction perpendicular to the axis. Accelerometers were fixed on the ground, 2.3 m below the rail. Mounting the sensor on the base was carried out according to the method described in [7, 8].

Stratygraphy		Lithological profile	Depth	Lithological profile	Soil symbol
Quaternary	Holocene	0	0.00	Brown soil	Gb
			0.10	Medium sand with an admixture of gravel brownish yellow	grMSa
			0.60	Medium sand with powder brownish yellow	siMSa
			0.70	Powder light brown	siMSa
		1	1.00	Medium sand with fine sand dark yellow	fsaMSa
		2	2.18	Medium sand with powder brownish yellow	siMSa
			2.56	Medium sand with fine sand dark yellow	fsaMSa
			2.80	Medium sand with powder brownish yellow	siMSa
		3	3.04	Powder brown	Si
			3.22	Medium sand with fine sand yellow	fsaMSa
		4	4.10	Medium sand with powder brownish yellow	siMSa
			4.22	Medium sand with powder light brown	siMSa
			4.35	Powder brown	Si
			4.50	Medium sand with powder brownish yellow	siMSa
			4.70	Powder brown	Si
		5	4.88	Medium sand with powder light brown	siMSa

Fig. 1. Geological cross-section profile photo in the audited profile [5]

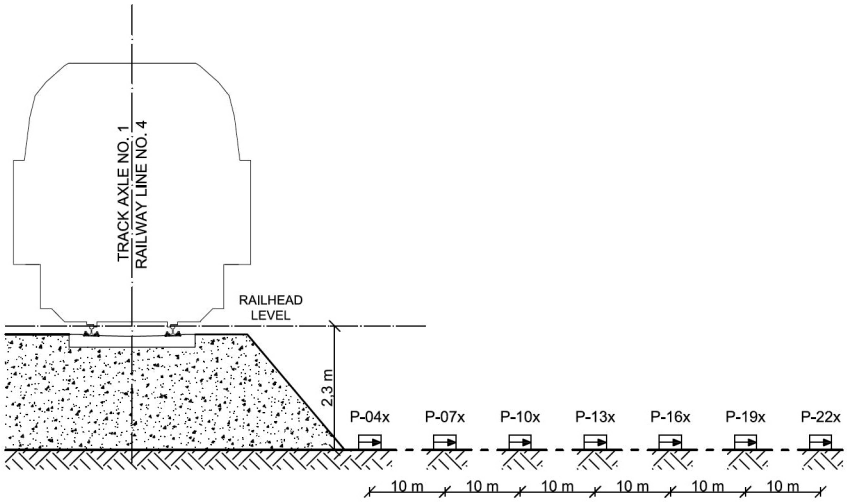

Fig. 2. Schematic arrangement of sensors in the measuring profile

3. Analysis of the acceleration records

All records were analysed. Summaries of the record for the speed of 160 km/h of the Pendolino train and a train of the Intercity type are shown in Fig. 3 and Fig. 4, respectively. For each of the passages of the trains, we imposed records of the horizontal component *x* of vibration measured at the points P-04*x* – P-22*x*. The maximum displacements of timelines achieve much lower values during the passage of the Pendolino; sensor placed under the embankment (P-04*x*) records the maximum acceleration not exceeding 70 cm/s^2, while extreme acceleration caused by passing through the InterCity rolling stock is more than twice the size and reaches values of up to 150 cm/s^2. In both cases, one can observe very high damping, particularly evident between the first and second sensor (a distance of 10 m).

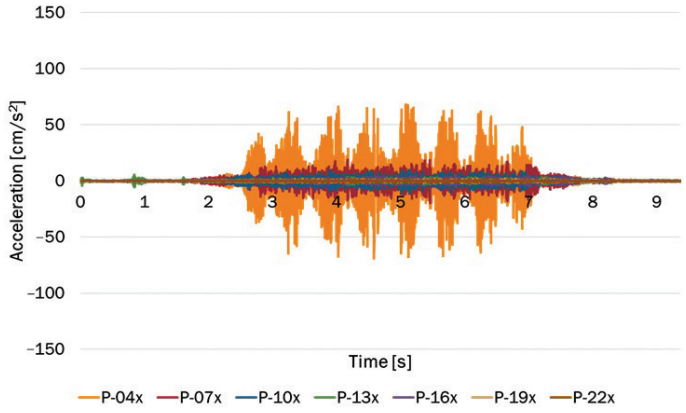

Fig. 3. Record of the horizontal component *x* of free-field vibrations caused by passing the Pendolino train at *v* = 160 km/h

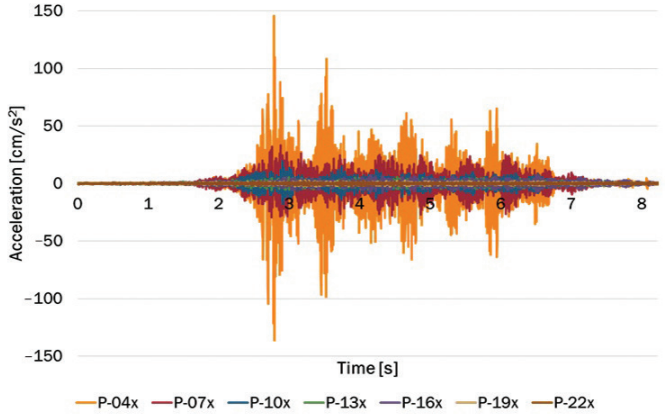

Fig. 4. Record of the horizontal component *x* of free-filed vibrations caused by passing the Intercity train at *v* = 160 km/h

Table 1 shows the maximum values obtained from the records of horizontal component x of free-field vibrations caused by passages of the Pendolino and InterRegio trains with a speed of 120 km/h and passages of the one Pendolino and four InterCity trains with a speed of 160 km/h. For passages of up to 120 km/h, only at the measuring point P-07*x*, slightly higher maximum values of vibration acceleration for the Pendolino train were recorded. In the other six points of the measurement, lower maximum acceleration vibration, caused by passing that trains, was recorded. At a speed of 160 km/h, a very large discrepancy in the results of maximum acceleration values of the horizontal component *x* of free-field vibrations can be seen due to passages of the same carrier (InterCity); at P-04*x*, a difference of up to 50 cm/s^2 is observed. During EMU 250 passages, the lowest intensity of free-field vibrations was registered at each measuring point.

Table 1

Statement of the maximum value of the horizontal component of free-field vibrations

Source of vibration	Measuring point number						
	P-04*x*	P-07*x*	P-10*x*	P-13*x*	P-16*x*	P-19*x*	P-22*x*
Pendolino 120 km/h track A – 12:50	81.11	14.1	4.92	2.75	2.24	1.27	0.99
InterREGIO 120 km/h track A – 11:50	85.93	12.55	7.54	3.78	2.61	1.82	1.18
Pendolino 160 km/h track A – 13:49	68.88	19.73	10.74	5.79	5.27	2.08	1.34
Intercity 160 km/h track A – 12:33	96.81	33.52	18.05	7.07	7.02	2.85	2.08
Intercity 160 km/h track A – 14:04	98.17	35.81	18.03	6.57	6.8	2.55	2.29
Intercity 160 km/h track A – 13:28	112.02	19.66	8.55	5.22	3.66	2.64	1.54
Intercity 160 km/h track A – 10:12	145.8	33.09	19.21	5.95	7.96	2.55	2.35

Figure 5 shows decay curves of the maximum values of vibration acceleration with distance when traveling the Pendolino and the InterREGIO trains at a speed of 120 km/h. For each set of data, there is a power function given. It describes the dependence of the maximum acceleration of the distance from the vibration source. The coefficients of determination R^2 for both functions is approximately 0.99. The maximum values of vibration acceleration did not show significant differences between the Pendolino and InterRegio train journeys.

Figure 6 summarises the maximum values of horizontal component *x* of free-field vibrations caused by trains passages at a speed of 160 km/h (one Pendolino and four InterCity trains). Next, the maximum acceleration values obtained from passages of InterCity were averaged. The values obtained from the Pendolino passes and averaged passages

from the InterCity are shown in Figure 7. The proposed power function describes well the disappearance of the maximum values of the horizontal component *x* of free-field vibrations with distance – the coefficient of determination R^2, respectively, 0.97 and 0.98. For the first three accelerometers (P-04*x* P-07*x* and P-10*x*), it clearly shows much larger maximum vibration acceleration values obtained from passages of InterCity trains. The difference very quickly dissapears with distance and the fourth measurement point (P-13*x*) is practically invisible.

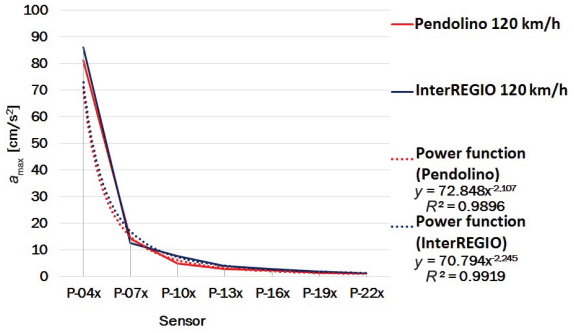

Fig. 5. The maximum value of the horizontal component *x* of free-field vibrations from the recorded accelerations caused by trains at a speed of *v* = 120 km/h

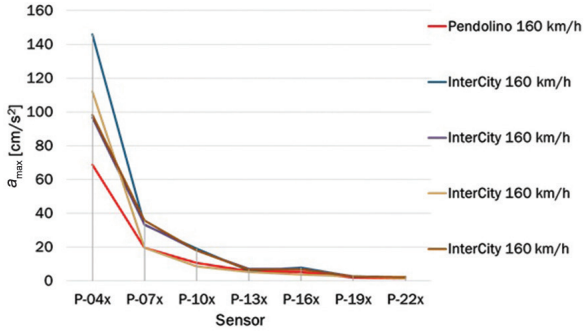

Fig. 6. The maximum value of the horizontal component *x* of free-field vibrations from the recorded accelerations caused by trains at a speed of *v* = 160 km/h

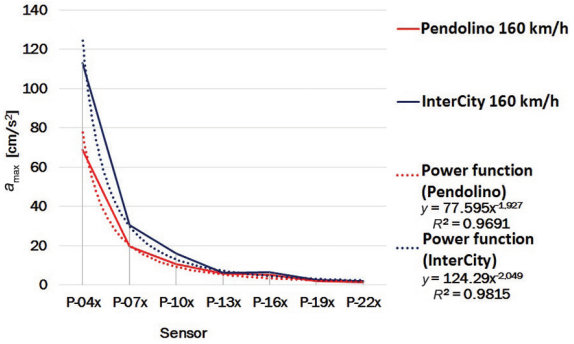

Fig. 7. The maximum value of the horizontal component *x* of free-field vibrations from the recorded accelerations caused by trains at a speed of *v* = 160 km/h

4. Vibration spectrum analysis

The recorded free-field vibrations were analysed using one-third octave band frequency filters, and distributed in one-third octave bands of the mid-band frequency from 1 to 100 Hz. For example, Fig. 8 and 9 summarise the results of the horizontal component *x* of free-field vibrations recorded at the measurement point P-04*x* from various trains passages at speeds of *v* = 160 and 120 km/h. In both cases, a band of less than 16 Hz shows almost zero acceleration for each of the rolling stock. A distinction can be made only in the bands from 16 to 100 Hz.

Comparing the maximum value of the horizontal component *x* free-filed vibrations in one-third octave bands, caused by passing InterCity trains and EMU 250, shows that newly purchased trains inspire some of the lowest vibration accelerations in all third octave frequency bands. Comparing the acceleration values in each one-third octave bands of excited Pendolino trains crossing and InterREGIO cannot clearly identify rolling stock generates less vibration acceleration. In the range of 16–50 Hz, EMU 250 generates a lower level of acceleration, which changes in the higher frequency band (63 to 100 Hz).

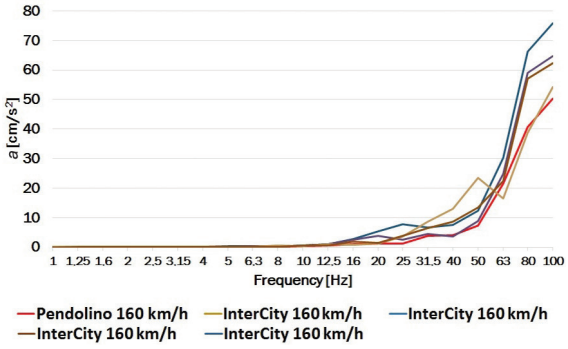

Fig. 8. Vibration spectrum in third octave frequency bands – the measuring point P-04*x* – speed trains *v* = 160 km/h

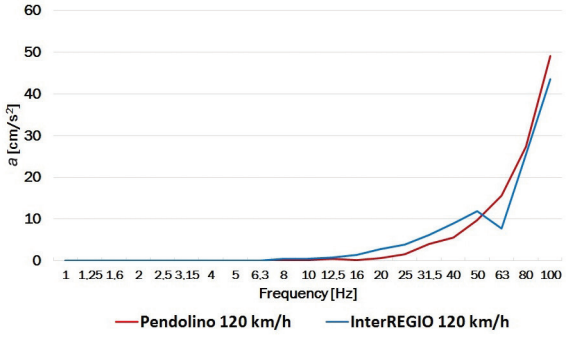

Fig. 9. Vibration spectrum in third octave frequency bands – the measuring point P-04*x* – speed trains *v* = 120 km/h

5. Continuous spectrum of vibrations

Using Fast Fourier Transform (FFT), the transition from the time domain to the frequency domain was performed to yield a continuous vibration spectrum. Transform was performed for frequencies of up to 100 Hz. Figure 10 illustrates the change of the frequency spectrum depending on the distance of the measuring point from the source of the vibration for the InterCity train. For the first measurement point (P-04*x*), higher vibration frequencies are dominant – range from 63 to 100 Hz. However, frequencies from the range 70–75 Hz for a sensor at a distance of 10 m (P-07*x*) dominate, reaching the maximum value equalling the values obtained at the measuring point P-04*x* in that band. Also, in the 70–75 Hz range of maximum acceleration values at the third (P-10*x*) and fourth (P-13*x*) measuring point, but these values are much smaller compared with the values obtained based on the records in the first (P-04*x*) and the second (P-07*x*) measurement point. In order to make better visualisation, the frequency spectrum is divided into a bandwidth of 3 Hz and average amplitude of the vibrations is calculated. Maps figure showing the obtained value of the acceleration from the frequency and distance of the sensor from the source of the vibration is shown in Fig. 11. The largest amplitude of the vibrations occurs in the first measuring point (P-04*x*) and corresponds to higher frequency bands, but the band of 66–72 Hz is a band in which there is the slightest damping with increasing distance from the source of vibration. The amplitudes greater than 0.1 cm/s^2 are transferred up to 40 meters from the embankment (fifth measuring point – P-16*x*).

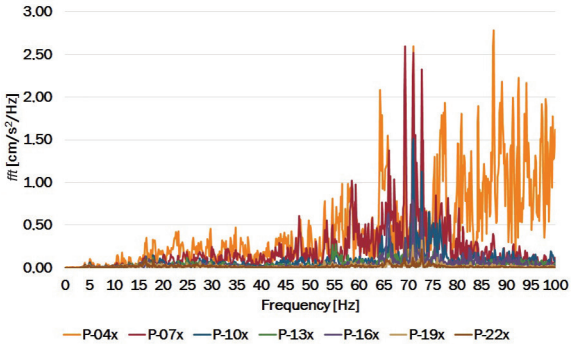

Fig. 10. Continuous vibration spectrum – InterCity train – velocity v = 160 km/h

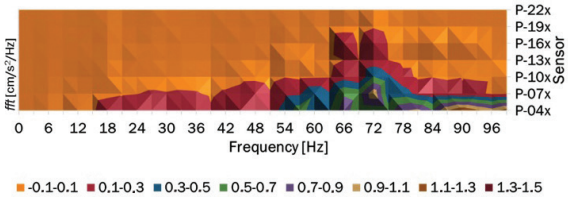

Fig. 11. Map propagation of vibration – InterCity train – velocity v = 160 km/h

To determine the frequency bands with the greatest damping of a continuous spectrum, we calculated the relation of the spectrum from record at the last sensor (P-22*x*) to the spectrum from the first sensor (P-04*x*). The calculated dependence is shown in Figure 12. Although the expected values should be less than 1.0, taking into account the decay of vibration with distance from the source, approx. 2% of the resulting relationship exceeds this value. It was not due to the presence of very large amplitudes of vibration on the last sensor (P-22*x*) and only very small values of records of vibration acceleration in the first measurement point (P-04*x*). This is not also the fact that the signals at these frequencies were strengthened. This was probably caused by changes in signal frequency resources after passing through a very heterogeneous material, which is ground.

In order to better visualise the damping, Figure 13 shows the same relationship, but after the removal of excess 1. Here, we can see that the greatest attenuation corresponds to the highest frequencies, which is in line with expectations.

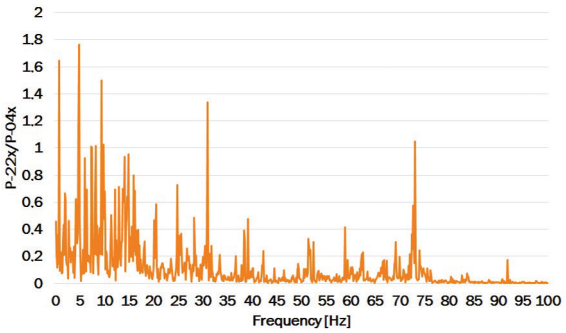

Fig. 12. The ratio of vibration spectrum transmitters P-22*x* and P-04*x* – Intercity train – the speed of 160 km/h

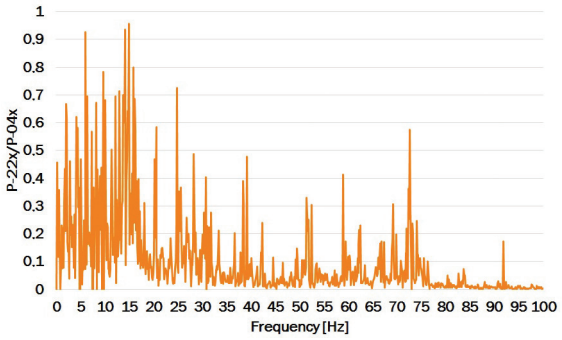

Fig. 13. The ratio of vibration spectrum transmitters P-22*x* and P-04*x* after verification – Intercity train – the speed of 160 km/h

Similarly as for the InterCity train, we examined continuous spectrum of free-field vibrations excited by passages of the Pendolino train at a speed of 160 km/h. Vibration spectrum and map of acceleration amplitudes induced by passages of the InterCity and the Pendolino train are shown in Fig. 14 and 15, respectively.

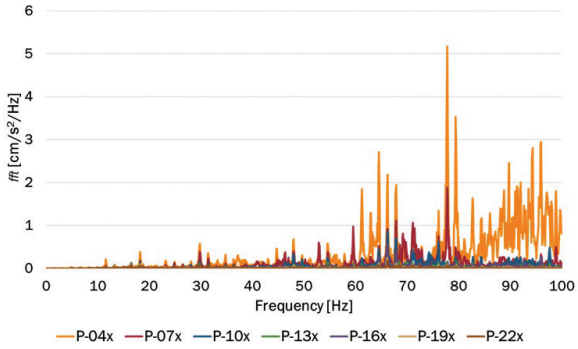

Fig. 14. Continuous vibration spectrum – Pendolino train – velocity v = 160 km/h

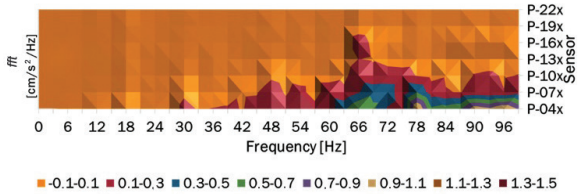

Fig. 15. Map propagation of vibration – InterCity train – velocity v = 160 km/h

Similarly, for EMU 250, the dominating frequencies of the recorded horizontal component x free-field vibrations are in the first measurement point (P-04x) and occur in the band with the highest frequencies. However, the bandwidth that is the least damped is a band with a centre frequency of 66 Hz.

Similarly as for the InterCity train, we compared the continuous spectrum of vibrations recorded at the last measuring point (P-22x) with the spectrum of the vibration record from the first measuring point (P-04x) – dependence is shown in Figure 16. The composition of the Pendolino, approx. 1.5% of the value exceeded the value of 1. Ratio spectra after the removal of greater than 1 are shown in Figure 17. As in the case of Intercity – see Fig. 13, an increase of damping can be observed with an increase of the frequency.

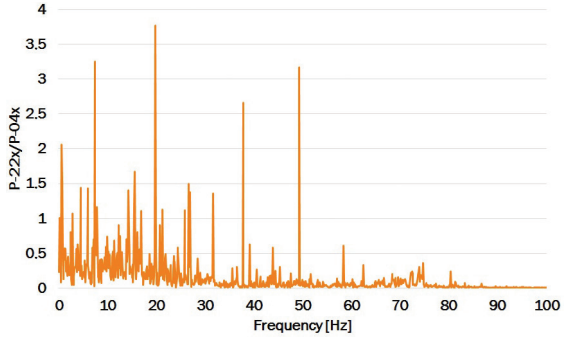

Fig. 16. The ratio of vibration spectrum for records from measurement point P-22x and P-04x – Pendolino train – the speed of 160 km/h

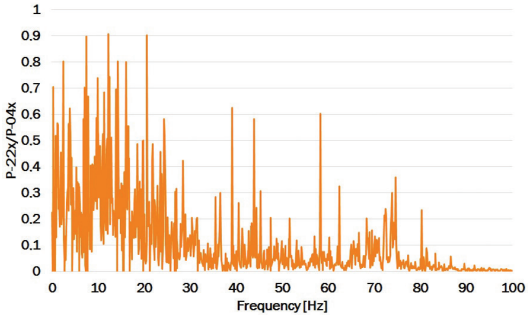

Fig. 17. The ratio of vibration spectrum for records from measurement point P-22*x* and P-04*x* –Pendolino train – the speed of 160 km/h – after verification

6. Analysis of vibration velocity

A continuous spectrum obtained by means of Fast Fourier Transform was used to calculate the free-field velocity. Using the formula for harmonic vibrations, integral formulae and amplitudes of vibration acceleration, we calculate the approximate values of velocity amplitudes [4].

The amplitudes of velocities were calculated for a frequency of 0.5–100 Hz. In both cases (vibration induced by passages of the old and new rolling stock), values of velocity amplitudes calculated at the measurement point under the embankment (P-04*x*) clearly exceed the values obtained at other measuring points, but there is a single frequency for which these velocity are smaller. The decrease in the values of velocity, depending on the distance, is not linear. Distribution of free-filed velocity vibration in frequency domain – the InterCity train – velocity $v = 160$ km/h for both kind of trains are shown in Fig. 18 and Fig. 19.

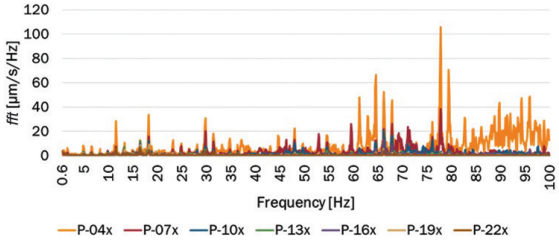

Fig. 18. Distribution of free-filed velocity vibration in frequency domain – the Pendolino train – velocity $v = 160$ km/h

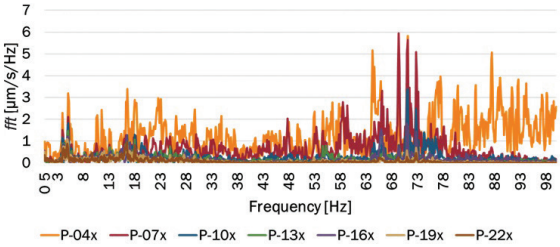

Fig. 19. Distribution of free-filed velocity vibration in frequency domain – the InterCity train – velocity $v = 160$ km/h

7. Analysis of vibration displacements

A continuous spectrum obtained by means of Fast Fourier Transform was used to calculate free-field displacement. Using the formula for harmonic vibrations, integral formulae and amplitudes of vibration acceleration, we calculated the approximate values of displacement amplitudes [4].

The amplitudes of displacements were calculated for a frequency of 0.5–100 Hz. Due to the very small displacement values (maximum value is less than 0.1 microns) for high frequencies, the charts show only the values in the frequency range of 0.5–2 Hz (amplitude of displacements exceeds 0.1 μm). In both cases (vibration induced by passages of the old and new rolling stock), values of displacement amplitudes calculated at the measurement point under the embankment (P-04*x*) clearly exceed the values obtained at other measuring points, but there is a single frequency for which these displacements are smaller. Although the distance between successive sensors is the same – a sharp decline in free-filed vibration displacements is not observed. The decrease in values of displacements depending on the distance is not linear. The calculated distribution of free-field displacement vibration in frequency domain for both kinds of trains are shown in Fig. 20 and Fig. 21.

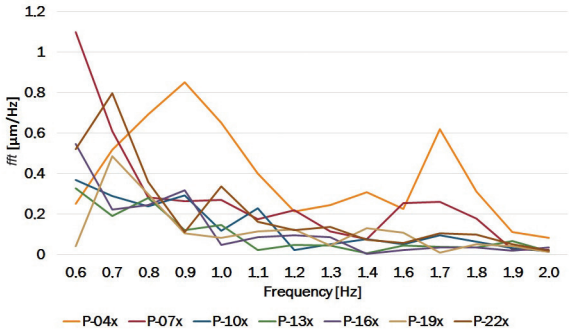

Fig. 20. Distribution of free-filed displacement vibration in frequency domain – the Pendolino train – velocity v = 160 km/h

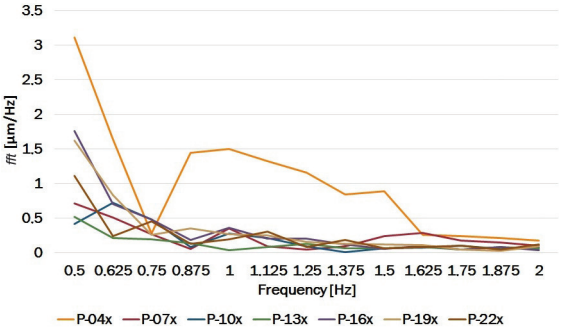

Fig. 21. Distribution of free-filed displacement vibration in frequency domain – the InterCity train – velocity v = 160 km/h

8. Conclusions

Railway line no. 4 (CRL), which is the "backbone" of high-speed rail in Poland, cannot allow speed limits because of vibration. Surface and rolling stock have to be designed so as to standard limits the propagation of vibration was not exceeded while enhancing the speed of rolling stock on the entire length of the line.

Operation of the Pendolino train in Poland will improve the "climate vibration" of railway lines. Based on measured and calculated values, decay curves of free-field vibrations, depending on the distance from the source of vibration, were analysed.

The designated frequency spectrum of the vibration records allowed to determine the dominant frequency bands and to compare them for different trains and ride speed. The results of the analysis indicated that travel at the speed of v = 160 km/h, the Pendolino attracted lower values of vibration acceleration compared to the InterCity train. On the other hand, when traveling by the InterRegio train (v = 120 km/h), for frequency f = 50 Hz, the induced vibration level was higher than in the EMU 250. For higher frequency bands, the Pendolino attracted a slightly higher level of vibration.

Another aspect is very large spread in the results obtained by the InterCity. This is due to the heterogeneity of rolling stock, which is associated with the technical condition of the different configurations. In order to improve the environmental conditions, this would limit the exploitation appropriate traction units, not the number of trips generally performed by all trains.

The displacement values were analysed and calculated based on the recorded vibration acceleration. Analysis of displacements in a band of frequency up to 2 Hz indicates that they rapidly decay with distance.

High speed trains are not an end in themselves, but only a means to achieve this objective, which is e.g. faster movement between towns, and improvement of comfort and quality of life of the user turn. However, improving the comfort of one man (here the passenger) cannot be at the expense of worsening the living conditions of the other (here people living in areas in the neighbourhood of railway lines). Therefore, aspirations to build high-speed rail cannot ignore the environmental aspects.

References

[1] Degrande G., Schillemans L., *Free field vibrations during the passage of a Thalys high-speed train at variable speed*, Journal of Sound and Vibration 247(1)/2001, 131–144.

[2] Tompson D., *Railway noise and vibration, Mechanisms, Modelling and Means of Control*, Institude of Sound and Vibration Research University of Southampton, UK, Elsevier, 2009.

[3] Lawrance T., *Noise and vibration from road and rail*, CIRIA, London 2011.

[4] Krylov V.V., *Noise and vibration from high-speed trains*, Thomas Telford, Londyn 2001.

[5] Pilecka E., Pietras J.S., Zięba J., Morman J., Przydatek P., *Dokumentacja badań podłoża dla zadania: Wstępne rozpoznanie warunków gruntowych w punktach pomiarowych dynamicznego oddziaływania składu Pendolino na otoczenie*, Praca własna Zakładu Współdziałania Budowli z Podłożem, Instytut Mechaniki Budowli, Wydział Inżynierii Lądowej, Politechnika Krakowska, archiwum, Kraków 2013.

[6] Stypuła K., Tatara T., *Wybrane wyniki pomiarów drgań wywołanych testowymi przejazdami pociągu Pendolino na CMK*, [in:] Materiały IX Seminarium Wpływ hałasu i drgań wywołanych eksploatacją transportu szynowego na budynki i ludzi w budynkach: diagnostyka i zapobieganie, Wibroszyn 2014, Politechnika Krakowska, Kraków 2014, 37–50.

[7] Maciąg E., Chełmecki J., Tatara T., *Badania gruntu i niskich budynków od wpływu komunikacji miejskiej*, Inżynieria i budownictwo 3/2005, 135–140.

[8] Ciesielski R., Kwiecień A., Stypuła K., *Propagacja drgań w warstwach przypowierzchniowych podłoża gruntowego*, Badania doświadczalne in situ, Politechnika Krakowska, Kraków 1999.

TECHNICAL TRANSACTIONS | CZASOPISMO TECHNICZNE
CIVIL ENGINEERING | BUDOWNICTWO
3-B/2016

DOI: 10.4467/2353737XCT.16.218.5967

ELŻBIETA PILECKA, MAGDALENA BIAŁEK*, TOMASZ MANTERYS**

THE INFLUENCE OF GEOTECHNICAL CONDITIONS ON THE INSTABILITY OF ROAD EMBANKMENTS AND METHODS OF PROTECTING THEM

WPŁYW WARUNKÓW GEOTECHNICZNYCH NA NIESTATECZNOŚĆ NASYPÓW DROGOWYCH I SPOSOBY ICH ZABEZPIECZENIA

Abstract

This article discusses the problem of the instability of road embankments. Two types of landslides located in various geotechnical conditions were analysed. The first case is where the stability of the road embankment itself is lost, in which the soil layers under the embankment have no influence. In the other case, the instability of the embankment is connected with landslides of the soil on which a given embankment is situated (slope stability loss). The authors proposed original solutions which were later on verified by MIDAS GTS NX®. The conducted studies show that the proposed protection strategies for both slopes are effective, thus yielding a high coefficient of general stability (FoS).

Keywords: instability, road embankment, landslide, flysch Carpathians, slope, Factor of Safety

Streszczenie

W artykule został poruszony problem niestateczności nasypów w drogownictwie. Analizie zostały poddane dwa rodzaje osuwisk drogowych zlokalizowanych w różnych warunkach geotechnicznych. W pierwszym przypadku doszło do utraty stateczności samego nasypu drogowego, na którą wpływu nie mają warstwy gruntu zalegające pod nasypem. W drugim przypadku niestateczność nasypu komunikacyjnego związana jest z osuwaniem się gruntów, na którym przedmiotowy nasyp się znajduje (utrata stateczności zbocza). Zostały zaproponowane autorskie rozwiązania, które następnie zweryfikowano w programie MIDAS GTS NX®. Przeprowadzone badania wykazały, że projektowane zabezpieczenia obu skarp są poprawne, co przekłada się na wysokie wartości współczynników stateczności ogólnej (FoS).

Słowa kluczowe: niestateczność, nasyp drogowy, osuwisko, flisz Karpacki, współczynnik stateczności

* Prof. Ph.D. D.Sc. Eng. Elżbieta Pilecka, M.Sc. Eng. Magdalena Białek, Institute of Structural Mechanics, Cracow University of Technology, Poland.
** M.Sc. Eng. Tomasz Manterys, The Provincial Road Administration in Cracow.

1. Introduction

Embankments, as elements of road infrastructure, can be classified as earthworks which are used to build the road surface. Their task is to transfer loads, both dead (the weight of the embankment) and live loads of the vehicles moving along the road sufrace, onto the native soil layers located below.

When designing road embankments, it is necessary to take into consideration the many problems connected with the need for settlement reduction, providing stability and the embankment load-bearing capacity as well as durability. One of the major difficulties is the presence of weak soils under the embankments which may considerably influence the structural stability, especially when it is located on a steep slope. A suitable soil load-bearing capacity under the embankment, characterised by low strength parameters, can be achieved by strengthening it by means of modern geoengineering methods. The incline of the area upon which the embankments are located also significantly influences their stability and durability. This problem causes difficulties in arranging and compacting the material – this requires detailed planning of works; it is also connected with a slower speed of work and an increase of investment costs.

2. Stability and the causes of stability loss in fill slopes and slopes

The stability of the fill slopes, slopes, embankments and excavations is one of the most important problems not only in geotechnical designing but also in evaluating the influence of the potential phenomenon on peoples' safety. As a measure of stability, the general Factor of Safety FoS (coefficient of the equilibrium state) is adopted – this is a ratio of the sum of maintaining forces (friction, cohesion of the material) and the sum of load forces (gravitation and filtration forces). Depending on the value of FoS we can clearly determine whether the analysed slope or embankment are in a state of general equilibrium [11]:

- FoS < 1 – instable slope or embankment
- FoS = 1 – slope or embankment in temporal stability
- FoS > 1 – stable slope or embankment

The surplus of coefficient $F = 1$ determines safety margin.

According to Section V of the Regulations of the Minister of Transport and Marine Economy from 2 March 1999 on technical conditions of public roads and their location (Dz.U.1999 nr 43 poz.430), and concerning load capacity and stability of earth road structures, the Factor of Safety FoS of slopes and embankments should not be smaller than FoS = 1.5.

In general, it may be understood that the slope remains stable when there are no mass movements in it. In reality, stability is a much more complicated problem, influenced by such varied factors as, for example, shape, dimensions and span of slope, water impact, atmospheric conditions or dynamic impact.

Two types of stability and loss of road embankments can be distinguished: loss of stability of the road embankment itself, independent of the influence of soil layers under

the embankment; loss of the embankment stability connected with landslides of the soil on which the said embankment is located (slope stability loss).

The most frequent cause of road-embankment instability are the weak soils used to build them and their inappropriate densities. Embankment structures built of various soil layers have a load capacity which when exceeded, causes the whole earth structure to lose its stability.

The other cause of road embankment stability loss is the lack of efficient drainage – this may bring about saturation of the embankment soils with precipitation waters which would then weaken and destroy the embankment.

It also happens that there are badly designed road embankments, with fill slopes that are too steep – this can also cause loss of their stability.

3. Determining general stability coefficients by means of MIDAS GTS NX®

Numerical methods based on an advanced method of solving systems of differential equations, the so-called discretisation into finite elements for which the solution is approximated by specific functions only for nodes of this discretisation. The Finite Elements Method is one of the most frequently used methods based on physical model discretisation. Physical model discretisation means that the continuous medium, which actually is a physical model, is substituted by a discreet model. MIDAS GTS NX® is a numerical programme based on the finite elements method FEM and used to simulate actual phenomena occurring in the soils. Basing on FEM, the programme carries out many kinds of analyses used in geoengineering. It also allows the modelling of complex soil and water conditions.

The method of shear strength reduction is based on the assumption that the movements of the slope are one of the factors leading to shear strength decrease and stress change in the analysed soil medium. Formation of the slide surface, according to this method, develops in a place in which reaching the state of shear stress equilibrium and shear strength is the fastest. In the analysis of stability by the shear strength reduction method, we seek the minimum value of the FoS of the embankment, depending on the shape, loads and boundary conditions. Shear strength and the angle of internal friction diminish gradually until the calculations no longer show convergence. The maximum reduction degree of the above mentioned parameters in the place of convergence loss serves to calculate the minimum FoS. In the calculations, it is assumed that the solid model is an elastic-plastic medium fulfilling Coulomb-Mohr's condition [4].

4. Stability analysis of chosen road embankments

The subject of the authors' studies are two kinds of landslides located in various geotechnical conditions. The aim of the performed calculations was to check stability of the slopes located in Sułoszowa (Krakow district, Małopolska province, Poland) and Lipie (Nowy Sącz district, Małopolska province, Poland). Landslide movements were observed on the slopes recently – this caused damage to provincial roads. These landslides are located

in the area of various geological structure. The problem of landslides is also found in other countries, for example, the Czech Republic and Croatia [1, 8].

The first road landslide in Sułoszowa on the map of tectonic units in Poland is located in the Silesian-Cracovian monocline, north west of Krakow. It is mainly made up of rocks such as conglomerates, limestone, dolomites, clays and sandstones. These rocks are slightly inclined towards the north east. Chalk formations developed as marls and marl limestone, sands and conglomerates. They occur locally in the form of klippes covering older sediments. We can also distinguish white limestone from the Upper Jurassic era forming rocks characteristic of the region of Ojców.

Favourable for the formation of landslides in the Silesian-Cracovian monocline are precipitation waters in the form of surface and underground water state changes. Among these conditions, we can include infiltration of precipitation waters as the main cause of weakening strength properties, erosion undercutting and abrasion. A complex tectonic structure of the Silesian-Cracovian monocline area is also influential in landslide formation. Rock layers subsiding at the same angle and in one direction are favourable for the gravitational movements of the earth masses.

Another landslide is in Lipie, in the area of the Flysch Carpathian (the northern rim of the Western and Eastern Carpathians). Polish Flysh Carpathians form a region especially predisposed to landslides formation. Generally, the structure of the region consists of alternative layers of sandstone and shales and to a lesser extent mudstone, conglomerate, clay, marl and limestone. In the structure of the Carpathians are also worth mentioning about complicated tectonics. Numerous faults of different displacement sizes divide the rock mass into two blocks. Strong tectonic violation are connected with the movement of rocks in the fault areas and with clear underthrusts.

Landslides in this area of Poland may also appear due to the area sculpture dynamics occurring as a result of big slopes and river valley slope inclinations. Undoubtedly, susceptibility to landslides in this area is influenced by complex hydrological and meteorological conditions. Violent rainfalls, spring melts or long, humid and cool periods lasting for several months are especially dangerous. Water is then stored in detrital covers and bedrock – this causes deep structural landslide formations.

5. Sułoszowa landslide stability analysis

The area covered by the studies is located in the village of Sułoszowa in the Krakow district of Małopolska province – the area is a part of the Pieskowa Skała settlement.

In this area in September 2014, a fragment of the embankment was damaged. The fragment was located at the junction of a provincial road with the Prądnik stream in Wernyhora street. The slope fragment runs along an asphalt road within which there is the Prądnik stream. The fill slope forms the left side of the stream valley slope and in this area, it is partly crumbled. At the top of the embankment, on its northern side runs, the provincial road (Fig. 1).

The studied area is situated within the Krakow, Częstochowa and Olkusz (Ojców plateau) uplands. In respect of geology, the discussed landslide is located within the Silesian-Cracovian monocline. The region is formed of Jurassic limestone with considerably

developed karst phenomena. The surface is slightly wavy and covered with a substantial layer of loess and outliers.

The embankment is located at the bottom part of the slope. Its height is around 3.1m and the whole length is around 20 m. A segment of around 8m was strengthened with a lime retaining wall of about 1.5 m in height at the bottom part the embankment. The inclination of the embankment in the places without the retaining wall varies from 55° to 60°. In the upper areas of the fill slope and in the segment with the retaining wall, the inclination angle is 70–80° [5].

Fig. 1. A damaged fragment of the fill slope and the Prądnik (Białucha) stream undercutting it (Source: [5])

Computer model of the embankment and material data used to model are presented below (Fig. 2, tab. 1).

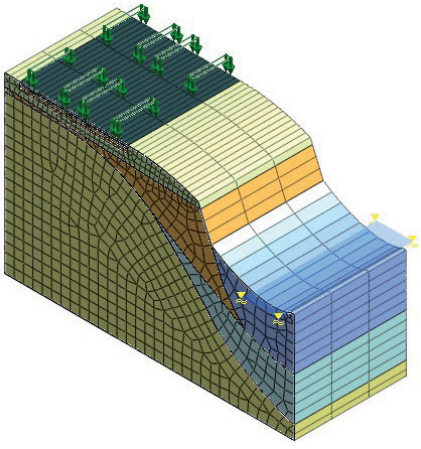

Fig. 2. Computer model of a road embankment (Source: the authors' own study)

Table 1

Geotechnical parameters of the layers in a calculation model

Marking	Soil symbol	Material model	Layer symbol	Poisson's ratio [–]	Natural humidity [%]	Volumetric density [t/m^3]	Cohesion [kPa]	Internal friction angle [°]	Young modulus [kPa]
	_	Elastic	**road**	0.2	–	2.50	–	–	50 000
	–	Elastic	**substructure**	0.2	–	2.20	–	–	50 000
	–	Elastic	**gabion**	0.2	–	2.80	–	–	100 000
	–	Elastic	**strengthened substratum**	0.2	–	1.70	–	–	300 000
–	–	Elastic	**geosynthetics**	0.2	–	1.70	–	–	130 000
	nB	Mohr-Coulomb	**I**	0.3	20	1.85	0	10	50 000
	G^{II} (pl)	Mohr-Coulomb	**IIa**	0.3	13	2.06	19	13	20 000
	G^{II} (pl)	Mohr-Coulomb	**IIb**	0.3	15	1.94	10	8	20 000
	W	Elastic	**IIIa**	0.2	–	2.20	–	–	2 000 000
	KW	Elastic	**IIIb**	0.2	–	2.20	–	–	2 000 000

(Source: the authors' own study)

Two kinds of slope stability analysis were carried out. The first analysis assumes a dry period (lack of water filtering from waterfall infiltration). The second analysis assumes a wet period (higher ground water level). During these two different periods, the strength and deformational parameters of the soils have not changed. The simulation was performed under drained conditions. Below, the results of stability analysis are presented.

On the basis of the obtained Factor of Safety FoS for the analysed fill slope (FoS = 0.8 – dry period, FoS = 0.7 – wet period) it can be stressed explicitly that it is unstable. In the enclosed figures (Fig. 3, 4, 6, 7) showing the displacements of the analysed solid, it can be seen that the largest deformations appear in the layers of the building embankment (humid silty clays and clays in plastic state). These layers initiate the formation of maximum shear strain zones connected with the appearance of a surface that has the potential to slide (Fig. 5, 8).

Vibrations and quasi-static loads caused by vehicle traffic on the provincial road cause mass movements in the area of the fill slope. Due to its strong inclination and continual washing and cutting by the waters of the Prądnik stream, it is probable that mass movements will develop further. The situation is worsened by the geological structure of the fill slope

in the form of coherent soils of low load-bearing capacity and high susceptibility to water influence – this negatively effects the strength of the slope causes increased levels of softness.

Dry period
Factor of Safety FoS = 0.80

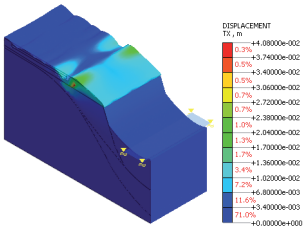

Fig. 3. Horizontal displacement [m] together with deformation (overstated scale)
(Source: the authors' own study)

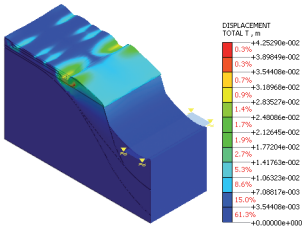

Fig. 4. Total displacement [m] together with deformation (overstated scale)
(Source: the authors' own study)

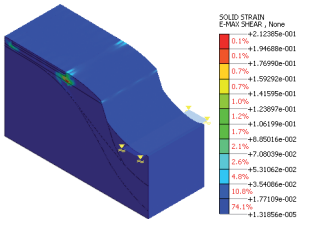

Fig. 5. Maximum shear strains [–]
(Source: the authors' own study)

Wet period
Factor of Safety FoS = 0.70

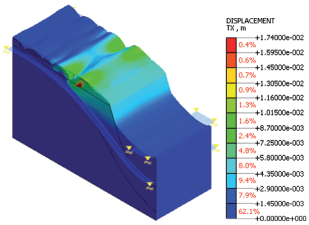

Fig. 6. Horizontal displacement [m] together with deformation (overstated scale)
(Source: the authors' own study)

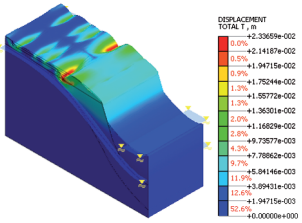

Fig. 7. Total displacement [m] together with deformation (overstated scale)
(Source: the authors' own study)

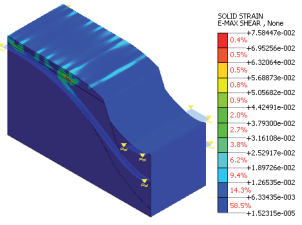

Fig. 8. Maximum shear strains [–]
(Source: the authors' own study)

To protect the unstable slope by the Prądnik stream, the priority is to limit washing and undercutting of the slope. An original solution was proposed and verified by calculations in the MIDAS programme. The protection was modelled in the form of a gabion consisting of four baskets of 1.0×1.0 m in dimension. The height of the whole designed structure is 4 m. Additionally, three layers of geosynthetics were laid directly under the building embankment;

their purpose task was to order water conditions in the area being stabilised, and protect it against uneven settling. Each geosynthetic layer was laid on a 30 cm strengthened substratum which could carry vibrations and loads caused by vehicle traffic on the province road and partly increase the load-bearing capacity and durability of the structure. The bottom geosynthetic layer was stretched along the rock layer for a length of 7 m to ensure durable strengthening under the embankment soil. Computer models of the reinforced embankment are presented below (Fig. 9).

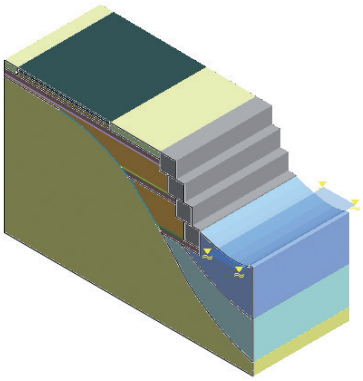

Fig. 9. Computer model of a road embankment
(Source: the authors' own study)

Dry period
Factor of Safety FoS = 4.19

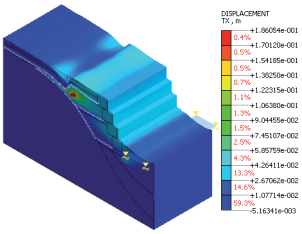

Fig. 10. Horizontal displacement [m] with deformation (overstated scale)
(Source: the authors' own study)

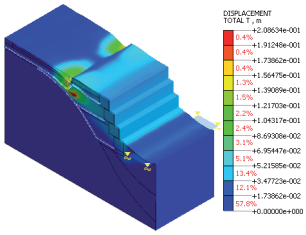

Fig. 11. Total displacement [m] with deformation (overstated scale)
(Source: the authors' own study)

Wet period
Factor of Safety FoS = 4.09

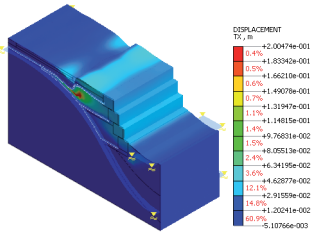

Fig. 13. Horizontal displacement [m] with deformation (overstated scale)
(Source: the authors' own study)

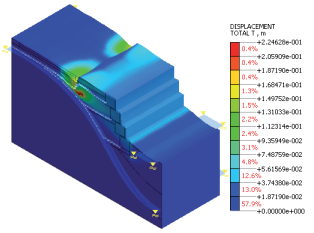

Fig. 14. Total displacement [m] with deformation (overstated scale)
(Source: the authors' own study)

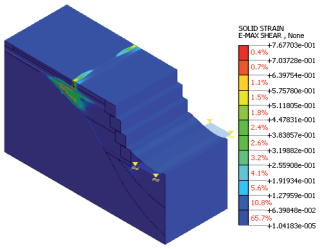

Fig. 12. Maximum shear strains [–]
(Source: the authors' own study)

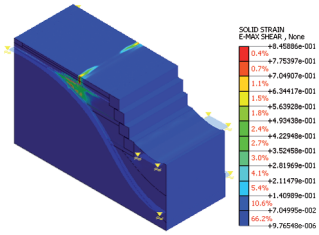

Fig. 15. Maximum shear strains [–]
(Source: the authors' own study)

Having protected the slope with gabions and three layers of geosynthetics on the strengthened substratum layer, it was possible to prevent soil masses from sliding. The solution is definitely favourable as it allowed achieving high Factors of Safety FoS = 4.19 (dry period) and FoS = 4.09 (wet period). The surface susceptible to sliding does not directly endanger the stability of the whole embankment.

As shown in the results of calculations presented in Figures 10–15, all of the used types of protection – gabion, synthetics and the strengthened layer of the soil substratum – fulfil the functions assumed earlier.

6. Stability analysis of the landslide in Lipie

The studied area is located in Lipie, about 3 km south of Gródek nad Dunajcem (Gródek over the Dunajec river), in Nowy Sącz district. The landslide occurred on the south-western shore of Rożnowskie lake, on a provincial road resulting in damage (Fig. 12).

As far as morphology is concerned, the area comprises a slope with a 14° inclination and a western orientation reaching Rożnowskie lake. The slope is cut through by provincial road no. 975 which is a single carriageway with an 8m width and built on an embankment with a height of 4.5 m.

Landslide movement has caused the destruction of a significant proportion of provincial road in recent years (Fig. 16). It is worth mentioning that the discussed landslide occurred within an older and deeper landslide covering a larger area.

The studied area is located within the flysch Carpathians. In the geological structure of the substratum, we can distinguish formations from the Eocene and Quaternary periods. Flysch Carpathians in the region of Poland are most at risk of landslides [7].

The older landslide starts slipped around 13 m over the fill slope above the provincial road. Its dimensions are about 90 m in width and 80 m in length. It is estimated that the landslide in Lipie covers an area of 0.68 ha. The form of the most recent landslide is marked with a main fill slope of up to 2 m in height, located above the access road.

On the basis of archive data, it can be stated that the landslide was already active in the 1950s. In 2001, the landslide caused the breaking of the provincial road. In 1997, 2010 and 2011, its renewal could be observed. In 2010, a geological expert opinion was commissioned

to be prepared and it proved that changes within the road traffic lanes were observed for several years and this was connected with road settling. In this period, the road embankment was strengthened with rock fill; however, it did not stop the discussed process [2].

The problem of landslide in Lipie was also dealt with by Stopkowicz & Cała [10].

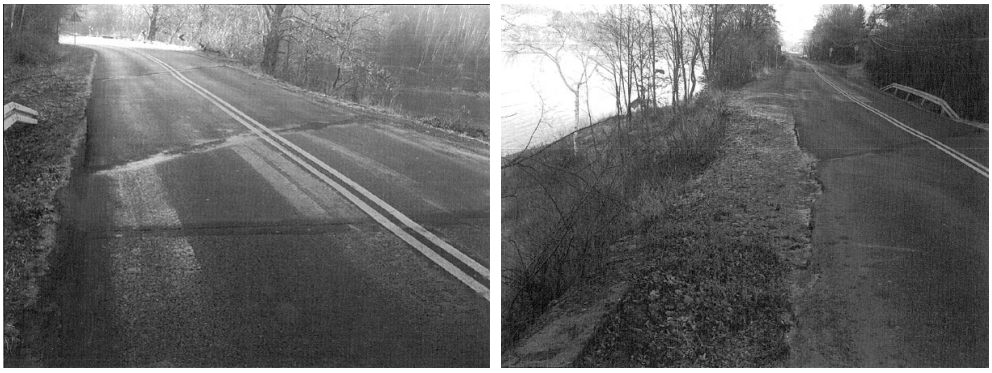

Fig. 16. Damage to provincial road no. 975 as a result of landslide movements
(Source: [3])

Three kinds of analysis of slope stability were carried out. The first analysis assumes the occurrence of a dry period (lack of water filtering from waterfall infiltration). The other analysis assumes the occurrence of a transitory period in which there appears, on a moderate level, waters from waterfall infiltrations. The third analysis was carried out under the assumption of the occurrence of a wet period with total saturation of the soil layers. The strength and deformational parameters of the soils remained unchanged. The simulation was performed under drained conditions. The computer model of the embankment and the material data used for modelling are presented below (Fig. 17, Table 2).

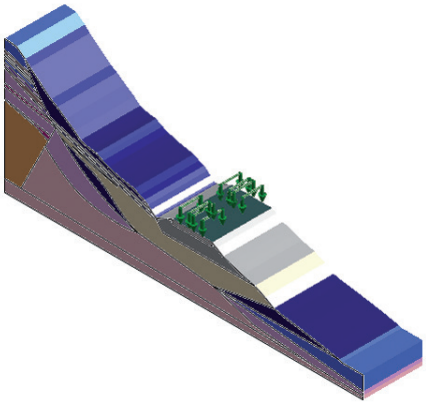

Fig. 17. Landslide computer model
(Source: the authors' own study)

Table 2

Geotechnical parameters of the layers in a calculation model

Marking	Soil symbol	Material model	Layer symbol	Poisson's ratio [–]	Natural humidity [%]	Volumetric density [t/m^3]	Cohesion [kPa]	Internal friction angle [°]	Young modulus [kPa]
	–	Elastic	**road**	0.2	–	2.50	–	–	50 000
	–	Elastic	**sub-structure**	0.2	–	2.20	–	–	50 000
	–	Elastic	**concrete wall**	0.2	–	2.50	–	–	50 000
	–	Elastic	**strengthened substratum**	0.2	–	1.70	–	–	300 000
–	–	Elastic	**geo-synthetic**	0.2	–	1.70	–	–	130 000
	nB	Mohr-Coulomb	–	0.3	20	1.85	0	10	50 000
	G, Gz,	Mohr-Coulomb	**Ia**	0.3	21	1.85	7	9	30 000
	G, Gz,	Mohr-Coulomb	**Ib**	0.3	16	2	8	15	50 000
	G, Gz	Mohr-Coulomb	**IIa**	0.3	13	2.15	18	15	22 000
	Pg, πp	Mohr-Coulomb	**IIb**	0.3	10	2.20	26	17	30 000
	Pd, Pπ	Mohr-Coulomb	**III**	0.3	6	1.85	0	29	38 000
	KW	Mohr-Coulomb	**IV**	0.3	12	2.00	57	12	20 000
	KW	Mohr-Coulomb	**V**	0.3	5	1.80	0	33	114 000
	SM	Mohr-Coulomb	**VI**	0.2	–	2.48	250	0	26 000
	ST	Mohr-Coulomb	**VII**	0.2	–	2.52	250	0	100 000

(Source: the authors' own study)

On the basis of the performed analysis and resulting stability coefficients (FoS = 0.73 – dry period, FoS = 0.74 – transitory period, FoS = 0.50 – wet period) it can be stated that the discussed embankment is unstable. The figures below (Fig. 19, 22, 23, 25, 26) show displacements of the analysed embankment. The highest displacement values can be seen in the layers of the building embankment, clayey sands and clays. In the figures showing

maximum shear strains (Fig. 21, 24, 27) the sliding surface was clearly marked – this shows that soil shear may take place in the layers mentioned earlier.

As the analysed road embankment is located in an area prone to landslides, it is constantly endangered by landslide activity. In periods of heavy rainfall, due to dramatic increases of water flow pressure within the colluvium, it may happen that the values of the soil substratum strength parameters reduce resulting in landslide movements. Undoubtedly, the presence of deposits sensitive to water activity and which quickly become waterlogged in the substratum is favourable for this process. In the autumn and spring periods, when intensive rainfalls and melts occur, the landslide movements can increase.

As we are dealing with an unstable road embankment located within an older and deeper landslide, a protection strategy was designed in the form of a reinforced concrete retaining wall (slab and angle) located on the Rożnowskie lake side (Fig. 18). The designed retaining wall, sunken to a minimum of 1.5 m below the lowest slide surface, has to transfer the pressure on the soil, caused by vehicles on the provincial road. Additionally, three layers of geosynthetics were laid directly under the building embankment – this was to order water conditions and limit uneven settlings. Each of the three layers of geosynthetics was laid on a 30 cm thick strengthened substratum layer, the purpose of which was to help to transfer vibrations and quasi-static loads caused by vehicle movement on the provincial road. For construction reasons, the layer of geosynthetics was also laid along the whole length of the retaining wall together with the bottom slab. A water drain was located above the bottom slab.

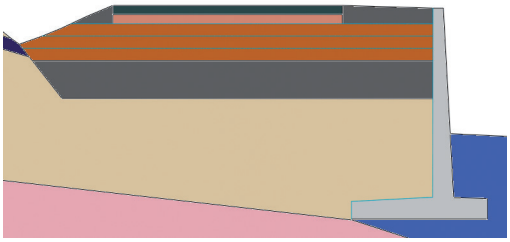

Fig. 18. Approximation of road embankment strengthening (2D view)
(Source: the authors' own study)

The dimensions of the retaining wall:

- height 8.9 m
- wall thickness 45–85 cm
- width of base – 5.85 m
- thickness of bottom plate – 90 cm

Proposed solution made the fill slope adequately protected. Stability coefficients increased significantly for all three calculation cases – FoS = 2.36 (dry period), FoS = 2.05 (transitory period), FoS = 1.66 (wet period) – this explicitly proves the accuracy of the realised solution. The displacements of the analysed solid (Fig. 28, 29, 31, 32, 34, 35) and maximum shear strains (Fig. 30, 33, 36) show that if the loss of stability occurs, then it will occur behind the road embankment strengthened by the retaining construction.

7. Summary

At present, there are many tools on the market, which allow the engineers to predict the possible behaviour of the soil masses. The dynamic development of software programs used for the analyses of embankment and slope stability not only allows the checking road embankments with regard to their predisposition to landslide activity but also to carry out analyses of the designed protection solutions.

The presented examples show that the best solution is to use a system of protection combining several methods. The analysed embankments were located in totally different geotechnical conditions. The first analysed example is in the Silesian – Cracovian monocline, the second is in the Carpathians. The road embankment in the flysch Carpathians, in Lipie, revealed higher levels of instability. This proves the view that there are serious landslide risks connected with the geological structure in the Carpathian flysch. Such a geological structure causes risks to road infrastructure. The proposed and modelled protections of road embankments presented in the works in Sułoszowa and Lipie combine the methods of protective construction with geosynthetic strategies and allow the obtaining of satisfactory stability indices and at the same time, to order water conditions. The final effect is not only to ensure the stability of the embankment but also the functionality of the structure located on it.

The problem the authors tried to present is rather a universal one. Correct and carefully built road embankments that use an adequate range of materials and ensuring proper drainage may, in given location conditions, prevent landslide movements. However, there may be cases when the road constructions are in advance endangered by stability loss. The knowledge and experience of the designer and people involved in the embankment and slope protection process then become especially important.

Dry period
Factor of Safety FoS = 0.73

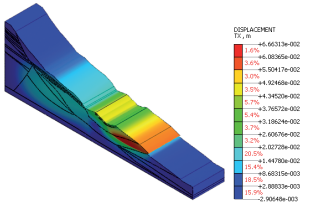

Fig. 19. Horizontal displacement [m] with deformation (overstated scale) (Source: the authors' own study)

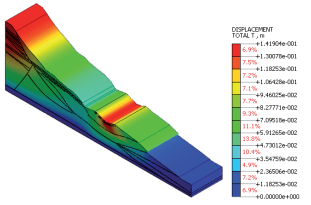

Fig. 20. Total displacement [m] with deformation (overstated scale) (Source: the authors' own study)

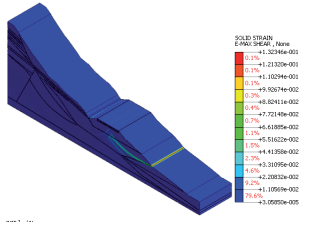

Fig. 21. Maximum shear strains [–] (Source: the authors' own study)

Transitory period
Factor of Safety FoS = 0.74

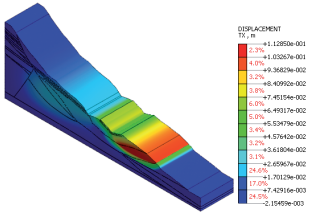

Fig. 22. Horizontal displacement [m] with deformation (overstated scale) (Source: the authors' own study)

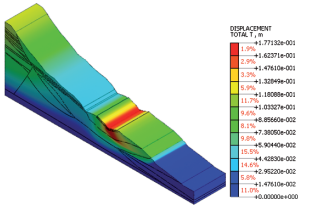

Fig. 23. Total displacement [m] with deformation (overstated scale) (Source: the authors' own study)

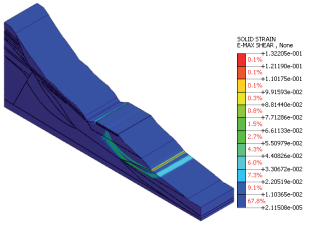

Fig. 24. Maximum shear strains [–] (Source: the authors' own study)

Wet period
Factor of Safety FoS = 0.50

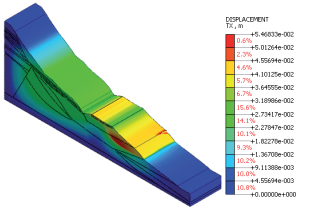

Fig. 25. Horizontal displacement [m] with deformation (overstated scale) (Source: the authors' own study)

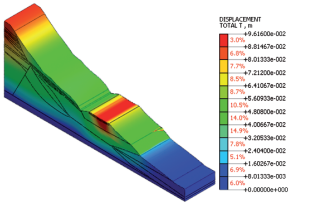

Fig. 26. Total displacement [m] with deformation (overstated scale) (Source: the authors' own study)

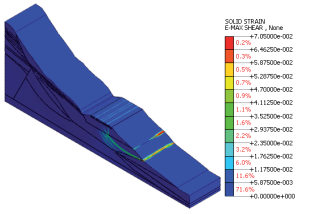

Fig. 27. Maximum shear strains [–] (Source: the authors' own study)

Dry period
Factor of Safety FoS = 2.36

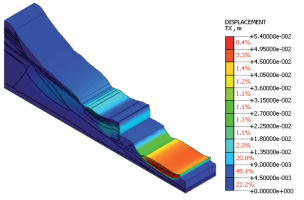

Fig. 28. Horizontal displacement [m] with deformation (overstated scale) (Source: the authors' own study)

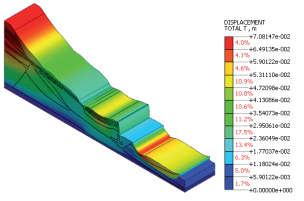

Fig. 29. Total displacement [m] with deformation (overstated scale) (Source: the authors' own study)

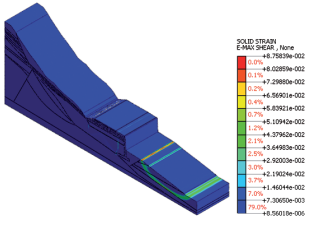

Fig. 30. Maximum shear strains [–] (Source: the authors' own study)

Transitory period
Factor of Safety FoS = 2.05

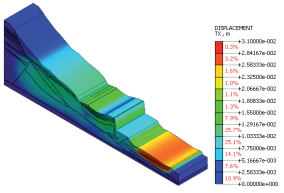

Fig. 31. Horizontal displacement [m] with deformation (overstated scale) (Source: the authors' own study)

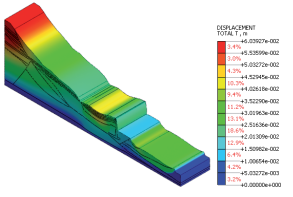

Fig. 32. Total displacement [m] with deformation (overstated scale) (Source: the authors' own study)

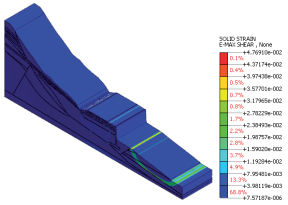

Fig. 33. Maximum shear strains [–] (Source: the authors' own study)

Wet period
Factor of Safety FoS = 1.66

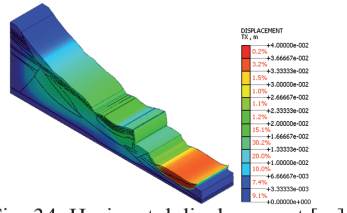

Fig. 34. Horizontal displacement [m] with deformation (overstated scale) (Source: the authors' own study)

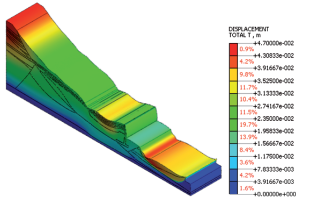

Fig. 35. Total displacement [m] with deformation (overstated scale) (Source: the authors' own study)

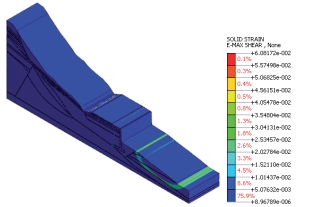

Fig. 36. Maximum shear strains [–] (Source: the authors' own study)

References

[1] Baron I., Agliardi F., Ambrosi C., Crosta G. B., *Numerical analysis of deep-seated mass movements in the Magura Nappe; Flysch Belt of the Western Carpathians (Czech Republic)*, Natural Hazards and Earth System Science, 5(3), 2005, 367–374.

[2] Białek M., *Analiza stateczności wraz z projektem zabezpieczenia nasypów drogowych zlokalizowanych w różnych warunkach geotechnicznych*, M.Sc. Thesis, Kraków 2015.

[3] *Dokumentacja geologiczno-inżynierska dla potrzeb zabezpieczenia osuwiska w ciągu drogi wojewódzkiej nr 975 w miejscowości Lipie, gm. Gródek nad Dunajcem*, Zakład usług Geologicznych i Projektowych Budownictwa i Ochrony Środowiska – GEOTECH, Kraków 2011.

[4] *MIDAS GTS NX, 2014*, New experience of Geo-Technical analysis System, Manual documentation, 2014.

[5] *Opinia geotechniczna celem zabezpieczenia skarpy na styku drogi wojewódzkiej nr 773 w Sułoszowej*, Przedsiębiorstwo Geologiczne S.A., Kraków 2014.

[6] *Problematyka osuwisk w budownictwie komunikacyjnym*, Zeszyty Naukowo-Techniczne Stowarzyszenia Inżynierów i Techników Komunikacji Rzeczpospolitej Polskiej Oddział w Krakowie, Materiały Konferencyjne, No. 8 (Issue 144), PiT, Kraków 2009.

[7] Raczkowski W., *Landslide hazard in the polish Flysch Carpathians*, Studia Geomorphologica Carpatho-Balcanica, Vol. XLI, 2007, 61–75.

[8] Soldo B., Ivandić K. & Orešković M., *Numerous landslides and landslide restorations – an example*, Acta Montanistica Slovaca Ročník 17 (2012), číslo 4, 257–262.

[9] Srokosz P. E., Damicz J., Bartoszewicz A., *Utrata stateczności skarpy nasypu drogowego*, XXIII Konferencja Naukowo-Techniczna Awarie Budowlane, Szczecin–Międzyzdroje 2007.

[10] Stopkowicz A., Cała M., *Analiza stateczności zboczy zlokalizowanych we fliszu karpackim z zastosowaniem metod numerycznych*, XXVII Zimowa Szkoła Mechaniki Górotworu, Zakopane 2004.

[11] Ukleja J., *Geotechniczne aspekty stabilizacji obszarów zagrożonych osuwiskami*, Oficyna Wydawnicza, Opole 2013.

[12] Wysokiński L., *Metody prognozowania i zabezpieczania osuwisk*, XXV Konferencja Naukowo-Techniczna Awarie Budowlane, Międzyzdroje 2011.

[13] Wysokiński L., *Ocena stateczności skarp i zboczy. Zasady wyboru zabezpieczeń. Instrukcje, Wytyczne, Poradniki 424/2011*, Instytut Techniki Budowlanej, Warszawa 2011.

TECHNICAL TRANSACTIONS | CZASOPISMO TECHNICZNE
CIVIL ENGINEERING | BUDOWNICTWO
3-B/2016

DOI: 10.4467/2353737XCT.16.219.5968

BARBARA SOŁTYSIK, ROBERT JANKOWSKI*

THE RESPONSE OF THREE COLLIDING MODELS OF STEEL TOWERS TO SEISMIC EXCITATION

BADANIA ODPOWIEDZI ZDERZAJĄCYCH SIĘ MODELI TRZECH WIEŻ STALOWYCH PODDANYCH WYMUSZENIU SEJSMICZNEMU

Abstract

A number of past and recent observations have confirmed that collisions between adjacent, insufficiently-separated structures occurring as a result of seismic excitation (structural pounding) may result in serious damage to structural elements and can even lead to their total destruction. This paper summarises the results obtained from a shaking table experimental study which investigated structural pounding between three adjacent models of steel towers. The study included different configurations of towers and distances between the structures. The results of the study confirmed that collisions have a significant influence upon the behaviour of the towers, leading to the increase as well as decrease in the structural response.

Keywords: structural pounding, collisions, experimental study, seismic excitations, steel towers

Streszczenie

Wielokrotne obserwacje potwierdzają, iż zderzenia podczas trzęsień ziemi pomiędzy zbyt blisko sąsiadującymi ze sobą budynkami mogą powodować znaczące zniszczenia elementów konstrukcyjnych, a czasem mogą nawet prowadzić do całkowitego zniszczenia konstrukcji. Niniejszy artykuł przedstawia wyniki badań eksperymentalnych przeprowadzonych na stole sejsmicznym dotyczących odpowiedzi zderzających się trzech modeli stalowych wież. W analizie tej uwzględniono różne ustawienie konstrukcji oraz zmieniającą się odległość pomiędzy nimi. Wyniki badań potwierdzają, iż interakcje pomiędzy konstrukcjami mają znaczący wpływ na zachowanie się wież, prowadząc zarówno do wzrostu, jak i redukcji odpowiedzi.

Słowa kluczowe: zderzenia, kolizje, badania eksperymentalne, wstrząsy sejsmiczne, wieże stalowe

* M.Sc. Barbara Sołtysik (Ph.D. student), Prof. Ph.D. D.Sc. Robert Jankowski, Department of Metal Structures and Construction Management, Faculty of Civil and Environmental Engineering, Gdansk University of Technology.

1. Introduction

In this age of high urbanization, the need to build structures very close one to another forces the designer to take interactions between closely separated buildings during ground motions into consideration. This phenomenon, referred to in the literature as earthquake-induced structural pounding, may cause local damage to structural elements [1, 11, 15, 16], and can even lead to the total collapse of the structure. Dangerous interactions between insufficiently separated structures during moderate to strong seismic excitations may occur due to differences in the dynamic properties of each structure [5]. Differences in mass or stiffness may lead to out-of-phase vibrations, which could finally result in collisions [2, 12].

Bertero & Collins [3] and Mahin et al. [9] reported that during the San Fernando earthquake in 1971, collisions between the main building of the Olive View Hospital and one of its independently standing stairway towers caused permanent titling of the tower. Serious pounding damage to parts of school buildings was observed and reported after the Athens earthquake of 7th September 1999 [15]. Additionally, the SSK Hospital in Izmit experienced major damage during the Kocaeli earthquake (17th August 1999) [4]. Extensive damage to and collapses of some buildings due to collisions were recorded after the Loma Prieta earthquake (17th October 1989) [8]. Structural interactions leading to some local damage at contact points was also observed during earthquakes which took place in Poland in 2004 [16, 17].

Earthquake-induced pounding between adjacent, insufficiently separated buildings has been investigated through the use of various structural models of interacting structures and different simulations of collisions [6, 10]. This phenomenon involves deformations at contact points, local cracking or crushing, fracturing due to impact, friction, etc., so it is very difficult for the mathematical analysis. The studies were mainly focused upon reinforced concrete buildings, and research into the behaviour of steel structures under similar circumstances is very limited [13]. Anagnostopoulos conducted a fundamental study of the interactions between adjacent structures in series, using single degree-of-freedom systems with linear and viscoelastic models [1]. Further analyses were performed on more detailed and advanced models of structures using multi degree-of-freedom models with masses lumped on each floor [7] and applying the finite element method [12–14] .

The aim of this paper is to summarise the results obtained from the shaking table experimental study concerning structural pounding between three adjacent models of steel towers subjected to ground motions. The experimental research was performed for different gap distances between the structures. In this paper, examples of the results for three distances (0 mm, 10 mm and 20 mm) are shown.

2. Experimental study

2.1. Experimental setup

The experimental study described in the paper concerned earthquake-induced structural pounding between three steel towers with different dynamic properties (differences in mass) arranged in different configurations (Fig. 1). The study was focused on the structural

response of each tower. Towers were constructed out of four columns with heights of 100 cm made of square box sections with dimensions of 15 mm×15 mm and wall thicknesses of 1.5 mm. At the base and the top, columns were connected with horizontal elements with the same cross-section. To prevent transverse and torsional vibrations, skew bracings were used (in addition to square box sections measuring 15 mm×15 mm×1.5 mm). Concrete plates with dimensions of 50 cm×50 cm×7 cm and weighing 42.2 kg were mounted at the top of each tower. The towers were rigidly fixed to the platform of the shaking table (see Fig. 1) and the influence of the foundation type, soil-structure interaction and the ground water conditions were not considered in the study. Two configurations were examined: configuration *C*1 was arranged in such a way that two concrete plates were mounted on the external towers (tower 1 and tower 3) and only one plate was mounted at the top of the middle tower (tower 2); for configuration *C*2, only one plate was mounted at the top of external towers and two plates were mounted on the middle tower.

To simulate the behaviour of each structure under ground motions, the unidirectional shaking table located at the Laboratory of Department of Metal Structures and Construction Management, Gdansk University of Technology was used [12]. This table allows the simulation of the strongest seismic excitations. A platform measuring 200 cm×200 cm, upon which the table is positioned, can be used to test structural models with a maximum weight of 1000 kg. The linear actuator, which may induce movement with a maximum acceleration of 10 m/s^2 and a maximum strength of 44.5 kN, is connected to the platform. The following equipment was used during the measurements:

- Four single-axis accelerometers (with mechanical restriction of frequency at 4 kHz);
- Twelve-channel amplifier with low pass filter of 100 Hz;
- Analogue-digital card to record the measurements.

Four accelerometers were used during the study. Three of the sensors were located at the top of each tower and one was placed on the shaking table platform (to control its movement).

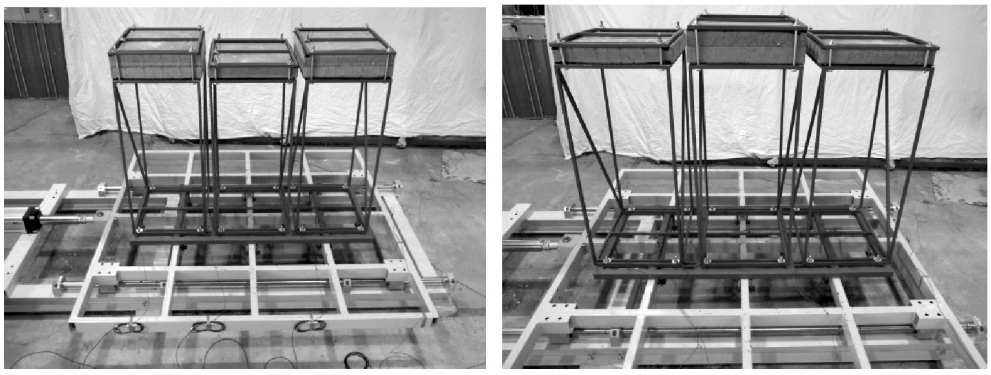

Fig. 1. Experimental setup: configuration *C*1 and configuration *C*2

2.2. Free vibration tests

To determine the dynamic characteristics of each tower, free vibration tests were first conducted. The tests were carried out by releasing a pre-angled tower. All measurements were recorded with a sampling rate of 500 Hz for a time of 100 seconds. The results obtained from the tests, in the form of values of natural frequency for tower 1, tower 2 and tower 3 for two configurations are summarised in Table 1. The exemplary acceleration time histories are also shown in Fig. 2.

Table 1

Natural frequency values for the towers

	Natural frequency [Hz]	
	Configuration *C1*	Configuration *C2*
Tower no. 1	2.400	3.190
Tower no. 2	3.380	2.450
Tower no. 3	2.260	3.120

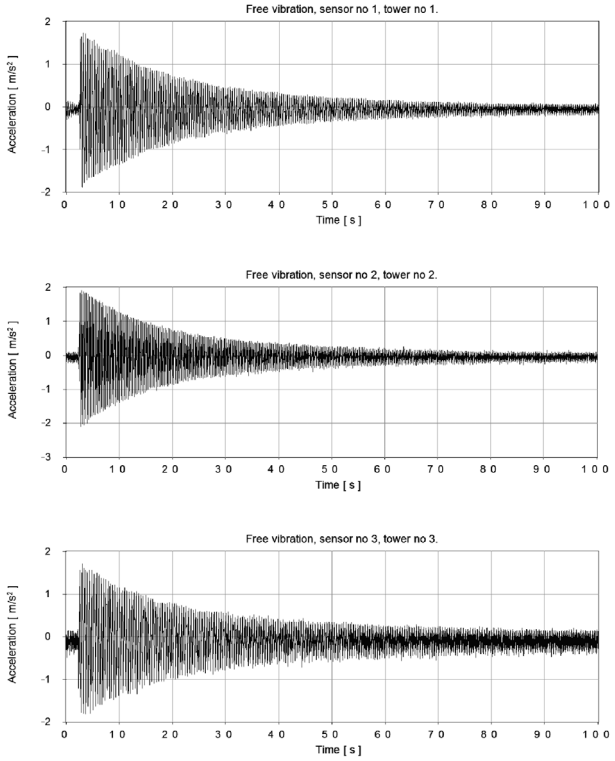

Fig. 2. Exemplary results from free vibration tests for tower 1, 2 and 3 for the configuration *C*1

2.3. Sweep sine test

In the next stage of the research, the sweep sine test was carried out. A single test involved measurements of the acceleration amplitude at the same four points as in the case of free vibration tests. Harmonic excitation of different frequencies was generated by the shaking table actuator. Measurements were recorded with a sampling rate of 500 Hz for a duration of 60 seconds. Table 2 shows the peak values of acceleration for towers arranged in two configurations. Fig. 3 and 4 present the dynamic characteristics of the structural response for configurations *C*1 and *C*2, respectively.

Table 2

Peak values of acceleration

	Acceleration [m/s^2]			
	Configuration *C*1		Configuration *C*2	
	Max	Min	Max	Min
Tower no 1	5.052	–5.124	10.996	–10.918
Tower no 2	10.657	–10.995	7.950	–8.034
Tower no 3	4.496	–4.675	10.127	–10.122

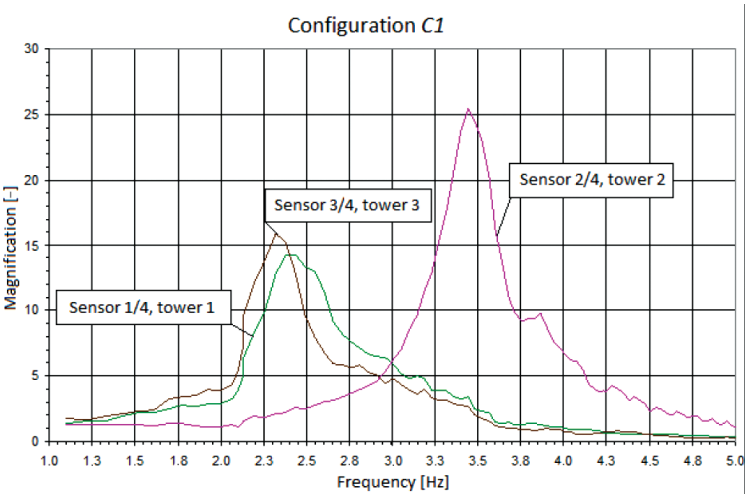

Fig. 3. Dynamic characteristics of the structural response for configuration *C*1

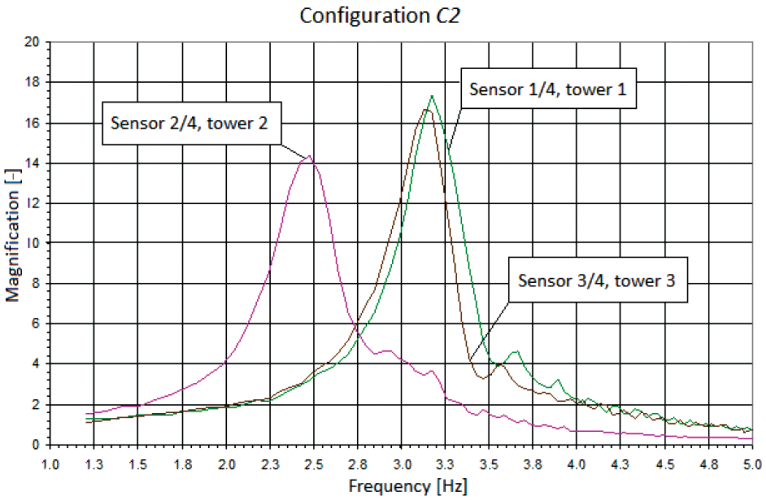

Fig. 4. Dynamic characteristics of the structural response for configuration *C2*

2.4. Seismic test

In the last stage of the experimental study, the response of colliding structures under real earthquake excitation was studied. The seismic test was conducted for the San Fernando earthquake (9th February 1971). The N16° component of the earthquake recorded at the Pacoima Dam station was applied in the study. The earthquake record was scaled to 25% (peak ground acceleration was 2.85 m/s^2) so as to prevent damage of the tower structures. In the test, three different gap sizes between structures were taken into consideration – Δ_1 = 0 mm and Δ_2 = 10 mm and Δ_3 = 20 mm. The peak values of the structural response acceleration for two different configurations are summarised in Table 3. Exemplary results in the form of the acceleration time histories are also presented in Fig. 5.

Results summarised in Table 3 clearly indicate that interactions between insufficiently separated structures have a significant influence upon the structural response under seismic excitation. Comparing different configurations, it can be seen from the table that, in the case of the 0mm gap, the response of all towers is lower for configuration *C*2, even by as much as 58% (tower 3). Additionally, all peak values of acceleration for the gap size of 10mm decrease in the case of configuration *C*2 (by 53% for tower 2). On the other hand, for the gap size of 20 mm, the peak acceleration for configuration *C*2 decreases for only one tower, while the increase trend is observed for the other two structures.

When we focus our attention on only one configuration, i.e. configuration *C*1, it can also be seen from Table 3 that increasing the gap distance from 0 mm to 20 mm leads to the increase in the structural response of tower 1 and tower 2 (even by over 778% in the case of tower 2). On the other hand, in the case of tower 3, the increase in the gap leads to an initial increase in the peak response which is followed by the decrease trend.

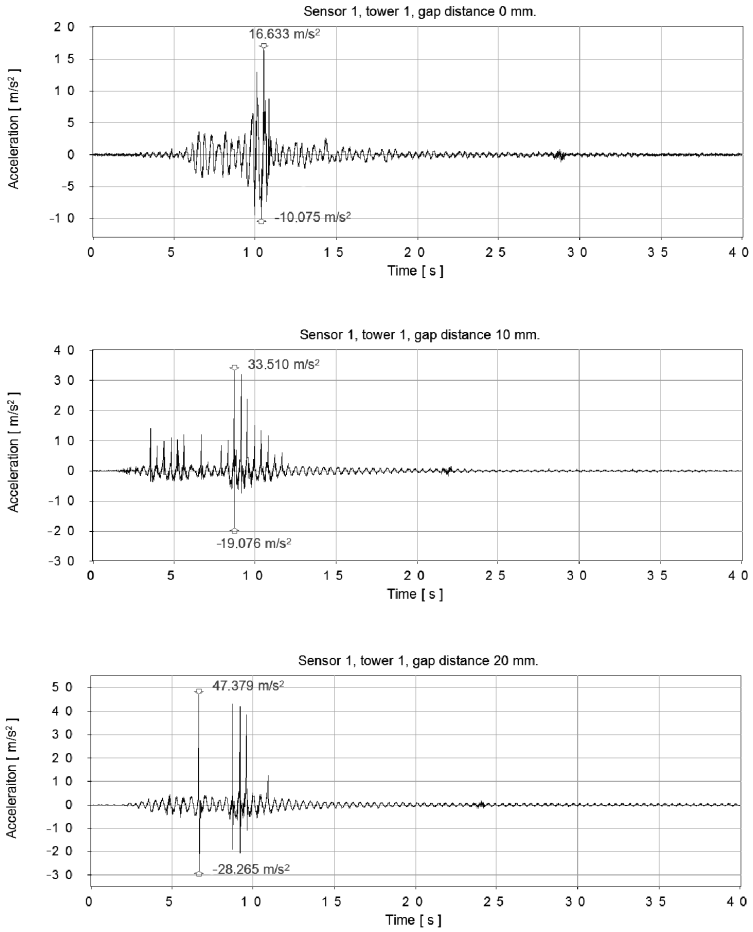

Fig. 5 Acceleration time history of the structural response for configuration *C*1 under the San Fernando earthquake for gaps of 0 mm, 10 mm and 20 mm for tower 1

Table 3

Peak values of acceleration under the scaled San Fernando earthquake for Towers 1, 2 and 3 for different configurations and gap sizes

	Peak values of acceleration [m/s²]		
	Configuration *C*1		
	Δ_1 = 0 mm	**Δ_2 = 10 mm**	**Δ_3 = 20 mm**
Tower no. 1	13.228	33.510	47.379
Tower no. 2	9.638	56.932	84.653
Tower no. 3	13.922	40.976	37.267

cd. tab. 3

	Configuration *C*2		
	Δ_1 = 0 mm	Δ_2 = 10 mm	Δ_3 = 20 mm
Tower no. 1	6.667	29.630	98.507
Tower no. 2	5.899	26.873	61.190
Tower no. 3	5.913	40.960	44.470

3. Concluding remarks

The results of the shaking table experimental investigation focusing on earthquake-induced pounding between three adjacent steel towers under earthquake excitation have been described in this paper. The study was performed for different configurations and distances between the structures.

The results of the study indicate that interactions between insufficiently separated structures may cause significant changes in structural response during periods of ground motion. In the case of the structures analysed in the present paper, pounding resulted in the decrease as well as in the increase of the peak responses.

Further experimental as well as numerical studies are required in order to investigate the effect of earthquake-induced pounding between structures in series in more detail. This remark especially concerns experimental tests on full scale models of real steel structures under different earthquake excitations. It should be underlined, however, that such tests would require appropriate laboratory equipment not available in Poland. On the other hand, the numerical investigation with the incorporation of the strain rate effect under dynamic excitation is also important and such analyses are planned to be conducted by the authors in the nearest future.

The authors would like to thank Mr. Henryk Michniewicz and Mr. Hytham Ali Abd Elaziz Elwardany for their help in conducting the experiments.

References

[1] Anagnostopoulos S.A., *Pounding of buildings in series during earthquakes,* Earthquake Engineering and Structural Dynamics, Vol. 16, 1988, 443–456.

[2] Anagnostopoulos S.A., Spiliopoulus K.V., *An investigation of earthquake induced pounding between adjacent building*, Earthquake Engineering and Structural Dynamics, Vol. 21, 1992, 289–302.

[3] Bertero VV., Collins RG., *Investigation of the failures of the Olive View stair towers during the San Fernando earthquake and their implications on seismic design*, EERC report No. 73–26, Berkeley: Earthquake Engineering Research Center, University of California, 1973.

[4] Gillies A.G., Anderson D.L., Mitchell D., Tinawi R., Saatcioglu M., Gardner N.J., Ghoborah A., The August 17, 1999, *Kocaeli (Turkey) earthquake – lifelines and preparedness*, Canadian Journal of Civil Engineering, Vol. 28, No. 6, 2001, 881–890.
[5] Jankowski R., *Impact force spectrum for damage assessment of earthquake-induced structural pounding*, Key Engineering Materials, Vol. 293–294, 2005, 711–718.
[6] Jankowski R., *Theoretical and experimental assessment of parameters for the non-linear viscoelastic model of structural pounding*, Journal of Theoretical and Applied Mechanics, Vol. 45, No. 4, 2007, 931–942.
[7] Karayannis C.G., Favvata M.J., *Earthquake-induced interaction between adjacent reinforced concrete structures with non-equal heights*, Earthquake Engineering and Structural Dynamics, Vol. 34, 2005, 1–20.
[8] Kasai K., Maison B., B*uilding pounding damage during the 1989 Loma Prieta earthquake*, Engineering Structures, Vol. 19, 1997, 195–207.
[9] Mahin S., Bertero V., Chopra A. & Collins R., *Response of the Olive View Hospital Main Building during the San Fernando Earthquake*, Earthquake Engineering Research Center Report (EERC 76–22), Univ. of California, Berkeley 1976.
[10] Mahmoud S., Jankowski R., *Modified linear viscoelastic model of earthquake-induced structural pounding*, Iranian Journal of Science and Technology, Vol. 35, No. C1, 2011, 51–62.
[11] Rosenblueth E., Meli R., *The 1985 earthquake: causes and effects in Mexico City*, Concrete International, Vol. 8, 1986, 23–34.
[12] Sołtysik B., Jankowski R., *Badania eksperymentalne zderzeń pomiędzy wieżami w szeregu poddanymi wymuszeniu sejsmicznemu*, Nowe trendy w naukach inżynieryjnych 4, Vol. I, 2013, 27–36.
[13] Sołtysik B., Jankowski R., *Non-linear strain rate analysis of earthquake-induced pounding between steel buildings*, International Journal of Earth Sciences and Engineering, Vol. 6, No. 3, 2013, 429–433.
[14] Sołtysik B., Jankowski R., *Numeryczna analiza zachowania się kolidujących ze sobą budynków stalowych poddanych obciążeniom sejsmicznym*, XIII Sympozjum Wpływy Sejsmiczne i Parasejsmiczne na Budowle, Kraków 2012, 1–12.
[15] Vasiliadis L., Elenas A., *Performance of school buildings during the Athens earthquake of 7 September 1999*, 12th European conference on earthquake engineering, Paper ref. 264, 2002.
[16] Zembaty Z., Cholewicki A., Jankowski R., Szulc J. *Trzęsienia ziemi 21 września 2004 r. w Polsce północno-wschodniej oraz ich wpływ na obiekty budowlane*, Inżynieria i Budownictwo, Vol. 61, No. 1, 2005, 3–9.
[17] Zembaty Z., Jankowski R., Cholewicki A., Szulc J., *Trzęsienie ziemi 30 listopada 2004 r. na Podhalu oraz jego wpływ na obiekty budowlane*, Inżynieria i Budownictwo, Vol. 61, No. 9, 2005, 507–511.

TECHNICAL TRANSACTIONS | **CZASOPISMO TECHNICZNE**
CIVIL ENGINEERING | BUDOWNICTWO
3-B/2016

DOI: 10.4467/2353737XCT.16.221.5970

MACIEJ ZAJĄC*

NUMERICAL EVALUATION OF THE INFLUENCE OF THE MODERNISATION OF SELECTED APARTMENT BUILDINGS SUBJECTED TO MINING TREMORS ON THEIR DYNAMIC RESPONSE

NUMERYCZNA OCENA WPŁYWU MODERNIZACJI WYBRANYCH BUDYNKÓW MIESZKALNYCH PODDANYCH WSTRZĄSOM GÓRNICZYM NA ICH ODPOWIEDŹ DYNAMICZNĄ

A b s t r a c t

This paper presents the results of numerical analysis of the dynamic response of 12 storey precast concrete apartment buildings of prefabricated system WWP, located in a seismically active mining region in Poland – Legnica-Glogow Copperfield (LGC). The study involved typical buildings and structures after modernisation. The results allowed to assess the influence of the type of structural reinforcements of the buildings on their dynamic response.

Keywords: dynamic response, prefabricated buildings, mining tremors

S t r e s z c z e n i e

W pracy przedstawiono wyniki obliczeń numerycznych odpowiedzi dynamicznej dwunastokondygnacyjnych budynków wielkopłytowych systemu Wrocławska Wielka Płyta (WWP) zlokalizowanych na terenie LGOM, poddanych wstrząsom pochodzenia górniczego. Badania dotyczyły budynków typowych oraz po modernizacji. Uzyskane wyniki pozwoliły na ocenę wpływu rodzaju wzmocnienia konstrukcji budynku na jego odpowiedź dynamiczną.

Słowa kluczowe: odpowiedź dynamiczna, budynki prefabrykowane, wstrząsy górnicze

* Ph.D. Maciej Zając, Institute of Technology, Pedagogical University of Cracow.

1. Introduction

A lot of prefabricated buildings are located in mining areas and they are subjected to paraseismic excitations induced by mining tremors, which in some regions can be comparable to low intensity earthquakes [7, 9, 11, 14]. For instance, in the most seismically active mining region in Poland – Legnica-Glogow Copperfield (LGC), the tremors' energy even reaches 1E10 J.

Most of the structures have not been designed to carry this kind of load. So modernisation and reinforcement of the buildings becomes necessary to assure safe operation [3, 5].

Numerical analysis of the influence of structural modifications (reinforcement) on the natural vibration frequencies of selected actual apartment high buildings was presented in [6]. In this paper, dynamic responses of buildings before and after modification were calculated and compared. Typical accelerograms registered in LGC were applied as kinematic excitation.

2. Analysed buildings and their numerical models

In the paper, four (A0, A1, B0, B1) 12 storey precast concrete apartment buildings, constructed according to one of the Polish prefabricated WWP systems [3, 4], were analysed.

Buildings A0 and B0 are typical for the WWP system. A1 and B1 were reinforced because of mine-induced kinematic excitations [2, 12]. All of them consist of a solid reinforced concrete basement (wall thickness – 30 cm) and precast panel walls (thickness – 14 cm). Each of the buildings is divided into single-stair and double-stair segments. All of them are located in a seismically active mining region in Poland – Legnica-Glogow Copperfield (LGC). Examples of the analysed buildings are presented in Figure 1 [6].

Buildings A0 and A1 consist of three identical sections "XI-9". A1 was strengthened with the inner and exterior structural reinforcements. New monolithic concrete spans along

a) b)

Fig. 1. Analysed structures: a) building "A0" – typical for the WWP system; b) building "A1" with inner and exterior structural reinforcements [6]

both the gable wall as well as the new monolithic load-bearing longitudinal ("*y*" direction) walls and reinforcements of existing load-bearing transverse ("*x*" direction) walls were applied. Floor plans of analysed structures (A0, A1) are presented in Figure 2 [2, 6, 12].

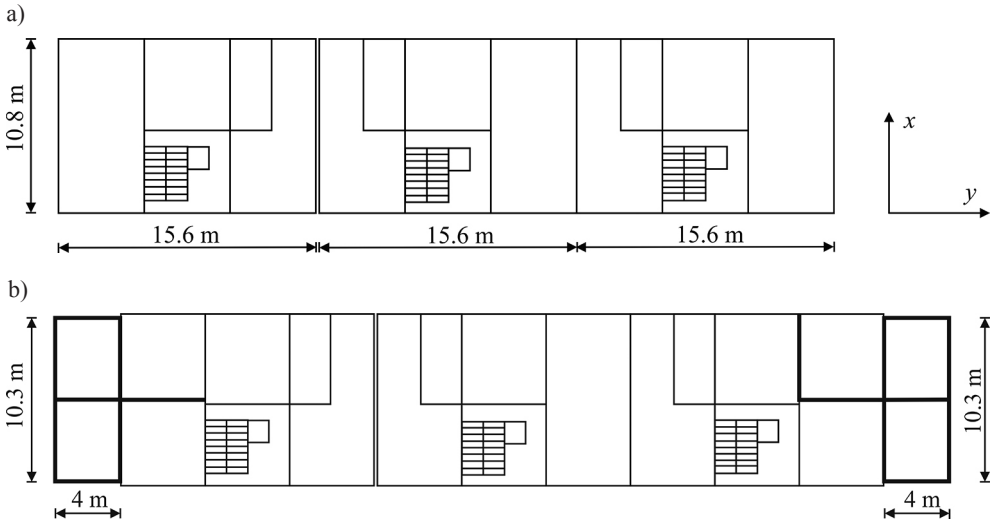

Fig. 2. Floor plans of analysed structures: a) building "A0"; b) building "A1" with reinforcement as lines marked in bold [6]

Buildings B0 and B1 consist of two different kinds of sections: "XI-9" and "XI-6". In B1, only inner structural reinforcements (new monolithic load-bearing longitudinal walls and reinforcements of some of existing load-bearing walls) were applied. The floor plan of building "B1" with reinforcement as lines marked in bold is presented in Figure 3 [2, 6, 12].

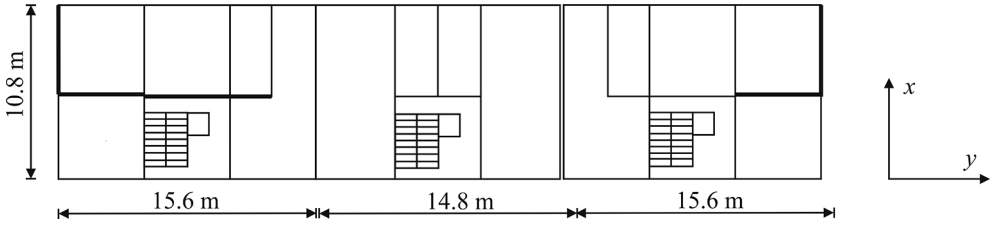

Fig. 3. Floor plan of building "B1" with reinforcement as lines marked in bold [6]

Numerical models of the analysed structures were built in finite element software Ansys [13]. All structural members were modelled using 4-node elastic shell elements with 6 degrees of freedom. The influence of panel joints by Young's modulus reduction of load bearing elements was applied. Soil flexibility was taken into consideration by the application of spring elements with stiffness calculated for layered subsoil using the Savinov model

[8]. A dynamic soil parameter (Cz) equal to 55 MPa was considered. Finite element models of the analysed structures are presented in figure 4 and the applied material parameters of structural elements are shown in Table 1[6].

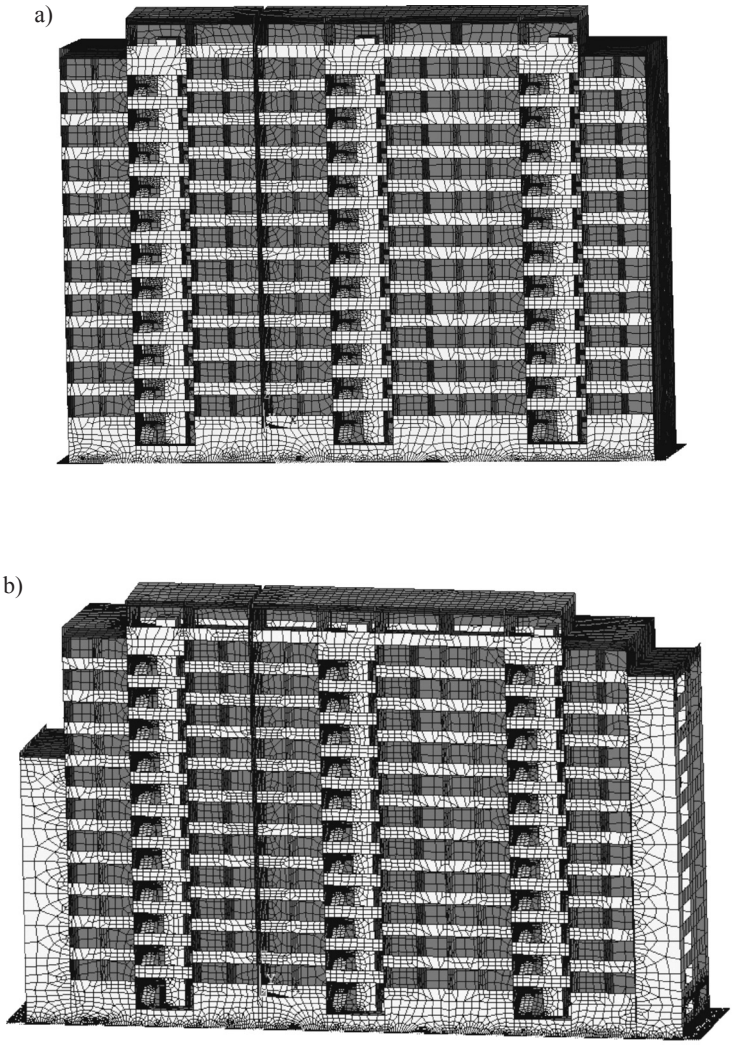

Fig. 4. Finite element models of the analysed structure: a) building “A0”; b) building “A1” [6]

Structural and material assumptions of finite element models of A0 and A1 buildings were verified by comparing the calculated natural frequencies of horizontal vibration with experimental ones obtained for actual structures [10]. Comparisons of the computed and experimental values are presented in Table 2 [6].

Table 1

Material parameters of structural elements [6]

Structure element	E [GPa]	ν	ρ [kg/m^3]
Foundation	23.1	0.2	2500
Basement	23.1	0.2	2500
Prefabricated elements	20	0.2	2500
Reinforced elements	23.1	0.2	2500
Cavity brick wall	0.72	0.25	1400

Table 2

Comparison of computed and experimental values of natural frequencies of building horizontal vibrations before and after modification [6]

Building		Natural frequencies of horizontal building vibrations [Hz]	
		computed	experimental [7]
A0	f_{1x}	1.59	1.60–1.63
	f_{1y}	1.73	1.71–1.76
A1	f_{1x}	1.79	1.64–1.71
	f_{1y}	2.47	2.17–2.28

3. Excitations

Two typical measured records of accelerations of foundation vibrations arising from mining shock in LGC in horizontal direction as a kinematic excitation were taken into consideration. Both of the mining tremors are high-energy, representative for the analysed area and could be dangerous for surface structures. However, they are different in the predominant frequencies band (Fig. 5b, 6b).

The acceleration profiles are presented in Table 3. The time history of component accelerations of vibrations in transverse (x) and longitudinal (y) direction as well as signal of fast Fourier transformation (FFT) is shown in Figure 5 and 6.

Table 3

Parameters of kinematic excitation

Excitation	Energy [J]	Epicentral distance [m]	Seismological coordinates [m]
Acceleration no. 1 (ACC1)	1.6E8	2684	X = 29204, Y = 7846
Acceleration no. 2 (ACC2)	1.3E8	650	X = 30800, Y = 6392

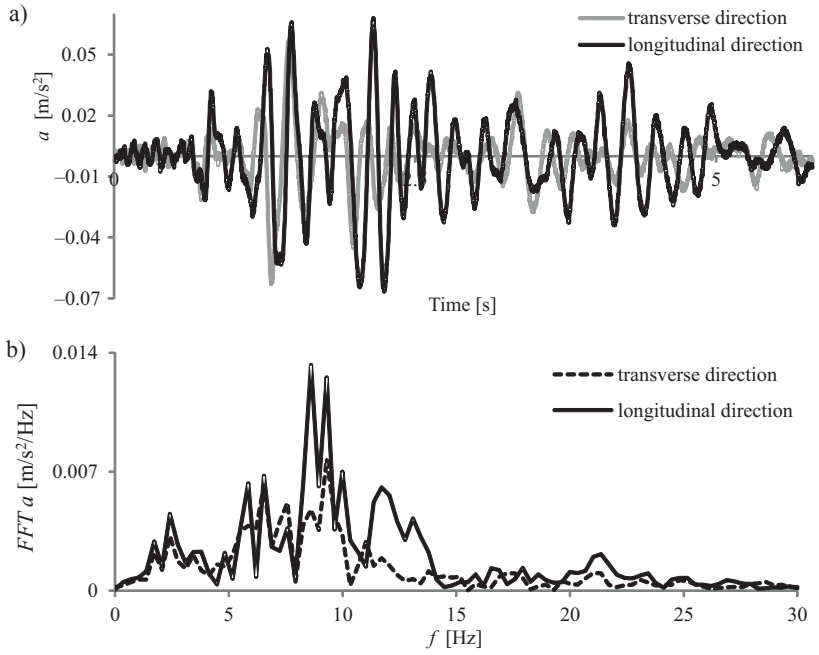

Fig. 5. Acceleration no. 1 of foundation vibrations: a) acceleration record, b) *FFT*

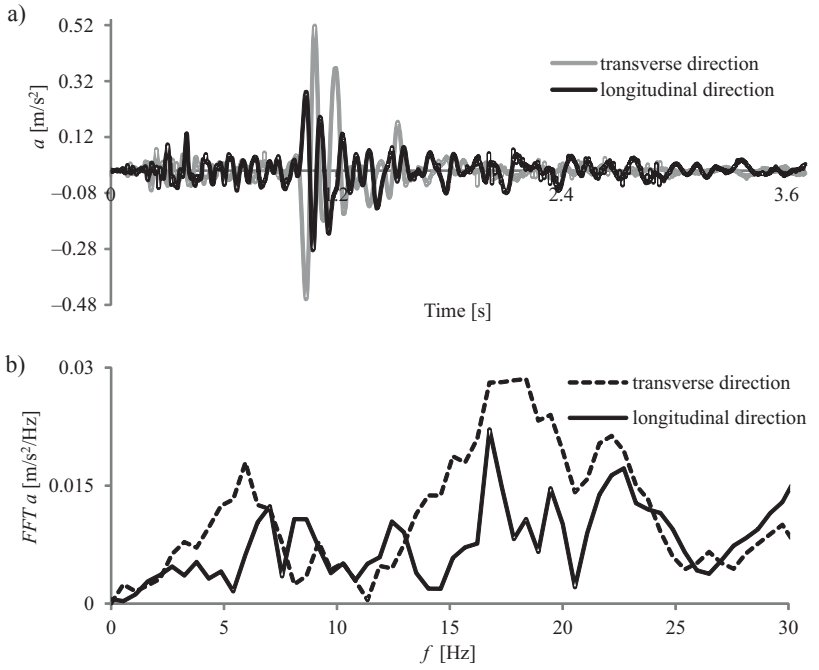

Fig. 6. Acceleration no. 2 of foundation vibrations: a) acceleration record, b) *FFT*

4. Results

Calculations of the dynamic response were carried out in Ansys software using transient analysis. The Newmark algorithm [13] with step 0.002s as well as the Rayleigh damping model [13] were applied. A damping ration equal 2% was taken into consideration [1]. As the kinematic excitation, two simultaneous mutually orthogonal horizontal components of the analysed accelerations of foundations were applied. In the paper, the influence of vertical component of acceleration has been omitted because the vertical inertia forces in typical buildings in the LGC region originating from mining rockbursts are smaller than the weight of these structures. This approach is typical in the case of vibration analysis from mining tremors [11].

The time range of all the calculated dynamic responses corresponds to the time range of the applied excitations.

In Figures 7 and 8, the measured and computed dynamic response of building A1 was compared. Experimental vibrations were registered on the 11th floor.

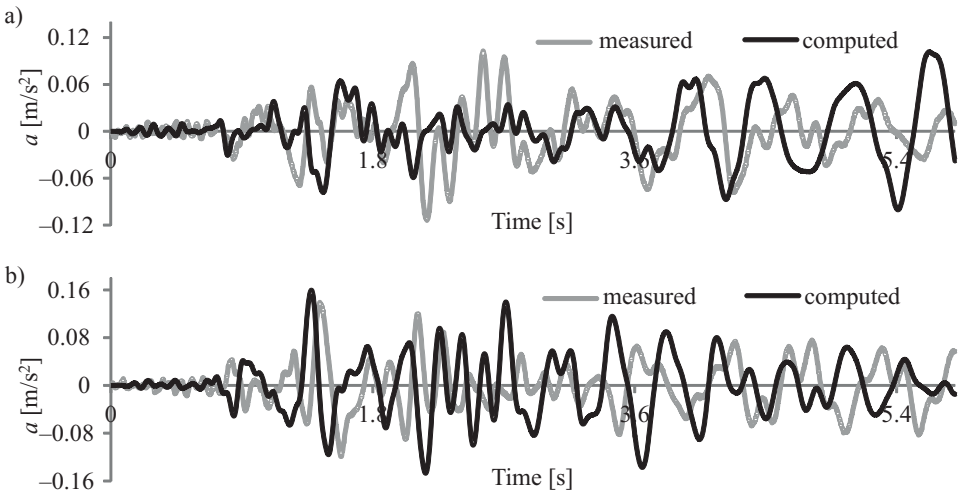

Fig. 7. Comparison of the measured and computed dynamic response of building A1 for excitation ACC1: a) transverse direction, b) longitudinal direction

A comparison of the computed dynamic response of buildings A0 (typical for system WWP) and A1 (reinforced) for excitation ACC1 and ACC2 is presented in figures 9 and 10.

Acceleration data are loaded in point of accelerometer position located on the 11th floor.

For building A1 with inner and exterior structural reinforcements (large structure modification), the difference between the dynamic responses of a typical and modified object is significant. However, the level of acceleration amplitudes' reduction strongly depends on the direction of vibrations.

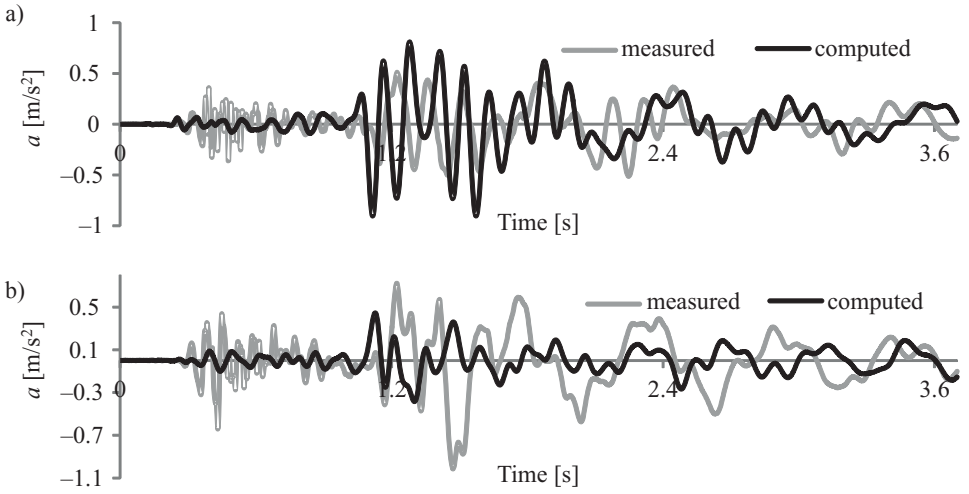

Fig. 8. Comparison of the measured and computed dynamic response of building A1 for excitation ACC2: a) transverse direction, b) longitudinal direction

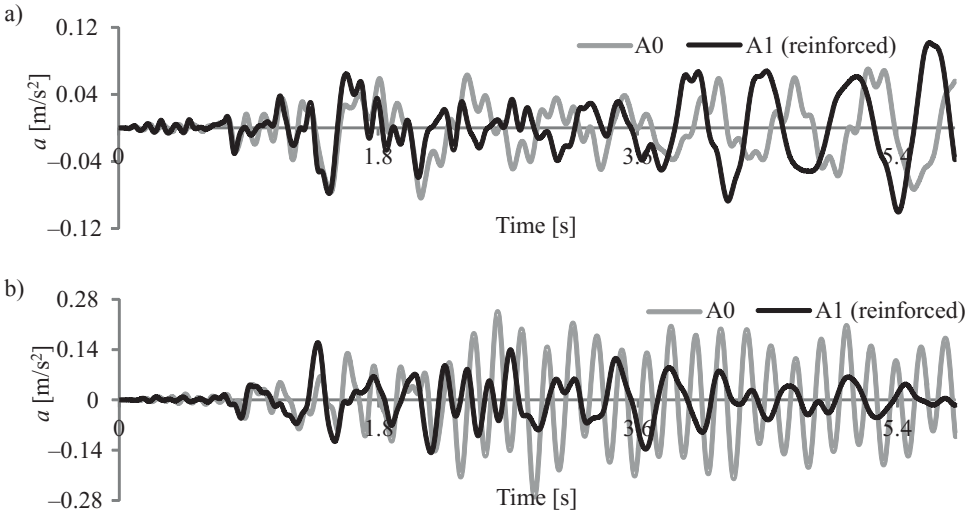

Fig. 9. Comparison of the computed dynamic response of building A0 and A1 for excitation ACC1: a) transverse direction, b) longitudinal direction

In case of the ACC1 excitation, a significant reduction of the amplitude (45% for maximal values of acceleration) is visible for the longitudinal direction of vibration (the main direction of the applied structural reinforcement). For the ACC2 excitation, greater reduction of acceleration amplitudes (28% for maximal values of acceleration) is connected to vibration along the transverse direction.

A comparison of the computed dynamic response of buildings B0 (typical for system WWP) and B1 (reinforced) for excitation ACC1 and ACC2 is presented in Figures 11 and 12.

In case of B1, where only the inner structural reinforcements were applied (small modification), changes of the dynamic response are not as visible as in A1, in spite of the increase of natural frequencies of horizontal vibration between B0 and B1 shown in Table 2.

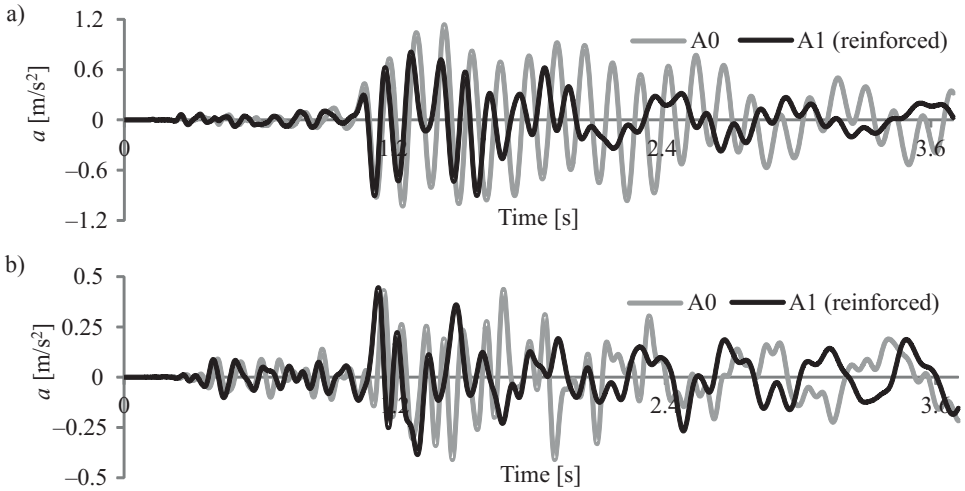

Fig. 10. Comparison of the computed dynamic response of building A0 and A1 for excitation ACC2: a) transverse direction, b) longitudinal direction

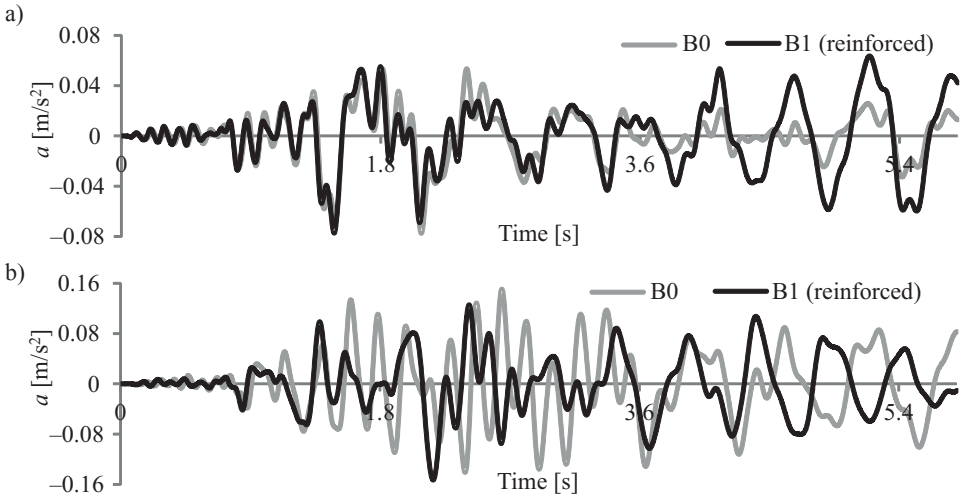

Fig. 11. Comparison of the computed dynamic response of building B0 and B1 for excitation ACC1: a) transverse direction, b) longitudinal direction

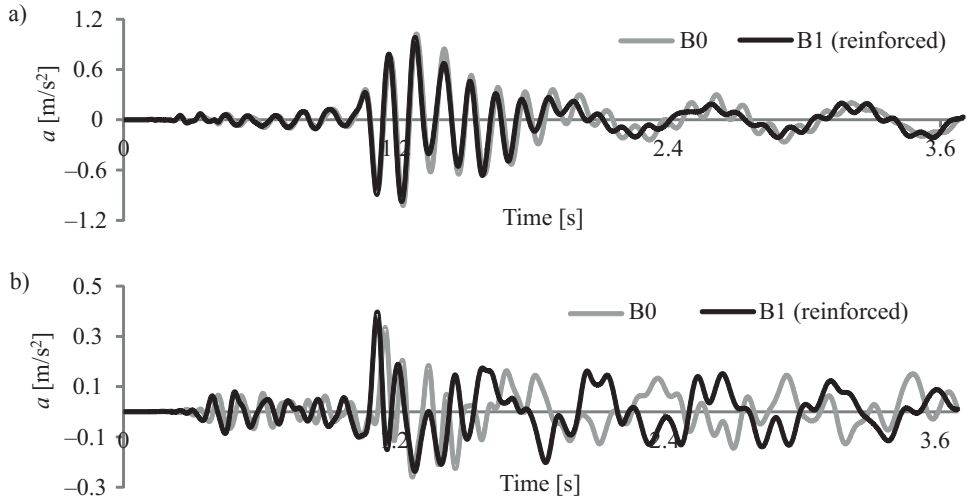

Fig. 12. Comparison of the computed dynamic response of building B0 and B1 for excitation ACC2: a) transverse direction, b) longitudinal direction

5. Conclusions

Calculations of the dynamic response of the analysed buildings show that in case of large modification (inner and outer reinforcement) significant change in the acceleration record (amplitude reduction) is visible.

For a small modification (only inner reinforcement), no amplitude reduction is observed in spite of the increase of natural frequencies of horizontal vibrations.

Despite the good coincidence between measured and computed natural frequencies of vibrations, differences in the dynamic responses are visible. In some cases, they concern both the amplitude as well as phase shift.

References

[1] Ciesielski R., Kuźniar K., Maciąg E., Tatara T., *Damping of vibration in precast buildings with bearing concrete walls*, "Archives of Civil Engineering", 40, 3, 1995, 329–341.

[2] Cholewicki A., Bociąga A., Kotlicki W., *Static analysis of XI-storey external reinforced prefabricated buildings located in Polkowic*e, Warsaw 1982.

[3] Cholewicki A., Szulc J., *Provisioning rules of buildings in designing phase*, eds. J. Kwiatek , Protection of buildings in mining areas, GIG, Katowice 1998, 642–698.

[4] Dzierżewicz Z., Starosolski W., *Precast concrete panel building systems in Poland in the years 1970–1985*, Wolters Kluwer Polska, Warsaw 2010.

[5] Kuźniar K., Maciąg E., Tatara T., *Prediction of Building Foundation Response Spectra from Mining-Induced Vibrations using Neural Networks*, "Mining & Environment", 4(4), 2010, 50–64.
[6] Kuźniar K., Zając M., *Numerical evaluation of vibrations natural frequencies of modified buildings with load-bearing walls*, "Inżynieria i Budownictwo", 2, 2013, 85–89.
[7] Li T., Cai M. F., Cai M., *A review of mining-induced seismicity in China*, "International Journal of Rock Mechanics and Mining Sciences", 44, 2007, 1149–1171.
[8] Lipiński J., Machine foundation, Arkady, Warszawa 1985.
[9] Lovchikov A.V., *Review of the strongest rockbursts and mining-induced earthquakes in Russia*, "Journal of Mining Science", 49, 2013, 572–575.
[10] Maciąg E., Kowalski W., *Estimation of changes of dynamic properties of buildings subjected to mining tremors*, "Folia Scientiarium Universitatis Technicae Resoviensis", Mechanics, 60, 2002, 405–414.
[11] Maciąg E., Kuźniar K, Tatara T., *Response Spectra of Ground Motions and Building Foundation Vibrations Excited by Rockbursts in the LGC Region*, "Earthquake Spectra", Vol. 32(3), 2016, 1769–1791.
[12] Technical Building Design, Structural design of reinforced XI-storey apartment building, Miedziana Street, Polkowice 1989.
[13] Release 11.0 Documentation for Ansys, 2007.
[14] Zembaty Z., *Rockburst induced ground motion – a comparative study*, "Soil Dynamics and Earthquake Engineering", 24, 2004, 11–23.

TECHNICAL TRANSACTIONS | CZASOPISMO TECHNICZNE
CIVIL ENGINEERING | BUDOWNICTWO
3-B/2016

DOI: 10.4467/2353737XCT.16.222.5971

ZBIGNIEW ZEMBATY*, PIOTR BOBRA*, MICHAŁ PAPROTNY**,
ANDRZEJ PÓDA**, CZESŁAW BUBAŁA**, JULIUSZ KUŚ*

A PROCEDURE FOR FORECASTING THE RESULTS OF INDUCED SEISMICITY ON BUILDINGS FOLLOWING EXCEPTIONALLY STRONG MINE TREMORS

PROGNOZOWANIE SKUTKÓW INDUKOWANEJ SEJSMICZNOŚCI DLA ZABUDOWY POWIERZCHNIOWEJ Z UWZGLĘDNIENIEM EFEKTÓW SZCZEGÓLNIE SILNEGO WSTRZĄSU GÓRNICZEGO

Abstract

Sometimes, deep mining introduces particular seismic risk to buildings on the surface; therefore, special procedures are needed to assess the safety limits of ground motion. This paper demonstrates such a procedure for use when the standard approach fails to properly asses intensity. Peak velocity is chosen to measure seismic intensity. Forecasted and past seismicity is compared with structural damage assessments to make a decision allowing safe mining in a given location.

Keywords: mine tremors, structural vibrations, ground motion, induced seismicity

Streszczenie

Zdarza się, że górnictwo podziemne stwarza podwyższone ryzyko sejsmiczne dla obiektów budowlanych, co wymaga specjalnych procedur oceny ograniczeń akceptowalnego ruchu podłoża. Niniejszy artykuł opisuje taką specjalną metodologię, gdy standardowe podejście nie może być zastosowane. Jako miarę sejsmicznej intensywności wybrano prędkość ruchu podłoża. Prognozowana i dotychczasowa sejsmiczność są porównane z uwzględnieniem uszkodzeń budowli w celu umożliwienia bezpiecznej eksploatacji dla zabudowy powierzchniowej.

Słowa kluczowe: wstrząsy górnicze, drgania budowli, ruch podłoża, sejsmiczność indukowana

* Prof. Zbigniew Zembaty, M.Sc. Eng. Piotr Bobra, Ph.D. Eng. Juliusz Kuś, Department of Mechanics and Structural Engineering, Faculty of Civil Engineering and Architecture, Opole University of Technology.

** M.Sc. Eng. Michał Paprotny, M.Sc. Eng. Andrzej Póda, Eng. Czesław Bubała, KWK Wujek S.A., Katowicki Holding Węglowy S.A.

1. Introduction

In addition to the static, surface deformations of mining basins [1], deep mining also introduces substantial seismic risk on the ground surface (see, for example, [2]). The resulting rockbursts are well described in the geophysical literature [2] and respective surface ground motions [5] may lead to structural damage similar to the effects of small earthquakes [6].

The majority of the strong rockbursts are of a moderate magnitude m_L with a value less than around 4; however, some exceed $m_L = 4$ leading to alarming vibrations and structural damages. In the case of South African mines, induced quakes may even reach up to $m_L = 5.3$ [7] with disastrous effects on surface infrastructure (see, for example, photographs of destroyed buildings shown in reference [9]). Such strong seismic risks have prompted research aimed at the adaptation of seismic engineering structural codes into the design of buildings and civil infrastructure [8, 9].

When deep mining is carried out in areas within the city perimeters, a more common type of engineering problem needs to be confronted; this involves the evaluation of the seismic resistance of existing buildings and civil infrastructure. This is a two-stage process:

- forecasting the level of expected surface ground vibrations – this is carried out using geophysical models of mining seismicity and eventually deciding whether to give the 'green light' for the mine to operate below the city [2];
- analysing respective building stock and its I'm not sure what you mean by this phrase, it doesn't seem to make sense, maybe change to 'affected buildings and their' seismic resistance to the expected levels of excitation as well as to the expected static ground deformations [6].

When it comes to assess dynamic effects on buildings, the key role is played by seismic data records gathered by surface seismic networks run by the mine or (sometimes) by the municipal authorities. Geophone sensors are installed directly in the ground in special seismic stations or on the foundations of selected buildings. An interesting account of the methodology used to analyse various types of these records is given in a recent paper by Maciąg, Kuźniar & Tatara [10]. The data acquired using surface seismic networks is used to calibrate the seismological models which forecast the surface effects of future mining [2–4].

To provide an insight into the structural destructiveness of generated ground motion for the purposes of surface protection, special 'scales' were developed by the Central Mining Institute in Katowice. One scale was prepared for the LGOM Copper Basin (Legnicko Głogowski Okręg Miedziowy) [11], and another for the Silesian Coal Basin GOW (Górnośląski Okręg Węglowy) [12]. Both scales are similar, particularly with respect to their two key parameters: horizontal peak ground velocity (PGV) and the duration of strong motion.

In some, exceptional cases, these scales can, however, be exceeded and decisions regarding the suitability of future mine exploitation with respect to building safety requires reconsideration.

The purpose of this paper is to present a methodology for assessing the safety of the building stock exposed to induced ground motion, based on existing seismic records and forecasts of mining activities for the years 2015–2017. The need to reassess seismicity

forecasts and the seismic resistance of civil infrastructure became apparent after a strong rockburst with a magnitude of m_L = 4.2 occurred on April 18th 2015 in Katowice. The paper proposes a unique methodology to reassess the resistance of the buildings which is based on the analyses of the damage from previous quakes and seismic risk forecasts. Using seismic networks of the mine, future horizontal peak ground velocities can be forecasted and compared with the ones associated with the past tremors. This may help to localise places where there are buildings requiring closer examination with respect to their eventual damage and reserves in seismic load capacity.

2. Description of the mine tremors from May 26th 2014 and April 18th 2015

On April 18th 2015, a rockburst of magnitude m_L = 4.2 occurred in the area of activity of the KHW S.A. KWK Wujek – Ruch – Śląsk mining holding. The rockburst resulted in a catastrophic underground failure as described by popular media as well as on the website of the State Mining Authority in Katowice [13]. The energy released during this rockburst was assessed as 4×10^9 Joule. Respective surface ground motion records were obtained using the mine network of acceleration sensors and six of these were analysed in detail (see e.g. [14])

In Fig. 1, the velocity version of GSI_{GZWKW} – *2012* scale is presented. The asterisk shows the value of peak ground velocity and strong motion duration, as obtained from the surface record of the April 18th 2015 rockburst, acquired at the Panewnicka street recording station.

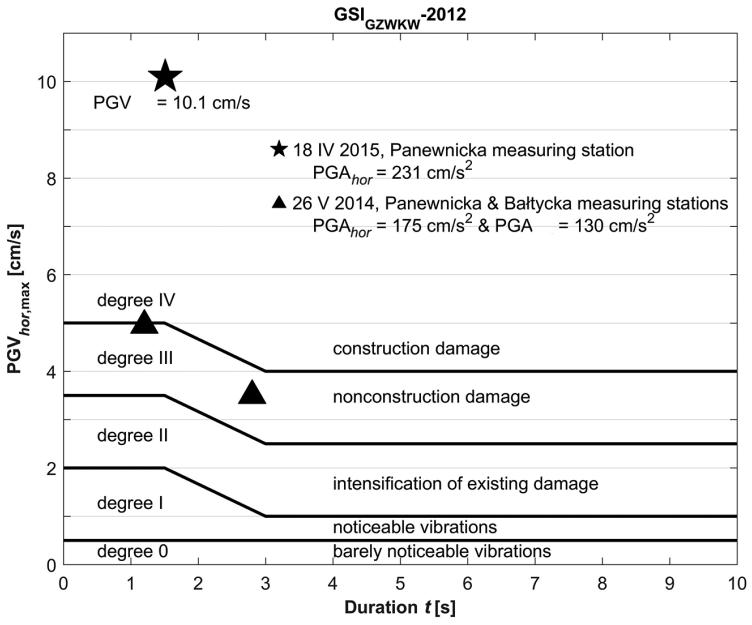

Fig. 1. GSI GZW KW – 2012 scale: Peak Ground Velocity vs. strong motion duration and three records of April 2015 and May 2014 rockbursts

Clearly, the value PGV_{hor} = 10.1 cm/s substantially exceeds the GSI scale. The image of spatial, horizontal ground accelerations is shown in the inset of Fig. 2 while in the upper part of this figure, a plot of horizontal accelerations along the *y* horizontal axis (the more intensive component) is shown together with the respective plot of velocity versus time (lower part). Note that 'hor' (horizontal) version of *PGV* it is its spatial horizontal maximum as obtained for any horizontal vector quantity $U(t) = [U_x(t); U_y(t)]$:

$$Peak_{hor}U(t) = \max\sqrt{\left[U_x(t)^2 + U_y(t)^2\right]}, \quad (1)$$

with U_x and U_y standing for respective two horizontal components of either acceleration, velocity or displacement . The term 'strong motion duration', as applied for the GSI scales, is defined in the next section of this paper.

About one year earlier than the previously mentioned incident, another strong rockburst took place in the same mining area on May 26th 2014. No destructive results were recorded either underground or at surface level in spite of what can still be described as a substantial local magnitude of m_L = 3.7 and an energy release of $E = 8\times10^8$ Joules. Values of PGV_{hor} versus duration are plotted in Fig. 1 as triangles. It can be seen that this time, the maximum values of the GSI scale were not exceeded, although the level of excitation was still very high.

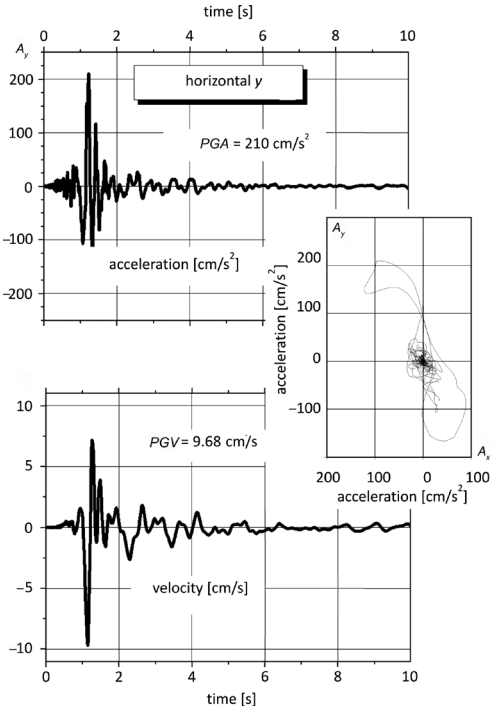

Fig. 2. Accelerations and velocities of the April 18th 2015 rockburst horizontal record as measured along the '*y*' axis of the Panewnicka Street recording station (inset: image of simultaneous spatial, horizontal *x* and *y* accelerations)

3. Surface ground motion of mine tremors and their measures

Surface records of natural earthquakes are characterised by their peak values of acceleration (PGA), velocity (PGV) and displacement (PGD), each value being along one of two horizontal directions, for example, for accelerations PGA_x and PGA_y, and vertical for PGA_z. If one wants the horizontal peak values to be independent of the instrument directions, a spatial maximum should be used according to equation 1. Another important parameter of seismic ground motion is the duration of strong motion. A proposal based on the gradual energy release rate based on the Arias intensity concept [15], defined by Trifunac & Brady [16], is widely accepted and tested [17].

In 2004, the surface ground motions of rockbursts were divided onto two types [5]:

- type I – substantial accelerations, low velocity and short duration resembling quarry blast records;
- type II – moderate accelerations, substantial peak velocity and longer durations, similar to small, shallow earthquakes.

This classification is in good agreement with the seismological classification of rockbursts based on their mechanism [18]. Type II rockbursts are similar to so-called 'regional mine tremors' characteristic of the Silesian coal basin which are usually induced on pre-existing faults by long term mining activities.

Examining the Panewnicka Street record, as shown in Fig. 2, one can note the characteristic pattern of a near surface ground motion which is also characteristic of natural small earthquakes i.e. clear velocity pulse [19], seen in the time record (lower plot) and in the form of well-pronounced directivity, as seen in the spatial plot of accelerations (see the inset of Fig. 2).

Consider the following formulas for time-dependent cumulated Arias intensity defined for vertical and horizontal accelerations [15, 7]:

$$I_A^{hor}(t) = \frac{1}{2}\int_0^t \left[A_x^2(\tau) + A_y^2(\tau) \right] d\tau \tag{2a}$$

$$I_A^{ver}(t) = \frac{1}{2}\int_0^t A_z^2(\tau) d\tau \tag{2b}$$

Plots of normalised Arias intensities, as given by equations (2), are called Husid plots (see, for example, [5]) and are used to calculate strong motion duration [16]. Strong motion duration is defined as a the duration of time between 5% and 95% of cumulative, normalised Arias intensity. In Fig. 3, the Husid plot of the Panewnicka Street station record from Fig. 2 is shown together with the strong motion duration. It can be seen from this plot that the horizontal duration (eq. 2a) equals, in this case, 1.51 seconds. As for the type II tremor, it is of a rather short duration (see e.g. [5]). The Fourier spectrum reveals, however, a clear domination of energy within the bandwidth of 0 to 5Hz (see Fig. 4). From this point of view, this is the classic, low frequency ground motion described in reference [5] as a type II record.

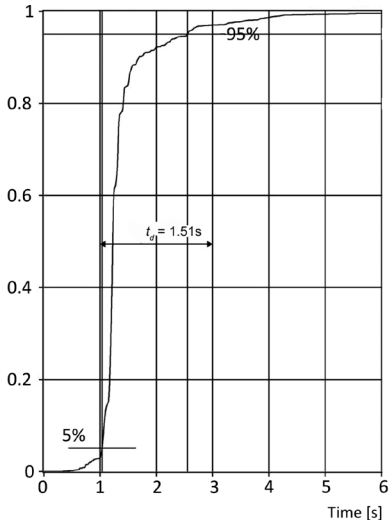

Fig. 3. Normalised Arias intensity versus time (Husid plot) for the Panewnicka Street station horizontal records of April 18th 2015 rockburst (Fig. 2)

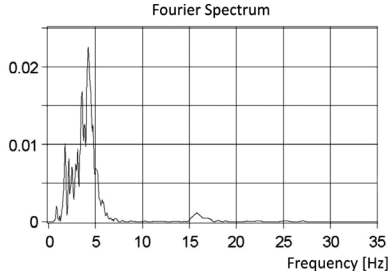

Fig. 4. Fourier spectrum of the acceleration component the Panewnicka Street station horizontal '*y*' record of April 18th 2015 rockburst

4. Re-assessment of seismic risk

The building stock of the Katowice Region belonging to KHW S.A. KWK Wujek – Ruch – Śląsk mining area consists of typical low-rise residential buildings, four ten-story panel buildings, two churches and an industrial plant [14].

Detailed analyses of the damage occurring to buildings on the ground after the rockburst of April 18th 2015 were routinely carried out by the surface protection services of the Mine. They revealed that all of the detected damage only fitted the category of 'cosmetic' or non-structural damage. Similar, or even lesser, post-tremor damage was noted after the rockburst of May 26th 2014. Moreover, the GSI scale classifies the rockburst of May 26th 2014 as belonging to degree III (see Fig. 1).

During these two events, the buildings were subjected to horizontal ground velocities reaching 10 cm/s in some places. Thus, a key observation is noted that **the two events may**

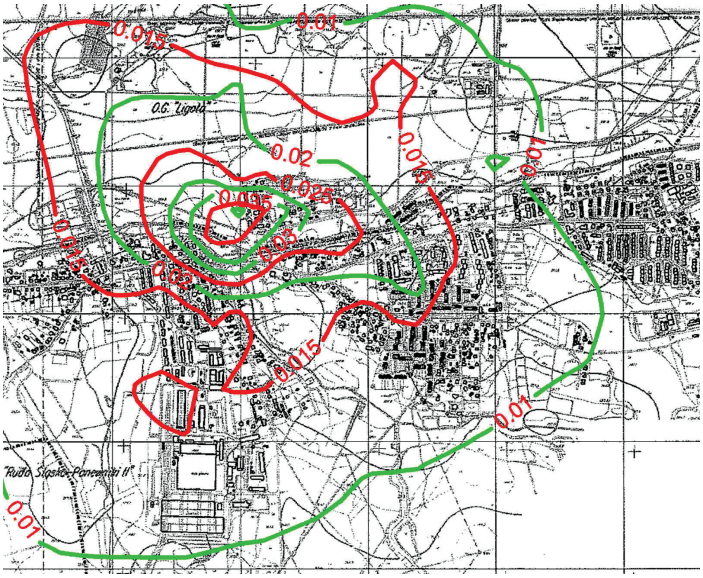

Fig. 5. Map of the Wujek – Ruch – Śląsk mining area marked with areas of expected maxima of horizontal velocities [m/s] forecasted for the years 2015–2017

serve as real-life seismic tests of the resistance of the existing building stock to mine tremor effects.

The Wujek – Ruch – Śląsk mine prepared exploitation plans for the years 2015–2017 in a new coal bed (no. 409). In the light of the recent two strong rockbursts, a question was formulated regarding the safety of the surface infrastructure and building stock during the planned exploitation. For these reasons, new forecasts of mining seismicity for the years 2015–2017, was undertaken by the Central Mining Institute. The results of these forecasts were given as maps of maximum peak horizontal velocities expected until the end of 2017. In Fig. 5, a section of such a map is presented. This map was compared with another map presenting horizontal ground velocities of the two rockbursts obtained by the Central Mining Institute when analysing ground motion records of the two rockbursts of 2014 and 2015. Overlapping these three maps gave an answer to the question if expected seismic intensity does not exceed the past seismicity so far safely sustained by the buildings. Since horizontal peak ground velocity is "most appropriate" single measure of destructiveness of the seismic excitation effects on buildings so far (see, for example, [5, 6, 8, 9, 11, 12, 17]), a procedure can be established which allows the exploitation of the underground mine if the area was already subjected to excitations from rockbursts leading only to minor, 'cosmetic' damage when peak horizontal velocity levels do not exceed the earlier measured PGV_{hor}.

5. Concluding remarks

This paper presents an analysis of an exceptionally strong mine tremor of April 18th, 2015, its strongest record and respective surface effects. A decision making procedure is described how to decide whether to allow safe deep mining exploitation with respect to the safety of surface infrastructure and building stock in terms of its dynamic response. The procedure consists of following three stages:

a) analyse existing rockbursts and provide maps of generated horizontal peak ground velocities and their effects on buildings;
b) prepare a map of forecasted mining seismicity in terms of the peak ground horizontal velocity using well-established methodology of mining seismology described in detail in, for example, references [3, 4];
c) localise eventual places where the expected future peak ground velocities exceed what the building stock already carried on;
d) decide if the resistance of the building stock to past seismicity makes it possible to allow deep mining exploitation.

The authors acknowledge the financial support of this research from *Katowicki Holding Węglowy* and the seismicity analyses and forecasts provided by the *Central Mining Institute* (see report [14] for details).

References

[1] Malinowska A, Hejmanowski R., *Building damage risk assessment on mining terrains in Poland with GIS application*, International Journal of Rock Mechanics and Mining Sciences, Vol. 47, 2010, 238–245.

[2] Gibowicz S.J., Kijko A., *An introduction to mining seismology*, Academic Press, San Diego 1994.

[3] Mutke G., Dworak J., *Czynniki warunkujące efekt sejsmiczny wstrząsów górniczych na powierzchniowe obiekty budowlane w obszarze GZW*, Publications of Institute of Geophysics of Polish Academy of Sciences, Vol. 245, M-16, 1992.

[4] Mutke G., Stec K. *Seismicity in the Upper Silesian Coal Basin, Poland: Strong regional seismic events*, Proc. 4th Int. Symp. – Rockbursts and Seismicity in Mines, (eds. Gibowicz S.J. and Lasocki S.), Rotterdam – A.A. Balkema, 1997, 213–217.

[5] Zembaty Z., *Rockburst induced ground motion – a comparative study*, Soil Dynamics and Earthquake Engineering, Vol. 24, 2004, 11–23.

[6] Tatara T., *Dynamic resistance of building objects under mine tremors (in Polish: Odporność dynamiczna obiektów budowlanych w warunkach wstrząsów górniczych)*, Politechnika Krakowska, Kraków 2012

[7] McGarr A., Bicknell J., Sembera E., Green R.W.E., *Analysis of exceptionally large tremors in two gold mining districts of South Africa*, Pure and Applied Geophysics, Vol. 129, 1989, 295–307.

[8] Zembaty Z., *How to model rockburst seismic loads for civil engineering purposes?* Bulletin of Earthquake Engineering, Vol. 9, 2011, 1403–1416.

[9] Zembaty Z., Kokot S., Bozzoni F., Scandella L., Lai C.G., Kus J., Bobra P., *A system to mitigate deep mine tremor effects in the design of civil infrastructure*, International Journal of Rock Mechanics and Mining Sciences, Vol. 74, 2015, 81–90.

[10] Maciag E., Kuzniar K., Tatara T., *Response Spectra of the Ground Motion and Building Foundation Vibrations Excited by Rockbursts in the LGC Region*, Earthquake Spectra, 2016.

[11] Dubiński J., Jaśkiewicz K., Lurka A., Mutke G., *Górnicza skala intensywności sejsmicznej GSI-2004/11 dla wstrząsów górniczych*, KGHM Polska Miedź S.A., Lubin 2012.

[12] Dubiński J., Mutke G., Tatara T., Muszyński L., Barański A., Kowal T., *Zasady stosowania zweryfikowanej Górniczej Skali Intensywności drgań GSI GZWKW-2012 do prognozy i oceny skutków oddziaływania wstrząsów indukowanych eksploatacją złóż węgla kamiennego w zakładach górniczych Kompanii Węglowej S.A. na obiekty budowlane i na ludzi*, Główny Instytut Górnictwa, Katowice 2012.

[13] State Mining Authority News, Katowice, 30th April, 2015, http://www.wug.gov.pl/o_nas/wiadomosci_wug/Eksperci-o-nietypowym-wstrzasie-w-KWK-Wujek-Ruch-Slask/idn:2204 (access: 9.02.2016).

[14] Zembaty Z., Mutke G., Stec K., Lurka A., Bobra P., Kuś J., *Assesment of dynamic effects on surface building stock based on forecasted seismicity from planned deep mining at coal bed 409 during years 2015–2017, (in Polish: Ocena wpływów dynamicznych planowanej eksploatacji górniczej w pokładzie 409 w latach 2015–2017 na powierzchniową zabudowę kubaturową na podstawie prognozowanej sejsmiczności)*, report: Politechnika Opolska, Główny Instytut Górnictwa, Opole–Katowice, August 2015, 1–109.

[15] Arias A. *A measure of earthquake intensity.* In: Hansen RI, editor. Seismic design of nuclear power plants, Cambridge, MA: MIT Press, 1970.

[16] Trifunac MD, Brady AG., *A study on the duration of strong earthquake ground motion*, B. Seismol. Soc. Am. 1975; 65: 581–626.

[17] Zembaty Z., *A note on non-stationary stochastic response and strong motion duration*, Earthquake Eng. Struc., 1988, 16: 1189-1200.

[18] Johnston J.C., *Rockbursts from a global perspective*, [in:] Knoll P, editor, *Induced seismicity*, Rotterdam, Brookfield: Balkema 1992, 63–78.

[19] Makris N., Black C.J., *Evaluation of peak ground velocity as a 'good' intensity measure for nearsource ground motions*, Journal of Engineering Mechanics, ASCE, Vol. 130, No. 9, 2004, 1032–1044.

TECHNICAL TRANSACTIONS | CZASOPISMO TECHNICZNE
CIVIL ENGINEERING | BUDOWNICTWO
3-B/2016
DOI: 10.4467/2353737XCT.16.223.5972

TERESA ZYCH*, WOJCIECH KRASODOMSKI*

POLYOLEFIN FIBRES USED IN CEMENTITIOUS COMPOSITES – MANUFACTURING, PROPERTIES AND APPLICATION

WŁÓKNA POLIOLEFINOWE STOSOWANE W KOMPOZYTACH CEMENTOWYCH – METODY WYTWARZANIA, WŁAŚCIWOŚCI I ZASTOSOWANIE

Abstract

This paper presents the manufacturing and properties of three types of polyolefin fibres: monofilament and fibrillated polypropylene microfibres and macro-synthetic (PP/PE) fibres – today, besides steel and glass fibres, these are the most widely used fibrous reinforcement of cement composites. Different types of fibres result from various methods of improving the low modulus of elasticity and poor adhesion of PP fibres (chemically inert) to the cement matrix. These methods are also described in the paper.

Keywords: polypropylene fibres, polyolefin fibres, macro-synthetic fibres, fibre reinforced cementitious composites, fibre-matrix bond strength

Streszczenie

W artykule przedstawiono metody wytwarzania i właściwości trzech rodzajów włókien poliolefinowych: mikrowłókien polipropylenowych elementarnych (przędzy) i fibrylowanych oraz makrowłókien syntetycznych (PP/PE), stosowanych obecnie najczęściej (obok włókien stalowych i szklanych) jako zbrojenie włókniste kompozytów cementowych. Występowanie kilku typów włókien wynika z różnych metod polepszania niskiego modułu sprężystości i słabej przyczepności włókien polipropylenowych (chemicznie obojętnych) do matrycy cementowej. Metody te także opisano w artykule.

Słowa kluczowe: włókna polipropylenowe, włókna poliolefinowe, makrowłókna syntetyczne, fibrokompozyty cementowe, wytrzymałość połączenia włókno-matryca

* Ph.D. Eng. Teresa Zych, Institute of Building Materials and Structures, Faculty of Civil Engineering, Cracow University of Technology.

** Ph.D. Wojciech Krasodomski, Department of Additives and New Chemical Technologies, Oil and Gas Institute – National Research Institute.

1. Introduction

Polyolefin fibres, like steel and glass fibres, are commonly used today to reinforce cementitious materials. Fibres made from **polyolefins**: polypropylene and polyethylene (Fig. 1) are the most popular polymer (synthetic) fibres for concrete. Polyolefins, along with other polymers from which fibres are produced, such as 'polyester, nylon, PVA, polyacrylic, aramids and blends of them', are listed in the standard EN 14889-2 'Fibres for concrete – Part 2: Polymer fibres' [35].

At present, there are three types of polyolefin fibres (polypropylene-based fibres) available:

- two types made from **polypropylene**, different in shape: **monofilament microfibres (**monofilaments) – individual extruded fibres, cut from a yarn (bundles of several fibres) and **fibrillated** (net-shaped) **microfibres** – cut from an extruded sheet (tape), both covered with a special surface finish,
- one type made from **polypropylene** and **polyethylene***:* **macro-synthetic fibres** (bi-component macrofibres) (individual extruded fibres).

Hence, polyolefin fibres represent all classes of fibres specified in the standard EN 14889-2 for polymer fibres [35]:

- class Ia fibres – microfibres having a diameter less than 0.3 mm, mono-filamented;
- class Ib fibres – microfibres having a diameter less than 0.3 mm, fibrillated;
- class II fibres – macrofibres having a diameter larger than 0.3 mm.

Class II fibres are distinguished as structural fibres, which affects the load-bearing capacity of the fibre reinforced concrete element – 'class II fibres are generally used where an increase in residual flexural strength is required' [35].

These three types of polyolefin fibres offered today have been obtained through the reduction of typical drawbacks of the first produced monofilament polypropylene fibres – specifically, the **low modulus of elasticity** of the fibres and **poor bonding** of the fibres with the cement matrix. Monofilament polypropylene fibres, first used as the fibrous reinforcement of cementitious composites by Goldfein a few decades ago (in the 1960s) [12], have been further improved. The changes in the **material**, surface (**texture**) and **shape** of fibres, introduced over the years to provide better mechanical properties and durability of polypropylene fibre reinforced cement composites (PFRC), are described in this paper. The experimental studies concerning PFRC are still carried out by research centres and universities. The paper contains up-to-date information on polypropylene microfibres and high-performance macro-synthetic fibres (their manufacturing, properties and the range of application).

2. Polypropylene-based fibres versus other types of polymer fibres

Polypropylene-based fibres: polypropylene microfibres (monofilaments and fibrillated fibres) and polyolefin macrofibres (also known as macro-synthetic fibres or bi-component macrofibres), used today as the reinforcement of cementitious composites, are characterised by Young's modulus of 2–10 GPa. Microfibres, having a modulus of elasticity in the range of 2–5 GPa, belong to the group of low-modulus polypropylene fibres whereas macrofibres are

high-modulus polypropylene fibres (5–10 GPa). However, Young's modulus for both types of polypropylene fibres is still not higher than that for the cement matrix (10–40 GPa) [4, 10]. The tensile strength is in the range 150–500 MPa for polypropylene microfibres and 470–690 MPa for polyolefin macrofibres. These mechanical parameters are lower than for other types of polymer fibres (Table 1).

Table 1

Properties of fibres [3, 4, 6, 7, 10, 11, 18, 40–56, 59–62]

Type	Density (specific gravity) [kg/dm^3]	Diameter or thickness [μm]	Length [mm]	Modulus of elasticity [GPa]	Tensile strength [MPa]	Failure strain [%]
Monofilament polypropylene microfibres	0.90–0.91	15–50	6–20	2–4	150–400	–
Fibrillated (chopped film) polypropylene microfibres		30–100	6–51	~5	300–500	10
Polyolefin (polypropylene/ polyethylene) macrofibres	0.91–0.97	~800–1100	30–65	5–10 (embossed fibres: 8–10)	470–690 (embossed fibres: 550–690)	15–25
Polyethylene HD filament	0.96	900	3–5	5	200	–
Polyethylene HD high-modulus	0.96	20–50	continuous	10–30	>400	>4
Polyacrylonitrile (PAN)	1.16	13–100	6	17–20	900–1000	8–11
Polyvinyl alcohol (PVA)	1.3	3–15	2–12	12–40	700–1500	2–6
Aramid (aromatic polyamide)	1.20–1.45	10–15	5-continuous	70–130	2900–3500	1.8–5.0
Steel	7.85	100–1000	30–60	210	500–2000	0.5–3.5
Carbon	1.16–1.95	7–18	3-continuous	30–390	600–2700	0.5–2.4
Basalt	2.6–2.8	9–24	5–50	85–90	1700–4800	2.5–3.1
Glass AR (alkali resistant)	2.6–2.7	12–20	10–50	70–80	600–2500	1.5–4.5
Asbestos	2.6	0.02–30	5–40	160	200–3500	2–3
Cement paste	2.0–2.2	–	–	10–40	3–6	–

Aramid (aromatic polyamide) fibres, the strongest polymer fibres, are characterised by the modulus of elasticity of 70–130 GPa and the tensile strength of ~3000 MPa. Other polymer fibres have the following mechanical properties (Young's modulus and tensile strength, respectively): 12–40 GPa and 700–1500 MPa for **polyvinyl alcohol** (PVA) fibres; 17–20 GPa and 900–1000 MPa for **polyacrylonitrile** (PAN) fibres; 4–8 GPa and 300–900 MPa for **nylon** (polyamide) fibres; 1–5 GPa and 400–1100 MPa for **polyester** fibres; 10–30 GPa and above 400 MPa for **high-modulus** HD (high density) **polyethylene** fibres; and 5 GPa and 200 MPa for HD **polyethylene** fibres (by comparison, the values of Young's modulus and the tensile strength for **steel** fibres are as follows: 210 GPa and 500–2000 MPa, respectively) [6, 10, 18, 53, 55].

Such large differences in the modulus of elasticity and the tensile strength between polymer fibres result from both the variety of material (polymer) and the varied methods used to manufacture the fibres.

Polymer fibres are produced through the process of extrusion and spinning [10, 18, 21]. At the beginning, the raw polymer is transformed from solid to liquid. Depending on the type of polymer, this transformation is achieved either by dissolving or melting. Synthetic polymers (**aramid**, **vinyl** and **acrylic** polymers) are dissolved in a suitable solvent whereas **polyolefin** (polyethylene, polypropylene), **nylon** and **polyester** polymers are transformed into molten liquid. A spinneret consisting of many holes is used to extend the liquid polymer, which then solidifies into continuous filaments (Fig. 1). After spinning, the filaments undergo further extension in the longitudinal axis (drawing process) increasing the level of orientation of molecular chains within the filament structure. By aligning (orienting along one direction) the molecular chains, high-strength and high-modulus fibres can be produced. In the manufacturing process, the technological factors (the speed of attenuation, the melting point, cooling time and many other factors) are strictly controlled since small deviations lead to significant changes in the basic properties of the fibres, and thus, in their performance characteristics.

The method of spinning (gel, wet, dry and melt spinning) and the type of drawing (hot and cold drawing) depends on the type of fibres [18, 21].

For solute polymers, three types of spinning are used. These are gel, wet and dry spinning. **Aramid** and **PVA** fibres are manufactured by gel spinning whereas **acrylic** fibres are produced by both wet and dry spinning. Melt spinning is used to obtain **polyolefin**, **nylon** and **polyester** fibres.

In **gel spinning**, the polymer chains (in the polymer solution) are not completely separated into a totally liquid state but are bound together locally to form so-called 'liquid crystals' – this results in strong inter-chain forces in the extruded filaments. During the extrusion process the liquid crystals are aligned along the fibre axis (by the shear forces). The high degree of orientation of polymer chains is achieved through this method, which allows the obtaining of stiff and strong fibres. Gel spinning is also described as dry-wet spinning since the filaments first pass through the air and are then cooled in a liquid bath [18]. This method of spinning is also used to manufacture **high-modulus polyethylene** fibres (in this case, a precisely heated gel of polymer is extruded through a spinneret).

In the case of **wet spinning**, the polymer solution is forced (by a spinning pump) through the spinneret, which is submerged in a chemical bath and the polymer precipitates in the

chemical bath (the polymer solution is converted to a gelatinous state and finally to a solid state) due to the action of diffusion processes. Regarding **dry spinning**, instead of precipitating the polymer by chemical reactions, the solidification of filaments is achieved by evaporating the solvent in a stream of air or inert gas.

In **melt spinning**, a spinning pump forces the molten polymer (not the polymer solution as in wet spinning) through the spinneret to form the filaments which are then solidified by air-cooling (see Fig. 1 and Sections 3.1, 4.1, 5.1).

The filaments are then subjected to the process of drawing, which is very important for improving their mechanical properties. Depending on the surrounding temperature during the process, there are two types of drawing. These are hot and cold drawing. High performance fibres require a high temperature during drawing, for example over 400°C for aramid fibres (**hot drawing**), whereas polypropylene fibres, nylon fibres, etc. are drawn without applying external heat or at a temperature no greater than about 70°C (**cold drawing**) [10, 21, 40].

As the result of the advanced processes described above, fibres that can provide effective reinforcement for cementitious composites are obtained. Nevertheless, due to expensive manufacturing methods (such as gel spinning and heat drawing), the **price** of high performance fibres (aramid fibres, PVA fibres, PAN fibres) with **aligned chain microstructures** is currently too high for their common use in cement composites [10]. All high performance fibres have been investigated for use in fibre reinforced composites but only PVA fibres are applied at present. Aramid fibres are used as the efficient reinforcement of FRP (fibre reinforced polymers [plastics]). Polyacrylonitrile (PAN) is a raw material used in the production of carbon fibres, the most popular reinforcement of fibre reinforced polymers. However, despite their high price, **polyvinyl alcohol** (PVA) fibres are used as the reinforcement of cement composites (e.g. bendable concrete, known also as Engineered Cementitious Composite [ECC]), because in addition to their relatively high modulus of elasticity and tensile strength (12–40 GPa, 700–1500 MPa, respectively), they are characterised by their strong chemical bond with the surrounding cement matrix due to their hydrophilic nature [10, 24].

As regards the application of other polymer fibres as the reinforcement of cementitious composites, only polypropylene-based fibres are commonly used.

Acrylic and **polyester** fibres are not stable in the high pH environment of most cement-based matrices and are thus unsuitable for cementitious materials.

The mechanical properties of **nylon** fibres are comparable to those of polypropylene fibres (see Table 1). There is some interest in using nylon fibres as a replacement for polypropylene fibres but its commercial use is not widespread [53, 55].

Polypropylene fibres have a number of advantages and also some weak points. Comparing their non-mechanical properties with **steel** fibres (the most popular non-polymer fibrous reinforcement of concrete), they are cheaper and lighter (density of about 0.9 kg/dm^3 for polypropylene fibres compared with 7.85 kg/dm^3 for steel fibres) (Table 1). Since polypropylene fibres are **chemically inert**, their durability in corrosive environments is excellent. Polypropylene fibres are **non-rusting**, unlike steel fibres which may corrode in cracked concrete. They are unaffected by both alkalis found in cementitious composites and acids and salts [4, 10, 41, 42, 51]. Polypropylene fibres are **not metallic** – this property is vital in, for example, hospital rooms with specialized devices that require non-metallic environments in which to function [41, 51, 61].

Despite the benefits mentioned above, polypropylene fibres also have some disadvantages. Apart from the low modulus of elasticity (stiffness) and the tensile strength, they are susceptible to **degradation by ultraviolet** (UV) **radiation** (sunlight), but the concrete matrix efficiently protects them [15]. The **melting point** of polypropylene fibres is around 165°C, which is relatively low compared with other fibre types (e.g. 220°C for PVA and nylon fibres, 260°C for polyester fibres, ~1500°C for steel fibres [18]). This may be a limitation in certain processes such as autoclaving. Polypropylene fibres are **hydrophobic**, thus, the bond with the cement matrix needs to be improved. Polypropylene fibres are **prone to creep** (have a tendency towards time-dependent deformation under constant load) as they are non-crosslinked thermoplastic polymer fibres [3, 10, 31].

Three types of polypropylene-based fibres which are different in composition, size and geometry are presented below. These are monofilament polypropylene microfibres, fibrillated polypropylene microfibres and macro-synthetic fibres. The manufacturing process, structure, properties and fields of application of these fibres are described in Chapters 3, 4 and 5.

3. Monofilament polypropylene microfibres

Monofilament polypropylene fibres have been applied as concrete reinforcement since the 1960s [12]. In the 1970s, large research programmes were started to test the properties of cementitious composites with polypropylene fibres (used as the replacement of asbestos fibres) (Zonsveld J.J., 1975; Walton P.L. & Majumdar A.J., 1975; Hannant D.J., 1980 [4]). Monofilaments have been one of the popular fibrous reinforcements of concrete for more than 40 years.

3.1. Manufacturing of monofilament polypropylene microfibres

Monofilament polypropylene fibres are manufactured from 100% virgin, isotactic polypropylene (homopolymer). A **monofilament** is any single filament (known also as fibril or elementary fibre) which is spun individually. A **multifilament** is a yarn consisting of a group of monofilaments [6]. Monofilaments (fibrils) are produced through **melt spinning** (Fig. 1) [4, 10, 21]. This is an **extrusion process**, used for polypropylene and other thermoplastic polymers that can be melted (e.g. nylon, polyester).

The process of manufacturing consists of many stages (Fig. 1). At the beginning, polypropylene is converted into a liquid state and extruded through the orifices of a spinneret to form continuous filaments. The filaments are then solidified by cooling (e.g. in a blast of cold air). After the application of a special finish, the filaments are drawn in-line to several times their original length in order to improve the stress-strain characteristics of the fibres. By orientation of the molecular structure of the polymer in one direction (the alignment of the long polymer chains along the longitudinal axis of the fibre), high-strength and high-modulus organic fibres can be produced [10]. The degree of the alignment of the polymer molecules affects the properties of the fibres. The closer the molecules are packed together, the greater the strength properties of the fibre [21]. The fibre modulus of elasticity can

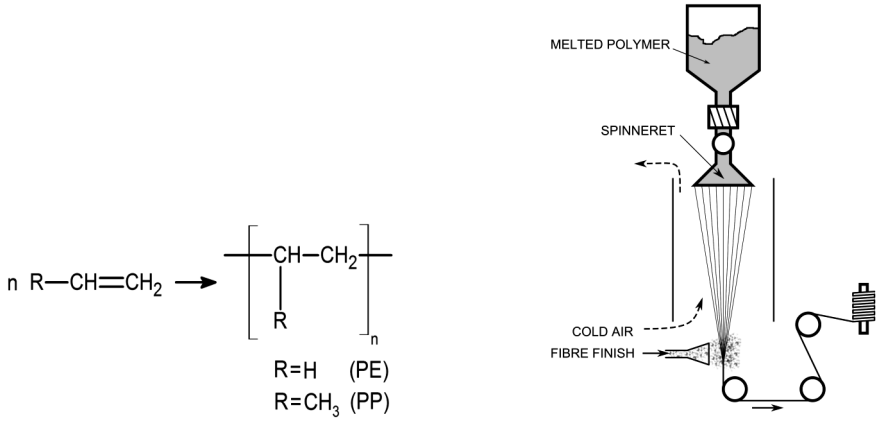

Fig. 1. Polyolefins (polyethylene – PE, polypropylene – PP); Melt spinning process [21, 59]

change in this process from around 2 GPa to 5 GPa or more [10]. The final stage is cutting the bundles (collected filaments) to the desired length.

The special fibre finish (coating), applied on the surface of the fibres, increases the wettability of fibres, enlarges the surface of fibres to improve the interfacial fibre–cement matrix bond and facilitates the dispersion of fibres in the cement paste [39].

3.2. Properties of monofilament polypropylene microfibres

The filaments (which are called staples after cutting) have different **lengths**. Monofilament fibres are available in the lengths of 3, 6, 12, 13, 18, 19 and 20 mm [40, 43, 47, 53, 55] (6 mm and 12 mm – long fibres are the most commonly used [42, 46, 51, 54, 61]) (Table 1). They are usually round in cross-section, ranging in **diameter** from 15 μm to 50 μm (usually 18, 32 and 38 μm [43, 47, 51, 54, 61]) (Fig. 2).

Due to their finefilament nature, hair-like monofilaments are virtually undetectable on the surface finish of concrete [53]. They are widely used in aesthetically demanding concrete elements.

They are characterised by the **tensile strength** of 150–300 MPa (300–400 MPa for fibres providing the fire resistance of concrete [43, 47]) and **Young's modulus** of ~2–4 GPa [43] (Table 1).

Monofilament polypropylene microfibres are recommended as the secondary reinforcement to reduce **plastic shrinkage cracking in early-age concrete** [4, 6, 7, 10, 41–43, 47, 51, 53, 55, 61]. In young concrete, when its strength and stiffness are developed (the compressive strength of concrete is of the order of 3 MPa, the tensile strength is only 0.3 MPa and the modulus of elasticity is less than 5 GPa), the fibres, having higher Young's modulus than the base material (cement matrix), may reinforce concrete [17]. Monofilaments do not provide improvements to the properties of hardened concrete (e.g. in a concrete pavement), due to the low modulus of elasticity (2–4 GPa) when compared with concrete (30 GPa) and steel fibres (210 GPa) (tensile strength: 150–400 MPa for polypropylene fibres, 700–2000 MPa for steel fibres). They can be applied as the replacement for steel mesh.

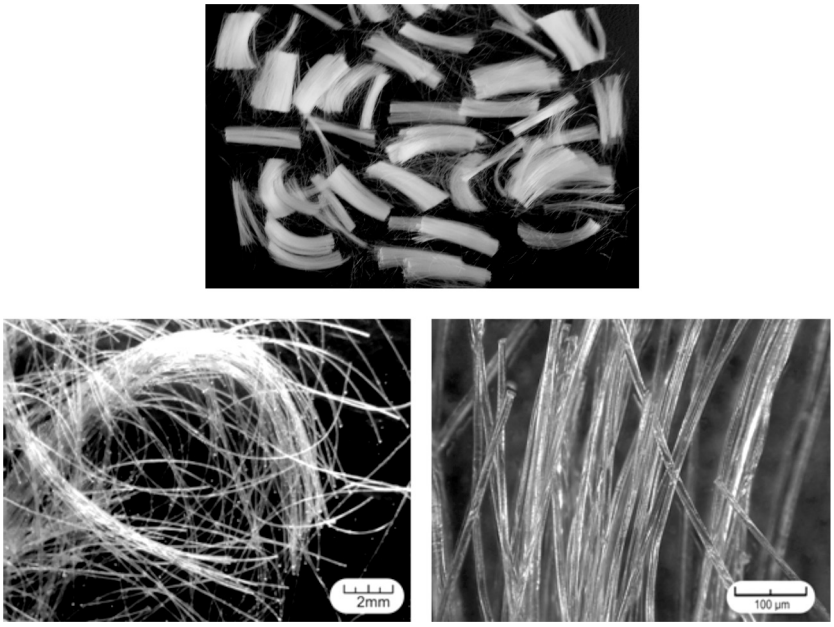

Fig. 2. Monofilament polypropylene fibres (10x, 200x) [51, 61]

Monofilament polypropylene fibres are added into concrete to increase its **fire resistance** (e.g. in tunnels) [4, 6, 10, 16]. The fibres protect concrete against **explosive spalling** (a rapid break-away of concrete fragments at very high temperatures, leading to the unveiling of the steel reinforcement and consequently, the loss of load-bearing capacity of the reinforced concrete element). High-performance concretes especially have a tendency to exhibit explosive behaviour under fire conditions. Spalling results from the high pressure of steam in the pores of concrete and, therefore, thermal stresses. At fire temperatures, the transformation of water (contained in damp concrete) into steam occurs. Steam which cannot escape causes high levels of internal pressure in concrete. A network of open pores (channels), formed after the melting of polypropylene fibres at a temperature of around 165°C, allows water vapour to escape so that the pressure of steam decreases and the internal stresses do not exceed the value at which the explosive destruction of concrete appears [4, 42, 45]. Fibres that are effective in reducing explosive spalling are very fine monofilament polypropylene fibres (18µm in diameter, 6mm long [43, 44, 46, 47]), used at the dosage of 1–3 kg/m^3 (with a modulus of elasticity of 2.3–3.9 GPa and the tensile strength of 300–400 MPa). Due to their dimensions and the extremely high number of fibres per cubic meter (more than 700 million per kg and typically also per cubic meter) [41, 43, 45, 47, 51], the fibres significantly increase the concrete durability in instances of fire. They are usually used in sprayed and precast concrete, e.g. in the lining of tunnels [45].

The **hybrid systems** of monofilament polypropylene microfibres and steel fibres (or fibrillated polypropylene fibres and steel fibres, or two different types of polypropylene fibres) are offered by manufacturers [51, 53, 61]. Blends of polypropylene and steel fibres

are used in order to combine the following benefits of both products: resistance to explosive spalling, improvements regarding plastic shrinkage provided by polymer fibres and structural improvements provided by steel fibres [6].

3.3. Application of monofilament polypropylene microfibres

Monofilaments are applied at the amount of 0.9–2 kg/m^3 [47] (usually 0.9 kg/m^3 (0.1% by volume) [47, 51, 54, 61] or 1 kg/m^3 [43]). The lower dosage (0.6 kg/m^3) is also recommended [42, 43, 46, 47, 53]. The minimum amount of 2 kg/m^3 [46] is used in the case of very fine monofilament fibres providing resistance to explosive spalling in the case of fire.

Polypropylene monofilaments are used as the reinforcement (non-structural) of the following concrete elements/structures:

- stucco, screeds and other aesthetically demanding concrete elements (fine multifilament fibres provide strong cracking resistance with a smooth surface);
- thin-walled façade elements (panels, etc.);
- elements of 'small architecture';
- layers of repair reinforced concrete (shotcrete method);
- overlays, toppings;
- sidewalks, pedestrian paths, curbs, etc.;
- floors;
- tunnel linings;
- water retaining structures, sewer pipes, etc.;
- sea coast protection elements [4, 6, 10, 40, 43, 45–47, 51–53, 55, 61].

Fine polypropylene fibres are also applied as the components of various repair materials, which are produced on the basis of cement binder.

Since the 1990s, monofilament polypropylene fibres have been used to increase the **fire resistance** of concrete, e.g. in tunnel linings [10, 16, 41, 43–47] (see Section 3.2).

4. Fibrillated polypropylene microfibres

The modification of the shape of monofilaments (straight, individual fibres) in the 1980s and 1990s [12, 37] allowed for the formation of net-shaped fibres (fibrillated fibres). This has resulted in higher bond strength between fibres and the cement matrix and thus, better mechanical properties of fibre reinforced cement composites for the fibrillated fibres compared to the monofilaments.

4.1. Manufacturing of fibrillated polypropylene microfibres

Fibrillated (chopped-film) polypropylene fibres are manufactured from 100% virgin, isotactic polypropylene in an **extrusion process** of molten polymer using a rectangular die. The product of the extrusion is a polypropylene film (**sheet**), which is slit longitudinally into **tapes** after the application of a special finish (Fig. 1, 3). The tapes are then uniaxially stretched over specially designed roller pin systems [64]. The process of drawing out the

tapes results in an increase in the level of molecular orientation of the polymer and hence in the improvement of the mechanical properties of the fibres, however, this process leaves the tapes weak in the lateral direction. The final stages are splitting polypropylene tapes to achieve the main- and cross-fibril networks (Fig. 3) and cutting the bundles of slit tapes to the desired length. Fibrillated fibres, contrary to monofilaments, prevent balling because the bundles, separated into individual fibres during mixing, are evenly distributed throughout the cement matrix. High-precision fibrillation is crucial to ensure the uniform dispersion of fibres. The fibres also reduce the segregation of components of the concrete mixture.

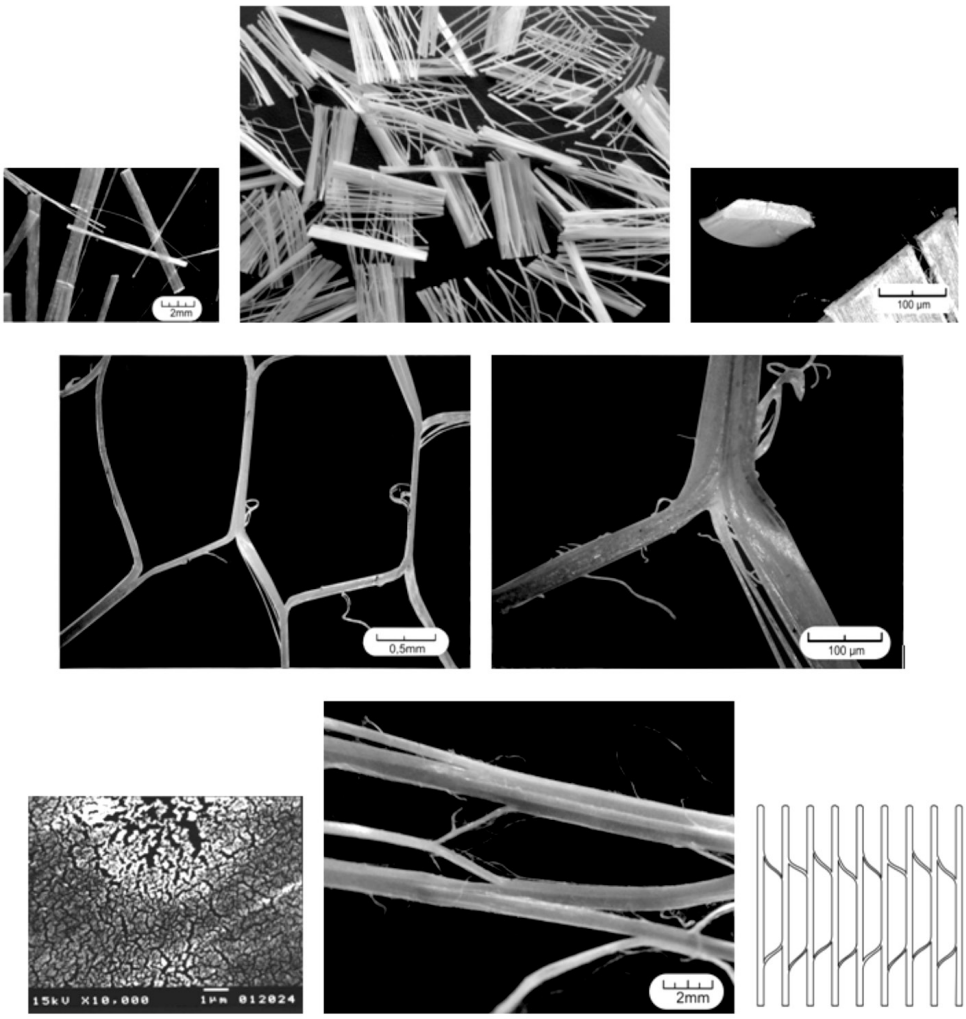

Fig. 3. Fibrillated (net-shaped) polypropylene microfibres (10x, 20x, 200x); surface of fibrillated polypropylene microfibres coated with a special substance (1000x) [37, 45, 51, 61]

A **net-like** physical structure of fibrillated fibres and the special fibre finish (coating) applied on the surface of fibres (as in the case of monofilament fibres; see Section 3.1) provide a good mechanical bond between the fibres and the cement matrix [39].

A very good mechanical anchorage has been obtained in the patented high tenacity polypropylene fibres (with an average cross-section of 30 μm by 200 μm), having mechanical properties which are significantly better than in the case of fibrillated fibres (with a tensile strength above 500 MPa and a modulus of elasticity above 7 GPa) [4]. High performance polypropylene fibres are manufactured from the extruded tapes, which are split mechanically into single rectangular fibres in such a way that the edges of the fibres become uneven and frayed to induce a good mechanical bond with the cement matrix. The process of splitting has been highly controlled to change the size of the cross-section of the fibres and the degree of fraying. The width may vary considerably both from fibre to fibre and also along the individual fibre.

Fibrillated fibres made from 100% recycled polypropylene are also available on the market [53].

4.2. Properties of fibrillated polypropylene microfibres

The **geometry** of fibrillated polypropylene fibres (with a rectangular cross-section) is described by the thickness of the film (tape), ranging from ~30 μm to 100 μm (35, 50, 80 μm are the most common) and the width of individual filaments (fibrils), ranging from ~200 μm to 600 μm (usually 330 μm, 500 μm) [4, 10, 45, 47, 54]. The bundles consist of several filaments (fibrils) cross-linked together (Fig. 3) (as presented in Patent [37]).

Fibrillated polypropylene fibres are available in **lengths** from 6 to 51 mm (19, 38 mm are the most common) [10, 40, 45, 47, 51, 53–56, 61, 62].

An increase in fibre length may result in a higher bond [64]; however, longer fibres and a higher amount (dosage) of fibres provide a greater reduction in the consistency of the concrete mixture and thus workability of the concrete mixture decreases.

A network of fibrillated fibres eliminates bleeding, because the collated, bundled filaments (fibrils), **cross-linked** together, are uniformly distributed in the cement matrix during mixing with the other components of concrete [4, 6, 55, 56].

Fibrillated polypropylene microfibres, as with other type of polyolefin fibres, provide strong adhesion when used in shotcrete; therefore, the **rebound** is lower than that in concrete without fibres and the application of thicker layers in one pass is possible [51, 56]. Moreover, they provide the resistance to fire-induced **explosive spalling** [45, 56].

Fibrillated polypropylene fibres are characterised by the **tensile strength** of 300–500 MPa (most often 300, 400, 500 MPa) and a **Young's modulus** of around 5 GPa (Table 1) [10, 45, 47, 51, 55]. They reduce the formation of cracks caused by **plastic** and **drying shrinkage** and **plastic settlement**. Therefore, they are applied as the secondary reinforcement of concrete. Polymer fibres cannot replace structural steel reinforcement, i.e. they cannot be used as the primary reinforcement providing post-peak strength and toughness [4, 10, 14, 47, 51, 53, 56, 61, 62, 64]. The fibres may be applied as an alternative to a welded wire mesh, e.g. in ground-floor slabs.

Lower amounts of fibres (less than around 1 percent of the volume fraction; see Section 4.3) are used to control shrinkage cracking in slabs, pavements, etc. which have large exposed surfaces that are highly susceptible to shrinkage cracking. The application of higher amounts of fibres may improve other properties of concrete such as **impact**, **abrasion** and **fatigue resistance**, etc. [40, 45, 51, 53–56]. For elements subjected to impact loading, the protection against initial cracking providing by the fibres is particularly important [6].

4.3. Application of fibrillated polypropylene microfibres

Fibrillated polypropylene microfibres are usually used at the **dosage** of 0.1–0.2% by volume (0.9–1.8 kg/m^3), most frequently in the amount of 0.9 kg/m^3 or 1 kg/m^3 [10, 45, 51, 53, 54, 62]. The maximum amount of 6 kg/m^3 for shotcrete is also given by the manufacturer [45].

The application areas of fibrillated polypropylene fibres are similar to that of monofilament polypropylene fibres [40–41, 45, 47, 51, 53–56, 61, 62] (see Section 3.3), since the properties of two types of polypropylene microfibres do not differ considerably. However, fibrillated fibres are recommended as the cracking reinforcement of, for example, ground-floor slabs and many prefabricated concrete elements [45, 51, 53, 61].

5. Macro-synthetic fibres

The weakpoints of polypropylene microfibres – their low modulus of elasticity: 2–5 GPa (by comparison, for steel fibres it is 210 GPa [10]) and their tensile strength of 150–500 MPa (for steel fibres this is 700–2000 MPa [10]) as well as the poor bonding of fibres (without the special fibre finish) with the cement matrix are improved in **macro-synthetic fibres**, also known as **monofilament polyolefin macrofibres**, **bi-component fibres** or **high performance macrofibres**. The modification of polypropylene microfibres, made in the **materials** that form a fibre and the **fibre morphology** allows the formation of macro-synthetic fibres. Macrofibres, first used as the concrete reinforcement in the mid-1980s [33], have been developed over recent years.

5.1. Composition, manufacturing and structure of macro-synthetic fibres

Regarding the **materials** that form a fibre, macro-synthetic fibres are not mono-component fibres made of polypropylene (contrary to polypropylene microfibres), but they are made from modified polyolefins (usually polypropylene and polyethylene; 100% virgin resins). Macrofibres are mainly **bi-component fibres** [1, 45, 48, 62].

Macrofibres are produced by **melt spinning** in the process of extrusion of individual fibres (as with monofilament polypropylene microfibres; see Section 3.1).

The popular structure of macro-synthetic fibres is the **sheath-core** structure with one of the fibre components (core) surrounded by another component (sheath, also known as shell) (Fig. 4, 6) [18, 39].

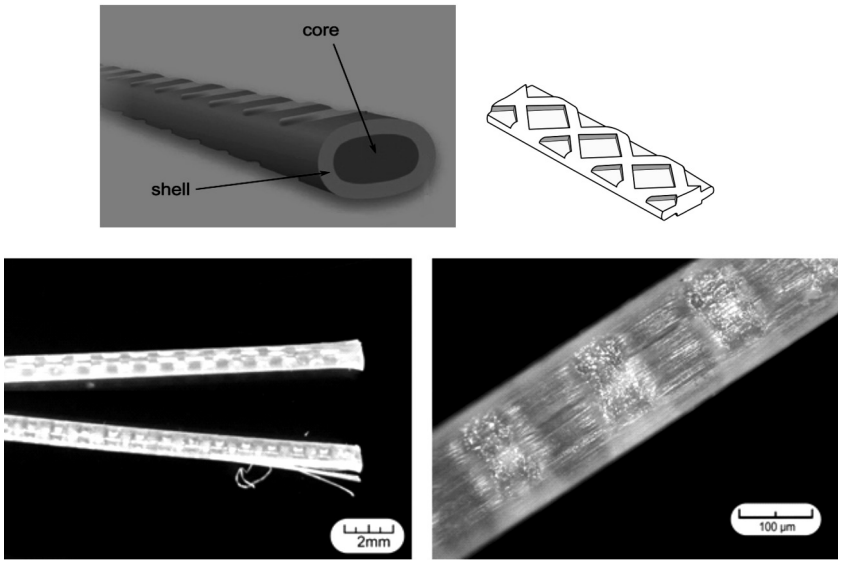

Fig. 4. Macro-synthetic fibres: bi-component, sheath-core (shell-core), embossed [45, 48]

Sheath-core fibres, described in Patent [39] (published in 2002), are monofilament bi-component fibres spun from two different types of polymers which are extruded side-by-side through a set of the holes [21]. As presented in Patent [39], sheath-core fibres may be fabricated with a ratio of sheath to core from 25:75 to 40:60 by weight. Moreover, a core should preferably be covered with a sheath on at least 90% of its surface; however, the percentage of a cover may be lower. Other structures of fibres, suggested in Patent [39] are **side-by-side**, **islands-in-the-sea**, **citrus type (segmented pie)**, depending on the arrangement of the polymer streams in the process of extrusion.

The material that forms an inner component (**core**) is a high strength and high E-modulus polymer or copolymer (also modified). The core provides the mechanical properties of the fibre. According to Patent [39], a core may be polypropylene or other polyolefins (linear high-density polyethylene, heterogeneously-branched linear low-density polyethylene, etc.), nylon, polyester or copolymers. The material used as a core should be compatible with sheath components. **Compatibile** means that there is sufficient adhesion of the core to the sheath. The core, proposed in Patent [38] (published in 2015), is a polymer blend of polypropylene grafted with maleic anhydride as the first constituent (maleic anhydride ensures a very good chemical bond between the core and the sheath) and polypropylene or polyethylene as the second constituent.

The outer component (**sheath**) determines the strength of the bond of the fibre with the cement matrix. The sheath is made from materials that provide a strong **chemical** bond. As proposed in Patent [38], ethylene-vinyl alcohol (EVOH) may be used as the sheath. According to Patent [39], a strong bond may be achieved by the application of a fusing-fraying polymer as the sheath. The examples of sheath composition are as follows: 80%

polyethylene (low density of 0.913 g/cm^3) and other constituents – 10% component A+10% component B or 10% component A+10% component C or 10% component B+10% component C; where component A refers to polyethylene grafted with maleic anhydride, component B refers to ethylene-styrene and component C refers to ethylene acrylic acid. Maleic anhydride and other additives provide very good chemical bonds between the sheath and the core as well as between the sheath and the cement matrix.

When macrofibres are made from only polypropylene (as **mono-component** fibres), specific **chemical compounds** should be incorporated into the base polypropylene resin before extrusion, as described in [2]. As polypropylene is chemically inert (polypropylene does not include functional groups that can chemically interact with the cement matrix), the added compounds provide a chemical bond between polypropylene fibres and the cement matrix through participation in the cement hydration reactions.

Experimental studies on the materials offering a good chemical bond have been carried out by many research centres and universities [2, 4, 6, 7, 10].

In the case of **mono-component** polypropylene macrofibres, not only the modification of a chemical bond by the addition of chemical compounds into polypropylene but also the increase in **wettability** (physical adhesion) of fibres by the application of a **special finish (coating)** on the surface of macrofibres (polypropylene is hydrophobic) may enhance the bond with the cement matrix, as in the case of microfibres (see Section 3.1) [10].

The materials that form a fibre have an infuence on **chemical** and **physical adhesion**. Two types of adhesion together with the mechanical bonds, **mechanical anchorage** and **frictional bond**, determine the interfacial bond between the fibres and the cement matrix [19, 25, 64]. The mechanical bonds depend on the morphology of macrofibres – their shapes and textures.

5.2. Morphology of macro-synthetic fibres

The **fibre shape** and the **fibre texture** strongly affect the mechanical bond of fibres with the cement matrix and subsequently, the mechanical properties of fibre reinforced cementitious composites.

Regarding the **mechanical anchorage** of macrofibres with the concrete matrix, the bond may be achieved through **fibrillation**, **fraying** and the use of various geometric fibre **shapes**.

As described by Trottier et al. [28], **self-fibrillating** macrofibres can be made (Fig. 5) when two polymers applied as the core and the sheath of bi-component fibres are incompatible (typically, they should be compatible; compatibility of the components with each other and with the cement matrix provides strong chemical bonds – see Section 5.1). The monofilament, formed through the process of extrusion of a blend of two polymers (77% polypropylene and 23% high-density polyethylene) may fray when mixed with other components of the concrete mixture. The fibrillation occurs due to the immiscibility of the two polymers, which are separated from each other during mixing. Self-fibrillating fibres are characterised by a strong mechanical bond with the cement matrix [28].

The mechanical bond may also be obtained through **fraying** (partial fibrillation of the fibre). A fusing-fraying polymer, proposed in Patent [39] as a sheath, should have a lower melting point than a core polymer. This affects the behaviour of the core and sheath polymers

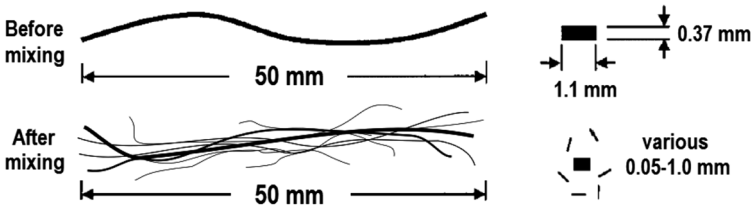

Fig. 5. 'Self-fibrillating' monofilament – fibre fibrillation and the change in dimensions before and after mixing [28]

during drawing. When the filament (fibre) is drawn, the two polymers extend to different degrees. During mixing with other constituents of the concrete mixture, the filaments fray at the ends into distinct fibrils. When fraying is too extensive, toughness of the fibre reinforced concrete can decrease. The controlled fraying overcomes the problem of inadequate bonding of large diameter fibres by giving them greater surface area to anchor to the cement matrix at the ends (Fig. 4, 6) [41, 45, 46, 48, 49]. Moreover, a lower melting temperature of the sheath compared to the core allows for melting of the sheath as the first and the fusing of filaments without substantially affecting the core polymer and thus without the changes in mechanical properties of fibre reinforced cement composites.

The mechanical anchorage strongly depends on the shape of fibres [20, 30]. The results of the investigations on the effect of the **geometry** of macro-synthetic fibres on the **interfacial bond strength** (known also as **interfacial shear strength** or **pullout strength**), conducted by Won et al. [30], in accordance with JCI SF-8 (Japan Concrete Institute) standard [36] are presented in Table 2.

Table 2

Interfacial bond strength of macro-synthetic fibres with various types of mechanical anchorage [30]

Fibre geometry (l = 50 mm)	Mechanical anchorage type	Cross-section $b \times h$ [mm]	Interfacial bond strength τ_b [MPa]	$\tau_b/\tau_{b,\text{straight}}$
	Straight	1.4 × 0.7	0.28	1.00
	Crimped	1.4 × 0.7	1.82	6.50
	Twisted	2.0 × 0.7	0.56	2.00
	Enlarged ends	Diameters: 1.0; 3.0	0.71	2.54
	Sinusoidal ends	1.4 × 0.7	0.72	2.57
	Hooked	1.4 × 0.7	0.40	1.43
	Double duoform	1.4 × 0.7; 2.0 × 0.7	1.10	3.93

Interfacial bond strength, the parameter describing the mechanical anchorage of the fibres [13], has been calculated according to the formula given in standard [36]:

$$\tau_b = \frac{P_{\max}}{\pi d_{eq} l_e} \tag{1}$$

where:

τ_b – interfacial bond strength (maximum) [MPa],
$P_{\max}$ – maximum pullout load [N],
d_{eq} – equivalent diameter of fibre [mm],
l_e – embedded length of fibre [mm].

For all types of deformed fibres tested (crimped, twisted, enlarged ends, sinusoidal ends, hooked and double duoform), the interfacial bond strength is greater than for straight fibres (Table 2). The highest bond strength (1.82 MPa) was obtained for **crimped** fibres, this was more than 6 times higher than for straight fibres (0.28 MPa). High bond strength was also observed in cases of fibres with sinusoidal ends, fibres with enlarged ends and fibres with twisted forms; fibres with hooked ends are less effective. Pullout failure was noticed for fibres with sinusoidal ends and hooked fibres [30].

A comparative analysis of the bond strength of macro-synthetic fibres and steel fibres was carried out by Richardson et al. [22]. In the pullout test, performed according to the procedure described in the paper, the bond strength observed in the case of macro-synthetic fibres (40 mm × 1.67 mm × 0.095 mm, composed of 90% polypropylene and 10% polyethylene, characterised by a tensile strength of 620 MPa and a modulus of elasticity of 9.5 GPa) is 0.47 MPa whereas for steel fibres (50 mm long and 1 mm in diameter, cold drawn, hooked-end, with a tensile strength of 1100 MPa), a bond strength of 4.12 MPa was obtained.

Not only crimping, but also denting is recommended in Patent [38] (published in 2015) as a very useful method of increasing the bond of fibres with cementitious materials. Currently, the produced macro-synthetic fibres are deformed fibres: **embossed** fibres (more popular) with various textures (Fig. 4) [25, 41, 45, 47, 48, 51, 55, 61] and **crimped** fibres (Fig. 6) [41, 42].

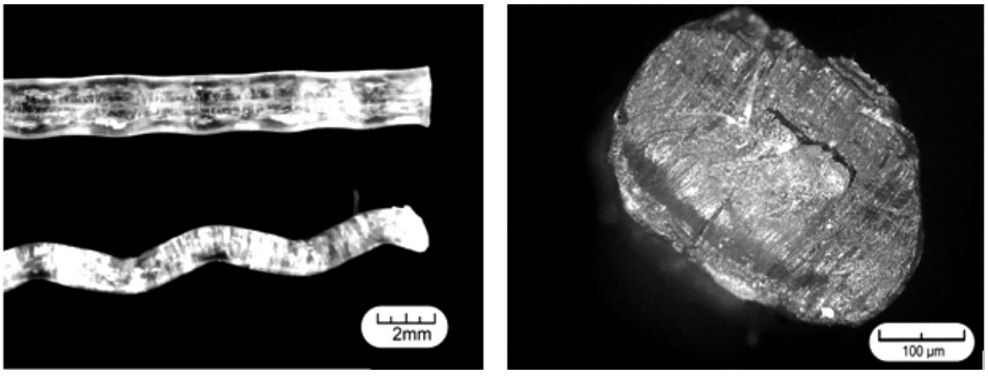

Fig. 6. Macro-synthetic fibres: crimped (10x, 200x) [41]

The use of embossed fibres, having a large lateral surface area, also results in a high **frictional bond** [25, 41, 47, 48]. Embossed fibres, which provide a strong interfacial fibre-cement matrix bond, are more effective than other types of macro-synthetic fibres.

The improvement in the frictional bond by the depositing of silica nanoparticles on the surface of polypropylene fibres (by sol-gel synthesis using ammonia as the basic catalyst) was proposed by Di Maida et al. [9].

Methods for the enhancement of the interfacial bond are constantly being developed.

5.3. Properties of macro-synthetic fibres

Macro-synthetic fibres differ from polypropylene microfibres in their **dimensions**. They are larger than polypropylene microfibres, with a diameter of ~0.8–1.1 mm (~0.8 mm or 1mm) and typically they are 50 mm long. Their diameters and lengths are similar to those of the steel fibres. Macro-synthetic fibres are available in lengths from 30mm to 65mm (the most common being 50 mm) [40–52, 54–56, 60–62].

The mechanical properties of macro-synthetic fibres are a **Young's modulus** from around 5 GPa to 10 GPa (crimped fibres – about 5 GPa; embossed fibres – 8–10 GPa) and a **tensile strength** of between 470 MPa and 690 MPa (crimped fibres – around 500 MPa; embossed fibres – usually 550 MPa) (see Table 1), which depend on the used polymers and the manufacture method; they are better in comparison with the properties of microfibres [1, 4, 22, 40–52, 54–56, 60–62]. However, their Young's modulus (5–10 GPa) is not larger than that of cement concrete (about 30 GPa). Since 'reinforcing fibres are fibres that have Young's modulus higher than a base material' (according to the definition given in [4, 17]), macro-synthetic fibres should not be used as 'structural' fibres – the primary reinforcement of concrete, i.e. they should not replace steel structural reinforcement (steel rebars and/or steel fibres) (by comparison, the values of Young's modulus and the tensile strength for steel fibres are 210 GPa and 500–2000 MPa, respectively) [4, 10, 17, 43, 51, 52, 57, 58, 61].

As fibrillated polypropylene fibres, macro-synthetic fibres protect concrete against **cracking** occurring in the fresh and hardening concrete caused by plastic and drying shrinkage, plastic settlement, etc. [10, 17, 20, 49–52, 55, 56, 61, 62].

Regarding the behaviour of hardened concrete with macrofibres at **bending**, 'macro synthetic fibres provide some post-cracking or residual moment capacity but with significantly lower performance than steel fibres' – 'The Design Code for Concrete Industrial Ground Floor Slabs – TR34', by the Concrete Society; cited in [1]. The **post-cracking zone** in macro-synthetic fibre reinforced concrete depends on the **dosage** (see Section 4.4) and the types of fibres (materials, geometry, etc.) [20, 26, 41, 49, 50–52, 55, 56, 61, 62]. The example of the post-peak behaviour during the bending of 28-day concrete containing 2 kg/m^3 of 50 mm-long, bi-component (polypropylene-polyethylene) macro-synthetic fibres (characterised by a Young's modulus of 10 GPa and a tensile strength of 618 MPa) is presented in Fig. 7 [32, 45]. Comparing the load-deflection curves for concrete with steel and macro-synthetic fibres, steel fibres strongly enhance concrete after the peak load whereas macrofibres slightly improve fracture toughness of the brittle concrete matrix. Thus, macro-synthetic fibres can be recommended as a secondary reinforcement for crack control, but not for the structural load-bearing application.

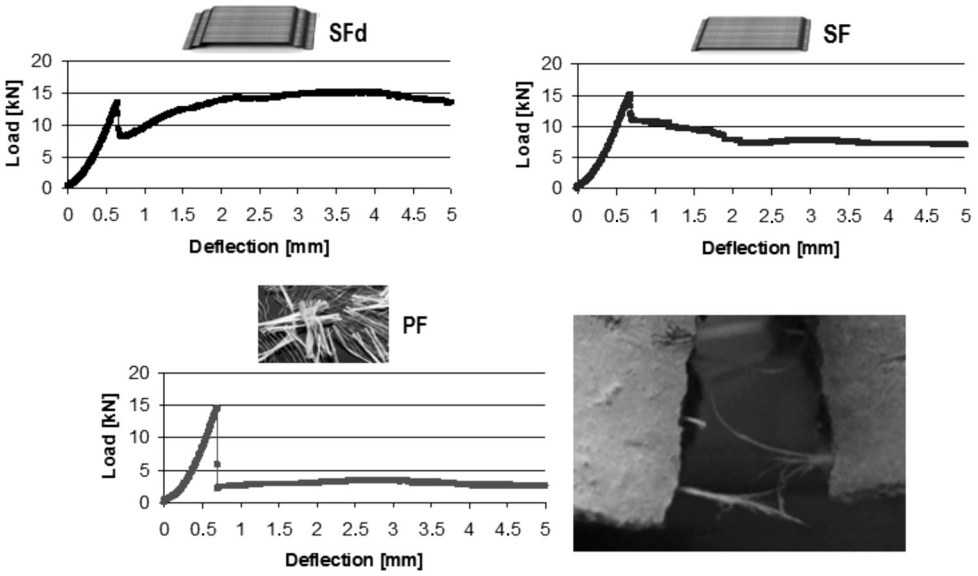

Fig. 7. Load-deflection curves recorded for 28-day concretes with bi-component (polypropylene-polyethylene) macro-synthetic fibres (PF), l = 50 mm, E = 10 GPa, tensile strength = 618 MPa, 2 kg/m^3; steel fibres with single hooks (SF), l = 60 mm, E = 210 GPa, tensile strength = 1225 MPa; steel fibres with double hooks (SFd), l = 60 mm, E = 210 GPa, tensile strength = 2300 MPa; SF or SFd – 30 kg/m^3; macro-synthetic fibres broken during the destruction of the beam [32]

As reported in [14, 26, 41–42, 46–52, 56, 61, 62, 64], macro-synthetic fibres improve not only flexural strength, but also **impact**, **fatigue** and **abrasion** resistance. The influence of the addition of macrofibres on the 28-day **compressive strength** of concrete is insignificant [10, 26, 32]. Increases in these mechanical properties of fibre reinforced concrete depend on the dosage of fibres (see Section 5.4) and their geometry [46–48]. However, macro-synthetic fibres are **prone to creep** (see Chapter 2).

In shotcrete applications, the fibres increase the compaction of concrete, reduce rebound and permit thicker layers per pass [49, 51, 55, 61].

Macro-synthetic fibres can reduce **spalling** of concrete at high temperatures [23, 48]. But, on the other hand, since macrofibres are **prone to heat damage**, they start to lose their mechanical properties as soon as the temperature reaches 50°C, by contrast steel fibres keep their mechanical performance up to a temperature of 350–400°C [43]. Synthetic fibres melt at around 165°C (the melting point ranges from 159°C to 179°C). The ignition point is higher than 450°C (maximum 590°C), depending on the type of fibres [48, 62]).

Macro-synthetic fibres are **non-magnetic**; therefore, they are widely used as concrete reinforcement in places where non-metallic materials are required, e.g. in hospital rooms equipped with specialist equipment [41, 51, 61].

Moreover, polypropylene-based macrofibres are chemically inert and provide excellent **corrosion resistance** – this allows their broad range of applications (see Section 5.4).

5.4. Applications of macro-synthetic fibres

Macro-synthetic fibres are applied at a significantly higher **dosage** (2–10 kg/m^3, depending on their application, this is frequently 5–7 kg/m^3) than polypropylene microfibres (usually 1 kg/m^3). The number of fibres, depending on the dosage, is 33000–62500 per kg [1, 4, 22, 45–48, 50, 55]. Macrofibres can be used as an alternative to welded steel wire mesh reinforcement which is used as anti-shrinkage reinforcement [41–43, 46–52, 55, 61, 62].

The advantageous properties of concrete reinforced with macro-synthetic fibres result in the application of these fibres in various concrete products, from architectural elements to structures exploited in harsh environmental conditions – they are also used when protection against spalling is required. Macrofibres are recommended as the reinforcement of concrete in the following concrete elements/structures [17, 23, 41–43, 46–49, 50–52, 55, 56, 61, 62]:

- precast or sprayed architectural elements such as cladding panels, elements of 'small architecture' and when complicated geometrical shapes are required;
- precast elements with fibres used as handling and transportation reinforcement;
- pathways, sidewalks, driveways, etc.;
- whitetoppings, pavements;
- external hardstandings, e.g. car parking areas, storage areas;
- floor slabs;
- sprayed concrete used for slope stabilisation, repair works, etc.;
- tunnel linings (e.g. mining, road tunnels);
- precast pipes, etc.;
- water tanks, etc.;
- tanks in sewage treatment plants, sewage tunnels, etc.;
- elements of marine structures.

Macro-synthetic fibres have been used as the non-structural (secondary) and structural (primary) reinforcement of concrete. The application of macro-synthetic fibres (e.g. in tunnel linings, slabs-on-ground [1, 8, 10, 23, 26, 29, 48]) as the only structural reinforcement of concrete (instead of steel rebars or steel fibres) is the subject of the wide discussion. There are many debates regarding the benefits that macro-synthetic fibres can offer and the fields of their application [5, 17, 22, 57, 58].

For structural applications of macro-synthetic fibres, the low E-modulus of these fibres (5–10 GPa compared to 210 GPa for steel fibres) is of great concern. Since the lower the Young's modulus, the higher the deformation ($\sigma = E\varepsilon$), macro-synthetic fibres are characterised by large elongation which is much higher than for steel fibres [17]. Moreover, polymer fibres are prone to creep – they have a tendency to time-dependent deformation under constant load.

Therefore, the required tests for macro-synthetic fibre reinforcement concrete refer not only to determining load-bearing capacity, but also to the time-dependent properties of concrete, specifically, **creep behaviour** and crack width [17]. The reinforcing effect of fibres, observed, for example, in the standard beam test does not represent the long-term behaviour of concrete with macro-synthetic fibres, which are prone to creep. The real residual load-bearing capacity of bending elements can be significantly lower than the design value based on short-term strength assessment (15-minute test).

The experimental investigations conducted by Zerbino at al. on the time-dependent behaviour of pre-cracked macro-synthetic fibre reinforced concrete (PFRC) subjected to flexural loading [31] revealed significant creep of cracked concrete with polymer fibres. Moreover, the research has also shown that the application of loading-unloading cycles does not imply significant changes in the creep rate when compared to permanent loads of a similar magnitude.

Significant creep, and thus considerable crack widening over time, has also been observed for PFRC under uni-axial tensile sustained loading (Babafemi et al. [3]). The experimental studies have indicated that the fibre creep and the time-dependent fibre pull-out are the major sources of creep behaviour. Furthermore, the time-dependent crack widening has not been stabilized for 8 months, even at loads as low as 30% of the post-peak resistance [3].

Creep of macro-synthetic fibres leads to various crack widths thereby adversely affecting the serviceability and durability of concrete. It may cause failure of concrete at service loads [3, 17, 31].

However, the research conducted by Winterberg et al. [29] has shown that macro-synthetic fibres used in combination with conventional reinforcing bars are very effective in reducing crack widths generated in reinforced concrete elements as a result of flexural loading. Macrofibres are capable of bridging large cracks – they control crack widths to achieve the value below a permissible value of crack width for various environments (e.g. the tested macro-synthetic fibre reinforced concretes have reached the crack widths lower than 0.10–0.15 mm [29]). Thus, in reinforced concrete, flexural elements subjected to aggressive environmental conditions, macro-synthetic fibres, instead of steel fibres, are recommended to be used to reduce crack widths.

The study of creep behaviour of macro-synthetic fibre reinforced concrete in the cracked state is one of the main subjects of interest nowadays. Many research groups in the world are working on this matter. The development of test methods and the definition of parameters for its characterisation have become crucial points [3, 31].

6. Summary

Polypropylene-based fibres, the most popular polymer fibres used nowadays for the reinforcement of cementitious composites, are presented in this paper.

Various types of these fibres, polypropylene microfibres (monofilaments and fibrillated fibres) and macro-synthetic fibres (made from polypropylene and polyethylene), are the result of years of research in the petrochemical and textile industries and experience in the field.

The changes related to the material, the morphology and the surface of fibres, achieved by the selection of appropriate raw materials and the modification of the sophisticated production process allows the production of new generations of polypropylene fibres.

Individual, straight polypropylene microfibres (monofilaments), cut from a yarn (bundles of several fibres), have been modified by the application of the special fibre finish coating on their surface – this increases the wettability of fibres and enlarges the surface area of the fibres, thus improving the bond between the fibres and the cement matrix. Nowadays,

a fibre finish designed to obtain a rough surface of the fibres is commonly used for all types of polypropylene fibres. The precise fibrillation, achieved by the application of the patented methods, has changed the fibre shape. The fibrillated (net-shaped) fibres, formed during this process, achieve stronger mechanical anchorage to the cement matrix than monofilaments. Macro-synthetic fibres, the last generation of polypropylene fibres, are similar in their dimensions and shape to steel fibres. Currently, macro-synthetic fibres have been produced using two kinds of polyolefins (polypropylene and polyethylene) and various manufacturing methods to improve the mechanical bond of the fibres with the cement matrix (the frictional bond and the mechanical anchorage) and their chemical and physical adhesion. The structures of the macro-synthetic fibres, formed in the process of production, are sheath-core (popular) with one of the fibre components (core) (polypropylene) surrounded by another component (sheath) (polyethylene); side-by-side; islands-in-the-sea; citrus type (segmented pie). The mechanical anchorage of macro-synthetic fibres is achieved not only by fibrillation and self-fibrillation but also by fraying and the complicated shapes of fibres. Among the macrofibres of different shapes (straight, embossed, crimped, twisted, enlarged ends, sinusoidal ends, hooked and double duoform), embossed and crimped fibres are those with the best interfacial bond strength. A strong chemical bond with the cement matrix is provided by the outer material (sheath) of bi-component macrofibres or by chemical compounds, incorporated into the base polypropylene resin in one-component fibres.

The details concerning the manufacturing processes, the properties and the application areas of all types of polypropylene fibres, as well as the other polymer fibres for the purpose of comparison, are provided in this paper. Moreover, the influence of the production process of the polypropylene-based fibres on their properties (modulus of elasticity, tensile strength, bonding with the cement matrix, etc.) and then on the long-term mechanical behaviour of both fresh and hardened concrete reinforced with the fibres (the formation of cracks caused by plastic and drying shrinkage, plastic settlement, service loading; the creep behaviour; etc.) is widely analysed.

This paper also presents the debates, reported in the literature, regarding the benefits that macro-synthetic fibres can offer and the fields in which they can be applied. The use of macro-synthetic fibres as a structural reinforcement of concrete has been the subject of intense debates.

These discussions highlight the need for further experimental studies on polypropylene-based fibres as the reinforcement of cementitious materials since these fibres, which are relatively cheap and have been in use for more than 40 years, are also ‘fibres of tomorrow’.

References

[1] Alani A.M., Beckett D., *Mechanical properties of a large scale synthetic fibre reinforced concrete ground slab*, Construction and Building Materials, Vol. 41, 2013, 335–344.

[2] Attiogbe E.K., Schaef S., Kerobo Ch.O., Vojtko D., Nmai Ch.K., *A new fiber for enhanced crack control. Polypropylene fiber with chemical bond to concrete*, Concrete International, December, 2014, 35–39.

[3] Babafemi A.J., Boshoff W.P., *Tensile creep of macro-synthetic fibre reinforced concrete (MSFRC) under uni-axial tensile loading*, Cement and Concrete Composites, Vol. 55, 2015, 62–69.
[4] Bentur A., Mindess S., *Fibre reinforced cementitious composites*, Taylor&Francis, 2007.
[5] Bernard E.S., *Design of fibre reinforced shotcrete linings with macro-synthetic fibres*, 11th International Conference on Shotcrete for Underground Support, Davos, Switzerland, 7–10 June 2009, 161–171.
[6] Brandt A.M., *Cement based composites: materials, mechanical properties and performance*, Taylor & Francis, 2009.
[7] Chawla K.K., *Fibrous materials*, Cambridge University Press, 2005.
[8] Clements J.K., Bernard E.S., *The use of macro-synthetic fiber-reinforced shotcrete in Australia*, Shotcrete, Fall, 2004, 20–22.
[9] Di Maida P., Radi E., Sciancalepore C., Bondioli F., *Pullout behavior of polypropylene macro-synthetic fibers treated with nano-silica*, Construction and Building Materials, Vol. 82, 2015, 39–44.
[10] Domone P., Illston J., *Construction materials. Their nature and behaviour*, SponPress, 2010.
[11] Glinicki M.A., *Concrete with structural reinforcement*, 25th Workshop for Structural Designers (WPPK'2010), Szczyrk, 10–13.03.2010, 279–308 (in Polish).
[12] Goldfein S., *Plastic fibrous reinforcement for Portland cement*, Technical Report No. 1757-TR, US Army Engineering Research & Development Laboratories, Fort Belvoir, VA, USA, 1963.
[13] Han J.-W., Jeon J.-H., Park C.-G., *Bond characteristics of macro polypropylene fiber in cementitious composites containing nanosilica and styrene butadiene latex polymer*, International Journal of Polymer Science, 2015, homepage: www.hindawi.com/journals/ijps/2015/207456/ (access: 24.06.2016).
[14] Hannant D.J., *Fibre-reinforced concrete*, [in:] J. Newman, B.S. Choo (Eds.): *Advanced Concrete Technology. Processes*, Elsevier Ltd., 2003, Chapter 6.
[15] Hannant D.J., *Durability of polypropylene fibers in Portland cement-based composites: eighteen years of data*, Cement and Concrete Research, Vol. 28, 1998, 1809–1817.
[16] Kalifa P., Chene G., Galle C., *High-temperature behaviour of HPC with polypropylene fibres. From spalling to microstructure*, Cement and Concrete Research, Vol. 31, 2001, 1487–1499.
[17] Lambrechts A., *Steel – and synthetic fibre reinforced concrete. Which fibre to use for which application and why?*, Bekaert, 2009, homepage: www.ribaproductselector.com/Docs/6/17706/external/COL717706.pdf (access: 24.06.2016).
[18] Milwich M., *Types and production of textiles used for building and construction*, [in:] G. Pohl (Ed.): *Textiles, polymers and composites for buildings*, Woodhead Publishing, 2010, Chapter 2.
[19] Naaman A.E., *New fiber technology*, Concrete International, July, 1998, 57–62.
[20] Oh B.H., Kim J.C., Choi Y.C., *Fracture behavior of concrete members reinforced with structural synthetic fibers*, Engineering Fracture Mechanics, Vol. 74, 2007, 243–257.

[21] Preston J., *Man-made fibre*, homepage:www.britannica.com/technology/man-made-fiber (access: 13.04.2016).
[22] Richardson A.E., Landless S., *Synthetic fibres and steel fibres in concrete with regard to bond strength and toughness*, Built Environment Research Papers, Vol. 2, December, 2009, 128–140.
[23] Ridout A., *Macro-synthetic fibre for segmental linings and other precast concrete elements*, Concrete, Vol. 42, September, 2009, 41–42.
[24] Sakurada I., *Polyvinyl alcohol fibers*, International Fiber Science and Technology Series, Vol. 6, Marcel Dekker Inc., 1985.
[25] Singh S., Shukla A., Brown R., *Pullout behavior of polypropylene fibers from cementitious matrix*, Cement and Concrete Research, Vol. 34, 2004, 1919–1925.
[26] Soutsos M.N., Le T.T., Lampropoulos A.P., *Flexural performance of fibre reinforced concrete made with steel and synthetic fibres*, Construction and Building Materials, Vol. 36, 2012, 704–710.
[27] Sun Z., Xu Q., *Microscopic, physical and mechanical analysis of polypropylene fiber reinforced concrete*, Materials Science and Engineering A, Vol. 527, 2009, 198–204.
[28] Trottier J.-F., Mahoney M., *Innovative synthetic fibers*, Shotcrete, Fall, 2004, 26–31.
[29] Winterberg R., Sedgman G., *In-service performance of macro synthetic FRC in tunnel linings*, Tunnelling Journal, February-March, 2015, 42–44.
[30] Won J.-P., Lim D.H., Park C.-G., *Bond behaviour and flexural performance of structural synthetic fibre-reinforced concrete*, Magazine of Concrete Research, Vol. 58(6), August, 2006, 401–410.
[31] Zerbino R., Monetti D.H., Giaccio G., *Creep behaviour of cracked steel and macro-synthetic fibre reinforced concrete*, Materials and Structures, Vol. 49, 2016, 3397–3410.
[32] Zych T., *Study of the properties of hybrid fibre reinforced concretes*, [in:] A. Zingoni (Ed.): *Research and Applications in Structural Engineering, Mechanics and Computation*, Taylor & Francis Group, 2013, 1579–1585.
[33] *Guidance on the use of macro-synthetic-fibre-reinforced concrete*, Technical Report 65, The Concrete Society, UK, 2007.
[34] ASTM C1116:2015. Standard specifications for fibre-reinforced concrete.
[35] EN 14889-2:2006 Fibres for concrete – Part 2: Polymer fibres. Definitions, specifications and conformity.
[36] JCI-SF8:1984 Method of testing for bonds of fibers, Japan Concrete Institute, Committee on Fiber Reinforced Concrete, Tokyo, Japan.
[37] Hogan, D.J., *Graded fiber design and concrete reinforced there*. Synthetic Industries, Chickamauga, GA. USA. Patent.US5456752 A. Pub.10.10.1995.
[38] Prasanna, K.J., *Bi-component fibers with EVOH on the surface for concrete reinforcement*. The Dow Chemical Company, Midland, MI. USA. Patent. US20150133018 A1. Pub.14.05.2015.
[39] Pyzik, A.J., et al., *Plastic fibers for improved concrete*. The Dow Chemical Company, Midland, MI. USA. Patent.US20020018895 A1. Pub.14.02.2002.
[40] http://www.abcpolymerindustries.com (access: 24.06.2016).
[41] http://www.adfil.co.uk (access: 24.06.2016).
[42] http://www.bautech.pl (access: 24.06.2016).

[43] http://www.bekaert.com (access: 24.06.2016).
[44] http://www.bm-underground.com (access: 24.06.2016).
[45] http://www.bruggcontec.com (access: 24.06.2016).
[46] http://www.chryso.com (access: 24.06.2016).
[47] http://www.danishfibres.com (access: 24.06.2016).
[48] http://www.elastoplastic.com (access: 24.06.2016).
[49] http://www.euclidchemical.com (access: 24.06.2016).
[50] http://www.fibercon.com.au/Macro-Poly.html (access: 24.06.2016).
[51] http://www.fibermesh.com (access: 24.06.2016).
[52] http://www.fibreistrice.com (access: 24.06.2016).
[53] http://www.forta-ferro.com (access: 24.06.2016).
[54] http://www.larsenbuildingproducts.com (access: 24.06.2016).
[55] http://www.nycon.com (access: 24.06.2016).
[56] http://www.sika.com (access: 24.06.2016).
[57] http://www.tunneltalk.com/TunnelTECH-Sep2014-Rossi-critique-of-Bernard-WTC-synthetic-FRS-paper.php (access: 24.06.2016).
[58] http://www.tunneltalk.com/Feedback-Nov2014-Response-to-macro-synthetic-fibre-critique.php (access: 24.06.2016).
[59] http://textileengineerr.blogspot.com (access: 24.06.2016).
[60] http://pol.sika.com (access: 24.06.2016).
[61] http://propexglogal.com (access: 24.06.2016).
[62] https://gcpat.com/construction/en-gb (access: 24.06.2016).
[63] https://worldwide.espacenet.com/publicationDetails (access: 24.06.2016).
[64] http://dtic.mil/dtic/tr/fulltext/u2/a262597.pdf (access: 24.06.2016).

CONTENTS

TREŚĆ

ISSN 0011-4561
ISSN 1897-628X